Alternative Neutralization Techniques for In-Space Charged Particle Thrusters and Electrodynamic Tethers

by

David Chia-Wei Liaw

A dissertation submitted in partial fulfillment
of the requirements for the degree of
Doctor of Philosophy
(Electrical Engineering)
in The University of Michigan
2014

Doctoral Committee:

Professor Brian E. Gilchrist, Chair
Professor Ronald M. Gilgenbach
Professor Mark Kushner
Professor John P. Verboncoeur

ACKNOWLEDGEMENTS

I would like to thank everyone who has guided and mentored me through my 20 years of education, and have shaped me into the person that I am today.

Firstly, I would like to give a large thank you to my research advisor, mentor, and chair of my dissertation committee, Professor Brian Gilchrist. As the one to impress upon me the importance and benefit of a Ph.D., I can undoubtedly state that without him I would not be where I am today. I would like to thank him for the guidance, mentorship, and support through my entire graduate career at the University of Michigan and providing me with absolutely all the resources I needed to be successful. His keen insights and technical capabilities have helped me solve the numerous problems I have encountered through this journey. Also thanks to his family (Marci, Thomas, and Patrick) for being a part of our large research family.

I would like to thank the rest of my dissertation committee, Professors Ronald Gilgenbach and Mark Kushner of the University of Michigan, and Professor John Verboncoeur of Michigan State University. All three have brought their own unique point of view, guidance, insight, and technical expertise to help shape my research. Professor Gilgenbach with his extensive practical plasma science knowledge, Professor Kushner with his plasma simulation and analysis expertise, and Professor Verboncoeur with his plasma simulation software acumen, especially with teaching me the ins and outs of the software he developed and that I used extensively.

A thank you to the Air Force and the Michigan Academic Center for Excellence in Electric Propulsion and the Michigan Institute of Plasma Science and Engineering for

the funding that they have provided me, my research would not be possible without it.

I would like to thank all the other faculty members I have worked with throughout my years for all the additional research experience they have provided me and their unique perspectives. Thanks to Professor Alec Gallimore, Sven Bilén, Joanna Mirecki-Millunchick, Michael Solomon, Nicholas Kotov, and Albert Shih. I would also like to thank Dr. Pete Peterson for his guidance on the NanoFET project.

An extended thank you goes out to all my fellow graduate students that I worked with, Dr. Louis Musinski and Dr. Thomas Liu, who were the early inventors and developers of NanoFET with Professor Gilchrist, for all the hands-on research experience they were able to impart on me (and help me avoid high voltage shocks), Dr. Rafael Ramos for providing a unique perspective on everything and great world experiences while sharing an office, and also to Iverson Bell, for keeping the office a fun place to come to and for his collaboration on numerous conference proceedings, best of luck to you as you close in on the finish line.

Also a thank you to all the undergraduates that have helped me with my research along my way, including the ones on the ZESTTR and MiTEE projects, especially Mike Huang, Vritika Singh, Dave Chen, Kyle Hagen, and Brandon St. Pierre. Special thanks to Scott Cooper for the two years he spent with our lab helping me run simulation after simulation and crunching piles of data. Thanks to Karla Johnson, Michelle Chapman, Beth Stalnaker, Eidilia Thomas, Marti Moon, John Eder, and Robb Gillespie for all the support you have provided along the way in navigating piles of paperwork, avoiding the wrath of OSEH, and machining parts to specifications I thought were impossible to meet.

A big thank you to the University of Michigan and the city of Ann Arbor for being the best place to grow up and call home for 20 years, and an incredible place to spend 8+ years as a college student. If I never had to leave, I would be ecstatic.

Thanks to all Ann Arbor residents for giving this college town a small town feel.

I would like to thank the Ann Arbor Public Schools, Huron High School and King Elementary School, for teaching me the value of education at a young age, and the great mentors and teachers they were able to provide, Mr. Peter Collins, Mr. Terrance Vogel, Mr. David Caine, and Mr. Eric Nelson as well as introducing me to the intriguing field of space sciences with Space Camp in the 5th grade.

I would like to thank all my friends that have kept me entertained and provided a necessary distraction throughout my years of education. You have provided me with the breaks I needed to get through this long, but fruitful learning experience. Thanks to those that I have stayed close with since my elementary school days, all the way up to those that I have met late in my graduate school career. Thanks for sharing my passion for all Michigan athletics and traveling all over the country in support of this, for wasting countless nights playing video games, board games, and poker, for going to Charley's with me, and for just being there whenever I needed some company. Without each and every one of you, college would not have been the unimaginably great experience that it has been for me.

Most importantly, I would like to thank my family, as none of this would be possible without the sacrifices that they have made. Thanks to my mom and dad for leaving everything they knew behind to come to the United States for a better life for my sister and me. Thanks for putting up with me through these last 25 years, and instilling the right principles in me, as well as motivating me to become a better person. Thanks to my sister, for being that tough older sister, the one that pretends not to care but is willing to listen to any problems. Through our numerous childhood arguments and our years spent apart we seem to have only grown closer together. And thanks to all my grandparents for everything they have done for me.

TABLE OF CONTENTS

CHAPTER

LIST OF FIGURES

Figure

LIST OF TABLES

Table

LIST OF APPENDICES

Appendix

LIST OF ABBREVIATIONS

$\mathbf{A}_e$ Electron Impact Area

$\mathbf{a}_{FN}$,$\mathbf{b}_{FN}$ Fowler-Nordheim Parameters

$\mathbf{A}_i$ Ion Impact Area

$\mathbf{b}_0$ Classical Distance of Closest Approach

$\mathbf{B}_0$ Magnetic Field

$\mathbf{d}$ Particle Diameter

$\mathbf{E}_\perp$ Electric Field Perpendicular to the Conductor Surface

$\mathbf{E}_0$ Charging Electric Field

$\mathbf{f}$ Frequency of Oscillation

FEAC Field Emitter Array Cathode

$\mathbf{G}$ Gravitational Constant

$\mathbf{I}_e$ Electron Current

$\mathbf{I}_{emitted}$ Current Emitted

$\mathbf{I}_i$ Ion Current

$\mathbf{I}_{load}$ Load Particle Density

$\mathbf{I}_{source}$ Source Particle Injection Rate

$\mathbf{J}_{SCL}$ Two-Dimensional Classical Space Charge Limited Current Density

$\mathbf{M}$ Mass of the Earth

$\mathbf{m}_e$ Electron Mass

$\mathbf{m}_i$ Ion Mass

$\mathbf{m}_R$ Reduced Mass

$\mathbf{n}$ Number Density

$\mathbf{n}_{21}$ Unit Vector Perpendicular to the Boundary

$\mathbf{n}_e$ Plasma Density

NP2C Ratio of Particles per Superparticle

$\mathbf{q}_0$ Charge Acquired by Particle

$\mathbf{r}$ Radius of the Orbit

$\mathbf{r}_c$ Gyroradius

SEM Scanning Electron Microscope

SVCTE Spatial-Varying, Common Time Emission

$\mathbf{T}$ Thrust Generated

$\mathbf{T}_0$ Initial Emission Energy

$\mathbf{T}_e$ Electron Temperature

$\mathbf{T}_i$ Ion Temperature

TVCSE Time-Varying, Common Spatial Emission

$\mathbf{v}$ Orbital Speed

$\mathbf{V}_0$ Potential Between the Cathode and the Surrounding Atmosphere

$\mathbf{v}_{emission}$ Emission Velocity

$\mathbf{v}_R$ Relative Velocity

$\mathbf{v}_{sp}$ Spacecraft Velocity

$\mathbf{v}_{Te}$ Electron Thermal Velocity

$\mathbf{v}_{Ti}$ Ion Thermal Velocity

$\mathbf{W}_R$ Center of Mass Energy

Γ_e Electron Flux

Γ_i Ion Flux

$\Delta\mathbf{t}$ Simulation Time Step

$\Delta\mathbf{v}$ Change in Particle Velocities

ϵ Voltage Equivalent of Energy

Λ Ratio of Debye Length to Minimum Impact Parameter

$\rho_{steadystate}$ Steady State Plasma Density

σ Surface Charge Density

σ_{90}**(large)** Large Angle Scattering Collisional Cross Section

σ_{90}**(small)** Effective Small Angle Scattering Collisional Cross Section

τ Mean Time Between Interactions

υ Differential Velocity

ω_c Gyration or Cyclotron Frequency

ABSTRACT

Alternative Neutralization Techniques for In-Space Charged Particle Thrusters and Electrodynamic Tethers

by

David Chia-Wei Liaw

Chair: Brian Gilchrist

Over the last few years, there has been growing interest in a new class of space propulsion for smaller satellites in low Earth orbit that utilize highly charged and accelerated nanoparticles (Nanoparticle Field Extraction Thruster or NanoFET) or liquid droplets (colloidal thrusters) to provide thrust. As with any electric propulsion system that emits charged particles, an issue to be examined is how to ensure charge neutral operation. Specifically, this work investigates potential methods to self-neutralize or use the surrounding ambient ionospheric plasma to avoid the complexity of an additional neutralization sub-system.

The NanoFET system operates by charging and expelling either positively or negatively charged nanoparticles drawn from a dry powder through a MEMS-based sieve and grid structure. Similarly, colloidal thrusters charge liquid droplet particles to either polarity. This ability to charge particles to either polarity offers the possibility to use the particles themselves to self-neutralize the system. Common in-space electric propulsion systems only emit positive ion propellant, which requires that electrons be separately emitted, using hollow cathodes or other electron emitters. If NanoFET

and colloidal thrusters did not need a separate sub-system for neutralization, it would improve efficiency and reduce complexity.

Plausible options to neutralize NanoFET and colloidal thrusters with as little increase in complexity as possible are to emit equal amounts of oppositely charged particles by either (i) simultaneous emission from separate locations (ii) emission from a single location with periodic polarity change, or (iii) emission of a negatively charged nanoparticle beam into a background plasma that can provide an electron return current.

Even smaller than the satellites that NanoFET and colloidal thrusters are envisioned for providing propulsion to are a class of satellites called femtosatellites. Femtosatellites require unconventional means of propulsion due to their low mass, power, and size budget, with one possible propulsion technique being electrodynamic tethers. An area of study for the electrodynamically tethered femtosatellite system is the electron emission scheme either through a field emitter array cathode or a thermionic cathode/hot filament.

This thesis investigates all of these neutralization methods primarily through simulation. The challenges that will be discussed include:

1. A spatial-varying, common time emission scheme is able to effectively self-neutralize with only a 0.01% loss in thrust due to image charge induced axial electric field when emitting 1 A/m^2 of oppositely charged particles simultaneously out of adjacent emission ports.

2. A time-varying, common spatial emission scheme is able to effectively self-neutralize with only a 0.025% loss in thrust due to image charge induced axial electric field when emitting 1 A/m^2 of alternating polarities of emitted particles at 100 kHz out of a single emission port.

3. A single negatively charged beam emitting 312.5 μA at 100 or 500 seconds

specific impulse emitted into the ionosphere is able to utilize a $6.5*10^{10}$ m^{-3}, 0.1 eV, 7500 m/s ambient ionospheric plasma to partially neutralize, and in addition a single negatively charged beam emitting 312.5μA at 1000 seconds specific impulse emitted into the ionosphere is able to utilize a $3*10^{11}$ m^{-3}, 0.1 eV, 7500 m/s or a $6.5*10^{10}$ m^{-3}, 0.08 eV, 7500 m/s ambient ionospheric plasma to fully neutralize.

4. Both field emitter array cathodes and thermionic cathodes are feasible to be implemented on electrodynamically tethered femtosatellites to adequately provide electron emission current to counteract the electron collection current by occupying less than 6% of one side of any sized femtosatellite under study.

CHAPTER I

Introduction

This thesis focuses on neutralization techniques for small satellites in low Earth orbit. For these small satellites, unconventional thrusters are being developed and used, which have particular advantages. The thrusters being discussed and examined in this thesis operate in the unique fashion of emitting electrostatically charged particles or liquid droplets to provide thrust. In particular, this thesis will discuss self-neutralization techniques that are feasible for these charged particle thrusters such as the in-development Nanoparticle Field Extraction Thruster (NanoFET) (*Musinski*, 2009) (*Liu*, 2010) and liquid colloidal thrusters. Self-neutralization will accomplished either through oppositely charged particle emission or negative particle emission into plasma in low Earth orbit (LEO). In addition, this thesis will explore the use of well-tested as well as untested neutralizers for a new class of femtosatellites, where space is at a premium, being propelled through an unconventional propulsion method.

1.1 Charged Particle Thrusters

Charged particle thrusters differ from the more common ion and hall thrusters in that rather than ionizing gas propellant to create charge to be emitted, charged particle thrusters electrostatically charge particles or liquid propellant to create the charge to be emitted. This provides numerous benefits which will be discussed further.

Figure 1.1: Depiction of Virtual Cathode Effect due to Single Polarity Emission

The one benefit that can be taken advantage of for the purposes of neutralization is the ability of charged particle thrusters to be able to charge particles positively or negatively.

1.1.1 Neutralization of Charged Particle Thrusters

A concern of any electric propulsion device that emits charge is how to neutralize the system. In the absence of a neutralization technique and in vacuum, when charge is emitted from the system for thrust, the spacecraft will charge up in the opposite polarity as the emitted charge. As this continues, the spacecraft will continue to charge up, and eventually a virtual cathode effect will happen where the spacecraft is heavily charged in one polarity, and the emitted charge forms an oppositely charged cathode as shown in Fig. 1.1. In such a situation, any additional emitted particles will be decelerated by the strong electric field created between the spacecraft and the virtual cathode, and eventually returned to the spacecraft. This will negate the thrust generated by the emission of charge.

Most conventional electric propulsion systems such as hall thrusters and ion thrusters utilize a hollow cathode neutralizer. The hollow cathode neutralizer consists of a hollow cylinder called an insert that is made of a material with a low work function, a heater wrapped around the insert that gets it up to the proper temperature, along with a cathode orifice plate, a reflective sheathing, and a keeper. The propellant, typically a gas, is flowed through the cathode, which causes electron-impaction ionization, which creates a high-conductivity plasma cloud in front of the emission area of the thruster (*Domonkos et al.*, 1997). When positive charge is emitted from the thruster, the small, fast, mobile electrons from the plasma cloud are pulled along with the positive charge, neutralizing both the beam and the spacecraft. An example of how an ion thruster uses a hollow cathode to neutralize the emitted positive ions is shown in Fig. 1.2. However, using a hollow cathode to neutralize normally adds complexity as it requires an additional component. In this case, more importantly, it can decrease efficiency by up to 20% (*Patterson*, 1997). In NanoFET and liquid colloidal thrusters, a hollow cathode neutralizer adds a significant amount of complexity, as there is no gas propellant readily available as there is for ion and hall thrusters. An alternative to hollow cathodes being explored is using field emitter array cathodes (FEACs) to emit electrons (*Gilchrist et al.*, 2000) (*Temple*, 1999) (*Marrese and Gallimore*, 1998). However, such technology has yet to be proven to be successful in a harsh space environment.

For charged particle thrusters, a separate hollow cathode neutralizer is not ideal for operation, and therefore an alternative neutralization technique must be developed that ideally is efficient as well as simple. This thesis will explore the feasibility of utilizing charged particle thrusters ability to charge particles both positively and negatively to create a neutral emitted beam as well as a neutral spacecraft, either through temporal or spatial variation, to neutralize, but potential problems to this seemingly simple neutralization solution may arise (*Byers*, 2009). However, this does add the increased complexity of either two power supplies (spatial variation) or a

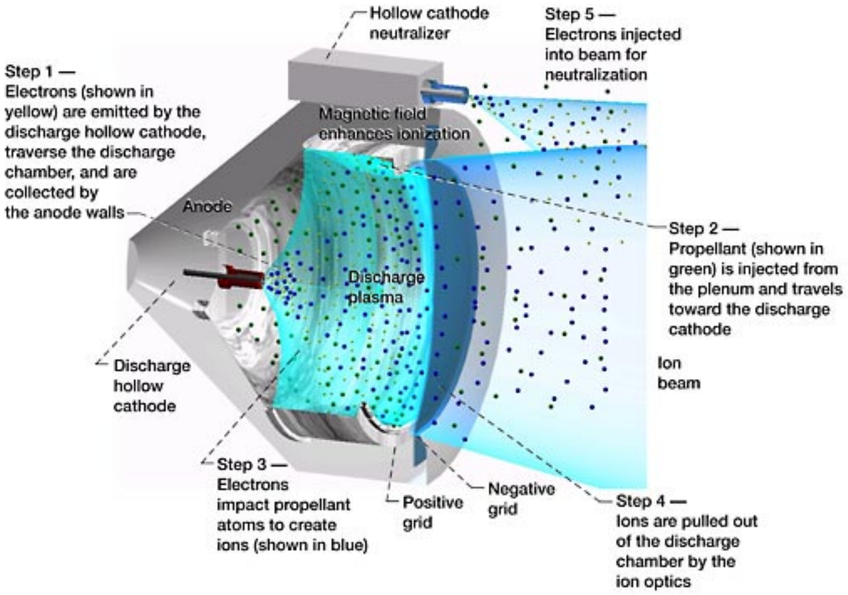

Figure 1.2: Operation of Ion Thruster and Hollow Cathode Neutralizer (*NASA*, 2004)

power supply that can switch back and forth between negative and positive high voltage polarities (temporal variation). Thus, this thesis will also explore the possibility of emitting just a single polarity of charged particle and utilize the ambient plasma environment to neutralize both the spacecraft and the beam properly.

The three neutralization schemes that will be explored in this thesis will be termed (i) Spatial-Varying, Common Time Emission Neutralization Scheme (ii) Temporal-Varying, Common Spatial Emission Neutralization Scheme and (iii) Neutralization by Background Plasma Scheme.

The spatial-varying, common time emission neutralization scheme (Section 2.4) is a scheme where there are separate regions, each which only emits positive or negative charge shown in Fig. 1.3. All regions will emit simultaneously, and as long as there are equal emission areas for positive and negative charge, and equal amounts of current coming out of the oppositely charged regions, there should be a net neutral beam and spacecraft.

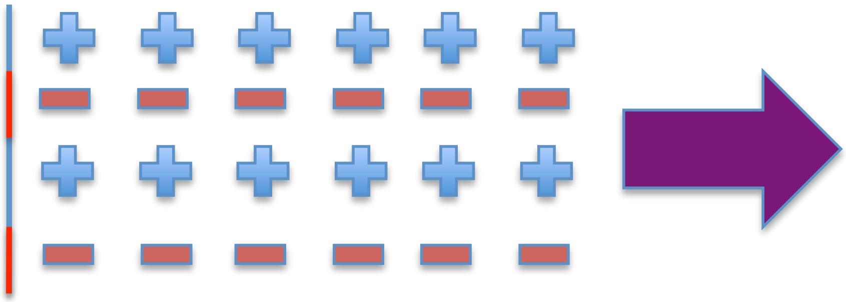

Figure 1.3: Spatial-Varying, Common Time Emission Scheme

The time-varying, common spatial emission neutralization scheme (Section 2.5) is a scheme where there is a single, large emission region, that emits only a single polarity of charged particle at any one time shown in Fig. 1.4. However, this emission region will vary between emitting positively and negatively charged particles. As long as the emission times and current are equal for the two polarities, the beam and spacecraft will be net neutral over time, with temporary charging of the beam and the spacecraft during polarity oscillations.

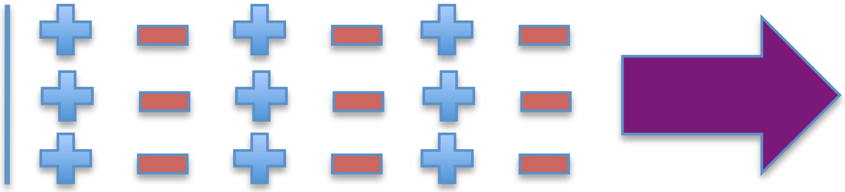

Figure 1.4: Time-Varying, Common Spatial Emission Scheme

The neutralization by background plasma scheme (Chapter III) is a scheme where a solely, negatively charged particle beam is emitted from the spacecraft, which will cause the spacecraft to charge up positively due to charge conservation. The premise is that if the emission current is low enough, or the plasma parameters are significant enough that the spacecraft can be neutralized, and that the electrons in the area of the particle emission are mobile enough that they will vacate the area leaving the beam neutralized because of the heavier, positive ionospheric ions. A depiction of this neutralization scheme is shown below in Fig. 1.5. This schematic shows the simulation space where the background + and -'s show the background plasma that is for the most part evenly distributed around the simulation space except for the spacecraft in the middle. This background plasma flows to the right at whatever the spacecraft velocity is desired to be, as it is easier to flow the plasma continuously than move the spacecraft through the simulation space. The large, red -'s illustrate the emission of the negatively charged particles or droplets from the spacecraft.

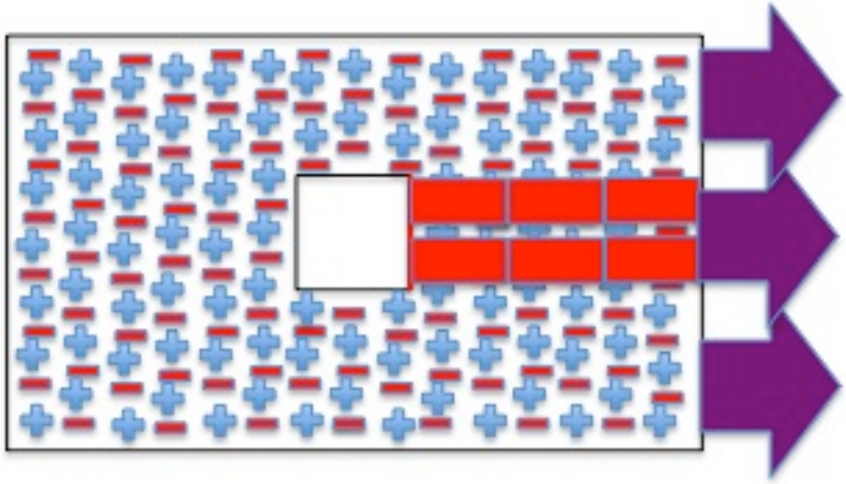

Figure 1.5: Background Plasma Neutralization Scheme

In addition to the general concerns that exist for neutralization of a thruster in space, there are specific concerns when emitting charged particles or liquid droplets from a thruster using the methods described above. Namely, what is the impact on the emitted particle beam if the beam is unneutralized or neutralized in various fashions? Will the beam cause the spacecraft to decelerate and lose some of its thrust due to the electric field interactions between the two? Will the charged beam spread in such a way that the thrust generated is not fully in the direction desired? If there are oppositely charged particles being emitted, will they interact in a detrimental fashion? Will space charge limited flow limit the current density that can be emitted to a point where such emission is not even feasible? Will the spacecraft charge up, or charge up to a large enough potential, that it draws in too much surrounding plasma or creates arcing effects to the beam?

1.2 Satellites Requiring Innovative Neutralization Techniques

Over the last few years, there is a new type of nanospacecraft thruster under development that utilizes liquid droplets (colloids) or nanoparticles to provide thrust. As with any electric propulsion system that emits charge, an issue to be examined is how to best neutralize it considering the issues discussed above. Here, the principal focus is on the needs of the nanoparticle field extraction thruster (NanoFET) to self-neutralize (although it applies to colloidal systems as well) (*Liaw et al.*, 2011a) (*Liaw et al.*, 2011b). The NanoFET system operates by expelling either positively or negatively charged nanoparticles through a gridded structure (*Liu*, 2010). This ability to charge and accelerate nanoparticles of either polarity offers the flexibility of using the nanoparticles to self-neutralize the thruster. Most common electric propulsion systems only emit positively-charged ions, which requires that electrons are also emitted, often through the use of hollow cathodes or other electron emitters. If NanoFET and colloidal thrusters can be implemented without a separate neutralization system, then the conjecture is that there would be no loss of efficiency or increase in complexity to address neutralization.

1.2.1 Introduction to NanoFET

The NanoFET (Nanoparticle Field Extraction Thruster) system is a micropropulsion thruster for nanospacecraft that charges then accelerates nanoparticles to be emitted for thrust. NanoFET is envisioned as being a scalable, MEMS-based device capable of being placed on multiple sides of a CubeSat (for example, a 3U CubeSat

Figure 1.6: Depiction of the NanoFET System (in blue) on a Single Side of a 3U Cubesat (*Liu*, 2010)

has dimensions of 10 cm by 10 cm by 30 cm, as shown in Fig. 1.6) and thus able to provide primary propulsion and attitude control.

Fig. 1.7 shows a visualization of the MEMS structure as well as the cutaway view of the NanoFET system. The NanoFET system uses a propellant of nanoparticles with conductive surfaces. These nanoparticles are stored in a particle reservoir, and when the system is to begin thrusting, there is a backpressure force applied to the particle reservoir pushing the particles up to the nanosieve interface where it can be charged by the charging sieve, which is held at a high electric field (*Liu*, 2010).

The charging sieve is designed such that only a single particle is allowed through each sieve hole at a time. This is so that each particle can be charged to a predictable and optimal amount once the particle comes into contact with the charging sieve through electrostatic charging. The charge can be predicted using Eq. 1.1 (*Félici*, 1966), which indicates that the larger the Charging Electric Field (E_0) and the larger the Particle Diameter (d), the more the Charge Acquired by Particle (q_0) the particle will be.

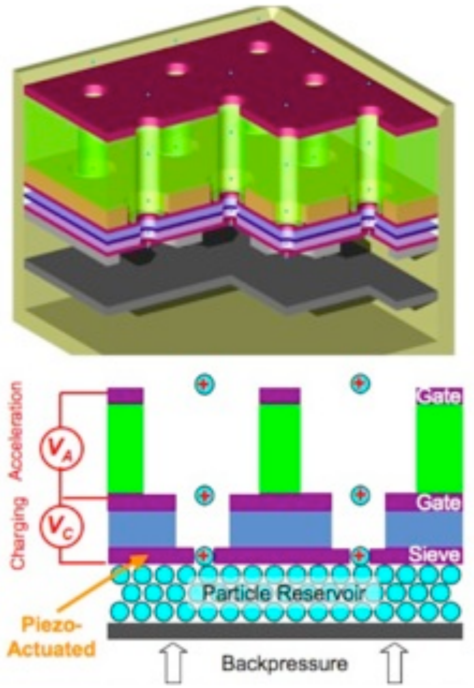

Figure 1.7: Visualization of the MEMS Structure and Cutaway View of the NanoFET System (*Liu*, 2010)

$$q_0 = \frac{\pi^3}{6}\epsilon_0 E_0 d^2 \tag{1.1}$$

Once the particle is charged, and an impulse of thrust is desired, a piezoelectric is actuated, giving the charged particles the additional force needed to overcome the Van der Waals forces that hold the particle to the charging sieve (*Liu*, 2010). When the charged particles are released from the nanosieve surface, they are accelerated across the charging and primary accelerating gate structures. Once these particles are no longer influenced by the electric fields connected to the spacecraft, the thrusting will be completed. (As will be presented, there is at least one more field beyond those between the charging and acceleration gates.) The NanoFET system envisions ultimately being able to emit particles with velocity ranging between approximately 1,000 and 20,000 m/s, which translates to 100 to 2000 seconds specific impulse. This range of specific impulse, as well as the moderate thrust to power that the NanoFET

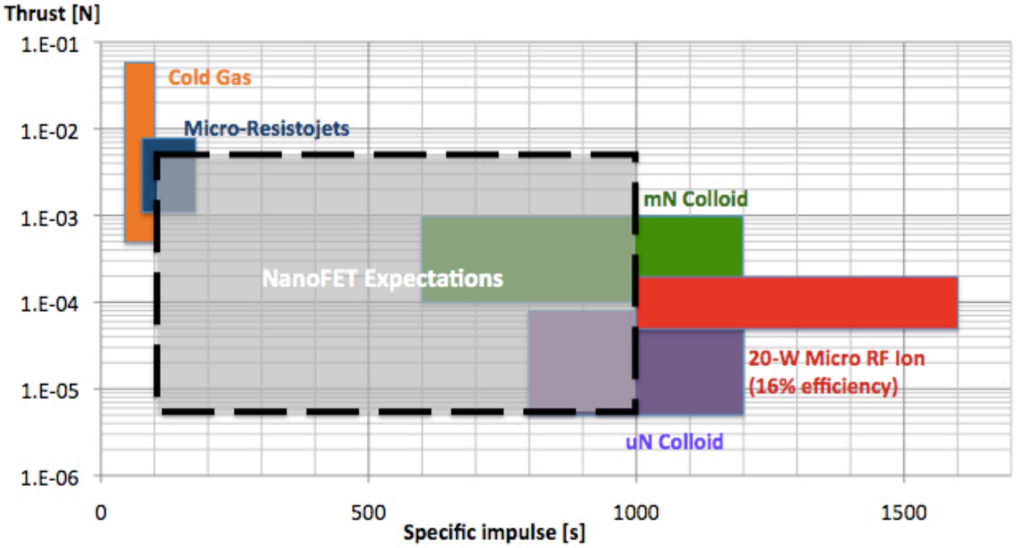

Figure 1.8: Micropropulsion Trade Space with NanoFET in Light Gray

system is capable of fulfills a portion of the trade space that is not currently occupied by existing micropropulsion technologies as shown in Fig. 1.8 (*VACCO*, 2010) (*Busek*, 2010).

A unique benefit of a charged particle thruster is the ability to vary the specific impulse as well as the thrust-to-power of the thruster. This range of specific impulses and thrust levels shown can be determined in situ as well as prior to launch by varying the specific charge (charge to mass ratio) of the propellant as well as the potential applied between the gates to control the acceleration. For 50 nm diameter particles, charged in electric fields of 400 V/μm, specific impulse and thrust-to-power will vary as shown in Fig. 1.9 (*Liu*, 2010).

The different particles shown in the plots have different masses but the same charge, since charge is only dependent on diameter and charging electric field as indicated in Eq. 1.1. As a result, their specific charge will only be determined by the mass of the particle. Therefore, the solid gold particles will have the lowest specific charge, while the hollow ceramic will have the highest specific charge. Also, it can be seen

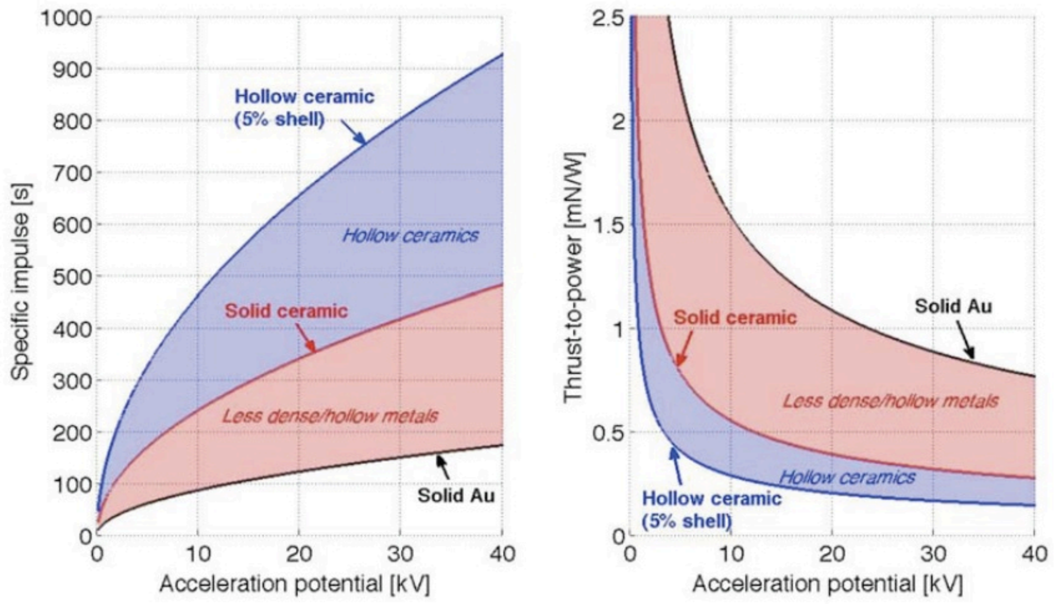

Figure 1.9: Varying Specific Impulse (left) and Thrust to Power (right) as a Function of Particle Type and Acceleration Potential for 50 nm Particles Ideally Charged in 400 V/μm Electric Fields (*Liu*, 2010)

in Fig. 1.9 that specific impulse and thrust-to-power have opposite relationships with specific charge and acceleration potential. Specific impulse increases with increasing acceleration potential or increasing specific charge, but thrust-to-power will decrease with increasing acceleration potential or increasing specific charge. This means that specific impulse will have to be traded off for thrust-to-power and vice versa.

The varying specific impulse based on acceleration and charging potential makes the NanoFET system a variable-Isp thruster as opposed to a constant-Isp thruster. This gives the NanoFET system the potential of consuming less propellant than a constant-Isp thruster, as it can always optimize its operation for the mission and mission profiles (*Casalino and Colasurdo*, 2004). This makes the NanoFET system ideal for missions where the requirements for thrust and power are either unknown or may change at any given time before launch as the thruster will not need to be redesigned in order to optimize performance. Once the satellite system is launched, as the propellant mass cannot change, the NanoFET system will be able to complete any

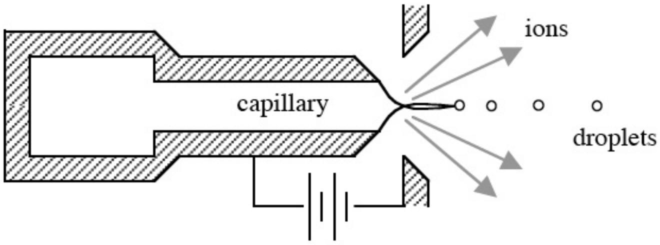

Figure 1.10: Schematic of a Single Emitter Colloidal Thruster (*Lozano*, 2003)

maneuver (orbit change, inclination change) faster than any constant-Isp thruster as it can adjust the specific impulse and thus acceleration to utilize propellant optimally (*Patel et al.*, 2006).

1.2.2 Introduction to Colloidal Thrusters

A thruster type similar to NanoFET is known as a colloidal thrusters, which relies on electrostatically accelerating charged liquid droplets for thrust. As such, the principle difference is the liquid droplet versus a nanoparticle as the propellant. Colloidal thrusters tend to have moderate specific impulse, high efficiency, and high thrust density, but low thrust levels (*Beynon et al.*, 1968); however, on small satellites, such as CubeSats, it can serve a useful purpose just like the NanoFET system can.

A colloidal thruster obtains its charged liquid droplets through a process called electrospray where a liquid is flowed through an emitter, called a capillary, and a high voltage is applied to this liquid. The high voltage liquid at the tip will form a Taylor cone, which will then eventually break off into charged droplets. Under certain conditions, these colloidal thrusters can also emit charged ions as well, with a single colloidal emitter schematic shown in Fig. 1.10.

The droplet and ion modes of a colloidal thruster in theory provides the opportunity to operate in significantly different regimes. The charged droplet regime is good for precise movements as it is a low specific impulse and low current emission, whereas the ion regime is good for strong performance as it provides high specific impulse and high current emission. However, one thing that can still be improved on colloidal thrusters is the neutralization scheme.

1.3 Introduction to Particle-in-Cell Simulations

All of the simulations conducted and shown in this thesis will be particle-in-cell simulations, which is a very common plasma physics simulation method. Particle-in-cell simulations are usually performed on a fixed mesh (does not mean it has to be a uniform mesh), where the particle's position and velocity are tracked regardless of the mesh, but the electric and magnetic field are tracked solely on the mesh points (*Birdsall*, 1991) as are the majority of the diagnostics such as current and density as is shown in Fig. 1.11. A key note about particle-in-cell simulations is that they lump groups of real particles into superparticles in the simulation in order for the simulation to run in a timely fashion. However, the movement of the superparticles will mimic the motion of the real particles as the superparticle is just a scaled up version of the real particles and thus will have the same charge to mass ratio, which is all that determines the movement of the particles with the Lorentz force, but will increase fluctuations as there are fewer particles being simulated.

Fig. 1.12 shows how the iterative particle-in-cell simulations work. Starting from the top of the figure, Lorentz force is used to calculate the acceleration of each particle, which is then used in turn to calculate the new velocity and new position of each of the particles. This information then gets passed on to the next step, where the collection of particle positions and velocities are aggregated to get the charge density as well as current density throughout the simulation space. This then is used at the next step to calculate the electric field and magnetic field at each of the mesh points. This is then used to calculate the force acting on each particle at their actual position using appropriate weighting of the surrounding magnitudes at the mesh points.

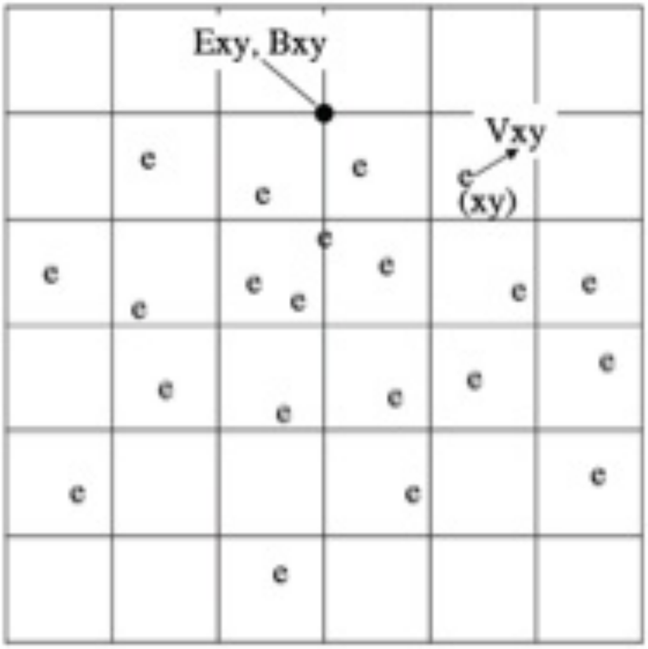

Figure 1.11: Example Mesh for a Particle-in-Cell Simulation (*Morris*, 2005)

There are additional intricacies such as calculating certain variables at half time steps, while other variables at the full time steps, as well as how to properly weight the field values at the surrounding mesh points when calculating the electric field and magnetic field magnitude acting on a particle that are not exactly on a mesh point.

The majority of the simulations conducted throughout this thesis will be conducted in OOPIC PRO^{TM}, which is a typical particle-in-cell simulation software. One thing of note is that this software conducts all of its simulations in two and a half dimensions (2.5D), meaning that it will track the position of the particles in two dimensions, but tracks the velocity in all three dimensions. This is so that magnetic fields will still have the appropriate effect on the simulation, without having to track the third position dimension, thereby simplifying the simulation. This also means that the particles being shown are not actually spherical particles, but instead they are rods that go into and out of the simulation space, and in this case they will have a rod length of 1 meter for normalizing currents and lumped circuit parameters.

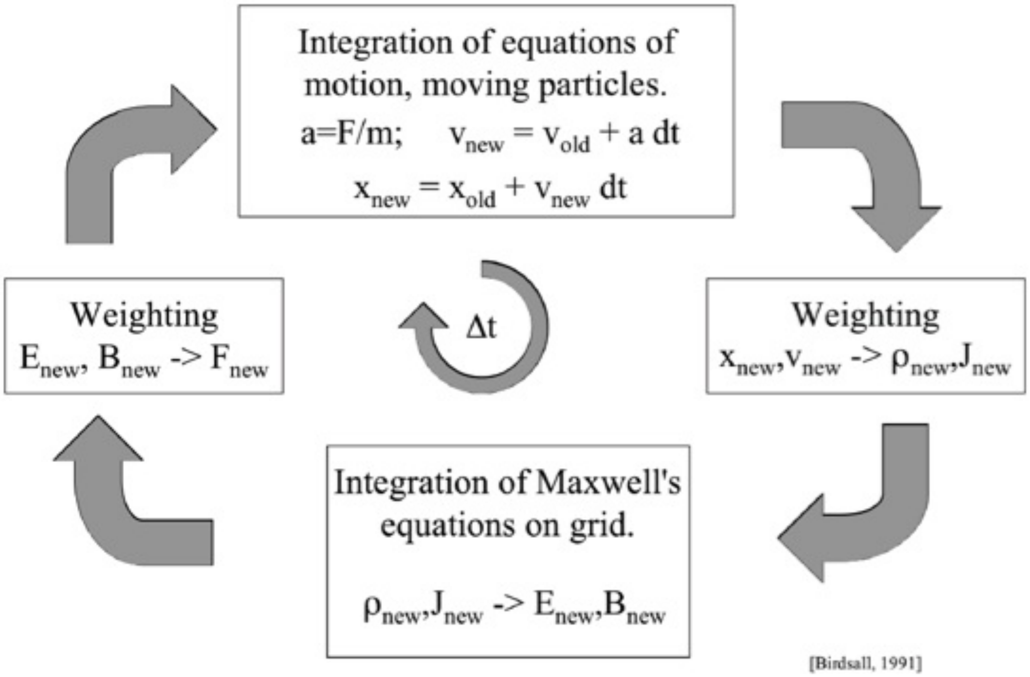

Figure 1.12: Iterative Flow Chart of a Particle-in-Cell Simulation (*Birdsall*, 1991)

1.4 Thesis Map

This thesis will principally focus on the potential for unconventional neutralization techniques applied to nanoparticle (e.g. NanoFET) and colloidal thrusters as described above. It will secondarily discuss electron neutralization as applied to femtosatellite sized spacecraft such as used for electrodynamic tethers. Chapter 2 will study the ability and challenges of charged particle thrusters to self-neutralize by emitting equal numbers of positive and negative charged particles. It specifically considers the worst case scenario of emission into vacuum. Chapter 3 will study the potential of using ionospheric electron "return currents" to neutralize a CubeSat sized nanosatellite emitting negatively charged particles, and the specific ionospheric conditions as well as emission characteristics needed for effective neutralization by the ionospheric plasma is assessed. Chapter 2 and 3 will draw the majority of its conclusions from particle-in-cell (PIC) simulations conducted using the 2.5-dimensional code, OOPIC

PRO^{TM}. Chapter 4 then transitions to a three-dimensional code called VSim^{TM}, and compares it to the previously 2.5-dimensional models developed in Chapters 2 and 3. Lastly Chapter 5 will introduce the concept of electrodynamically tethered femtosatellite systems and various ways to emit electrons to complete the circuit for that system. It will also provide parametric studies as to what the capability of the various electron emission technologies need to have in order to occupy certain amounts of area on the femtosatellites in order to provide enough current through the system. The appendix will contain samples of the simulation code used throughout the thesis.

1.5 Research Contributions

This thesis seeks to provide alternative or unconventional neutralization techniques to thrusters that would be significantly detrimentally affected by conventional neutralization techniques either due to efficiency, complexity, volume, mass, or power as well as determining the feasibility and requirements of using existing neutralization techniques on a new class of satellites utilizing a revitalized electric propulsion system. Research topics and contributions in this thesis include the following:

- The feasibility of a spatial-varying, common temporal emission scheme is examined as a possible neutralization technique for a charged particle thruster. The image charge, maximum electric field, force pulling back on the spacecraft, and the percentage of thrust lost due to the electric field interaction will be examined for various situations, and will determine how the emission region must be formed in order to properly neutralize both the spacecraft as well as the emitted beam.

- The feasibility of a temporal-varying, common spatial emission scheme is examined as a possible neutralization technique for a charged particle thruster. Again, the image charge, maximum electric field, force pulling back on the spacecraft, and the percentage of thrust lost due to the electric field interaction will be examined for various situations. The frequency of the temporal-variation will be the main variable that will be examined as to what controls the feasibility of this neutralization scheme, but emission current will also be examined.

- The relationship between emission parameters and minimum plasma parameters required to neutralize the spacecraft is determined. The relationship will depend on the parameters of the single negatively charged beam coming out of the spacecraft including emission current, emission velocity, and emission area. The relationship will also depend on the parameters of the background plasma including plasma density, plasma temperature, and plasma or spacecraft speed. This relationship can be used to determine what altitudes, solar environments, and orbits a spacecraft can fly in if it requires certain velocities or emission parameters to generate the necessary thrust and still maintain a neutral spacecraft.

- The difference in simulation results between a 2.5D particle-in-cell simulation tool (OOPIC PRO^{TM}) and a 3D particle-in-cell simulation tool (VSim^{TM}) is explored. By conducting the same simulation in 2.5D and 3D while comparing various diagnostic results, we are able to establish when there are differences between the two software.

- Two possible electron emitting or neutralizing technologies for use on an electrodynamically tethered femtosatellite are explored and the feasibility of such technologies is examined. The feasibility depends on the altitudes that the tethered femtosatellite system desires to fly at as that will determine the required current through the electrodynamic tether, which in turn establishes the current that must be emitted through the electron emitter. This will then determine what the necessary capability of the electron emitter must be in order to satisfy this minimum current emission, based on the available area devoted to the emission technology. However, this will be constrained by the space charge limit, which provides an upper bound for the amount of current coming out of any specific area.

CHAPTER II

Simulation of Positive and Negative Particle Emission for Neutralization

2.1 Introduction

With charged particle thrusters such as the NanoFET system and colloidal thrusters, as with all electric propulsion systems, it is important to consider the neutralization aspect of the system when designing it. A perceived major benefit of the NanoFET system is that it has the capability to charge particles both positively and negatively. It appears intuitive that this ability provides the charged particle thrusters, such as NanoFET and colloidal thrusters, the ability to self-neutralize. It would stand to reason that as long as equal amounts of positively and negatively charged particles are emitted, the emitted beam would be neutral, and the spacecraft would be neutral as well possibly resulting in a non-degraded emitted beam.

2.2 Neutralization Schemes

Two separate emission configurations for self-neutralization have been identified previously. These are the (i) Spatial-Varying, Common Time Emission (SVCTE) scheme as shown previously in Fig. 1.3 and (ii) Time-Varying, Common Spatial

Emission (TVCSE) scheme as shown previously in Fig. 1.4. The schemes are explained in more detail previously in Section 1.1.1.

The main question that needs to be examined with these neutralization methods is whether NanoFET and other particle thrusters, such as colloidal thrusters, can utilize both positive and negatively charged particles to neutralize while maintaining performance and whether there are practical with these configurations (e.g., unacceptably strong electric fields at transitions between polarities).

2.3 Methodology

The majority of the exploration of the two neutralization methods is done through simulation in OOPIC PRO^{TM} assuming the case of charged nanoparticles (NanoFET). OOPIC PRO is a 2.5D, object-oriented, particle-in-cell simulation tool. In OOPIC PRO, it is possible to choose the simulation space, simulated particles, and simulated emitter. In the course of these simulations, a Cartesian coordinate system is chosen, with particles emitted in the positive X direction, and the emitters spanning the Y direction. In this case there is an X-distance of 0.2 m and a Y distance of 0.15 m. In the past, simulations have been conducted using a cylindrical coordinate system; however, in such cases it is much more difficult to maintain symmetry between the positively and negatively charged beams while keeping equal emitter areas.

There are two different types of particles being simulated. The more common nanoparticle that is simulated is a 200 nm solid polystyrene particle (assume metalized) that is intended to be used in the NanoFET system (a 5 μm gold coated solid polystyrene particle powder Scanning Electron Microscope (SEM) image is shown in Fig. 2.1, which is the smallest size particle of this type currently available, with 200 nm diameter particles being envisioned for use in the future). These particles have a mass of 4.4×10^{-18} kg and obtain a charge of 7.32×10^{-16} C based on a charging electric field of 4×10^{8} V/m. These particles are approximately seven orders of magnitude heavier than a normal Xe$^+$ ion and contains about 4500 elementary charges. This mass and charge translates to approximately a 100 C/kg charge to mass ratio. This is significantly lower than the specific charge of both electrons (˜10^{11} C/m) and Xe$^+$ ions (˜10^7 C/m), which means that these particles for simulation are much heavier compared to their relative charge compared to normal neutralizing electrons. In addition, the oppositely charged particles have the same specific charge as opposed to a large specific charge electron neutralizing a smaller specific charge ion as in ion thrusters and Hall thrusters. The other particle that is simulated is a 50 nm hollow polystyrene particle (assume metalized). These particles are representative of what is ultimately desired for use in the NanoFET system. These particles have a mass of 4.45×10^{-20} kg and a charge of 4.46×10^{-17} C based on a charging electric field of 4×10^8 V/m translating to a charge to mass ratio of approximately 1000 C/kg, moving slightly towards the charge to mass ratio of an electron.

The emitter that is simulated for the most part emits particles at a current density of 0.967 A/m^2 for each emitter beam. This is compared to approximately 525 A/m^2 current density as determined by the Two-Dimensional Classical Space Charge Limited Current Density (J$_{SCL}$) calculated using the Child-Langmuir Law (*Luginsland et al.*, 1998) and the two-dimensional ratio (*Luginsland et al.*, 2002) as calculated in Eq. 2.1. This 0.967 A/m^2 current density is what NanoFET may physically be capable of emitting out of an entire 10 cm by 10 cm side of a CubeSat.; however, NanoFET is expected to operate at significantly lower current densities due to power considerations. In addition to operating at just a current density of 0.967 A/m^2, a range around this current density will be explored to determine a trend between degradation of thrust and changing current density. Although NanoFET is envisioned to have the capability to emit particles at roughly between 100 and 2000 seconds (s) specific impulse, these simulations will concentrate on a mid-level of 1000 s. With a 1000 s specific impulse, particles will be emitted at approximately 10^4 m/s. In addition, it is

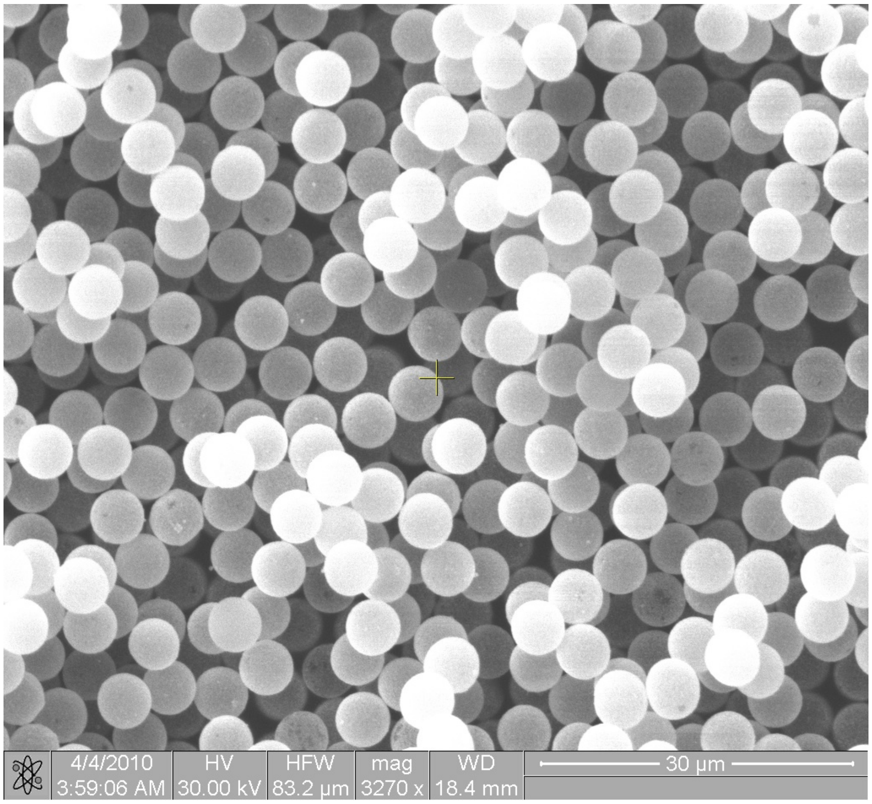

Figure 2.1: SEM of Gold Coated Solid 5 um Polystyrene Particle Powder

anticipated that emitted particles are at the spacecraft temperature (approximately 0.03 eV), which is extremely cold relative to traditional electric propulsion thrusters (e.g. ion or Hall thrusters).

$$J_{SCL} = \frac{4\epsilon_0}{9D^2 q}\sqrt{\frac{2}{m}}E^{1.5}\left[1 + \left(\sqrt{1 + \frac{eV}{E}}\right)\right]^3 \cdot \left(1 + \frac{D}{4R}\right) \tag{2.1a}$$

$$\begin{gathered} J_{SCL} = \frac{4 \cdot 8.85 \cdot 10^{-12}\left[\frac{F}{m^2}\right]}{9 \cdot 0.015[m]^2 \cdot 7.32 \cdot 10^{-16}[C]}\sqrt{\frac{2}{4.4 \cdot 10^{-}18[kg]}}(2.2 \cdot 10^{-10}[J])^{1.5} \\ \cdot \left[1 + \left(\sqrt{1 + \frac{1.602 \cdot 10^{-19} \cdot 1[J]}{2.2 \cdot 10^{-10}[J]}}\right)\right]^3 \cdot \left(1 + \frac{0.015[m]}{4 \cdot 0.015[m]}\right) \end{gathered} \tag{2.1b}$$

$$J_{SCL} = 420.3 \cdot 1.25 = 525\ \frac{A}{m^2} \tag{2.1c}$$

The issues that will be examined here are whether there are local electric field effects near the emitter that should be of concern, and whether non-neutral beams are significantly disrupted and when it is of concern. In both schemes there will be regions of localized charge, and because of that there will be an image charge induced on the spacecraft wall of the opposite polarity. This causes an image charge induced electric field that is either pointing towards or away from the spacecraft depending on the polarity of the emitted particles as shown in Fig. 2.2. Either way, this image charge induced electric field will slow down particle velocities as well as negate some of the thrust of the spacecraft due to the emission of these particles. It needs to be examined what kind of effect this image charge induced electric field has, and if such an effect can and must be mitigated. The other primary concern is that both schemes will emit oppositely charged particles, resulting in convergence of the oppositely charged particles towards one another.

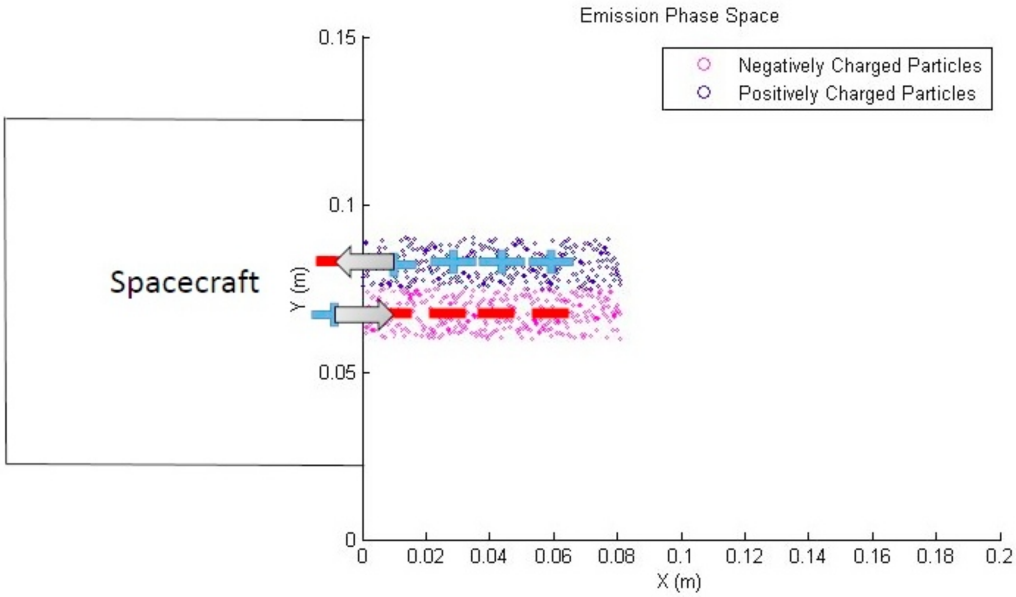

Figure 2.2: Depiction of Image Charge Building up on Spacecraft and Electric Field

2.4 Spatial-Varying, Common Time Emission Scheme

In the following 2.5D simulations, four diagnostics are principally used: X vs Y Particle Propagation, Electric Field, Velocity in the Y direction with respect to X position, and Velocity in the X direction with respect to X position (See Fig. 2.3 as an example). The X vs Y particle propagation diagnostic shows the simulation space with the spacecraft wall being simulated on the left (y-axis) and particles being emitted to the right. In all the simulations shown, particles have not quite reached the right edge of the simulation space and thus are not subjected to any edge effects that may occur. However, a set of simulations (not shown) have been conducted that prove the major electric field effects that are observed in the shown simulations are not transient effects, and exist in steady state as well. In addition, as will be shown in the particle propagation diagnostics from the lack of scattering, there are no collisions being modeled in this OOPIC PRO code. This is something that needs to be simulated as well; however, no significant issues due to collisions are anticipated, as they occur far enough away from the emitter that scattering back to the spacecraft is not expected. The velocity in the Y direction plots show velocity in the vertical direction primarily between the two beams, and the velocity in the X direction plots show velocity in the horizontal direction away from the emitter.

The following sections will explore the spatial-varying, common time emission (SVCTE) scheme as various parameters are varied. Section 2.4.1 will show the base case (shown in Table 2.1) of the SVCTE scheme as the emitted particles propagate across the simulation space. Section 2.4.2 will do the same for a 1000 C/kg particle. Section 2.4.3 and Section 2.4.4 explore what happens when beam separation and beam width are varied respectively. And Section 2.4.5 explores varying the current density for the otherwise base case conditions.

The code for this neutralization scheme is shown in Appendix A.

Specific Charge	Specific Impulse	Current Density	Beam Separation	Beam Width
100 C/kg	100 seconds	0.967 A/m^2	0.015 m	0.015 m

Table 2.1: Base Case Conditions for Spatial-Varying, Common Time Emission Scheme

2.4.1 Time Progression of 200 nm Solid Polystyrene Particles at 1000 Seconds Specific Impulse

First the SVCTE scheme is explored as shown in Fig. 1.3. Again, this is the scheme that has separate regions, each of which emit only positive or negative charge simultaneously. The first simulation looks at how the image charge induced electric field as well as the velocities of the particles change as nanoparticle beams are emitted. In this simulation 200 nm solid polystyrene particles are emitted that have a mass of 4.4×10^{-18} kg and contain 7.32×10^{-16} C of charge. These particles are emitted at 1000 s specific impulse and 0.03 eV. Two beams of oppositely charged particles positioned next to one another are emitted. Each of these emitters is 1.5 cm in width and emitting 14.5 mA of current resulting in a current density of 0.967 A/m^2, which means that there will be equal amounts of positive and negative charge emitted, resulting in a beam that has no overall charge. This current density is well below the space charge limit of 525 A/m^2 (Eq. 2.1) in this case. Fig. 2.3 and Fig. 2.4 show the propagation of this beam when the particles are 25% of the way across the simulation space, and right before the particles get to the end of the simulation space.

From these figures it can be seen that as the beams continue to propagate across the simulation space, they begin to slowly converge towards one another and overlap because they are oppositely charged. It can be seen that the radial electric field draws the beams slowly on top of one another over the 0.2 m of the simulation space. This slow convergence is not a concern for performance; however, it illustrates that the relatively massive particles (with respect to electrons and even ions) are relatively

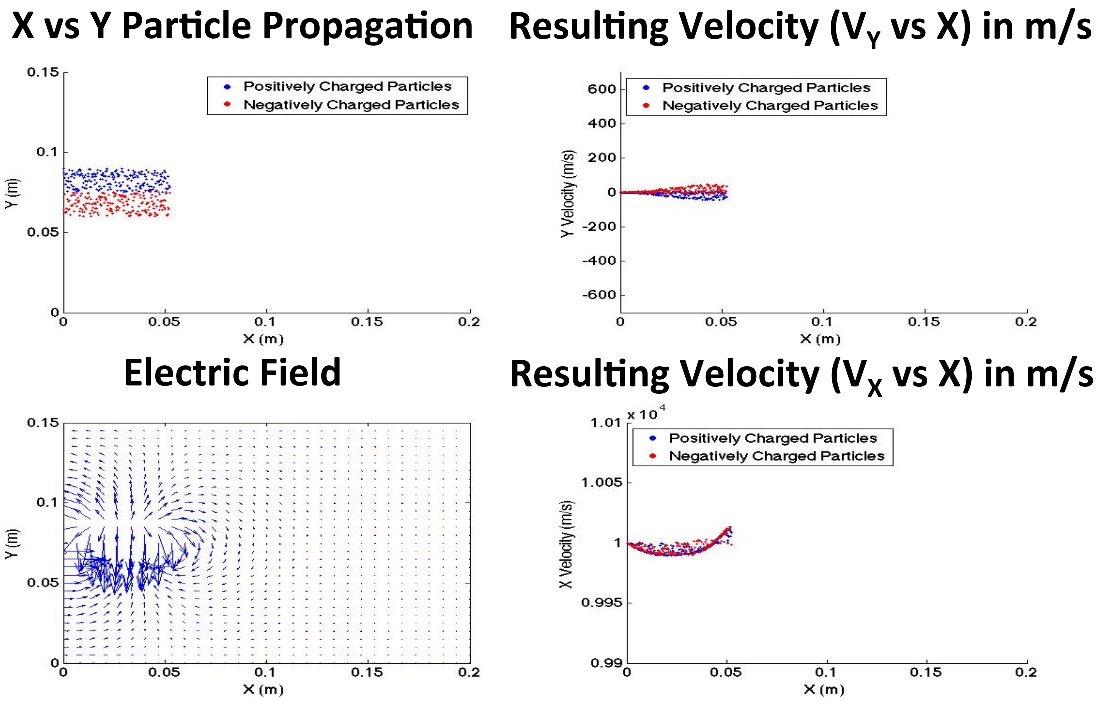
X vs Y Particle Propagation

Resulting Velocity (V_Y vs X) in m/s

Electric Field

Resulting Velocity (V_X vs X) in m/s

Figure 2.3: Beam Propagation of 200 nm Solid Polystyrene Particles at Early Time Stage

slow to neutralize. Also, the image charge induced axial electric field local to the emitter causes a decrease in velocity resulting in a maximum velocity drop of 0.22% relative to the initial emission velocity. This relatively small decrease in velocity should be expected to increase as the current density continues to increase towards the space charge limit. As time progresses the electric field continues to push the two beams towards one another, resulting in the stronger overlap between the two beams at the final time stage, along with a larger drop in velocity. Furthermore, there is an increase in velocity, even above the original velocity, on the leading edge of the beam. This is due to the unneutralized charge cloud behind the leading edge accelerating it forward.

The drop in velocity of the emitted particles is due to the image charge induced axial electric field directly in front of the emission port. This axial electric field will

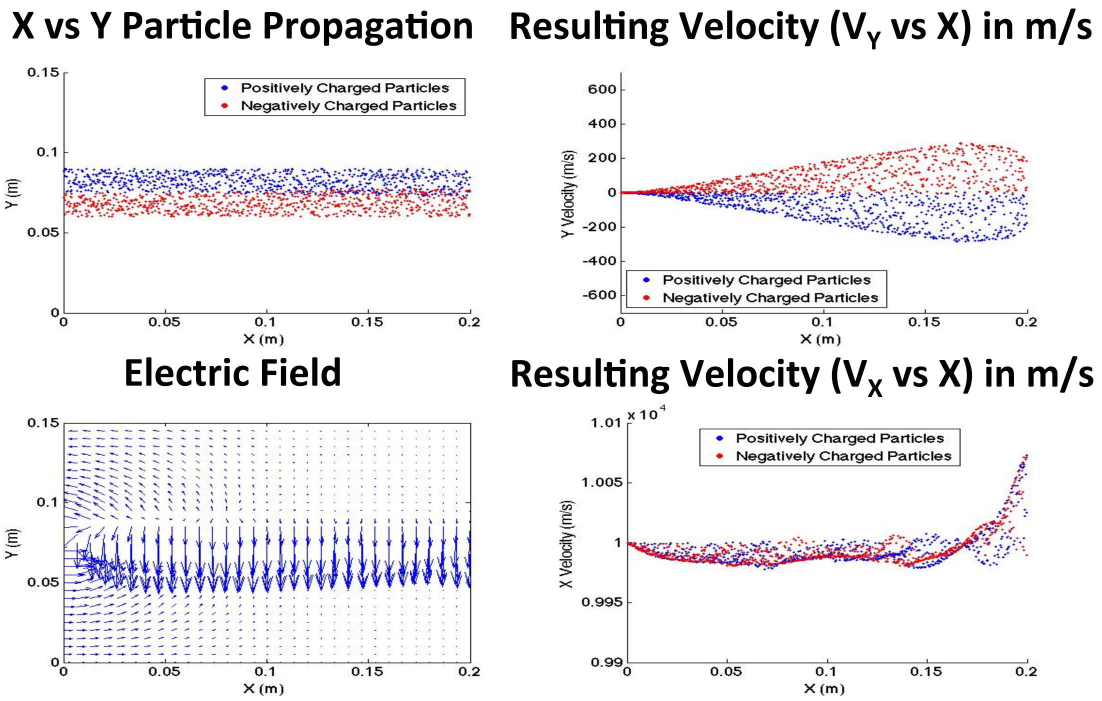

Figure 2.4: Beam Propagation of 200 nm Solid Polystyrene Particles at Final Time Stage

not only slow down the particles being emitted, but will also negate a portion of the spacecraft thrust generated by the emission. First, it is important to establish that the electric field outside the emission port of the spacecraft is solely responsible for the decrease in velocity. This was corroborated by confirming the simulated Change in Particle Velocities (Δv) between one time step and the next using the average of simulation electric field values at mesh points around the particle. This will allow for comparison using the estimated change in velocity and based on the average electric field as is shown in Eq. 2.2.

$$\Delta v = v(t+1) - v(t) = \frac{q}{m} E \Delta t \tag{2.2}$$

In order to get moderately accurate results, the emission current of particles needs to be relatively high in order for the change in velocity to be sufficiently large in the diagnostics, and so for this purpose a current of 14.49 mA (0.967 A/m^2 from a 0.015 m^2 emitter) was used. For this analysis, the velocity change of a recently emitted positive particle that is near the first X mesh point at the 200th time step followed by its velocity at the 201st time step is compared to the change in velocity using an average electric field of the three nearby mesh points (coordinates of [1,16], [1,17], [1,18]). The calculations are shown in Eq. 2.3, which are in good agreement (the difference being attributed to the inaccuracy in calculating the exact electric field).

$$\Delta v = v(201) - v(200) = 9995.68 \left[\frac{m}{s}\right] - 9996.06 \left[\frac{m}{s}\right] = -0.38\, m/s \tag{2.3a}$$

$$\Delta v = \frac{q}{m} E \Delta t = \frac{7.32 \cdot 10^{-16}[C]}{4.4 \cdot 10^{-18}[kg]} \cdot \frac{-33583.7 - 51507 - 45005.8}{3} \left[\frac{V}{m}\right] \cdot 5 \cdot 10^{-8}[s] = -0.36\, m/s \tag{2.3b}$$

This gives confidence to use the electric field to calculate the loss of thrust due to this electric field. But first the image charge deposited on the spacecraft must be calculated as that will determine the force experienced by the spacecraft due to the electric field at its boundary. The surface of the spacecraft for charge calculation can be approximated as 0.015 m in the Y dimension and a 1 meter distance in the Z direction ("out of the page") for the 2.5D simulation. Using Gauss' Law and a standard "pillbox" geometry allows for calculation of the approximate charge on the surface.

Using the pillbox model, an equation for the charge on the spacecraft can be determined as a function of the electric field as shown in Eq. 2.4 where n_{21} is the unit vector perpendicular to the boundary.

$$(E_2 - E_1) \cdot n_{21} = \frac{\sigma}{\epsilon_0} \tag{2.4a}$$

$$E_{1\parallel} = E_{2\parallel} = 0 \tag{2.4b}$$

Eq. 2.4b applies only inside conductors or at conductive boundaries as the spacecraft wall is in the simulations, whereas Eq. 2.4a applies to all surfaces (including dielectrics). Thus, it can be confirmed that the conductor is accurately being simulated by observing the tangential components at the conductive boundary to ensure that they are 0. Also, since the one surface of the Gaussian pillbox is within a conductor, where all electric fields are 0, Eq. 2.4a can be simplified to Eq. 2.5 where $E_\perp$ is the electric field perpendicular to the conductor surface right at the conductor boundary.

$$\sigma = \epsilon_0 \cdot E_\perp \tag{2.5}$$

This allows for a simple way of calculating the Surface Charge Density (σ) by knowing the electric field at the boundary. The surface charge density can be approximated for both the positively charged emission portion, and the negatively charged emission portion, and an average of the two as shown in Table 2.2.

	Positively Charged Beam	Negatively Charged Beam	Average
σ	$2.32 \cdot 10^{-7}$ C/m^2	$2.36 \cdot 10^{-7}$ C/m^2	$2.34 \cdot 10^{-7}$ C/m^2

Table 2.2: Calculated Surface Charge Density Magnitude on Spacecraft

In this example, there is an average surface charge density magnitude of 2.34×10^{-7} C/m^2 across the length of the spacecraft (0.03 meters) and depth of the simulation space (1 meter) or a total of 7.03 nC magnitude of charge at this time, but nearly a net zero charge across the entire spacecraft wall. The average electric field magnitude at the seven mesh points on the spacecraft wall in this example is 22.81 kV/m, giving a force pulling back on the spacecraft of 160.4 μN. This can be compared to the Thrust Generated (T) by multiplying the Current Emitted ($I_{emitted}$), the inverse of the specific charge, and the Emission Velocity ($v_{emission}$) as is shown in Eq. 2.6

$$T = \frac{2 I_{emitted} v_{emission}}{specific\_charge} \tag{2.6a}$$

$$\frac{C}{s} \cdot \frac{kg}{C} \cdot \frac{m}{s} = kg \cdot \frac{m}{s^2} = N \tag{2.6b}$$

In this example, the thrust generated would be 1.74 N as shown in Eq. 2.7 across a 0.015 m^2 area, which translates to 116 N/m^2 or 26.1 mN for a 0.015 m by 0.015 m area, which means that the loss in thrust due to the pullback on the spacecraft from the emitted particles is a very small percentage of the thrust generated.

$$T = \frac{2 \cdot 0.01449 \left[\frac{C}{s}\right] \cdot 10000 \left[\frac{m}{s}\right]}{166.36 \left[\frac{C}{kg}\right]} = 1.74\,N \tag{2.7}$$

These calculations are taken just at a single time step, but it is also important to observe how the percentage of thrust lost performs as a function of simulation time. Thus the electric field component in the X direction is captured every fourth time step in the simulation, and this allows for the average image charge on the spacecraft to be calculated as well as the average normal electric field at the emission region as shown in Fig. 2.5 and Fig. 2.6.

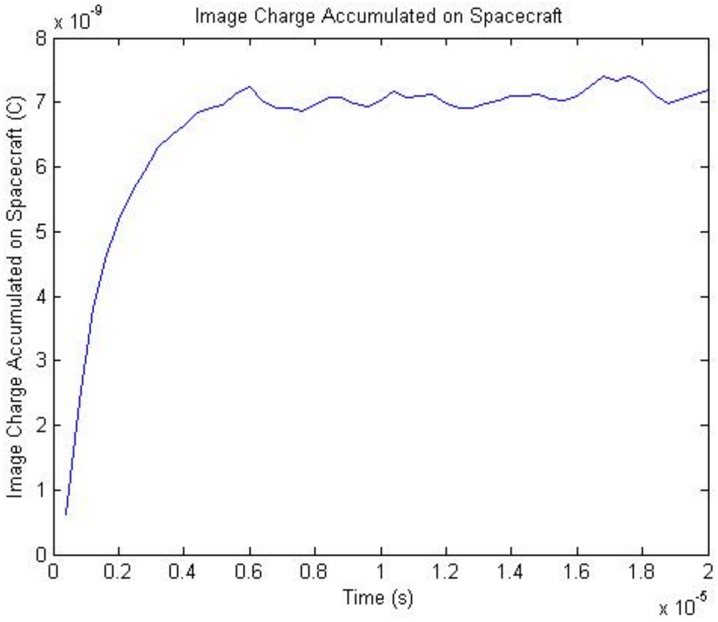

Figure 2.5: Average Image Charge on Spacecraft over Time

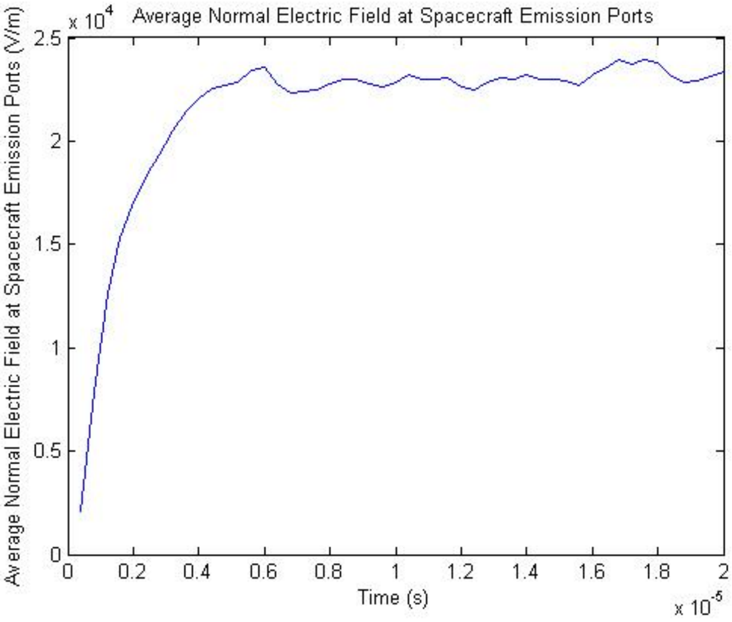

Figure 2.6: Average Normal Electric Field over Time

These two pieces of data allow for calculation of electric field force pulling back on the spacecraft as shown in Fig. 2.7 and then the percentage of thrust lost due to the spacecraft being pulled back by the image charge induced axial electric field as shown in Fig. 2.8.

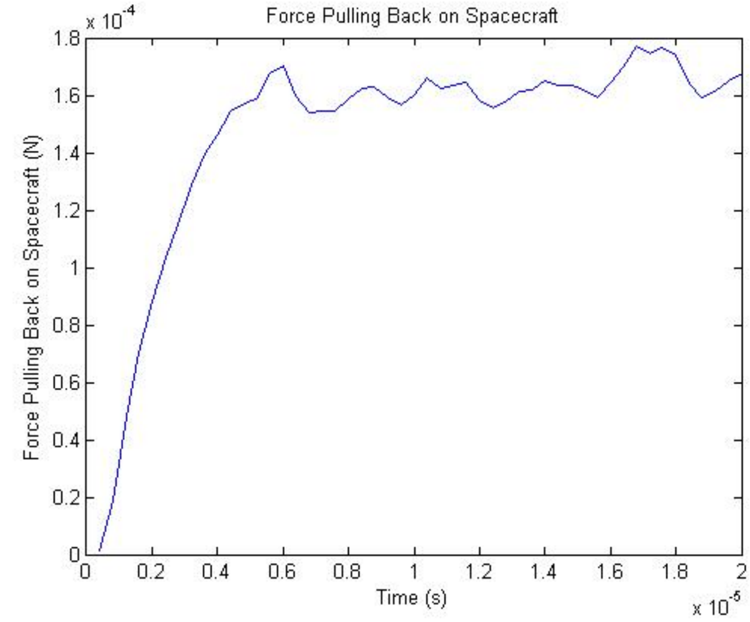

Figure 2.7: Electric Field Force Decelerating Spacecraft over Time

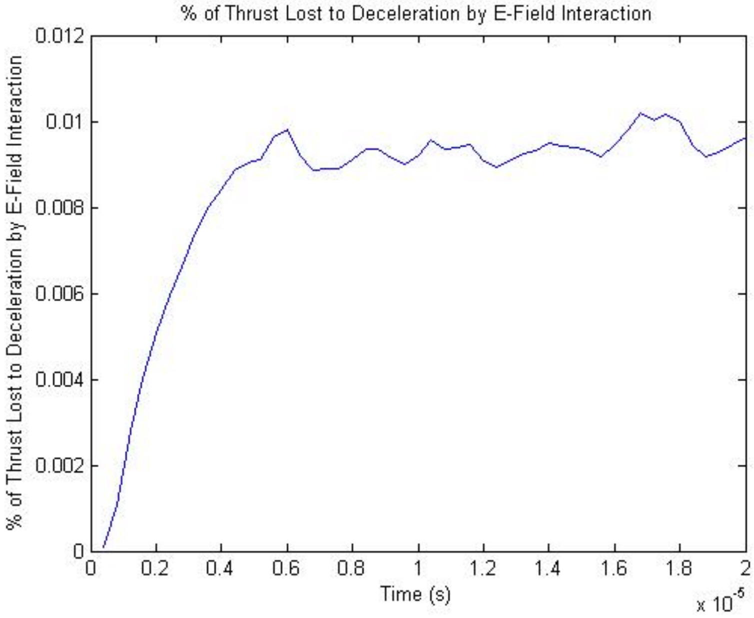

Figure 2.8: Percentage of Generated Thrust Lost over Time

All four of these figures show the same general trend of a sharp ramp up in image charge, electric field, and electric field force as particles initially are emitted, then a relatively steady plateau with just slight oscillations. The ramp up time only requires the beam to transit 20% of the simulation space to reach a simulation steady state. And the maximum percentage of thrust lost due to the electric field interaction with the spacecraft is very small, approximately 0.01% of the total beam energy.

With the previous plots reporting performance at a single current level, it is also important to evaluate multiple current levels at steady state. The following plots vary the emission current from 0 to 0.12 A, while observing minimum spacecraft velocity (Fig. 2.9), percentage of velocity decreased (Fig. 2.10), image charge (Fig. 2.11), average electric field (Fig. 2.12), force decelerating spacecraft (Fig. 2.13), and percentage of thrust lost due to electric field interaction (Fig. 2.14) and show the results after 20 μs (appropriately after initial transients have stopped). As these plots show, there is a clear linear relationship between current emission levels, and minimum velocity, image charge accumulated on the spacecraft, and average normal electric field at the emission ports of the spacecraft. As the thrust is determined by both electric field and total image charge, there is a quadratic relationship between emission current and percentage of thrust lost due to the electric field interaction; thus, as emission current continues to grow, there is an increasing percentage of thrust lost.

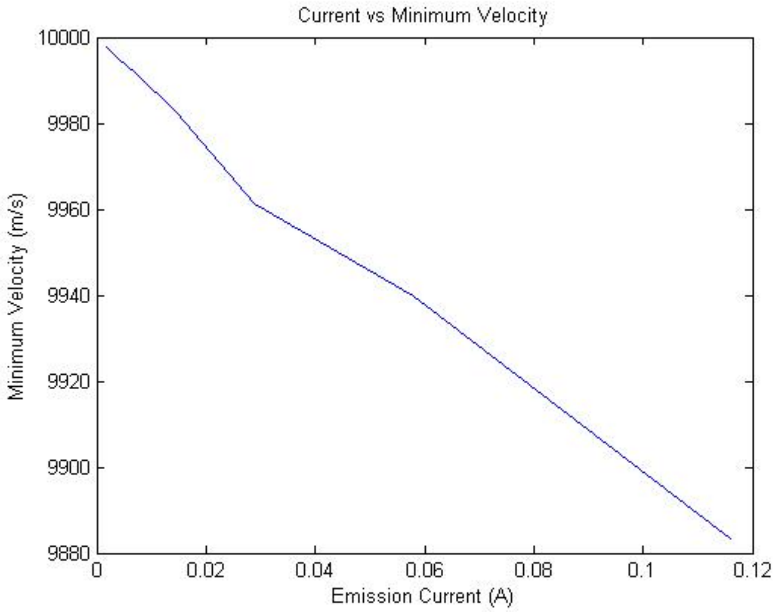

Figure 2.9: Current vs Minimum Velocity

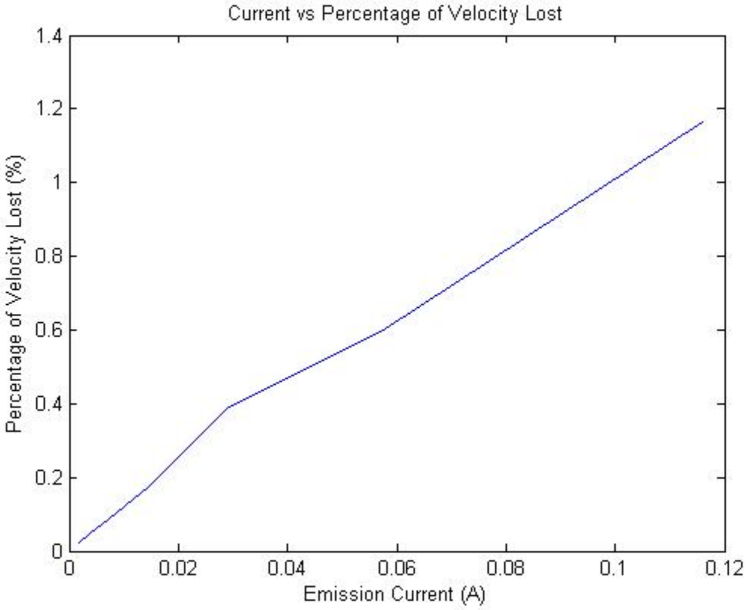

Figure 2.10: Current vs Percentage of Velocity Dropped

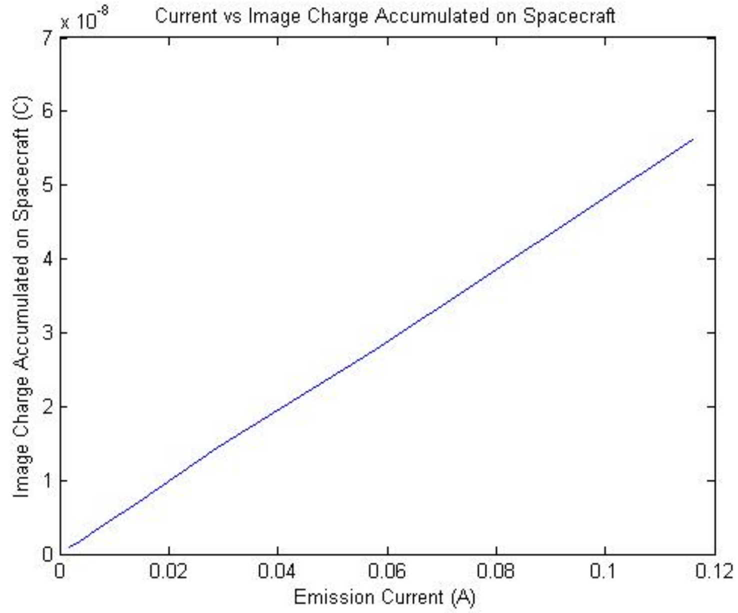

Figure 2.11: Current vs Image Charge Accumulated on Spacecraft

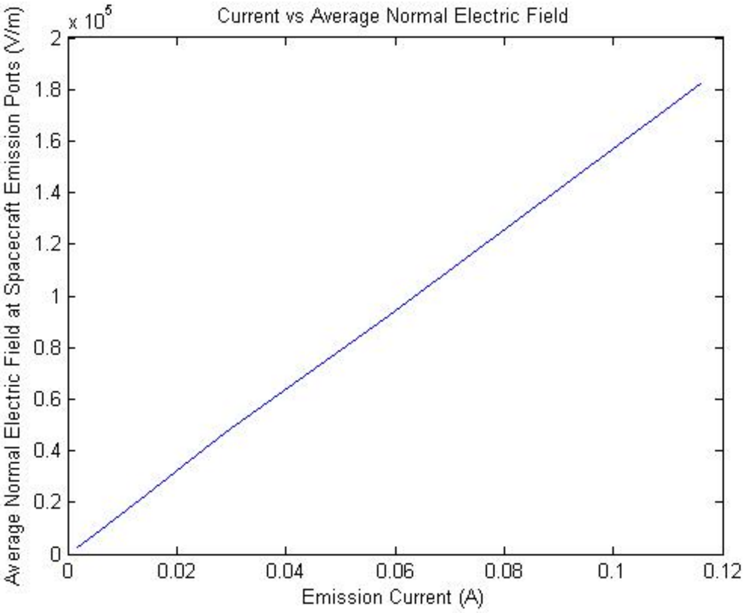

Figure 2.12: Current vs Average Normal Electric Field at Emission Ports

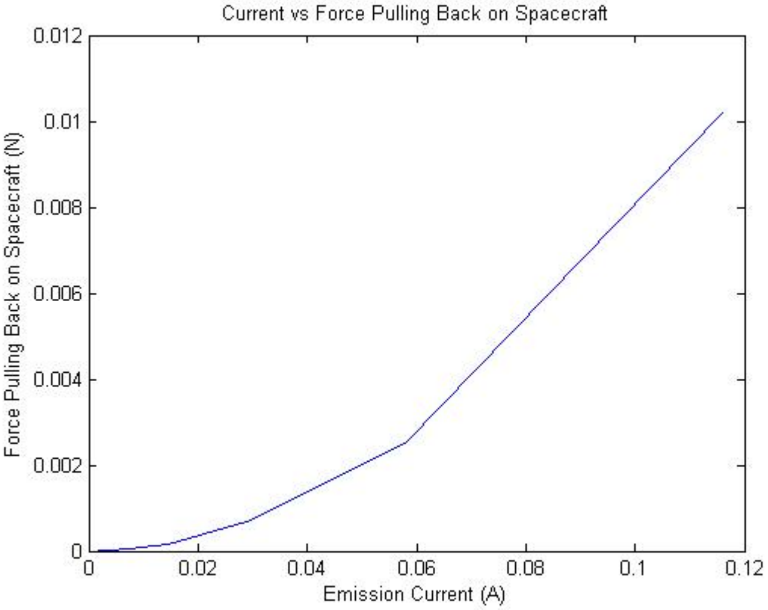

Figure 2.13: Current vs Thrust Lost Due to E-Field Interaction

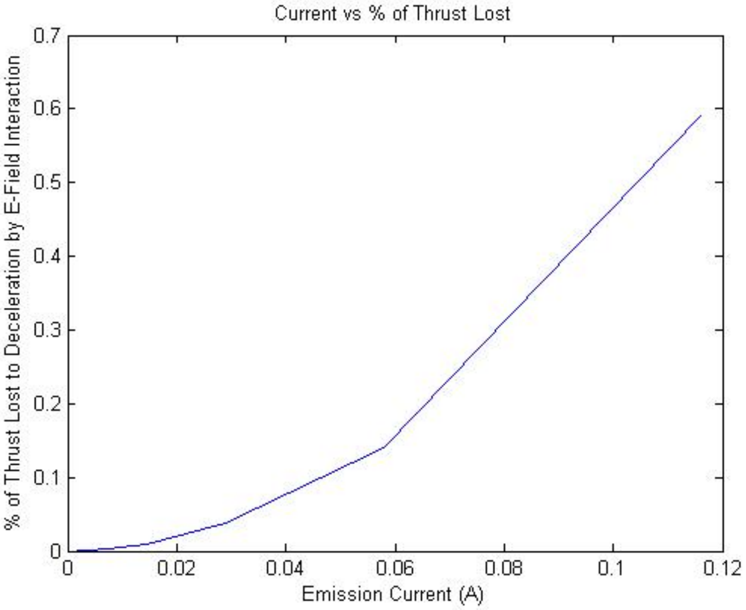

Figure 2.14: Current vs Percentage of Thrust Lost Due to E-Field Interaction

2.4.2 Time Progression of 50 nm Hollow Polystyrene Particles at 1000 Seconds Specific Impulse

Similar simulations were done to assess the time progression of a net neutral emitted beam with 50 nm hollow polystyrene particles rather than 200 nm solid polystyrene particles, which were selected as representative of smaller, higher charge-to-mass particles. The particles have a mass of 4.45×10^{-20} kg and contain a charge of 4.46×10^{-17} C. This results in approximately a 1000 C/kg charge to mass ratio, which is ten times higher than the specific charge in the previous simulation. All other emitter and simulation space parameters are the same as the previous simulation. Since the charge on each particle is less than the previous simulation, and the current density and velocity of emission are kept the same, there will be more particles emitted; however, in this simulation, it will appear as if there are similar numbers of particles emitted between this and the previous simulation. This is because in particle-in-cell simulations, oftentimes numerous particles will be represented by a single *superparticle*, where the number of particles represented by a single superparticle is the NP2C number, and in this case the number of simulation superparticles are kept the same. Fig. 2.15 and Fig. 2.16 show the progression of this beam at two time steps.

In this case similar results as the previous case are shown, namely the convergence of the two oppositely charged beams towards one another. The image charge induced axial electric field causes the initial emitted beam to be slowed down much more than in the previous case, but the maximum is still only a 1.1% velocity decrease. Since these particles have a higher charge to mass ratio they move more easily, and thus the two beams more readily converge upon one another. In addition to the larger slow down in velocity near the spacecraft (left side of the simulation space), there is a larger increase in velocity on the leading edge again due to the unneutralized charge cloud behind the leading edge accelerating it forward (right side of the simulation space) than the 100 C/kg particle. All of these results can be understood and compared to

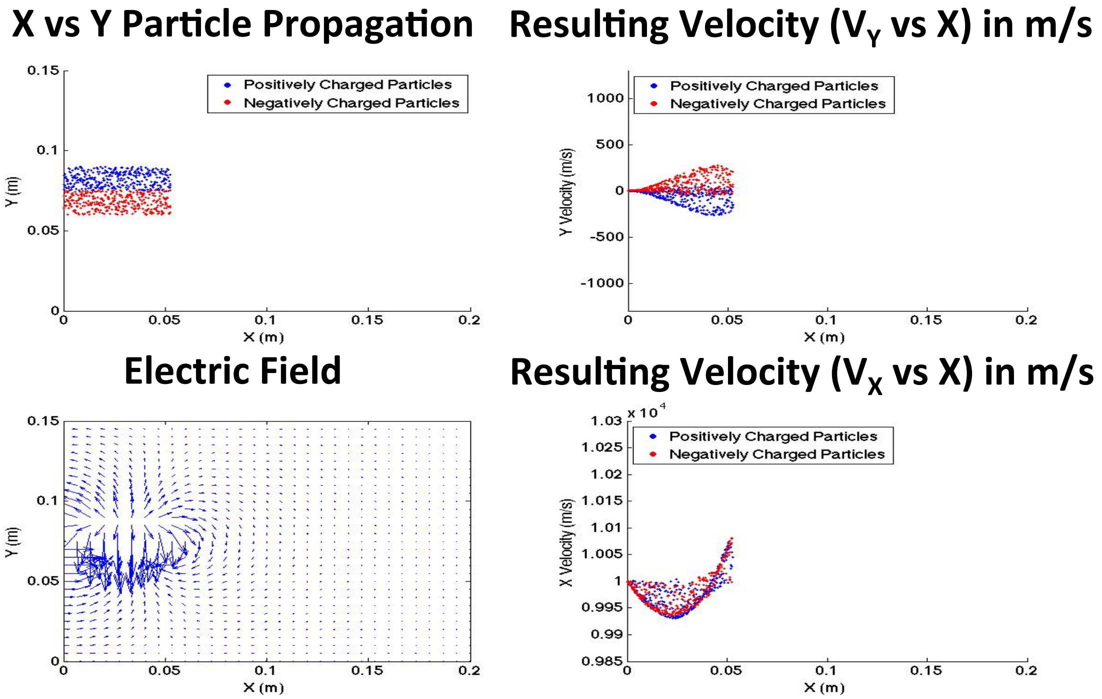

Figure 2.15: Beam Propagation of 50 nm Hollow Polystyrene Particles at Early Time Stage

the previous simulation using a series of force equations as is seen in Eq. 2.8.

$$qE = F = ma \tag{2.8}$$

Changing this equation around gives Eq. 2.9.

$$a = \frac{q}{m}E \tag{2.9}$$

From this equation it can be seen that with higher specific charge, as in this case, the acceleration of the particles will increase. Since the same amount of current is being emitted, there will be similar initial electric fields, thus, the higher specific charge will result in both the axial velocity being slowed down more initially as well as reaching a higher leading edge velocity as well as the oppositely charged beams converging upon

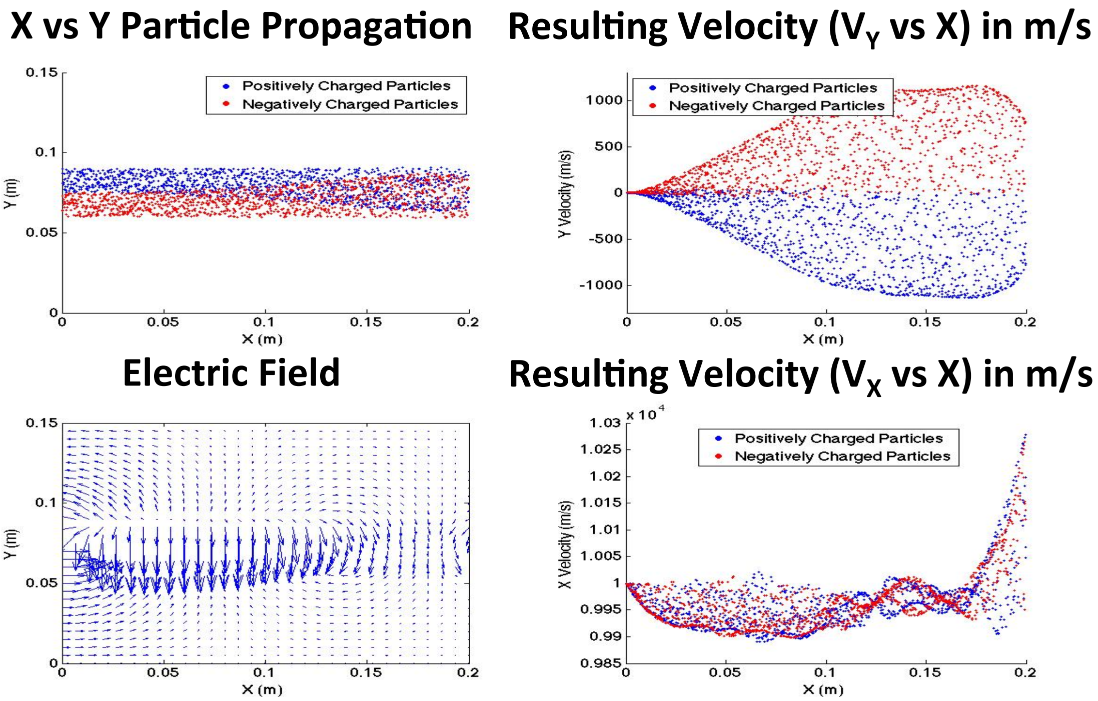

Figure 2.16: Beam Propagation of 50 nm Hollow Polystyrene Particles at Final Time Stage

one another more rapidly.

2.4.3 Varying Beam Separation while Emitting 200 nm Solid Polystyrene Particles at 1000 Seconds Specific Impulse

In these next two sets of simulations beam separation and beam width are varied to assess how the image charge induced axial electric field can be minimized. In these simulations the simulation space and the emitter parameters are kept consistent with the two original time progression simulations. The simulation space is in Cartesian coordinates with 0.2 m in the X direction and 0.15 m in the Y direction with particles emitted in the +X direction. Again the current density for each emitted beam is kept at 0.967 A/m^2, with the emission being of 200 nm polystyrene particles as was used in Section 2.4.1. In this simulation the beam separation (Fig. 2.17) between two

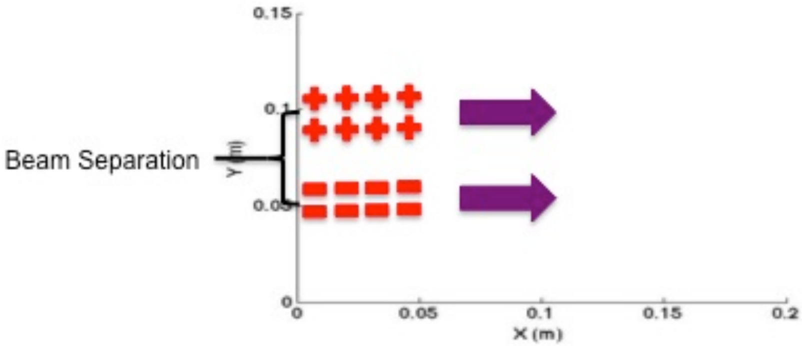

Figure 2.17: Depiction of Beam Separation Simulations

oppositely charged beams is varied, while keeping the emission width constant at 1.5 cm. The beam separation is varied from completely overlapping beams up to 8.5 cm between beam centers. Fig. 2.18, Fig. 2.19, and Fig. 2.20 show the beam propagation and diagnostics when the beam is almost to the end of the simulation space.

Fig. 2.18 shows a beam center-to-center separation of 8.5 cm, Fig. 2.19 shows a beam center-to-center separation of 1.5 cm (which means that the beams are right next to one another), and Fig. 2.20 shows a beam center-to-center separation of 0 cm (which means that the beams are completely overlapping). In this case, as the beams are moved closer together, while keeping the beam widths constant, the image charge induced axial electric field decreases. This also means there is less velocity degradation and less thrust degradation. In this case there is a maximum velocity drop of 0.9% when the beams are 8.5 cm apart, and a velocity drop of just 0.2% when the beams are right next to one another. When the beams are completely overlapping, there is virtually no velocity drop because for all intents and purposes, the beam is completely neutral and there is no image charge induced on the spacecraft wall. This is what is considered a neutral emission beam, and a neutral spacecraft. However, this may be difficult to generate in particle thrusters like NanoFET because emission beams cannot straightforwardly be placed exactly next to one another because this effectively doubles the positive and negative potential

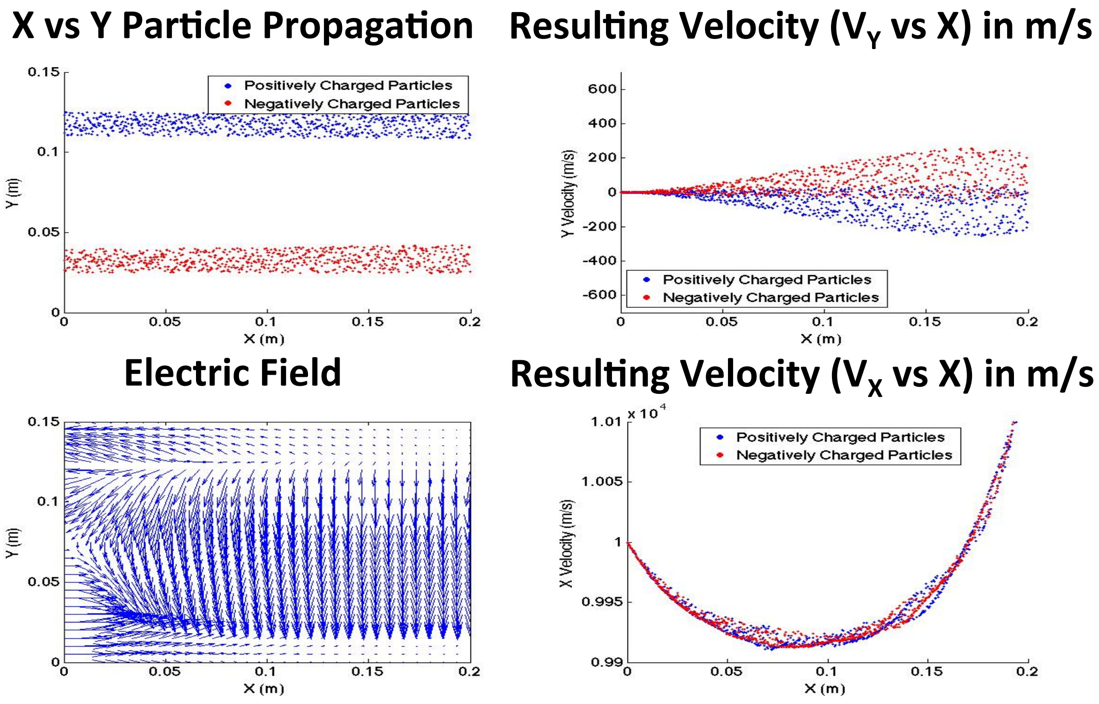
X vs Y Particle Propagation

Resulting Velocity (V_Y vs X) in m/s

Electric Field

Resulting Velocity (V_X vs X) in m/s

Figure 2.18: Beam Propagation and Diagnostics with a Beam Center Separation of 8.5 cm

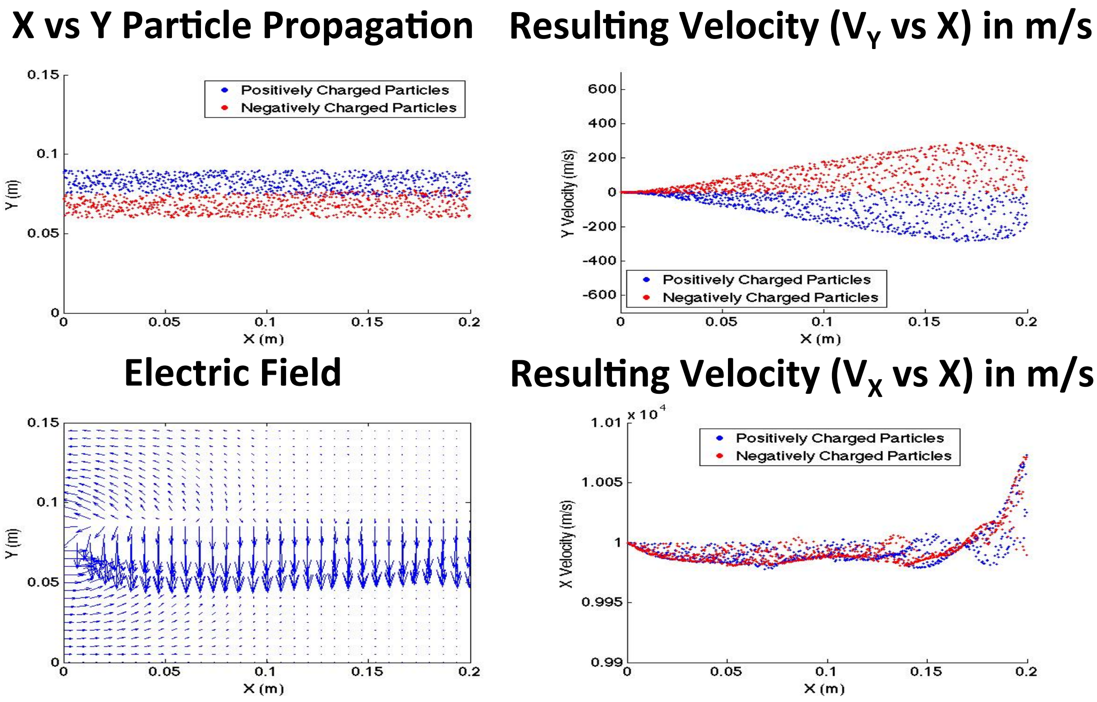

X vs Y Particle Propagation

Resulting Velocity (V_Y vs X) in m/s

Electric Field

Resulting Velocity (V_X vs X) in m/s

Figure 2.19: Beam Propagation and Diagnostics with a Beam Center Separation of 1.5 cm

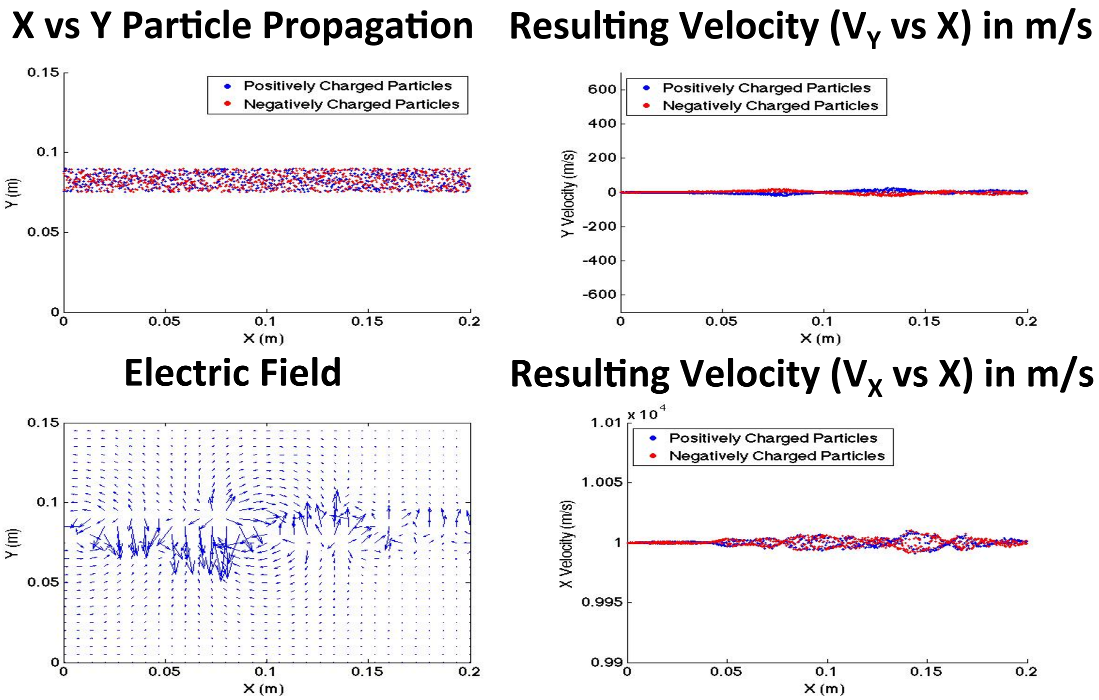

Figure 2.20: Beam Propagation and Diagnostics with a Beam Center Separation of 0 cm

difference creating greater electrical breakdown concerns.

2.4.4 Varying Beam Width while Emitting 200 nm Solid Polystyrene Particles at 1000 Seconds Specific Impulse

The next simulations are done by keeping beam separation constant (the two beams right next to one another), while varying the beam width from 0.5 cm up to 3.5 cm (Fig. 2.21). In this case, the simulation space and particles are kept the same as the previous simulations. However, the current level is varied in order to keep the current density for both beams constant at 0.967 A/m^2 as this will keep the simulations more consistent and realistic with regards to charged particle thruster operation. In addition, the number of particles that are represented by a simulated superparticle needs to be changed in order to keep the number of superparticles constant as the emission velocity is held constant. Fig. 2.22, Fig. 2.23, and Fig. 2.24 show the beam propagation and diagnostics as the beam width is decreased from 3.5 cm to 1.5 cm to 0.5 cm. Again these simulations show that as beams get thinner, the image charge induced electric field continues to decrease, decreasing the drop in axial electric field from 0.9% for 3.5 cm wide beams to no velocity drop when the beams are 0.5 cm wide. This goes to show that as beam widths are reduced, the image charge induced axial electric field in the negative X direction gets weaker.

These two simulations suggest that there are ways of mitigating the image charge induced axial electric field by moving the beams closer together as well as decreasing the widths of the beams. Combining these two effects with increasing the number of alternating beams in the SVCTE scheme is similar to creating overlap of the two beams, which was also shown to have a neutralizing effect (Fig. 2.20). However, for use in a particle thruster such as NanoFET there are limits to which this can be done including how close oppositely charged gates can be placed, and how narrow these gates can be without incurring a strong likelihood of dielectric breakdown in

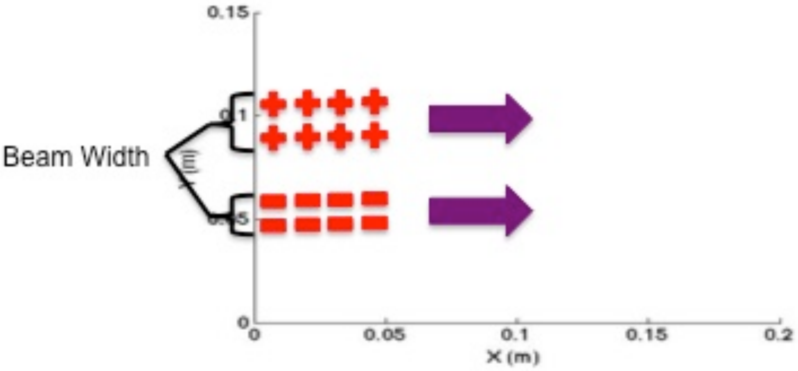

Figure 2.21: Depiction of Beam Width Simulations

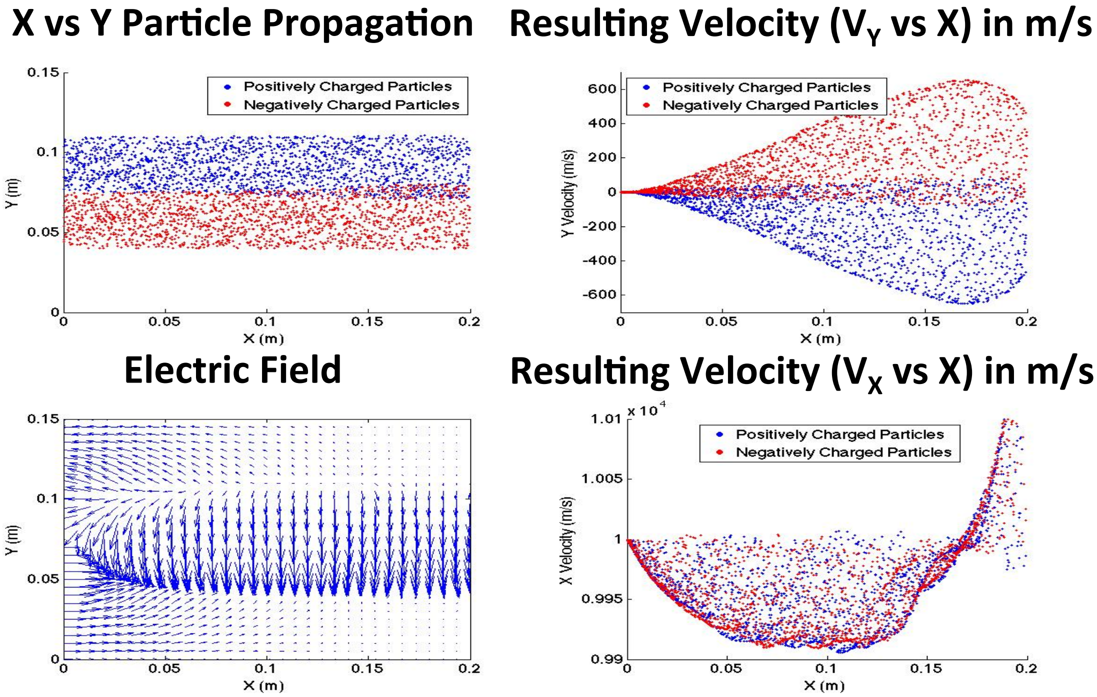
X vs Y Particle Propagation

Resulting Velocity (V_Y vs X) in m/s

Electric Field

Resulting Velocity (V_X vs X) in m/s

Figure 2.22: Beam Propagation and Diagnostics with a Beam Width of 3.5 cm

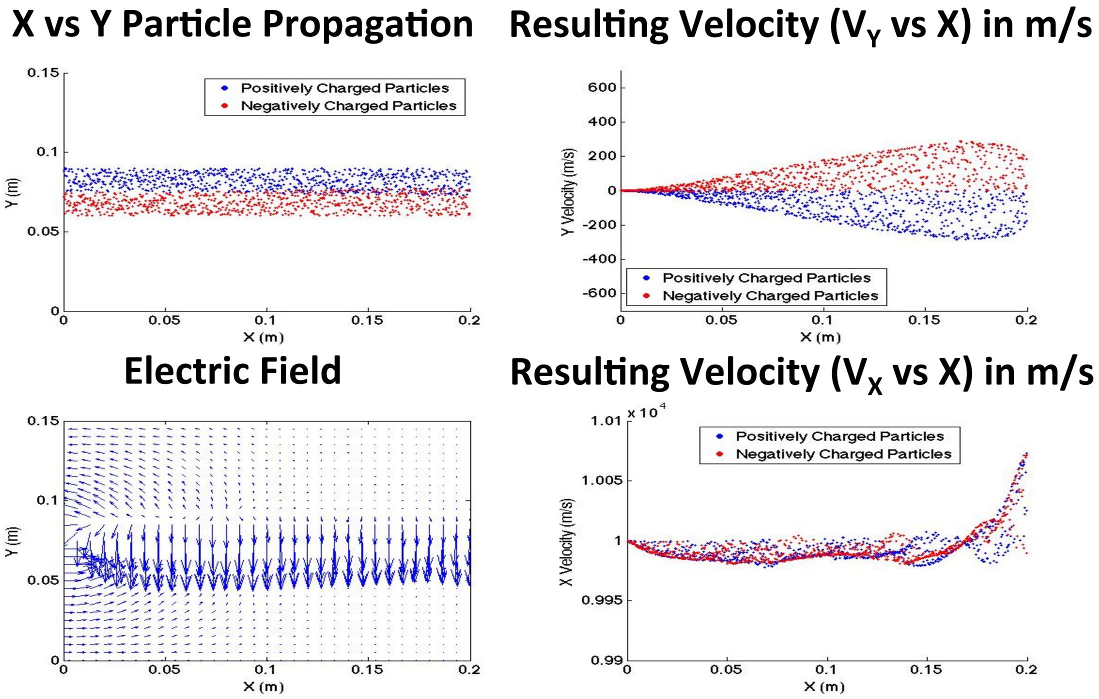
X vs Y Particle Propagation

Resulting Velocity (V_Y vs X) in m/s

Electric Field

Resulting Velocity (V_X vs X) in m/s

Figure 2.23: Beam Propagation and Diagnostics with a Beam Width of 1.5 cm

the supporting structures. This is an issue that is still of concern and will continue to be explored.

2.4.5 Varying Current Density while Emitting 200 nm Solid Polystyrene Particles at 1000 Seconds Specific Impulse

This last SVCTE scheme simulation shows the effects when current density is increased towards the space charge limit. As has been mentioned previously, the space charge limit in these simulations with a 1000 s specific impulse emitter is approximately 525 A/m^2 as was shown previously in Eq. 2.1. The previous simulations had been emitting particles with a current density of approximately 1 A/m^2. The following simulations show the results when the current density is increased to approximately 10 A/m^2, which is still well below the space charge limit. These simulations will have the same simulation space parameters as previous simulations (Section 2.4.1) with

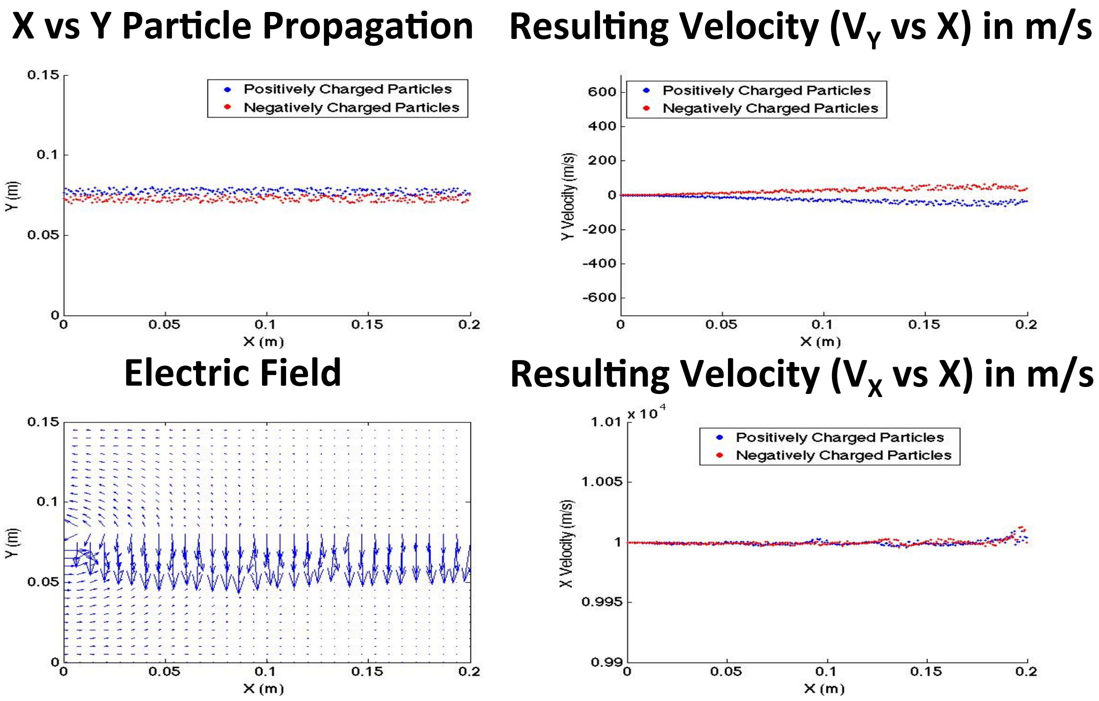

X vs Y Particle Propagation

Resulting Velocity (V_Y vs X) in m/s

Electric Field

Resulting Velocity (V_X vs X) in m/s

Figure 2.24: Beam Propagation and Diagnostics with a Beam Width of 0.5 cm

an emitter width of 1.5 cm and the beams placed adjacent to one another. As in the varying beam width simulation set, as current density is varied, the number of particles being emitted will change as well as the emission velocity is held constant; however, the number of particles to superparticle ratio is again changed to keep the number of simulated particles constant. Fig. 2.25 and Fig. 2.26 show the diagnostics with a current density at 1 and 10 A/m^2 respectively.

These two plots show that as current density is increased by a factor of 10, while this is well below space charge limit, the maximum drop in velocity increases a factor of ten from 0.22% to nearly 2%. This shows that even though the maximum drop in velocity seemed insignificant in previous simulations, as the current density is increased these effects will be very important and detrimental. This seems to indicate that if current density were to be dropped, there would be a proportional drop in maximum drop in velocity. Thus, if this thruster were to operate in the expected

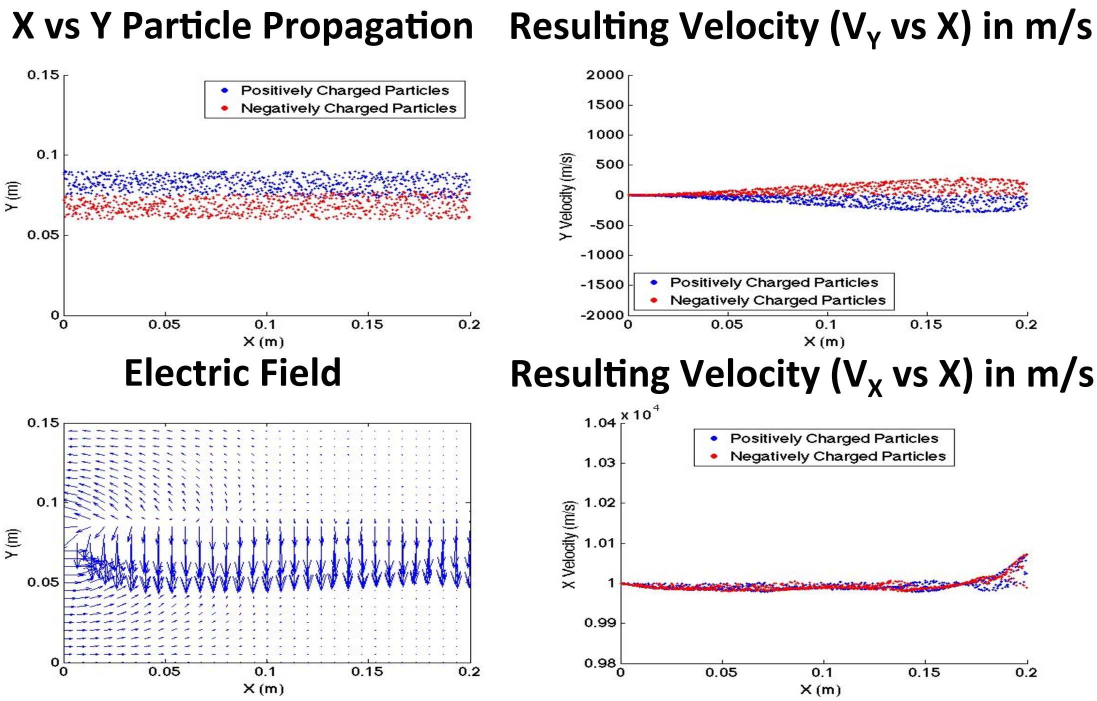
X vs Y Particle Propagation

Resulting Velocity (V_Y vs X) in m/s

Electric Field

Resulting Velocity (V_X vs X) in m/s

Figure 2.25: Beam Propagation and Diagnostics with a Current Density of 1 A/m^2

NanoFET range, which includes a much lower current density, there will be very little thrust degradation. Since it is envisioned that the NanoFET system would be ideally suited for nanosatellites, specifically CubeSats, and that there are visions to provide a CubeSat with 25 W at 50% duty cycle in the future, and thus that is what will be assumed to be the maximum power level. With 25 W at 50% duty cycle, and a voltage range of between 5 kV and 40 kV, current will range between 312.5 μA and 2.5 mA.

2.5 Time-Varying, Common Spatial Emission Scheme

Next, the time-varying, common spatial emission (TVCSE) scheme that was introduced earlier is examined. It bears repeating that this is the scheme that has a single emission area that emits particles of a single polarity at any one time. How-

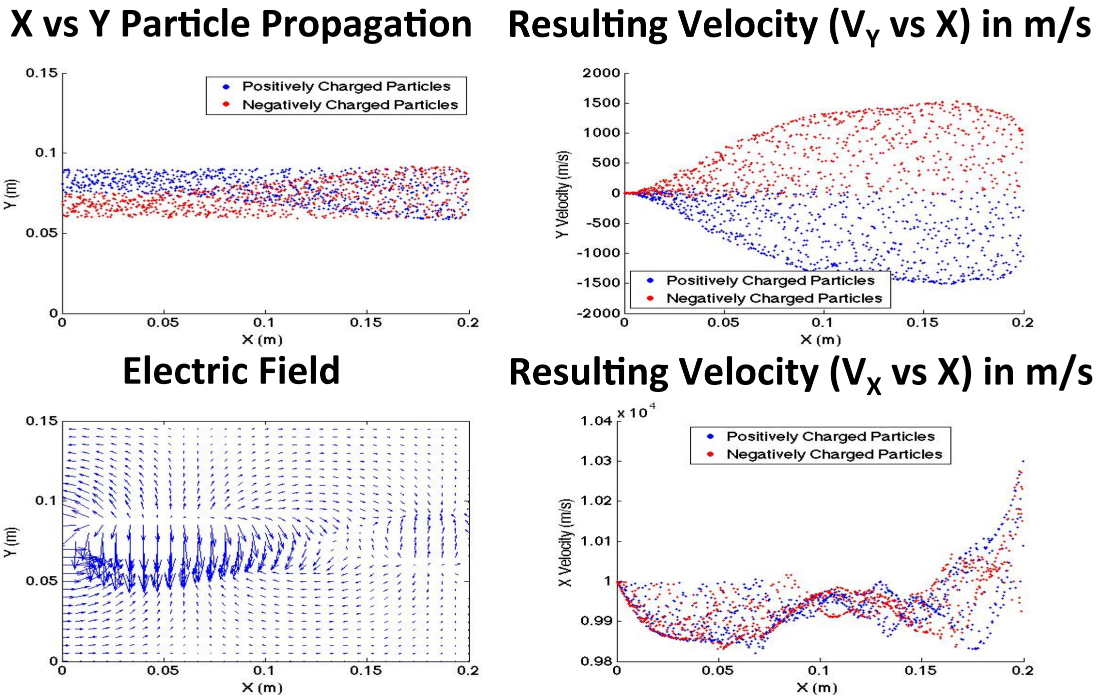
X vs Y Particle Propagation

Resulting Velocity (V_Y vs X) in m/s

Electric Field

Resulting Velocity (V_X vs X) in m/s

Figure 2.26: Beam Propagation and Diagnostics with a Current Density of 10 A/m^2

ever, the single emission area will change the polarity of particles that it emits over time in an oscillating manner. Over time, the beam and the spacecraft is net neutral; however, over short time scales both the beam and the spacecraft will charge up.

2.5.1 Analytical Model of Time-Varying Common Spatial Emission Scheme

First a simplified spacecraft charging model is mathematically analyzed. This simplified spacecraft charging model will ignore the ionospheric plasma effects. This model assumes that the 3U CubeSat that NanoFET will be placed on is a sphere rather than a rectangular prism. This sphere has a diameter equal to the length of the CubeSat, thus giving it a diameter of 30 cm as shown in Fig. 2.27.

For a sphere, there are two ways to approach a formulation for correlating voltage that the sphere has charged up to, to the charge being expelled from the sphere, the first being Gauss' Law and the second being using capacitance of a sphere, with both

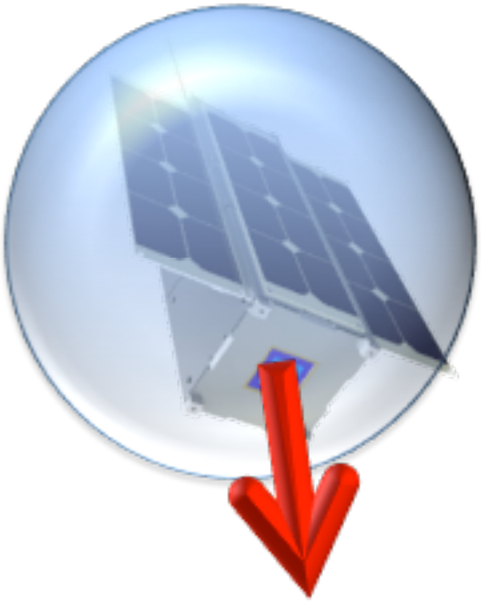

Figure 2.27: CubeSat Modeled by a 30 cm Diameter Sphere

giving the same result. With Gauss' Law being more basic, that approach starting with Gauss' Law in integral form as shown in Eq. 2.11 will be utilized.

$$\oint E \cdot dA = \frac{Q}{\varepsilon_0} \tag{2.10}$$

$$\oint E \cdot dA = \frac{Q}{\varepsilon_0} \tag{2.11}$$

Knowing that it is a sphere meaning a constant radius this equation can be transformed to Eq. 2.12.

$$\frac{V}{r} \cdot 4\pi r^2 = \frac{Q}{\varepsilon_0} \tag{2.12}$$

Giving an equation as shown in Eq. 2.13.

$$V = \frac{Q}{4\pi\varepsilon_0 r} \tag{2.13}$$

Lastly since current is simply flow of charge over time, it can be substituted in for charge and a relationship for how quickly a spacecraft will charge up to certain voltages given a determined amount of current leaving the sphere can be found as shown in Eq. 2.14.

$$t = V\frac{4\pi\varepsilon_0 r}{I} \tag{2.14}$$

From this equation it can be determined how quickly the hypothetical 3U spherical CubeSat will charge up to different percentages of the charging voltage of the NanoFET system. In this case it is assumed that the NanoFET system is charging and accelerating the particles out at 40 kV. Fig. 2.28 shows how quickly the simplified spacecraft will charge up to 1%, 5%, 10%, and 20% of that charging and accelerating voltage depending on how much current is being emitted from the spacecraft. From this it can be seen that if 14.5 mA of current are emitted as in previous simulations, the unneutralized 3U CubeSat will charge up to 5% of the charging and accelerating voltage in under 10 μs. If it is desired to keep the spacecraft charge below this 5% value, then there is a need to be oscillating between emitting positively and negatively charged particles at over 100 kHz. Predictably, this is very difficult to do when charging charged particle thrusters such as NanoFET up to high voltages in one polarity in order to emit particles of a certain polarity, then quickly discharge and charge up to high voltage in the opposite polarity to emit the opposite charge. On the other hand if particles were to be emitted at a current of between 312.5 μA and 2.5 mA, it would take the spacecraft approximately hundreds of μs to charge up to 5% of the charging and accelerating voltage. This means that the pulses could oscillate at around 10 kHz, which is possible. On the other hand this indicates at lower current levels the spacecraft does not charge up too quickly, thus indicating that there may be other ways of neutralizing the spacecraft.

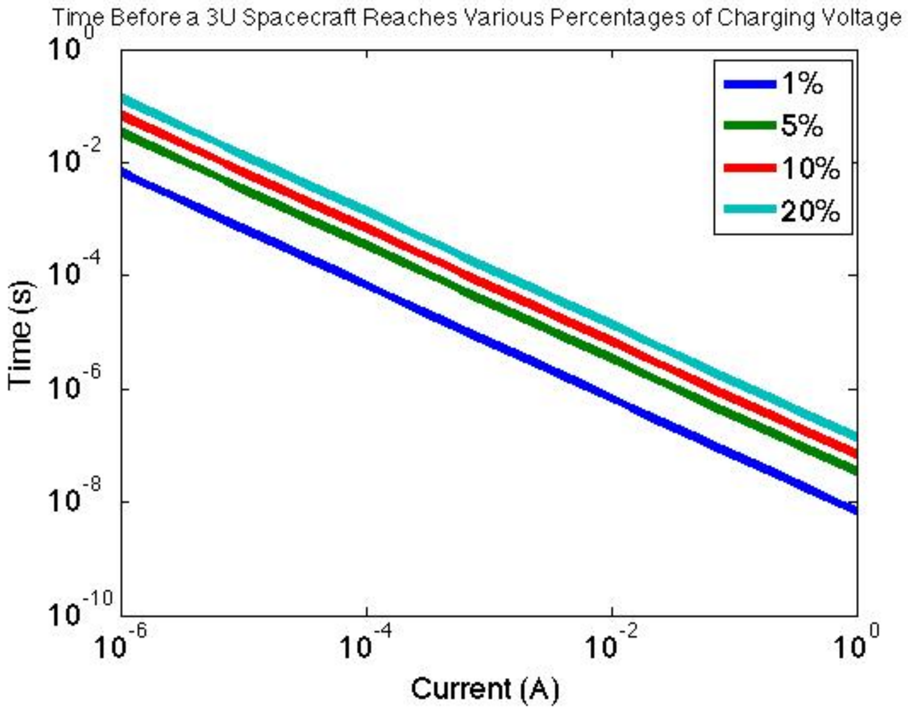

Figure 2.28: Time Before a 3U Spacecraft Reaches Various Percentages of Charging Voltage

2.5.2 Simulation of Time-Varying, Common Spatial Emission Scheme

In addition to the analytics of the TVCSE scheme, simulations must also be conducted of this scheme. The first step is to compare this scheme to the SVCTE scheme along with an unneutralized beam. (The code for this neutralization scheme is shown in Appendix B.)

The TVCSE scheme simulation setup is similar to that of the spatial-varying, common temporal emission scheme with regards to the particles being used, the simulation boundaries, the mesh, and the boundary reflections. The only major difference being the beam emitter. The positive and negative beam emitters in these simulations are stacked on top of one another so that both positive and negatively charged particles can come out of the same emission port. In order to have exactly a single polarity particle emitted at any point in time, alternating sinusoidal patterns are necessary. In addition, it is desirable to have equal current levels at all times rather than increasing and decreasing current levels. OOPIC PRO^{TM} provides an additional "step" function that is defined as shown in Eq. 2.15.

$$f(x) = \begin{cases} 1 & x \geq 0 \\ 0 & x < 0 \end{cases} \tag{2.15}$$

Thus positive particle emission current is multiplied by Eq. 2.16 and negative particle emission current is multiplied by Eq. 2.17 where f is the frequency of oscillation.

$$F_1(t) = step(sin(2\pi ft)) \tag{2.16}$$

$$F_2(t) = 1 - step(sin(2\pi ft)) \tag{2.17}$$

With these opposite equations, only positive or only negative particles will be emitted at any time with equal length pulses and a full pulse starting at the start of the simulation as at any time exactly one of Eq. 2.16 and Eq. 2.17 will be 1 and the other one will be 0.

By comparing the SVCTE scheme (two oppositely charged 14.49 mA beams emitted simultaneously) with an oscillating TVCSE scheme that is always emitting a 28.98 mA beam, it gives a good starting point as to how effective each neutralization scheme is. In this case, the emission of the beams is stopped well before it reaches the far right wall of the simulation space at 400 time steps.

For the SVCTE scheme, the minimum velocity drops to 9980 m/s for the positive and negative particles, showing an approximate 0.2% drop in velocity in this case.

For the TVCSE scheme, the frequency of oscillation between emitting positive and negatively charged particles will have a significant effect on the simulation results. With a frequency of 1 MHz, the minimum velocity drops to 9999.94 m/s for the positive particles closest to the emission port and 9999.65 m/s for the negative particles closest to the emission port (with different values due to their different X positions), showing an approximate 0.0006% and 0.0035% drop in velocity. The next two particle pulses from the emission port have a minimum velocity of 9999.54 m/s for the positive particles and 9998.96 m/s for the negative particles, which corresponds to an approximate 0.0046% and 0.0104% drop in velocity. The velocity in the X direction vs X position with the values described above is as shown in Fig. 2.29.

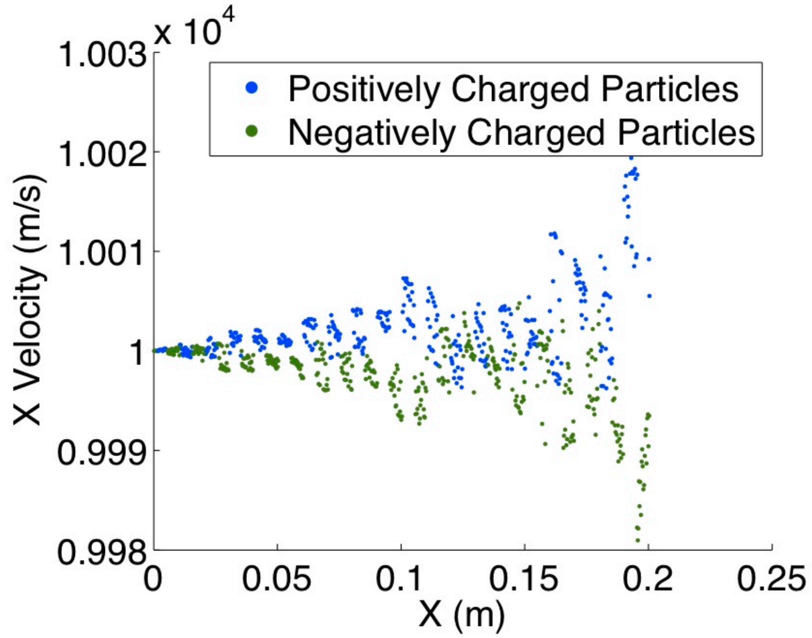

Figure 2.29: X Velocity vs X position for a Time-Varying Constant Spatial Emission Scheme at 1 MHz

With a frequency of 200 kHz at the 14.49 mA current level, there is a drop in velocity to 9995.68 m/s, corresponding to a 0.0432%, from the positive pulse closest to the spacecraft, and a drop in velocity to 9973.84 m/s, corresponding to a 0.26164% drop in velocity from the negative pulse closest to the spacecraft. The velocity in the X direction vs X position with the values described above is as shown in Fig. 2.30. The simulation space for this simulation is as shown in Fig. 2.31.

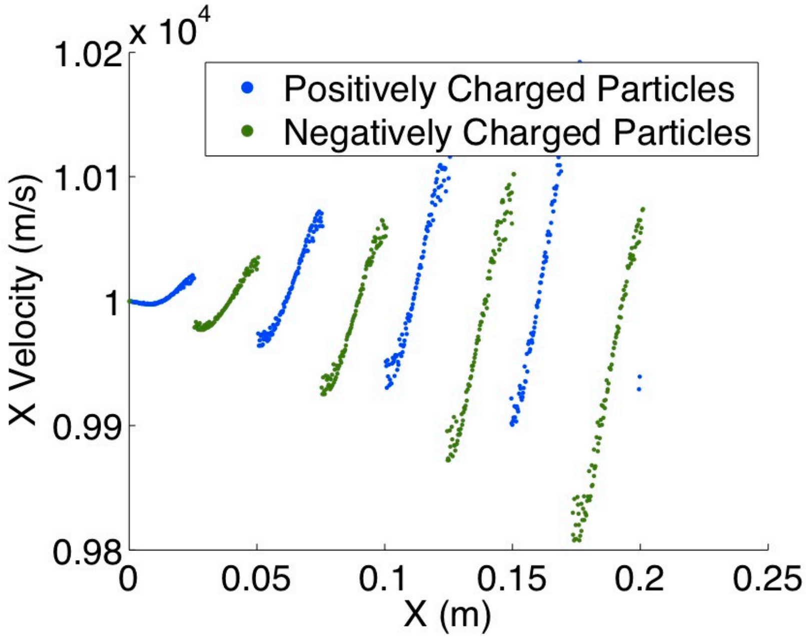

Figure 2.30: X Velocity vs X position for a Time-Varying Constant Spatial Emission Scheme at 200 kHz

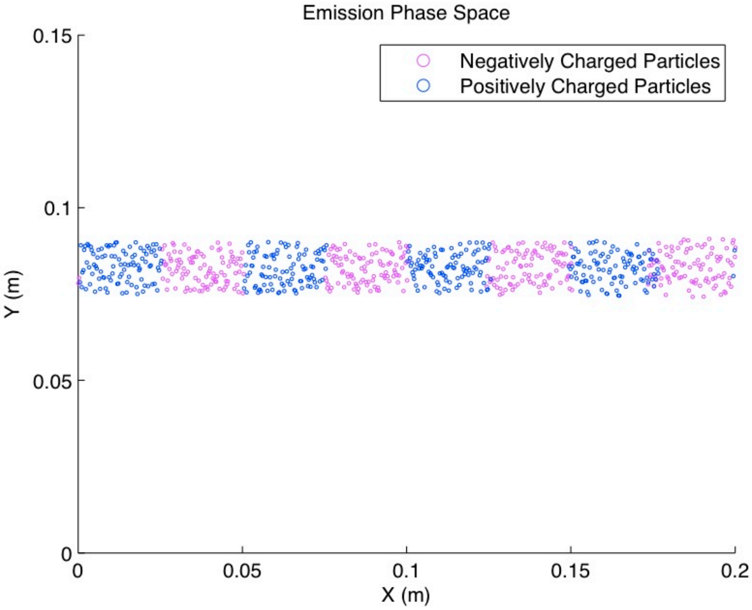

Figure 2.31: Simulation Space for a Time-Varying Constant Spatial Emission Scheme at 200 kHz

With a frequency of 100 kHz, which is the estimated oscillation frequency that will cause the 3U CubeSat to charge up to 5% of the charge and accelerating voltage, there is a drop in velocity to 9989.4 m/s, corresponding to a 0.106% drop in velocity, from the positive pulse closest to the spacecraft and a drop in velocity to 9915 m/s, corresponding to a 0.85% drop in velocity from the negative pulse closest to the spacecraft. The velocity in the X direction vs X position with the values described above is as shown in Fig. 2.32.

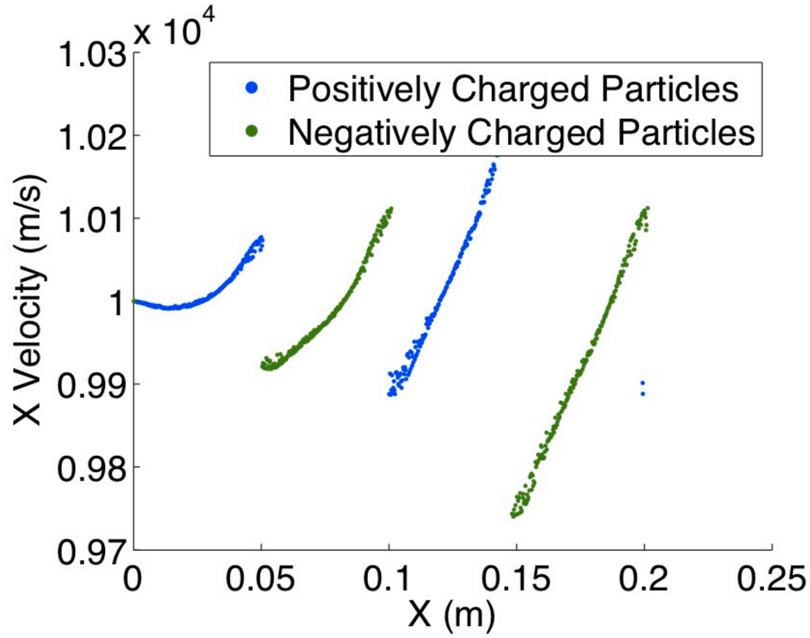

Figure 2.32: X Velocity vs X position for a Time-Varying Constant Spatial Emission Scheme at 100 kHz

While velocity versus position results are helpful to understand the physical response of the emitted particles, impact to spacecraft thrust is the primary concern. As was shown for the SVCTE scheme in Section 2.4.1, the image charge on the spacecraft surface, average electric field at the thruster emission ports, spacecraft deceleration force, and percentage of thrust lost due to the electric field interaction are shown in Fig. 2.33, Fig. 2.34, Fig. 2.35, and Fig. 2.36 respectively.

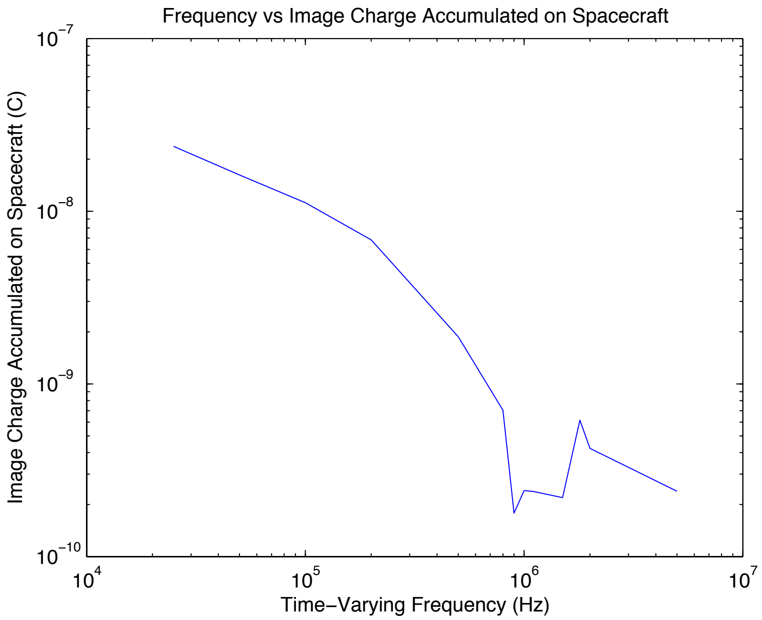

Figure 2.33: Image Charge Accumulated on the Spacecraft over Time-Varying Frequency After 1.2 ms

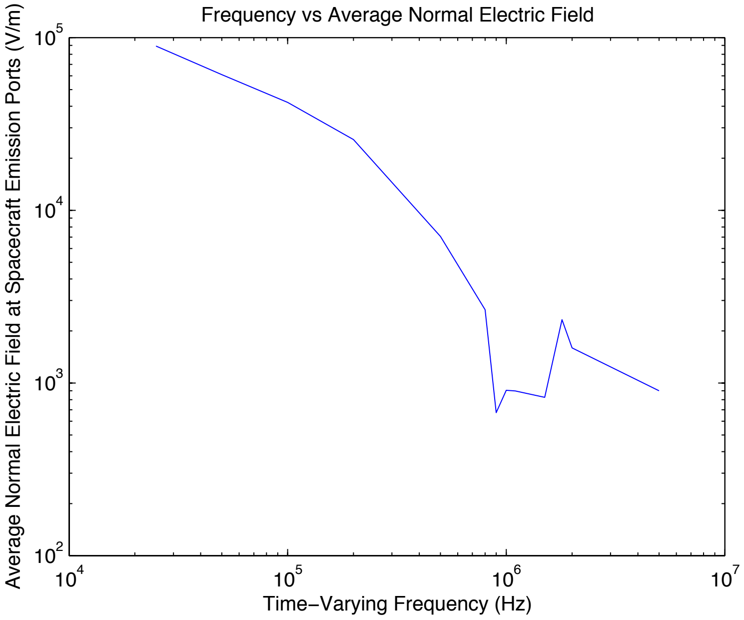

Figure 2.34: Average Normal Electric Field at the Emission Ports over Time-Varying Frequency After 1.2 ms

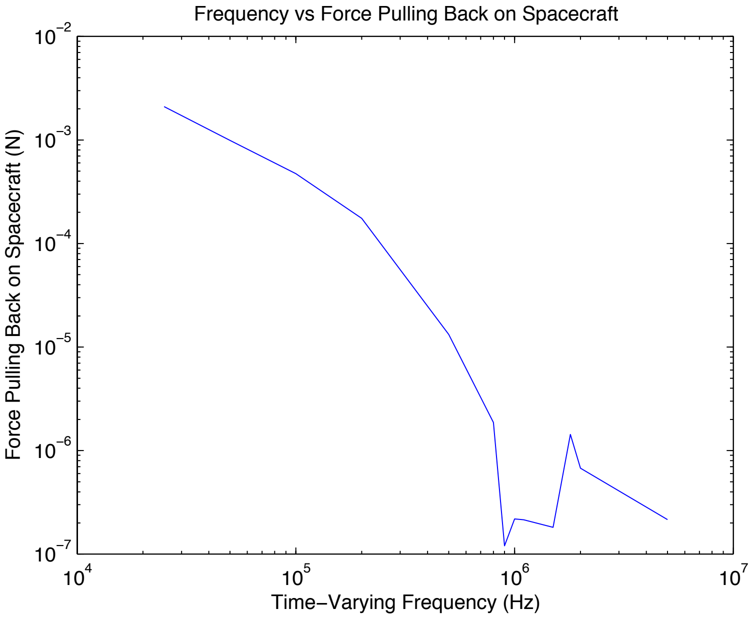

Figure 2.35: Force Decelerating the Spacecraft due to Electric Field Interaction over Time-Varying Frequency After 1.2 ms

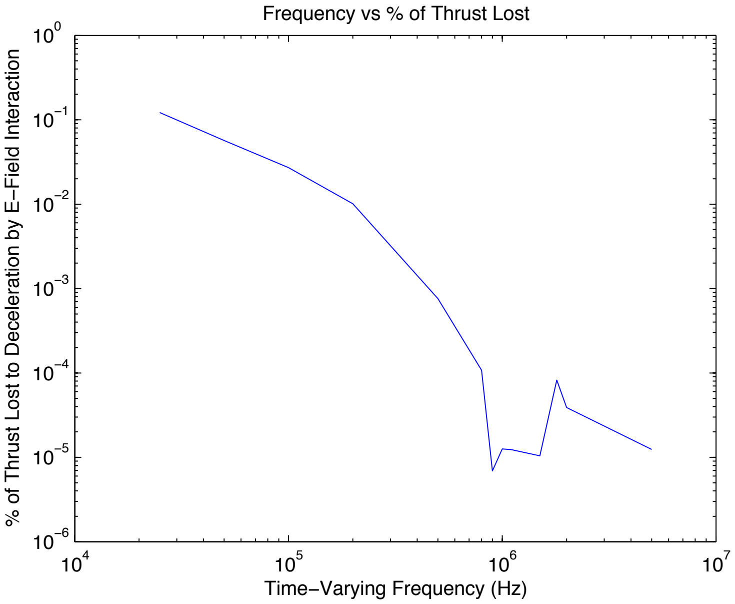

Figure 2.36: Percentage of Thrust Lost due to Electric Field Interaction over Time-Varying Frequency After 1.2 ms

These four plots all show the same general trend with a decrease in image charge, electric field, force, and percentage of thrust lost as frequency increases, except for a repeatable sharp plateau drop around 1 MHz. In order to explain why there is such a plateau, it is important to look at the four plots over time rather than over frequency. The following four plots, Fig. 2.37, Fig. 2.38, Fig. 2.39, Fig. 2.40, will show the four diagnostics for a 100 kHz TVCSE scheme pulse calculated primarily from the electric field on the spacecraft. Although the forces on the spacecraft are calculated over the entire spacecraft wall and not just the emission region, the electric field is largest at the emitters meaning that there is no danger of the image charge on the surface of the spacecraft leaving the confines of the emitter region as shown in Fig. 2.41.

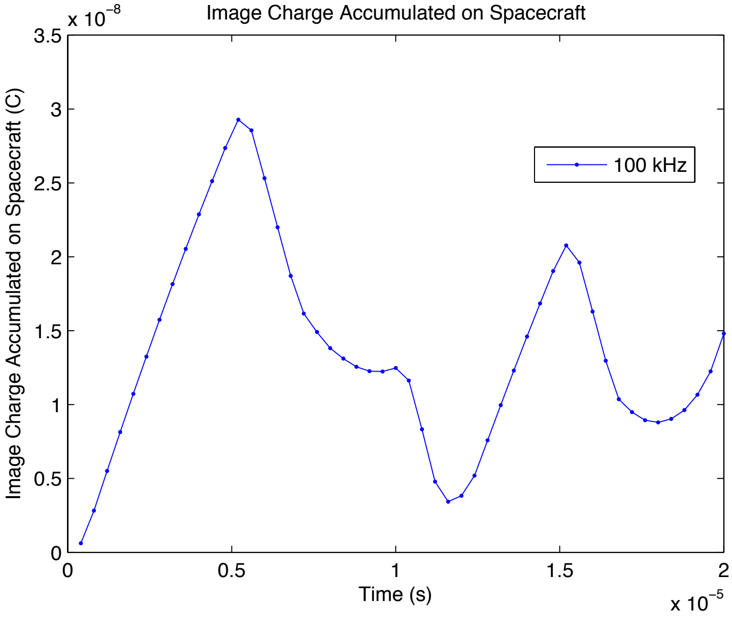

Figure 2.37: Image Charge Accumulated on the Spacecraft over Time for a 100 kHz Time-Varying, Common Spatial Emission Scheme Pulse

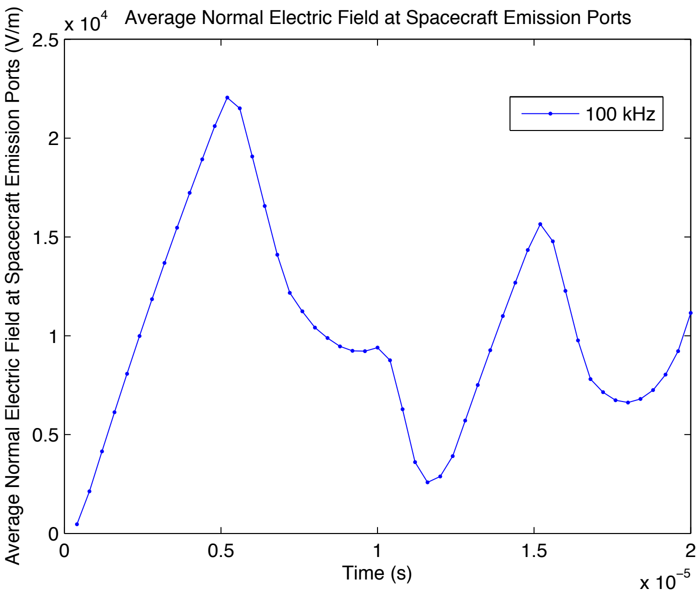

Figure 2.38: Average Normal Electric Field at the Emission Ports over Time for a 100 kHz Time-Varying, Common Spatial Emission Scheme Pulse

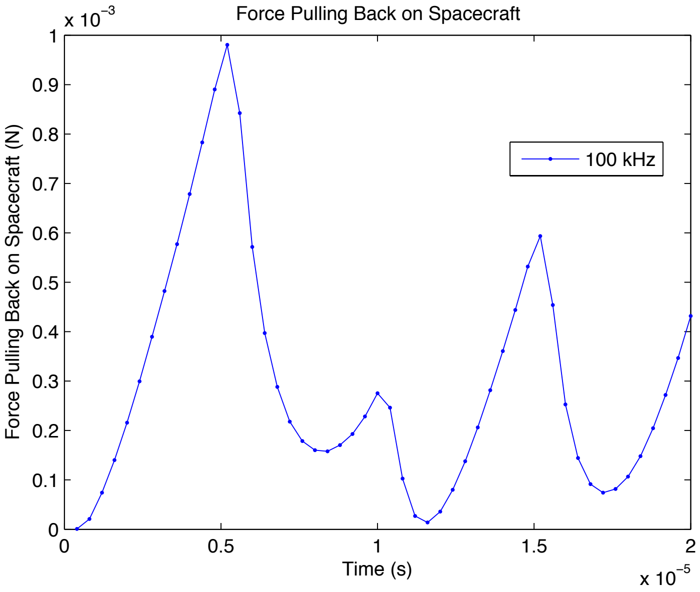

Figure 2.39: Force Decelerating the Spacecraft due to Electric Field Interaction over Time for a 100 kHz Time-Varying, Common Spatial Emission Scheme Pulse

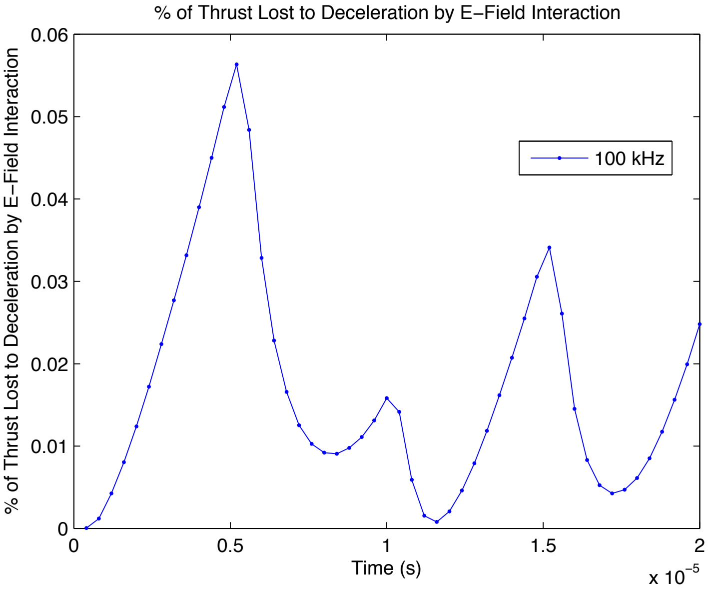

Figure 2.40: Percentage of Thrust Lost due to Electric Field Interaction over Time For a 100 kHz Time-Varying, Common Spatial Emission Scheme Pulse

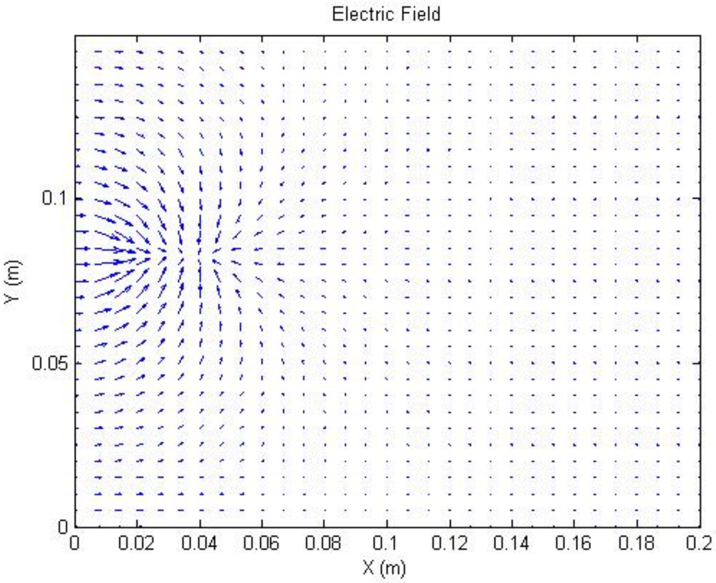

Figure 2.41: Electric Field Vectors for a Time-Varying Constant Spatial Emission Scheme at 100 kHz Illustrating Confinement of Electric Field to the Emitter Region

A 100 kHz pulse means that negative particles are emitted for the first 5 μs followed by a 5 μs positive emission with this sequence then repeating. This is illustrated in the X direction velocity plots in Fig. 2.32. In all four diagnostics a mostly linear response is seen during the first 5 μs of negative particle emission. However, in the next 5 μs, which is all positive particle emission, the first approximately 2 μs decays in a mostly linear fashion, but the fall off rapidly slows and plateaus and eventually begins to rise. This can be explained by the fact that although the beam is not truly "net neutral" until the 10 μs point, the newly emitted positive particles are closer to the spacecraft than the originally emitted negative particles, and thus the positive particles exhibit more of a force on the spacecraft than the negative particles, and thus there are less of them needed to fully negate the impact of the negative particles. Since only some of the newly emitted positive particles are needed to neutralize the previously emitted negative particles, part of the electric field from the positive beam is directed to the right towards the negative beam and a portion of the electric field is directed back towards the spacecraft instead of all being directed towards the positive beam (Fig. 2.42). Thus, after this local minimum is reached, any additional positive particles that are emitted will just increase each of the diagnostics.

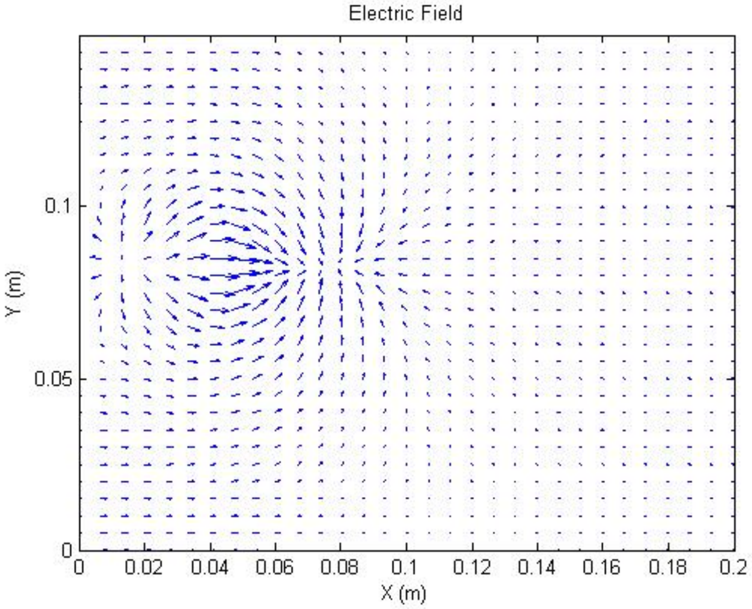

Figure 2.42: Electric Field Vectors for a Time-Varying Constant Spatial Emission Scheme at 100 kHz with Electric Field Pointing Back Towards the Spacecraft and Forward in the Beam

In the next 5 μs, the diagnostics all start to decrease again even though it is now negative particles being emitted. This is because the smaller amount of newly emitted negative particles close to the spacecraft, are well balanced by the overall positive pull on the spacecraft from the "net neutral" particles to the right of the spacecraft as the fully emitted positive particles are closer to the spacecraft wall than the fully emitted negative particles. Fig. 2.43 illustrates the simulation space at 12 μs, which is when all the diagnostics are approximately at their local minimum. Fig. 2.44 shows the electric field at this local minimum time and it shows almost no electric field to or from the spacecraft, with all the electric field lines being confined within the beam. This lack of electric field to or from the spacecraft is what provides the local minimum as there is almost no effect on the spacecraft thrust from the electric field interaction. After this 12 μs time, the diagnostics all start to rise as the continued negative particle emission overtakes the positive pull from the "net neutral" beam to the right until negative particle ends and positive particle emission begins. It also appears that the rate of increase in the diagnostics during the negative particle emission are equivalent between the first 5 μs and between 12 μs and 15 μs.

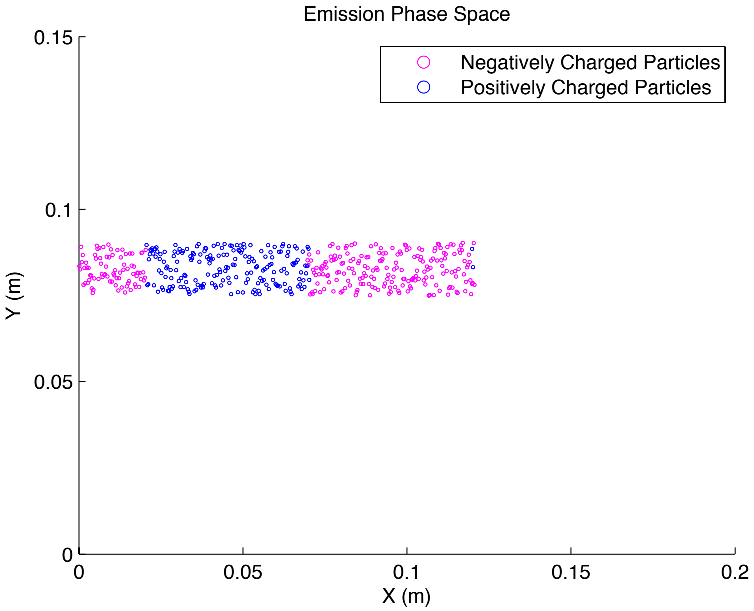

Figure 2.43: Simulation Space for a Time-Varying Constant Spatial Emission Scheme at 100 kHz when the Negative and Positive Particles are Best Balanced at 12 μs

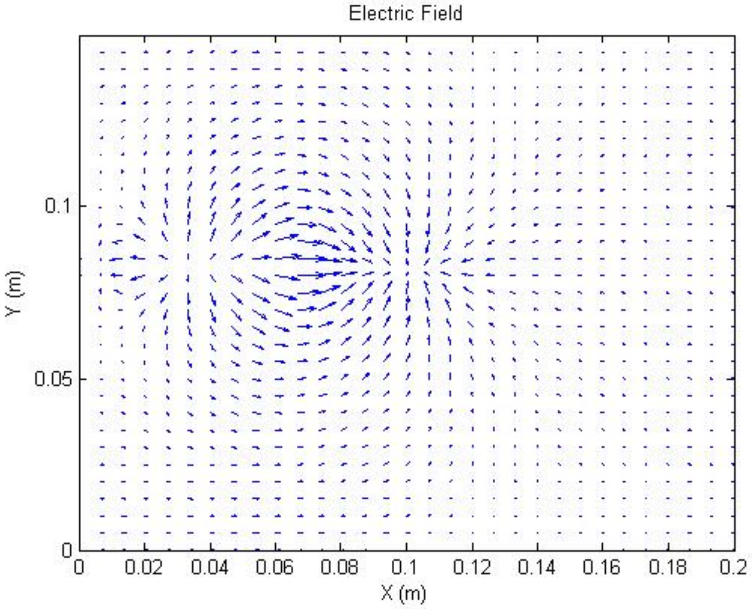

Figure 2.44: Electric Field Vectors for a Time-Varying Constant Spatial Emission Scheme at 100 kHz when the Negative and Positive Particles are Best Balanced at 12 μs

In the last 5 μs, as soon as the negative particle emission stops and positive particle emission begins, there is a drop in all the diagnostics similar to what was displayed the last time negative particle emission stopped and positive particle emission began. Similar to the minimum at 12 μs, there is a minimum at approximately 18 μs for the same reason as there was previously. Fig. 2.45 illustrates the simulation space at 18 μs, which is when all the diagnostics are approximately at their local minimum. It is important to note that it took 2 μs into the negative particle emission for the diagnostics to reach a local minimum, whereas it took a longer 3 μs into the positive particle emission for the diagnostics to reach a local minimum. This can be attributed to the fact that the beam to the right of the negative particle emission was “net neutral”, whereas the beam to the right of the positive particle emission was not “net neutral” but instead negatively charged, thus it will take slightly more positive particle emission for it to reach a minimum. After it reaches this local minimum, the diagnostics will start to increase again as the balance starts to shift to the positively charged particles that continue to be emitted. It also is important to note that the local maxima appear exactly 10 μs apart, which matches up with the 100 kHz frequency that the pulses are coming out at; however, the local minimums don't occur halfway between the maxima and thus are not a good indication of the frequency of the pulses.

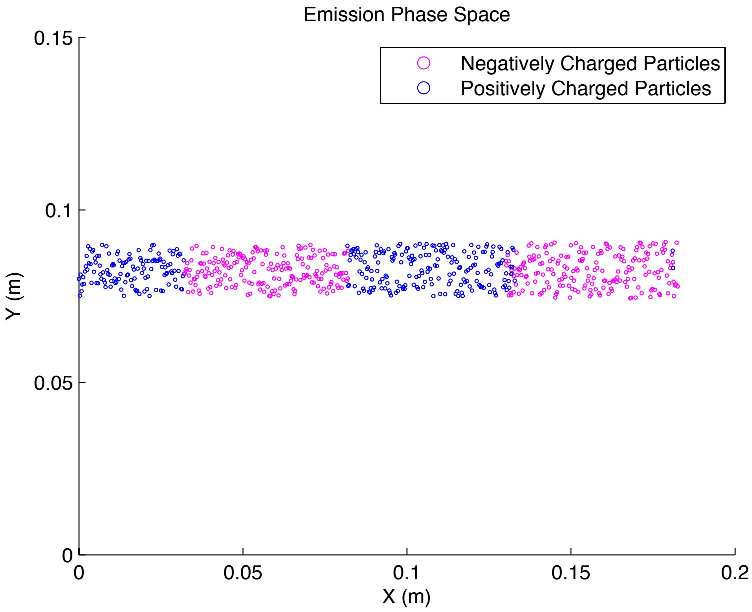

Figure 2.45: Simulation Space for a Time-Varying Constant Spatial Emission Scheme at 100 kHz when the Negative and Positive Particles are Best Balanced at 18 μs

Now that a TVCSE schemed pulse has been shown at a single frequency, it is helpful to observe multiple frequencies on the same plot. The following four plots, Fig. 2.46, Fig. 2.47, Fig. 2.48, Fig. 2.49, show the diagnostics for different frequency pulses.

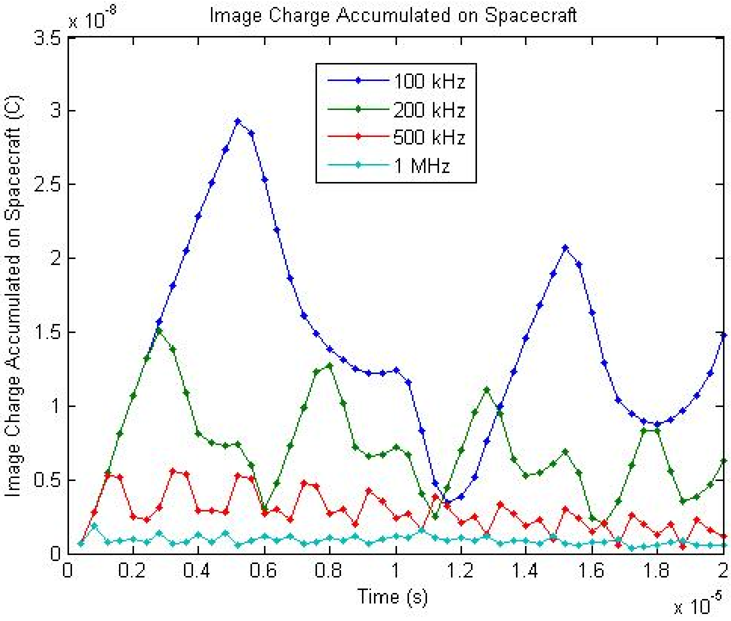

Figure 2.46: Image Charge Accumulated on the Spacecraft over Time for 100 kHz, 200 kHz, and 500 kHz

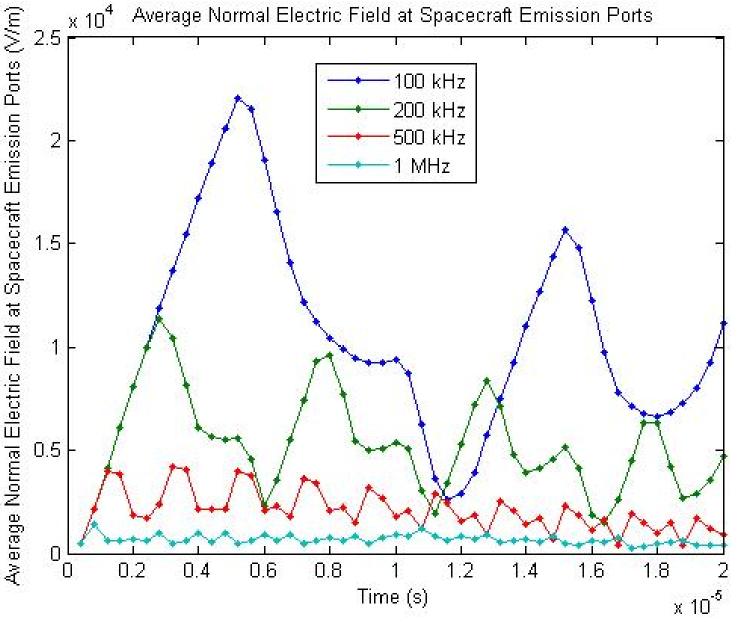

Figure 2.47: Average Normal Electric Field at the Emission Ports over Time for 100 kHz, 200 kHz, and 500 kHz

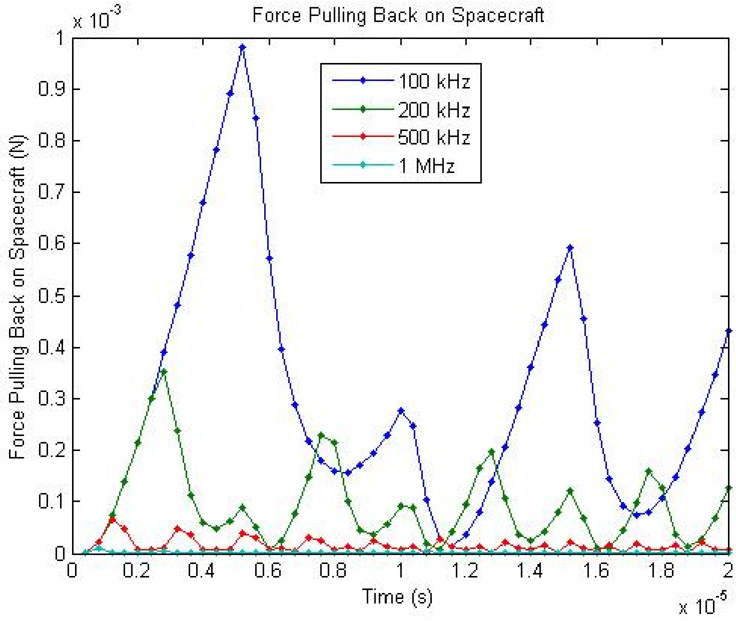

Figure 2.48: Force Decelerating the Spacecraft due to Electric Field Interaction over Time for 100 kHz, 200 kHz, and 500 kHz

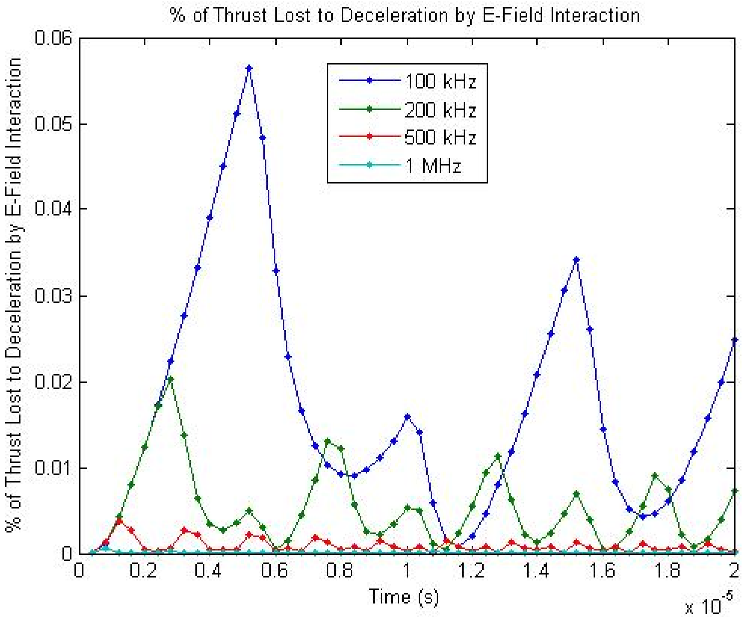

Figure 2.49: Percentage of Thrust Lost due to Electric Field Interaction over Time for 100 kHz, 200 kHz, and 500 kHz

The 100 kHz pulse already has been examined in depth in Fig. 2.37-Fig. 2.40. It appears that the 200 kHz and the 500 kHz pulse show a similar pattern to that of the 100 kHz pulse, with the same local maxima at the appropriate points where the negative beam stops emitting and the positive beam starts emitting, which provides a period that corresponds to the pulse frequency. They also have the same drop in the diagnostics to a local minimum that occurs partway through every instance of negative and positive particle emission, except for the initial ramp up through the first negative particle emission.

Another interesting note is that the local maxima continue to decrease in magnitude as time continues, which is an indication that the fully emitted negative beam does not have as much effect as the previous fully emitted negative beam had, as there is a slightly larger number of “net neutral” particles out in front of the beam to help neutralize the newly emitted negatively charged beam. Also, since the 100 kHz and 200 kHz pulses are frequency multiples of one another, it would initially be expected that they would exhibit some maxima and some minimums at the same time; however, that is not the case as the pulses are all shifted by half a period, which is due to the non-neutral behavior of the first initial charged beam (in this case negatively charged). For example, the local maxima of the 100 kHz beam occur at 5 μs and 15 μs, whereas the local maxima of the 200 kHz beam occur at 2.5 μs, 7.5 μs, 12.5 μs, and 17.5 μs. It is very important to note that the average value of each of the diagnostics decreases as the pulse frequency increases. This is because with a larger pulse frequency, the period of each pulse decreases, there is less charge emitted, and thus the average value will continue to drop. As these simulations continue to run, these local maxima each end up plateauing but at different values, with an increasingly higher percentage of thrust lost at lower frequencies. In addition, there is a non-zero average charge on the spacecraft due to the initial full cycle (DC bias), but when this bias is removed by starting the simulation with an initial half pulse of oppositely charged particles, the trends remain the same except with a lower initial local maximum to begin with.

It is difficult to see the relationship between the 500 kHz and 1 MHz plots in the previous plots. Thus, the following four plots, Fig. 2.50, Fig. 2.51, Fig. 2.52, Fig. 2.53, zoom in on those lines only.

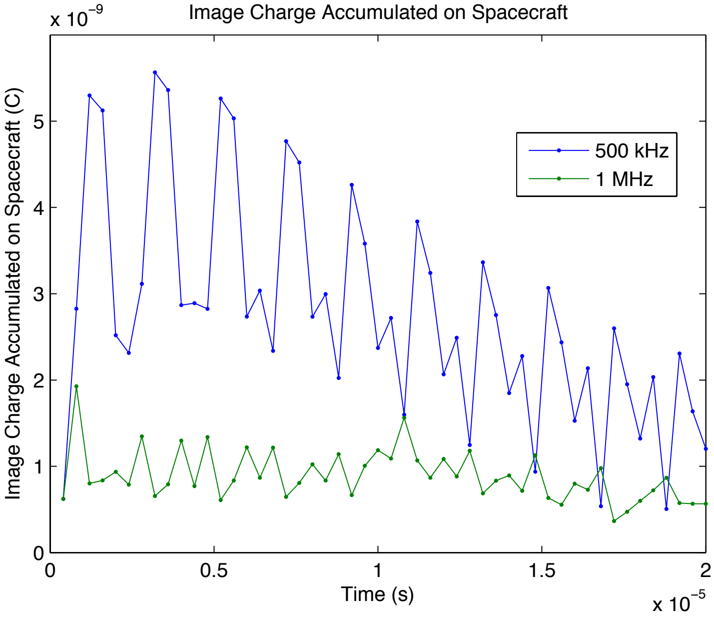

Figure 2.50: Image Charge Accumulated on the Spacecraft over Time for 500 kHz and 1 MHz

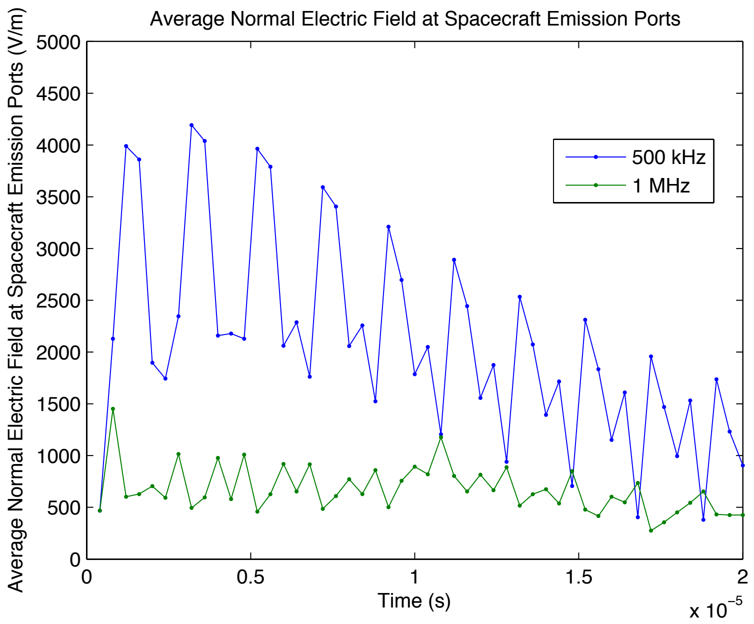

Figure 2.51: Average Normal Electric Field at the Emission Ports over Time for 500 kHz and 1 MHz

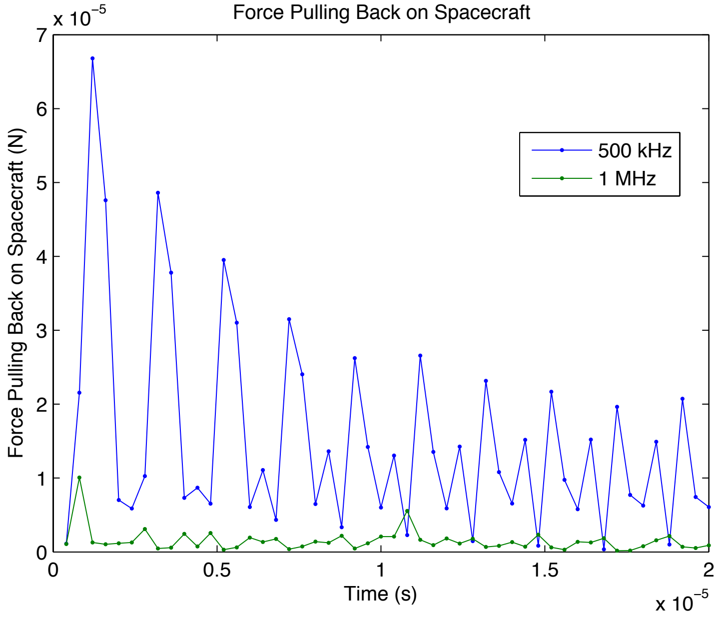

Figure 2.52: Force Decelerating the Spacecraft due to Electric Field Interaction over Time for 500 kHz and 1 MHz

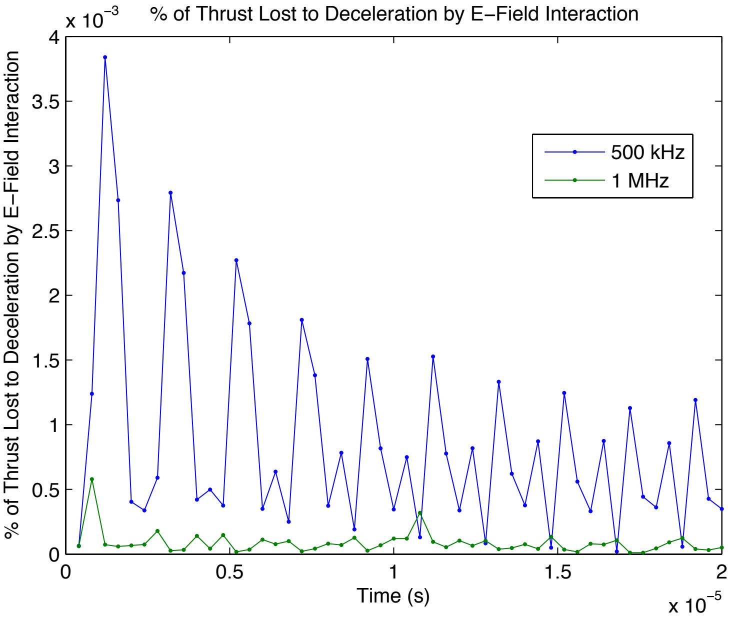

Figure 2.53: Percentage of Thrust Lost due to Electric Field Interaction over Time For 500 kHz and 1 MHz

The 500 kHz simulation shows the local maxima occur as expected every 2 μs, resulting in ten local maxima as the pulse frequency would dictate. It also shows a decay in magnitude of the local maximum as exhibited previously. However, the 1 MHz pulse does not exhibit such patterned diagnostics. This is largely due to under-sampling when grabbing diagnostics at various times while the simulation is running. Each diagnostic is gathered every 0.4 μs, and for the 1 MHz time-varying pulse, the period is 1 μs, so the sampling rate is just slightly above the Nyquist rate, thus it is sufficient to establish trends, but makes it difficult to see the frequency at which the diagnostics are oscillating. It is important to note that for the majority of the time the diagnostics for the 500 kHz beam have a larger magnitude than the 1 MHz beam, but there are four data points where the 1 MHz beam surpasses the 500 kHz beam, which occur at 10.8 μs, 14.8 μs, 16.8 μs, and 18.8 μs. These happen to be close to the local maxima of the 1 MHz beam which occur at 0.5 μs, 1.5 μs, 2.5 μs, etc as well as the local minimums of the 500 kHz beam. So although the average magnitude is lower for the 1 MHz beam than the 500 kHz beam, there are points where they do overlap. This helps explain why there is a lower plateau when looking at the diagnostics at a simulation time of 20 μs across difference frequencies as was shown previously in Fig. 2.33, Fig. 2.34, Fig. 2.35, Fig. 2.36.

By observing two different frequencies, one in the low plateau, and another at a higher frequency, but with higher diagnostic values, it is possible to see why there is the low plateau. In this case, 1 MHz and 2 MHz are chosen for simplicity and the diagnostics are as shown in Fig. 2.54, Fig. 2.55, Fig. 2.56, Fig. 2.57

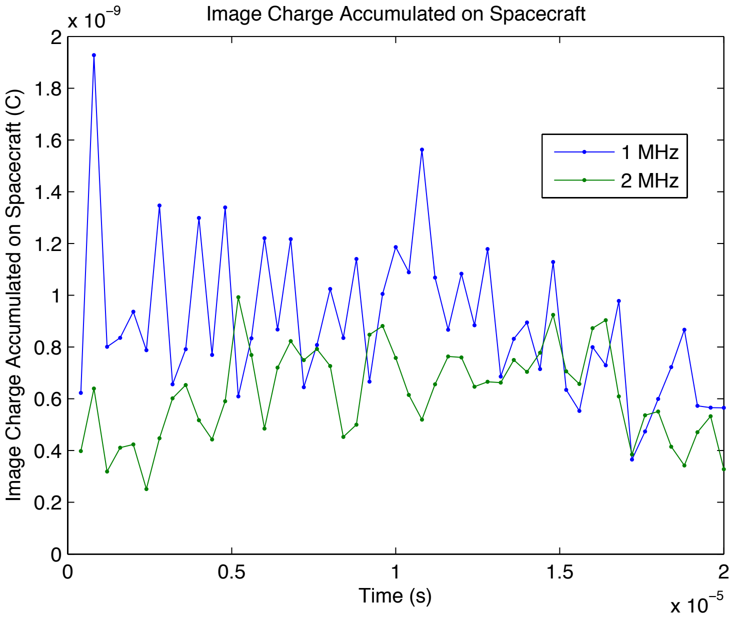

Figure 2.54: Image Charge Accumulated on the Spacecraft over Time for 1 MHz and 2 MHz

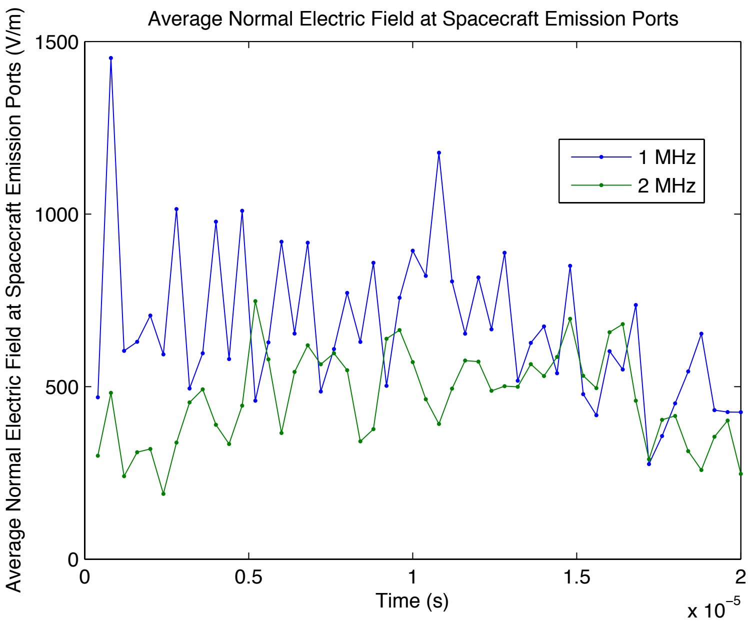

Figure 2.55: Average Normal Electric Field at the Emission Ports over Time for 1 MHz and 2 MHz

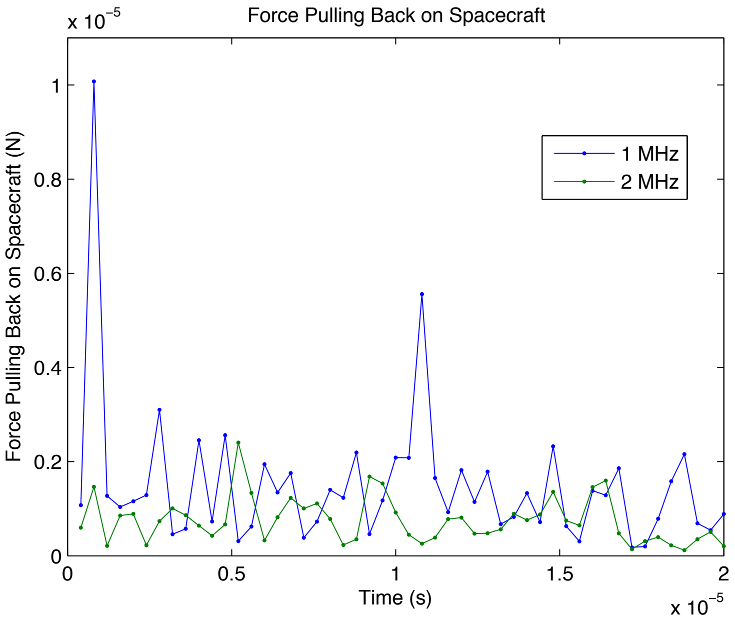

Figure 2.56: Force Decelerating the Spacecraft due to Electric Field Interaction over Time for 1 MHz and 2 MHz

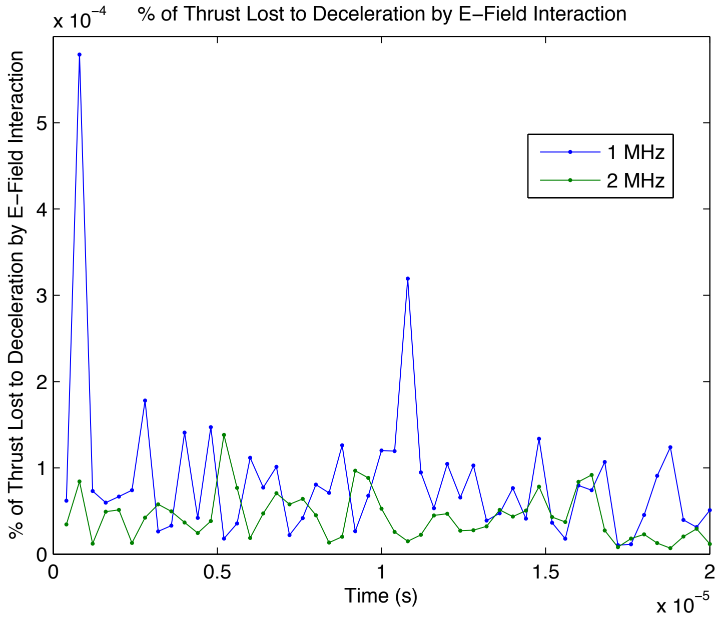

Figure 2.57: Percentage of Thrust Lost due to Electric Field Interaction over Time For 1 MHz and 2 MHz

These plots show that although the average magnitude of the diagnostics is once again higher for the lower frequency pulse, as was seen with the 500 kHz and 1 MHz pulse, there is overlap between the two lines, but in this case there is significantly more overlap. This is possibly due to the fact that with such high frequencies, there is very little time for the spacecraft to charge up, so it is not able to get up to very high magnitudes at the local maximum, and thus when the spacecraft starts to discharge, it can drop very low and thus overlap with the higher frequency pulse. This creates the end result at 20 μs of having a 2 MHz magnitude that is higher than the 1 MHz magnitude which is unexpected. This explains the low plateau as seen in the varying frequency at 20 μs plots shown previously in Fig. 2.33, Fig. 2.34, Fig. 2.35, Fig. 2.36. However, this does not negate the overall trend that the average magnitude of the diagnostics is lower for higher frequency pulses. This indicates that if the spacecraft can not charge up as much, then the TVCSE scheme must be operated at a higher frequency. However, even at the lowest simulated frequency of 100 kHz, the maximum percentage of thrust lost due to deceleration is less than 0.06%, and drops to below 0.04% by the second time the negative particle emission ceases. Thus, it seems as if emitting a TVCSE scheme pulse at this relatively high current level does not seem to be much of a concern.

Finally the response at a lower current is also considered. Using a 312.5 μA emission current, which was for a NanoFET nanoparticle thruster on a CubeSat, and operating at a frequency of 100 kHz, the particle velocity only drops 0.0056% 0.03 m away from the spacecraft. In addition, similar to how plots were generated for the image charge accumulated on the spacecraft, the electric field at the spacecraft, the force decelerating the spacecraft, and most importantly the percentage of thrust lost to the electric field interaction diagnostics versus the frequency for the 14.49 mA emission, such diagnostic plots versus frequency are generated for the 312.5 μA emission as is shown in Fig. 2.58, Fig. 2.59, Fig. 2.60, Fig. 2.61.

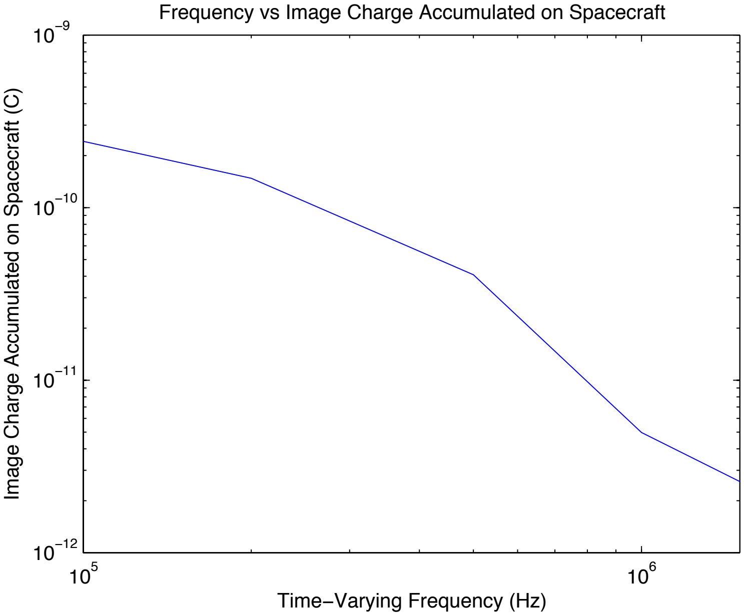

Figure 2.58: Image Charge Accumulated on the Spacecraft over Time-Varying Frequency for a 312.5 μA Emission Current

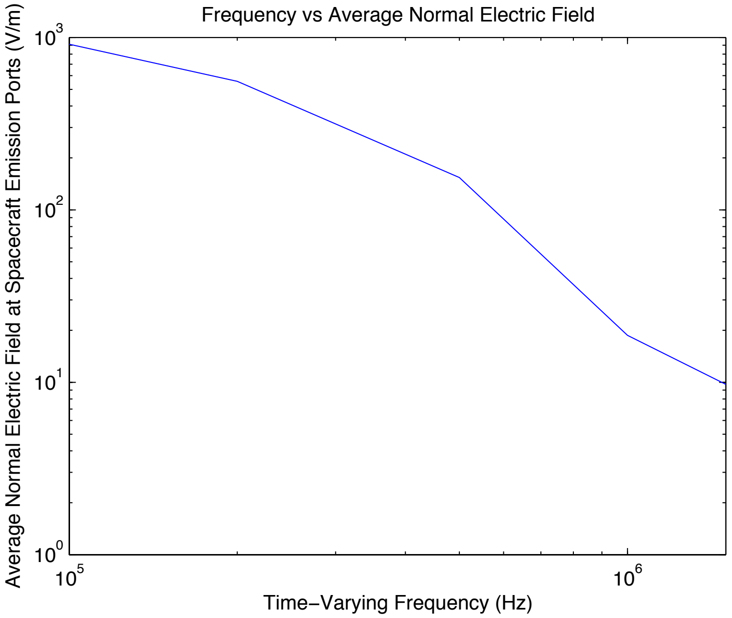

Figure 2.59: Average Normal Electric Field at the Emission Ports over Time-Varying Frequency for a 312.5 μA Emission Current

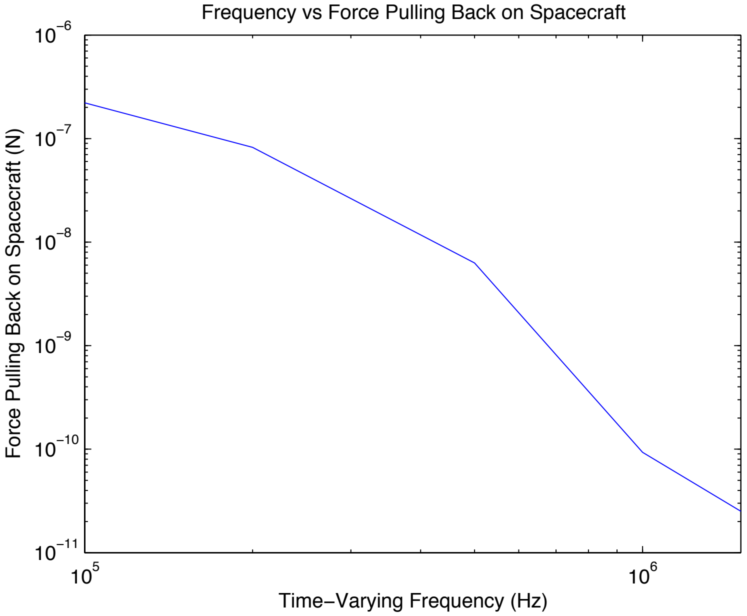

Figure 2.60: Force Decelerating the Spacecraft due to Electric Field Interaction over Time-Varying Frequency for a 312.5 μA Emission Current

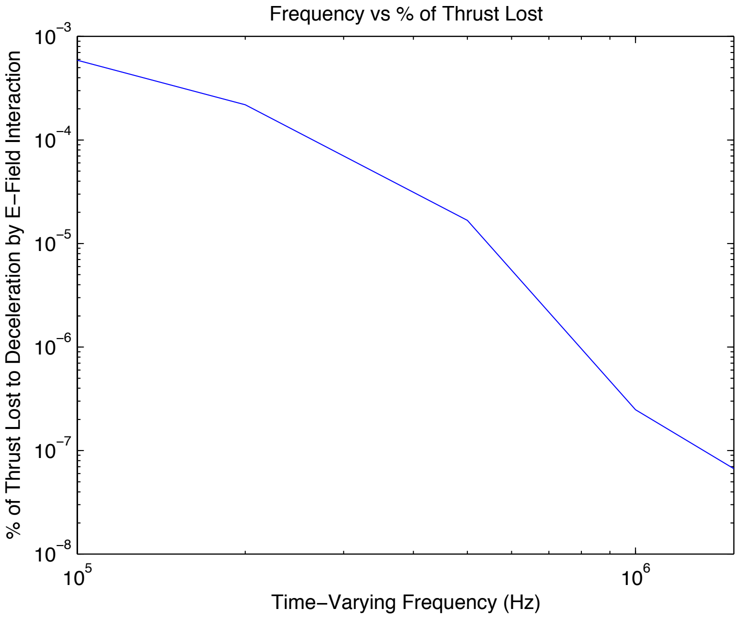

Figure 2.61: Percentage of Thrust Lost due to Electric Field Interaction over Time-Varying Frequency for a 312.5 μA Emission Current

These plots once again show the same trend of less thrust lost to deceleration by electric field interaction as frequency is increased. At a low frequency of 100 kHz there is less than a 0.001% loss in thrust.

2.6 Limitations of the Simulation

OOPIC PRO^{TM} is a reasonably supported particle-in-cell simulation tool with good capabilities up to 2.5D; however, one its limitations is not having a particle-particle collision model, including small and large angle scattering as well as charge-neutralizing collisions. An additional limitation is the 2.5-dimensionality of the simulation, as a 3-dimension simulation would simulate the real world situation more accurately (this is explored in Chapter IV).

Collisions can be divided into elastic and inelastic collisions, where elastic collisions conserve total kinetic energy of the colliding particles whereas inelastic collisions do not. When dealing with charged nanoparticle collisions exclusively, collisions will be primarily elastic as there are limited destructive collisions, with the majority of collisions being Coulomb collisions where the nanoparticles approach one another at a close enough distance to have an effect, but do not actually collide. Elastic collisions can be broken down into Coulomb collisions where two charged particles, for example, scatter due to their respective electric fields (there is both large angle and small angle scattering) and polarization scattering which occurs between charged particles and neutral particles and as such will not be a concern for these simulations between charged particles.

Large angle scattering as opposed to small angle scattering occurs when a single particle-particle interaction causes the incident particle (or in this case where both particles are of equal mass, charge, and size both particles), to change directions by more than 90°. The collisional cross section is a parameter that indicates the area around a target particle where a particle incident on this area will result in a collision (*Lieberman and Lichtenberg*, 2005). The Large Angle Scattering Collisional Cross Section (σ_{90}(large)) is shown in Eq. 2.18 where b_0 is the classical distance of closest approach (Eq. 2.19), W_R is the center of mass energy (Eq. 2.20) and m_R and v_R are the reduced mass and relative velocity respectively.

$$\sigma_{90}(large) = \frac{1}{4}\pi b_0^2 \tag{2.18}$$

$$b_0 = \frac{q_1 q_2}{4\pi\epsilon_0 W_R} \tag{2.19}$$

$$W_R = \frac{1}{2}m_R v_R^2 \tag{2.20}$$

In addition, multiple small angle scattering collisions (particle-particle interactions that do not deflect either particle more than 90°) can collectively scatter a particle more than 90° and this can at times be more prevalent than large angle scattering collisions. The Effective Small Angle Scattering Collisional Cross Section (σ_{90}(small)) is shown in Eq. 2.21.

$$\sigma_{90}(small) = \frac{8}{\pi} b_0^2 \ln \Lambda \tag{2.21}$$

In Eq. 2.21, b_0 is again the classical distance of closest approach shown and Λ is the ratio of Debye length to minimum impact parameter shown in Eq. 2.22.

$$\Lambda = \frac{2\lambda_D}{b_0} \tag{2.22}$$

Using a m_R of 2.2×10^{-18} kg (the reduced mass is the average of the target and incident particle masses) and a differential X velocity of 30 m/s (variance in X velocity at a given X position from Fig. 2.4), the center of mass energy is shown in Eq. 2.23.

$$W_R = \frac{1}{2} 2.2 \cdot 10^{-18}[kg] \cdot 30 \left[\frac{m}{s}\right]^2 = 9.9 \cdot 10^{-16}\ J \tag{2.23}$$

Using the center of mass energy, a charge of 7.32×10^{-16} C, and an approximate "Debye length" of 0.00357 m, the classical distance of closest approach (Eq. 2.24) and Λ (Eq. 2.25) can be calculated.

$$b_0 = \frac{(7.32 \cdot 10^{-16}[C])^2}{4\pi \cdot 8.85 \cdot 10^{-12} \left[\frac{F}{m^2}\right] \cdot 9.9 \cdot 10^{-16}[J]} = 4.9 \cdot 10^{-6}\ m \tag{2.24}$$

$$\Lambda = \frac{2 \cdot 0.00357[m]}{4.9 \cdot 10^{-6}[m]} = 1500 \tag{2.25}$$

From these two values, the large angle scattering collisional cross section (Eq. 2.26) and the effective small angle scattering collisional cross section can be calculated (Eq. 2.27).

$$\sigma_{90}(large) = \frac{1}{4}\pi(4.9 \cdot 10^{-6}[m])^2 = 1.9 \cdot 10^{-11}\ m^2 \tag{2.26}$$

$$\sigma_{90}(small) = \frac{8}{\pi}(4.9 \cdot 10^{-6}[m])^2 \ln 1500 = 4.4 \cdot 10^{-10}\ m^2 \tag{2.27}$$

To explore the worst case scenario (most likely scenario for collisions), the largest cross section, which is the effective small angle collisional cross section is used.

An elastic collision of an incident particle against a center of mass centered target has a maximum scattering angle of 90°; however, for an elastic collision between equal mass particles in the laboratory frame, this maximum scattering angle is actually a scattering of a maximum 45° of both particles. Thus, in order to have a detrimental effect on the spacecraft (e.g. striking the spacecraft), a particle emitted in the +X direction will have to make four 45° turns (regardless of whether it is due to small angle or large angle scattering) in order to return in the -X direction to the spacecraft. In addition, the first turn needs to be made within the 0.2 m of simulation length to be considered in this simulation, and the subsequent three turns needs to be made within the maximum 0.015 m of Y distance beam width. The worst case scenario occurs (highest probability of collision) occurs when each of those three turns takes place over 0.005 m of Y distance (Fig. 2.62).

With the collisional cross section, the probability of incurring four collisions within the simulation space can be calculated by Eq. 2.28. In the worst case scenario (where the Number Density (n) is highest), the number density can be calculated by Eq. 2.29.

$$prob(collision) = n \cdot \sigma \cdot dx \tag{2.28}$$

$$n = \frac{J}{qv} = \frac{0.967\left[\frac{A}{m^2}\right]}{7.32 \cdot 10^{-16}[C] \cdot 10^4\left[\frac{m}{s}\right]} = 1.3 \cdot 10^{11}\ m^{-3} \tag{2.29}$$

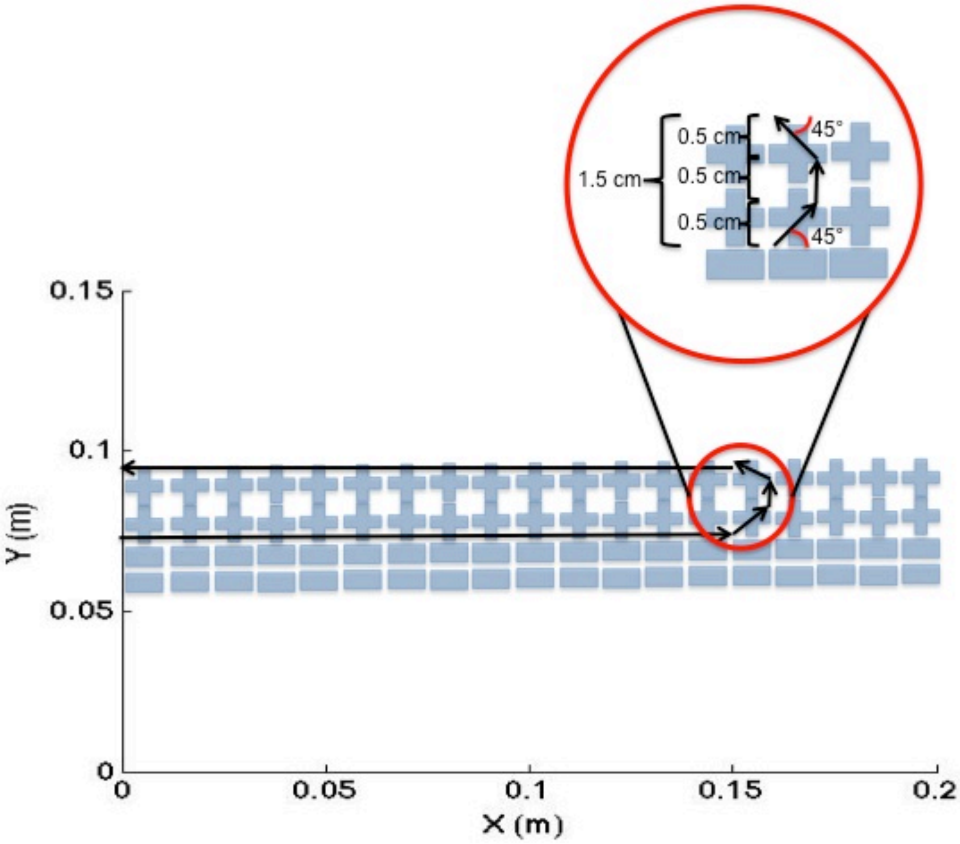

Figure 2.62: Depiction of Collisions Required to Turn Around Emitted Particle

This results in a worst case (largest collision cross section) four small angle collisions probability across the 0.2 m of X direction simulation space and 0.015 m of Y direction beam width shown of approximately 0.00029% as shown in Eq. 2.30. This shows that there is an extremely low likelihood that a particle will endure enough collisions to turn around completely and head in the -X direction back towards the spacecraft.

$$prob(collision) = 1.3{\cdot}10^{11}[m^{-3}]{\cdot}4.4{\cdot}10^{-10}[m^{2}]{\cdot}(0.2{\cdot}0.005\sqrt{2}{\cdot}0.005{\cdot}0.005\sqrt{2})[m] = 0.0000029 \tag{2.30}$$

Another way to look at the possibility of collision is to compare how often collisions occur with how long it takes a particle to leave the simulation space. The mean time between interactions, τ, is shown in Eq. 2.31 where Λ is the mean free path (Eq. 2.32) and υ is the differential X direction beam velocity, which is at the worst case of approximately 30 m/s.

$$\tau = \frac{\lambda}{\upsilon} \tag{2.31}$$

$$\lambda = \frac{1}{n_g \sigma} \tag{2.32}$$

With the worst case collisional cross section of 4.4×10^{-10} m^2 (Eq. 2.27) and a number density of 1.3×10^{11} m^{-3} (Eq. 2.29), the mean free path is shown in Eq. 2.33. And the mean time between interactions in the X direction is shown in Eq. 2.34.

$$\lambda = \frac{1}{1.3 \cdot 10^{11} [m^{-3}] \cdot 4.4 \cdot 10^{-10} [m^2]} = 0.0175\ m \tag{2.33}$$

$$\tau_X = \frac{0.0175[m]}{30 \left[\frac{m}{s}\right]} = 5.83 \cdot 10^{-4}\ s \tag{2.34}$$

This is compared to the time a particle traveling at 10^4 m/s across 0.2 m in the X direction which is 2×10^{-5} seconds. Thus, on average, it would require a simulation length some thirty times longer for a particle traveling in the X direction to have a collision with another particle.

For a beam that has a 10° beam spread (significant), a beam with a 10^4 m/s beam velocity, will have a 1700 m/s velocity in the Y direction (differential Y direction beam velocity of 3400 m/s). And for oppositely charged beams spreading towards one another, the mean time between interactions in the Y direction is shown in Eq. 2.35.

$$\tau_Y = \frac{0.0175[m]}{3400 \left[\frac{m}{s}\right]} = 5.03 \cdot 10^{-6}\ s \tag{2.35}$$

This is compared to the time two particles traveling towards one another at 3400 m/s across a 0.015 m beam in the Y direction which is 4.32×10^{-6} seconds. Thus, on average, there will be one collision by the time it travels across the beam in the Y direction, and not the three collisions required to turn a particle around fully.

In the case of charge-neutralizing collisions, for the most part, the oppositely charged particles at a specific X position and near the positive and negatively charged particle boundary are traveling in the X direction with a similar velocity. This means that when they collide (not just scatter), they will only be moving relative to each other in the Y direction, meaning that any collisions will result in the nanoparticles changing momentum in the Y direction, but not in the X direction. This causes the now neutral nanoparticle will not scatter back to the spacecraft as it now has no net charge and will not be affected by the background electric fields and will continue on its original trajectory, and is of no concern physically.

Thus, although the simulations focus on particle-field interactions instead of particle-particle interactions, there appears to be less need for particle-particle interactions as they do not occur frequently enough to turn a particle around and return to the spacecraft. Therefore, there may not be detrimental effects on the spacecraft (e.g. sputtering of the spacecraft surface due to high velocity particle-spacecraft impacts) due to collisions between emitted particles. With future software updates that will add particle-particle interaction capabilities, this is an issue that can be validated by simulation in the future.

2.7 Summary

From these simulations and models it can be observed that the two seemingly obvious neutralization methods, spatial-varying, common time emission (SVCTE) and time-varying, common spatial emission (TVCSE) both have challenges associated with their implementation. In the case of the SVCTE scheme, even though the overall beam and the overall spacecraft are always both net neutral at all times (ideally), the large, heavy particles that are being used to self-neutralize (as opposed to using light, fast electrons to neutralize as other systems use) cause some difficulties. These large, heavy particles are slow to react to the electric field generated between particles and thus the beam that is net neutral, is not immediately neutralized locally. This creates a potentially important image charge induced axial electric field back near the spacecraft that pulls the spacecraft back to the emitted beam, and thus negating some of the generated thrust.

There are ways to make this neutralization method possible. As the width of the beams are shrunk, and as the oppositely charged beams are placed closer to one another, the local image charge effects are minimized. In order to utilize the full surface, rather than using just two beams like is shown in these simulations, multiple beams will be utilized alternating between positively and negatively charged beams. Thus, as the beams are shrunk and moved closer together, these beams will start to look like two oppositely charged beams stacked on top of one another which has been shown to have no local charge issues. However, there are constraints as to how close oppositely charged beams can be placed and how thin the beams can be as it increases the number of total beams needed. This is due to the high voltages that are necessary to charge and accelerate the particles, and concerns of arcing between the highly, oppositely charged gates.

For the specific application of these charged particle thrusters to nanospacecraft, there are important power and thus current density limitations on the thruster. In the most extreme case, where a charged particle thruster is operating well above its power limitations and at its physical size limitations, there is still only a 0.01% loss in generated thrust when the oppositely charged beams are placed adjacent to one another. Thus, it seems that charged particle thrusters on nanospacecraft will not be significantly affected by image charge induced E-field deceleration. However, if this device were to be used on larger spacecraft, and the current density were to be increased, image charge induced E-field deceleration may need to be carefully considered.

In the TVCSE scheme, it was seen through basic modeling that the spacecraft can charge up to an important percentage of the charging and accelerating potential in relatively short time scales when significant current levels are emitted. However, simulation results show here that a 0.967 A/m^2 beam current emission (well below space charge limit, but the physical limitation of the NanoFET system) will exhibit a 0.01% thrust lost to deceleration by electric field interaction in the SVCTE scheme when the beams are placed adjacent to one another. The corresponding emission utilizing a TVCSE scheme exhibits the same 0.01% thrust lost to deceleration by electric field interaction at a frequency of 200 kHz, which may be possible to oscillate between opposite high voltages at. However, at a relatively low frequency of 20 kHz, there is still only a 0.1% loss in thrust due to deceleration by electric field interaction. As frequency is decreased from there, a more significant portion of the thrust will be lost to the electric field interaction.

CHAPTER III

Simulation of Background Plasma as a Neutralizer

3.1 Introduction

Simulations discussed in Chapter II showed that it would be possible to use the emission of equal amounts of positively and negatively charged particles to self-neutralize and maintain the neutrality of the spacecraft that utilizes a charged particle thruster capable of emitting particles of both polarities with minimal detrimental effects as long as the emission current was not significantly higher than a typical nanospacecraft is able to emit power-wise. One thing that was discussed in Chapter II was the emission of oppositely charged particles into vacuum, a worst case scenario.

For some applications, the charged particle thrusters will be operated in environments where there is a background plasma of useful levels that may enable neutralization of both the spacecraft and particle beam without having to emit both particle polarities. Questions to be addressed include how does charged particle polarity affect neutralization when emitting into a background plasma and what is an adequate background plasma density versus emission current?

To take it a step further, it may be possible to emit particles of a single polarity and allow the background plasma to do the neutralization work naturally. This would simplify the thruster as it would only have to be capable of emitting particles or droplets of a single polarity, and thus it would not need to have the extraction or acceleration gates be able to switch polarities. However, there is significant work to be done to show not only that such a neutralization scheme is feasible, but also what emission currents can be neutralized by what background plasma parameters.

Previous studies have examined how electron emitting spacecraft have used background plasma to neutralize. One such experimental study (*Sasaki et al.*, 1987), examined the effect that 10^{19} electron-ion pairs injected into the space that 300 mA of electron current was emitted into had on neutralizing the spacecraft.

3.2 Plasma Neutralization of Charged Particle Thrusters on Spacecraft

This neutralization scheme hinges on the fact that with a background ionosphere, the spacecraft will charge up negatively due to the fast, mobile electrons impacting it more often than the heavy ions in the plasma. Thus, a completely negatively charged beam is emitted from the spacecraft and the background plasma is used to neutralize the spacecraft and the beam as is shown previously in Fig. 1.5, with a more detailed description in Section 1.1.1. Another neutralization scheme would be one that emits solely positively charged particles and the electrons and ions behave in an opposite fashion, but ionospheric ions are much heavier than background electrons making it more difficult for the background ionosphere to compensate for the charging spacecraft resulting in a higher spacecraft floating voltage.

3.3 Simulation Parameters

A caveat for using the background plasma to neutralize the spacecraft is that there must be enough of a background plasma to provide the electrons and ions for neutralization, thus it is imperative to examine the plasma environment. The altitudes of importance here are the low ionosphere in low Earth orbit between 150 and 1000 km. Examining the ionospheric density plot shown in Fig. 3.1 (*di Geofisica e Vulcanologia*, 2011), it is determined that at the altitudes of interest, the number density ranges from 10^9 m^{-3} to 10^{13} m^{-3}, with the majority of the plasma densities located between 10^{10} m^{-3} to 10^{12} m^{-3}. The plasma number density depends on not only the altitude that the spacecraft is flying at, but also on time of day (dotted versus solid lines) as well as solar activity (R=0 and R=200 lines) and the solar cycle phase.

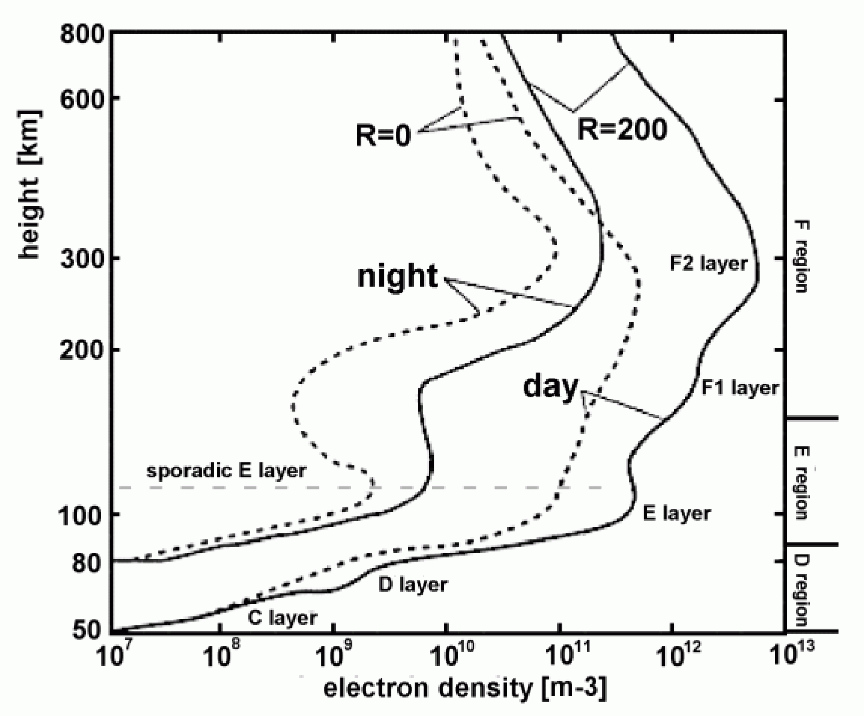

Figure 3.1: Plasma Density in Ionosphere

In addition to the plasma density in the ionosphere, it is important to establish the range of thermal electron temperatures. A low energy electron spectrometer (HARP) and a cylindrical Langmuir probe were launched in 1971 on a sub-orbital rocket from White Sands Missile Range (NASA 13.51), with electron temperatures gathered from both instruments as shown below in Fig. 3.2 (*Hays and Nagy*, 1973).

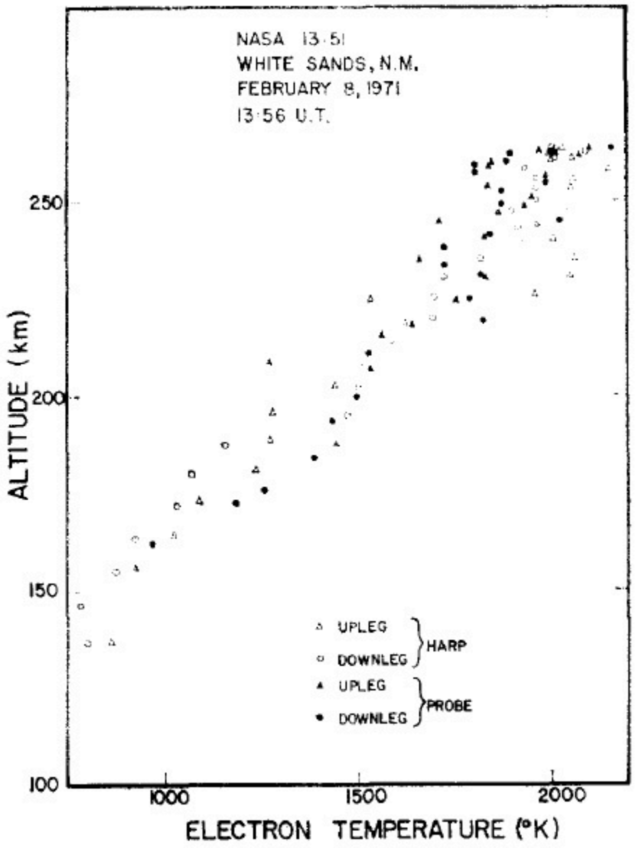

Figure 3.2: Electron Temperature in Ionosphere (*Hays and Nagy*, 1973)

This shows an approximate electron temperature range of 500-2500 K (0.043-0.215 eV). It will be assumed here that a representative electron and ion temperature is 0.1 eV (*Otsuka et al.*, 1998) as the plasma in space has had sufficient time to reach thermal equilibrium, and thus the electron and thermal temperatures can be approximated to be the same. For an electron in a Maxwell-Boltzmann distribution, the Electron Thermal Velocity (v_{Te}) can be determined by Eq. 3.1 and Ion Thermal Velocity (v_{Ti}) can be determined by Eq. 3.2.

$$v_{Te} = \sqrt{\frac{kT_e}{m_e}} \tag{3.1}$$

$$v_{Ti} = \sqrt{\frac{kT_i}{m_i}} \tag{3.2}$$

Given an Electron Temperature (T_e) and Ion Temperature (T_i) of approximately 0.1 eV, and an Electron Mass (m_e) of 9.11×10^{-31} kg, the electron thermal velocity is approximately 133,000 m/s. For a nanospacecraft using a charged particle electric propulsion thruster such as in low Earth orbit (LEO), the dominant neutral and ion species that will be encountered is atomic oxygen as shown in Fig. 3.3 (*Cairns*, 1999), with an Ion Mass (m_i) of 2.67×10^{-26} kg.

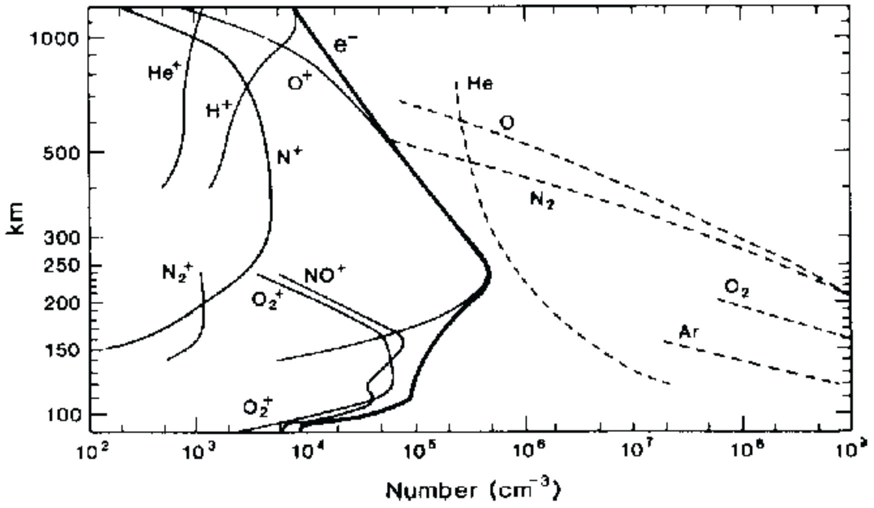

Figure 3.3: Neutral and Ion Composition in Ionosphere

From these values, the ion thermal velocity is calculated to be approximately 774 m/s. (It is noted for reference that this velocity is near the lower end of emitted nanoparticle velocities of 1000 m/s to 10000 m/s). However, at the expected altitudes, the spacecraft is orbiting Earth at approximately 7500 m/s relative to the co-rotating background plasma, and the ion thermal velocity is an order of magnitude lower.

The relationship between current and velocity are as shown by Eq. 3.3.

$$I = nqvA \tag{3.3}$$

In the 2.5-dimensional simulation space, electrons and ions are emitted over a 0.15 m by 1 m region, giving an emission area of 0.15 m^2, as the 2.5D simulation space has a depth of 1 meter as was described previously in Section 1.3. However, in a thermal plasma, there is no net current.

In the plasma simulations, Cartesian coordinates are chosen to be 0.2 m in the X direction and 0.15 m in the Y direction, with a cell spacing of 0.0067 m in the X direction and 0.005 in the Y direction, providing 30 cells in both directions. In addition, the outer walls of the simulation space are simply periodic in both directions (*Luginsland et al.*, 1996) meaning that any particle that leaves the simulation space on the far right comes back in on the far left, and vice versa and any particle that leaves the simulation space on the top comes back in on the bottom and vice versa. This is the most efficient and realistic way to simulate the boundaries in OOPIC PRO^{TM} as there are plasma particles continuously streaming in from all directions, which simulates the spacecraft being surrounded infinitely by plasma.

In addition, the spacecraft is sized at 0.026 meters in the X direction and 0.02 meters in the Y direction to be smaller than a 1U CubeSat, with all four walls of the spacecraft connected together to simulate a single conducting surface that can float to a potential by having a blocking capacitor (high capacitance) between the spacecraft and ground, which in OOPIC PRO^{TM} is labeled a "current source", which also acts a blocking capacitor when there is no current flowing to the surface. The current source boundary was chosen over a dielectric (can either allow charge to build up or dissipate), equipotential, or a conductor. The outside of the spacecraft should be conductive allowing the entire spacecraft to float to a single potential, which violates the dielectric boundary condition in both ways. Conductor and equipotential boundaries are very similar except that equipotential boundaries are tied to ground. The problem with conductor and equipotential boundaries for the spacecraft are that they are held at a specified voltage, so the current to the spacecraft will create a transient sheath around the spacecraft, which asymptotes at steady state. Thus, a "current source" offered the closest boundary to reality. These assumptions are further tested below.

One important consideration when sizing the different components of the simulation space, spacecraft, and cells is the Debye length in a plasma simulation. Debye length expressed in centimeters can be expressed as a function of electron temperature (eV) and plasma density (cm^{-3}) as shown in Eq. 3.4.

$$\lambda_D[cm] = 743\sqrt{\frac{T_e[eV]}{n_e[cm^{-3}]}} \tag{3.4}$$

For an assumed ionospheric electron thermal temperature of 0.1 eV with the range of plasma densities from 10^9 m^{-3} to 10^{13} m^{-3} or 10^3 cm^{-3} to 10^7 cm^{-3}, Debye lengths will vary from 0.0743 m for lower densities to 0.000743 m for higher densities. A relaxed particle-in-cell constraint is that the cell size must be less than 3.4 times the Debye length as summarized by Eq. 3.5 (*Tskhakaya et al.*, 2007), thus for the lower densities it is very easy to satisfy, but at the highest densities, it becomes harder to satisfy. Cell sizes will need to vary from being less than 0.256 m to 0.00256 m to satisfy this condition for the range of plasma densities to be simulated at a electron temperature of 0.1 eV.

$$\Delta cell < 3.4\lambda_D \tag{3.5}$$

Thus, a cell spacing of 0.0067 m in the X direction and 0.005 m in the Y direction satisfies all but the highest plasma densities. In addition, the spacecraft size varies from being 1/10 of a Debye length in length to being 10 Debye lengths in length, which will be problematic. However, a more stringent cell size constraint is that the cell size must be less than 2 times the Debye length as shown by Eq. 3.6 (*Verboncoeur*, 2005).

$$\Delta cell < 2\lambda_D \tag{3.6}$$

3.4 Background Plasma Simulations

In order to properly simulate the use of a background plasma as a neutralization source, the background plasma must first be properly initialized and simulated. This is complicated by the simulated orbiting spacecraft in the middle of the simulation space, which requires a flowing plasma around the spacecraft. This is further complicated by the need to simulate the interaction of the plasma with the spacecraft and the continuous flux of electrons and ions impinging on the spacecraft surface. Finally, we need to simulate open boundaries at the edges of the simulation space. This will be made difficult by the constant electrons and ions that are striking the simulation walls, but the simulation walls cannot take on any charge as that will affect the rest of the simulation, thus this needs to be closely examined.

Initially the OOPIC PRO^{TM} load function is utilized to set up a one-time plasma in the simulation space, with a density (called load density here), ion and electron thermal velocity, and a drift speed for the bulk plasma. The orbital speed of a spacecraft can be determined by setting the centripetal force equal to the gravitational force as shown in Eq. 3.7. From here, the spacecraft parameters can be related to Earth parameters as shown in Eq. 3.8 where v is the orbital speed in m/s, r is the radius of the orbit in meters, G is the gravitational constant, and M is the mass of the Earth. Thus for a spacecraft at the bottom of low Earth orbit at 160 km, the orbital speed is approximately 7800 km/s (Eq. 3.9a), but for a spacecraft at the top of low Earth orbit at 2000 km, the orbital speed is approximately 6900 km/s (Eq. 3.9b). These values are the orbital speed in an inertial frame, with the actual speed of the spacecraft relative to the plasma being lower as the plasma/atmosphere tends to co-rotate with it. In the simulation, a moderate spacecraft velocity of 7500 m/s is chosen, thus the plasma drift speed is set at 7500 m/s to simulate the spacecraft moving through the plasma in orbit.

$$\frac{GMm}{r^2} = \frac{mv^2}{r} \tag{3.7}$$

$$v^2 r = GM \tag{3.8}$$

$$v = \sqrt{\frac{6.673 \cdot 10^{-11}[m^3 kg^{-1} s^{-2}] \cdot 5.98 \cdot 10^{24}[kg]}{160000 + 6371000[m]}} \approx 7800 \ \frac{m}{s} \tag{3.9a}$$

$$v = \sqrt{\frac{6.673 \cdot 10^{-11}[m^3 kg^{-1} s^{-2}] \cdot 5.98 \cdot 10^{24}[kg]}{2000000 + 6371000[m]}} \approx 6900 \ \frac{m}{s} \tag{3.9b}$$

In addition to the initial plasma load, it is necessary for the plasma to be continuously sourced into the simulation space to account for the initial loss of plasma to the spacecraft until steady state is achieved. Thus, the plasma source function in OOPIC PRO^{TM} is utilized by placing a plasma source along the entire left wall, having one cell in width (the simulation requires that the plasma source be at least one cell width as the upcoming analysis will make apparent). The Source Particle Injection Rate (I$_{source}$) must be equivalent to the Load Particle Density (I$_{load}$) so a relationship between the two is established and then expressed as currents using the simulation parameters as shown by Eq. 3.10 and Eq. 3.11

$$I_{load} = I_{source} \tag{3.10}$$

$$\rho h q v = r A q \tag{3.11}$$

where ρ is the load density, h is the height of the simulation space, q is the charge of the particle, v is the speed of the particle, r is the source rate in m^{-3}s^{-1}, and A is the area of the plasma source and since the volume of the plasma source is just one cell in the X direction and the height of the simulation this equation can be simplified to Eq. 3.12.

$$r = 150\rho v \tag{3.12}$$

Assuming the 7500 m/s spacecraft orbital velocity, Eq. 3.12 can be simplified to Eq. 3.13.

$$r = 1.125 \cdot 10^6 \rho \tag{3.13}$$

Through simulation, relationships between load density and steady state plasma density can be established as shown in Eq. 3.14 and Fig. 3.4 as well as relationships for source rate to steady state plasma density as shown in Eq. 3.15 and Fig. 3.5. Eq. 3.14 and Eq. 3.15 predicts 99.8% of the variance in the steady state plasma density.

$$n_s = \rho_{steadystate} = 5.813\rho_{load} + 9.712 \cdot 10^9 \tag{3.14}$$

$$n_s = \rho_{steadystate} = 5.167 \cdot 10^{-6} r_{source} + 9.712 \cdot 10^9 \tag{3.15}$$

An additional parameter of the simulation is the Simulation Time Step (Δt). This time step is chosen carefully so that it follows the relaxed particle-in-cell rule shown in Eq. 3.16 where the time step needs to be smaller than the inverse of twice the plasma frequency (ω_{pe}), in Hz, so that the electrons are not missing an oscillation in a single time step (*Tskhakaya et al.*, 2007) as well as the more strict particle-in-cell rule shown in Eq. 3.17 (*Verboncoeur*, 2005).

$$\Delta t \leq 2\omega_{pe}^{-1} \tag{3.16}$$

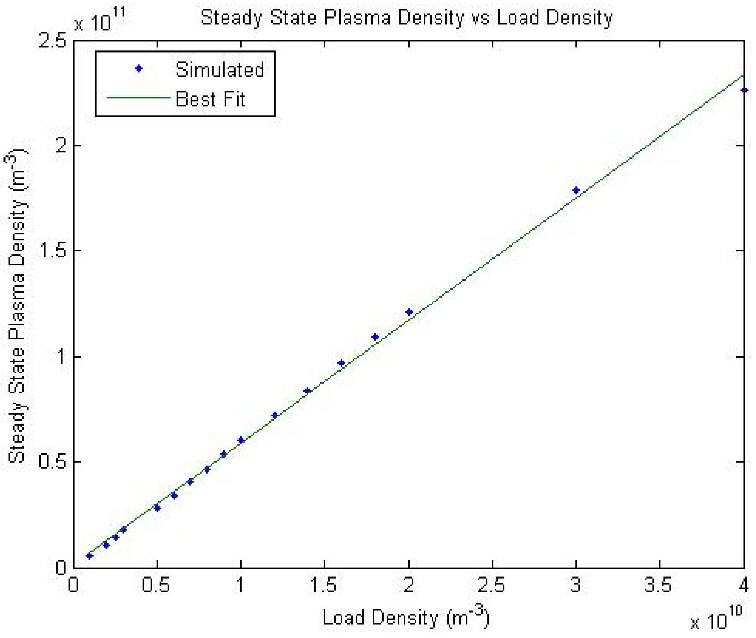

Figure 3.4: Steady State Plasma Density vs Load Density

$$\Delta t \leq 1.66\omega_{pe}^{-1} \tag{3.17}$$

The plasma frequency and thus the time step inequality can be made into a function of the Plasma Density (n_e) by using Eq. 3.17 and Eq. 3.18 where n_e is in cm^{-3} as shown in Eq. 3.19.

$$\omega_{pe} = 2\pi \cdot 8980\sqrt{n_e} \tag{3.18}$$

$$\Delta t \leq \frac{1}{10820\pi\sqrt{n_e}} \tag{3.19}$$

At the applicable range of plasma densities from 10^9 m^{-3} to 10^{13} m^{-3} or 10^3 cm^{-3} to 10^7 cm^{-3}, the time step needs to be less than 9.3×10^{-7} s at the lower densities and 9.3×10^{-9} s at the higher densities. Some simulation texts recommend a time step that is 20 times shorter than this maximum as a rule-of-thumb (*Tskhakaya et al.*,

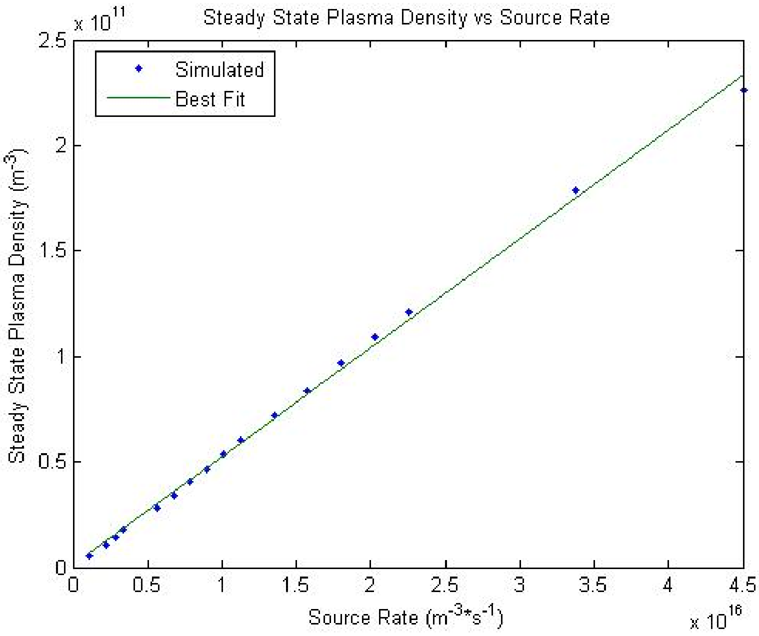

Figure 3.5: Steady State Plasma Density vs Source Rate

2007) meaning that the time step would need to be less than 4.7×10^{-8} s at the lower densities and 4.7×10^{-10} at the higher densities, giving an overall range of 9.3×10^{-6} to 4.7×10^{-10}. However, this is not a hard and fast rule, and thus a moderate time step of 5×10^{-8} s is chosen. (The code for this neutralization scheme is shown in Appendix C.)

3.4.1 Steady State Plasma

With a relationship established between the initial load density and the source rate, then it can be observed how long and under what conditions it takes for the plasma around the spacecraft to reach a steady state. By varying both load density and source rate at the same time, it can be determined how long it takes for the plasma to reach a steady state. The most noticeable way to see when the plasma density has reached steady state is to observe the number of superparticles in the simulation space and see when it has plateaued (a general rule of thumb is having thousands of superparticles in the simulation space to achieve an accurate simulation (*Humphries*, 1990)). This means that as many electrons and atomic oxygen ions are leaving the simulation space as are entering and that the current to the spacecraft is net zero (ion flux is equal to the electron flux). It is important to note that the number of superparticles will not change when particles reach the edges of the simulation space as the simulation is set up with periodic boundaries such that any particle that leaves through one spacecraft wall, comes back in through the opposite spacecraft wall. Thus the flux through the simulation walls is 0.

An example of this is shown in Fig. 3.6 where the simulation is run for a total of 1.2 ms, but it looks like a steady state is reached at approximately 0.8 ms. Hypothetically, it would be possible to use the current diagnostic (IDiagFlag) to the spacecraft walls to determine that the plasma has reached steady state when there is net zero current to the spacecraft. However, with electrons and ions impacting the spacecraft so randomly due to low particle statistics it is difficult to determine when the current has reached net zero, even when applying smoothing functions to the current diagnostic.

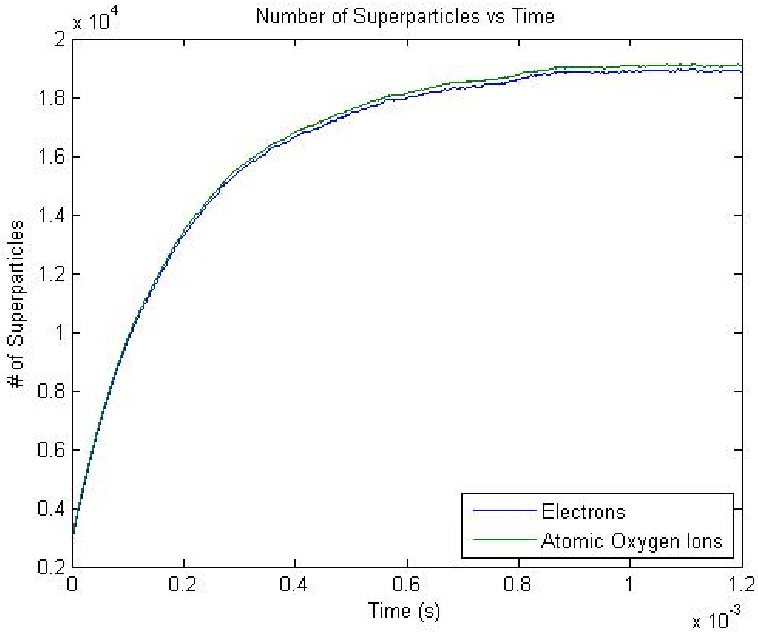

Figure 3.6: Sample Number of Superparticles of Electrons and Atomic Oxygen Ions

In addition, using the number of superparticles as a function of time plot (Fig. 3.6) and Ratio of Particles per Superparticle (NP2C) allows one to calculate Steady State Plasma Density ($\rho_{steadystate}$) using Eq. 3.20 where area is the non-spacecraft area of the simulation space (the entire simulation space area except for the center square occupied by the spacecraft without plasma), as is shown in Fig. 3.7. Fig. 3.7 plateaus at approximately 6.5×10^{10} m^{-3} at approximately 0.8 ms as before. This spatially averaged steady state plasma density, which remains relatively constant between 0.8 and 1.2 ms, matching up with the steady state plasma density shown in Fig. 3.4 when the load density is 10^{10} m^{-3} and the steady state plasma density shown in Fig. 3.5 when the source rate is 1.125×10^{16} $m^{-3}s^{-1}$ as expected.

$$\rho_{steadystate} = \frac{number \cdot NP2C}{area} \tag{3.20}$$

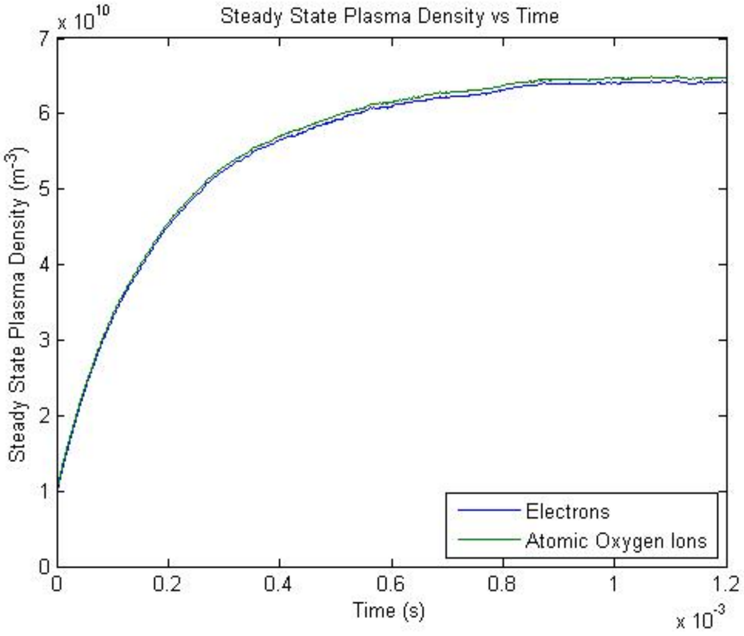

Figure 3.7: Sample Number of Plasma Density Converted from Superparticles

3.4.2 Spacecraft in Plasma

Now that the simulation space, including the spacecraft in the flowing plasma, has been established, it is important to start observing the diagnostics as the simulations progress besides just the number of superparticles. Of particular interest is how the spacecraft charges up as the simulation progresses, as this will provide the baseline prior to the neutralization. First, a variety of diagnostics will be observed at various times throughout the 1.2 ms for the plasma to reach steady state. Then the floating potential of the spacecraft under various plasma conditions will be studied carefully.

3.4.2.1 Base Case Simulation

As described previously, the spacecraft will be placed in the middle of the simulation space and is sized at 0.026 meters in the X direction and 0.02 meters in the Y direction, which varies from 25 Debye lengths to a quarter of a Debye length depending on plasma density or thermal temperature, with all four walls of the spacecraft connected together as if it were a single conducting surface that can float to a potential by having a blocking capacitor between the spacecraft and simulation electrical ground, where charge that contacts the spacecraft redistributes along the surface. The simulation spacecraft is placed into a flowing plasma, and the sample simulation run is examined at these base conditions. The main diagnostics that are examined are the electric field, electric field magnitude in the X direction, number of superparticles, phase space for both electrons and atomic oxygen ions, and potential throughout the phase space. Figures 3.8 - 3.16 show the time progression of this base case simulation with just plasma flowing past a spacecraft up to the 1.2 ms time.

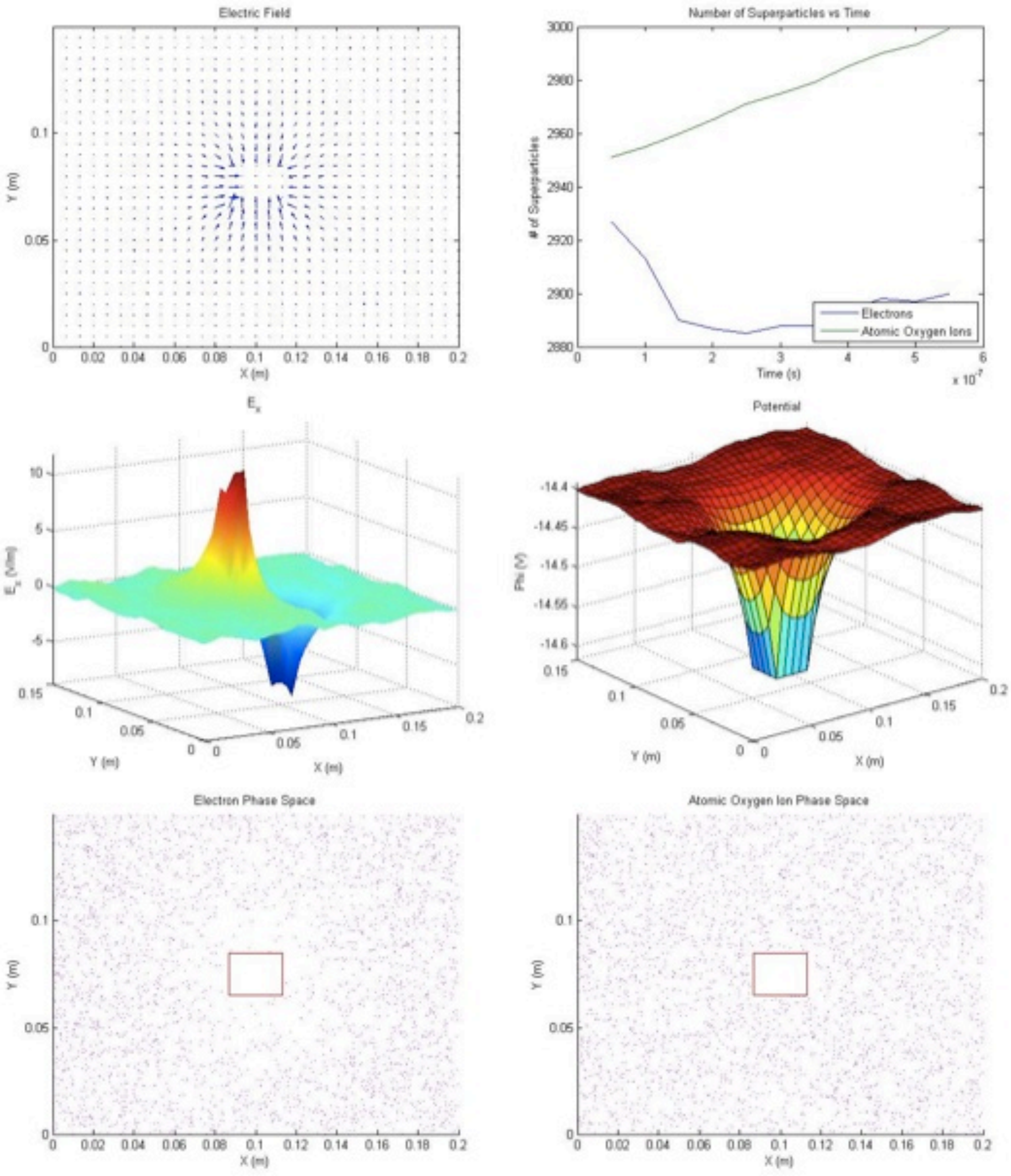

Figure 3.8: Sample Simulation Run of Base Cases at 0.5 μs

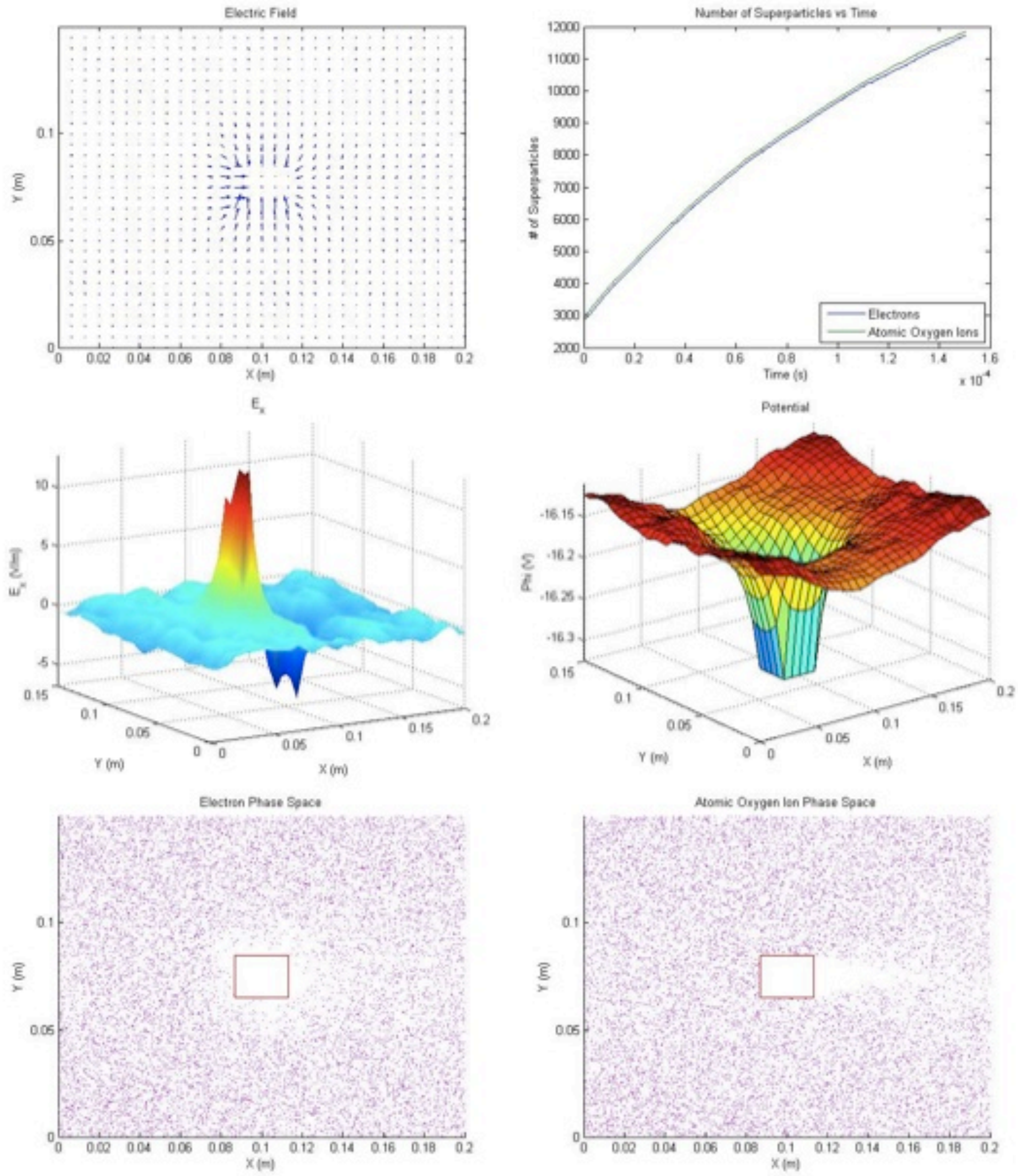

Figure 3.9: Sample Simulation Run of Base Cases at 0.15 ms

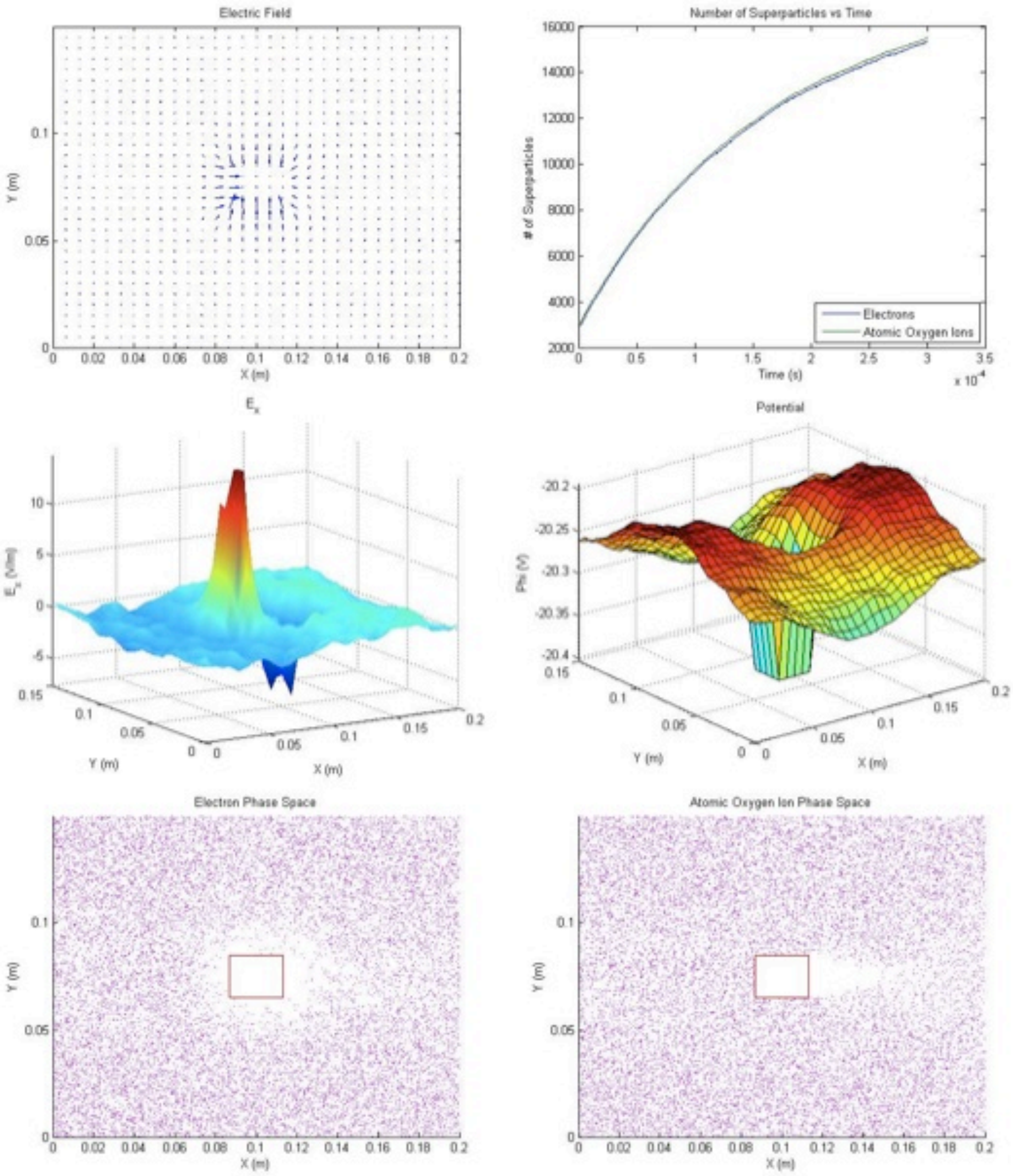

Figure 3.10: Sample Simulation Run of Base Cases at 0.3 ms

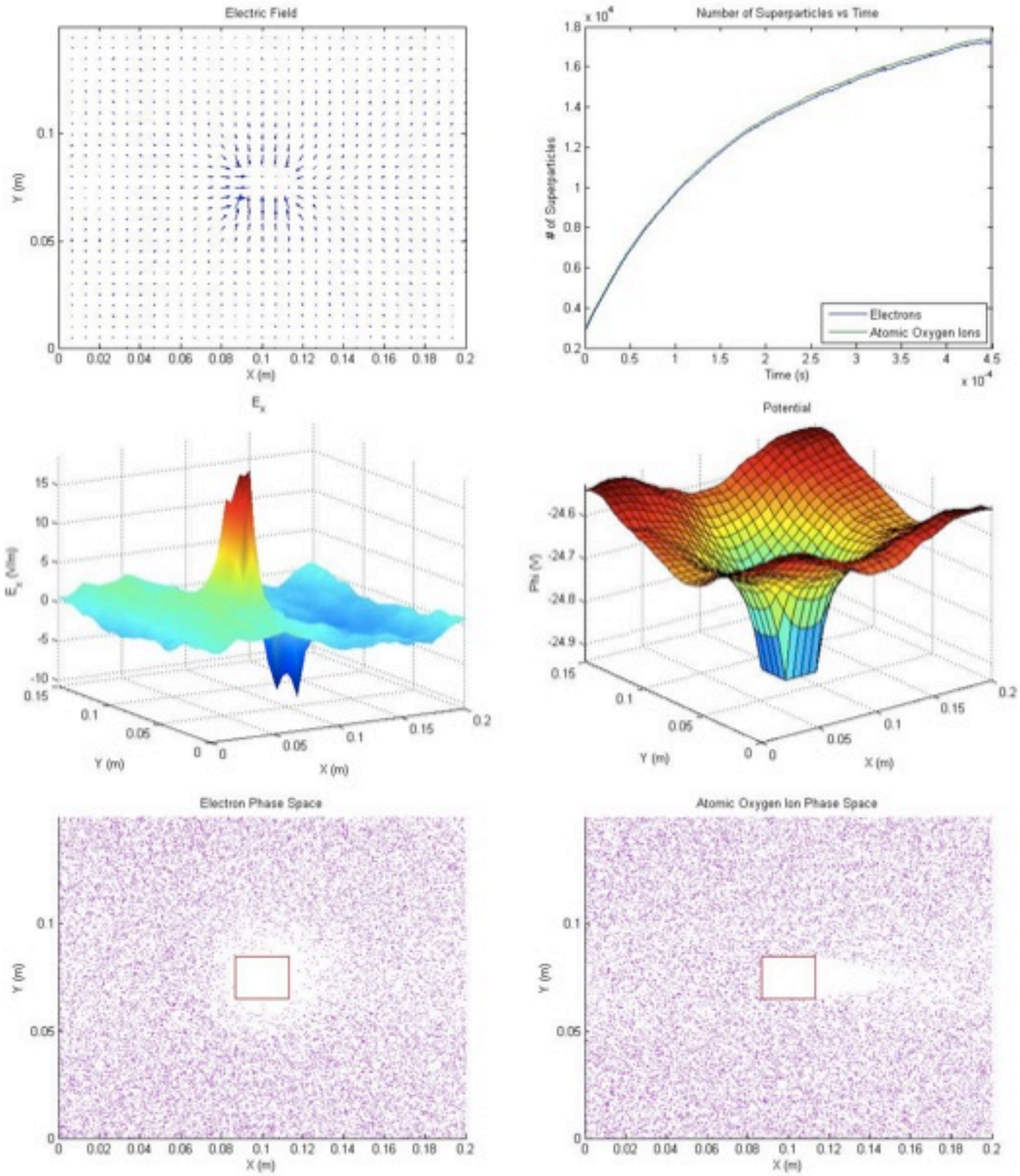

Figure 3.11: Sample Simulation Run of Base Cases at 0.45 ms

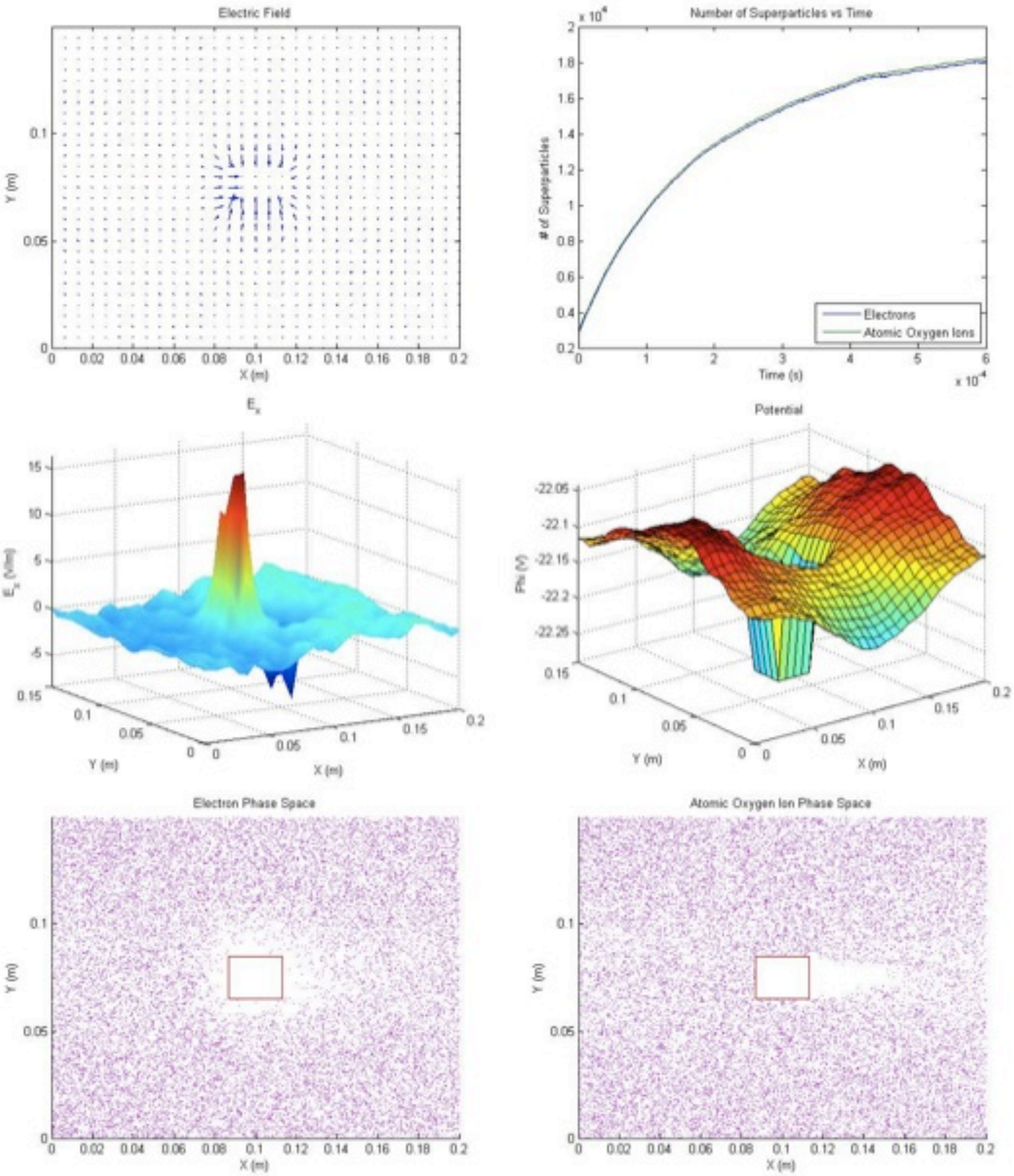

Figure 3.12: Sample Simulation Run of Base Cases at 0.6 ms

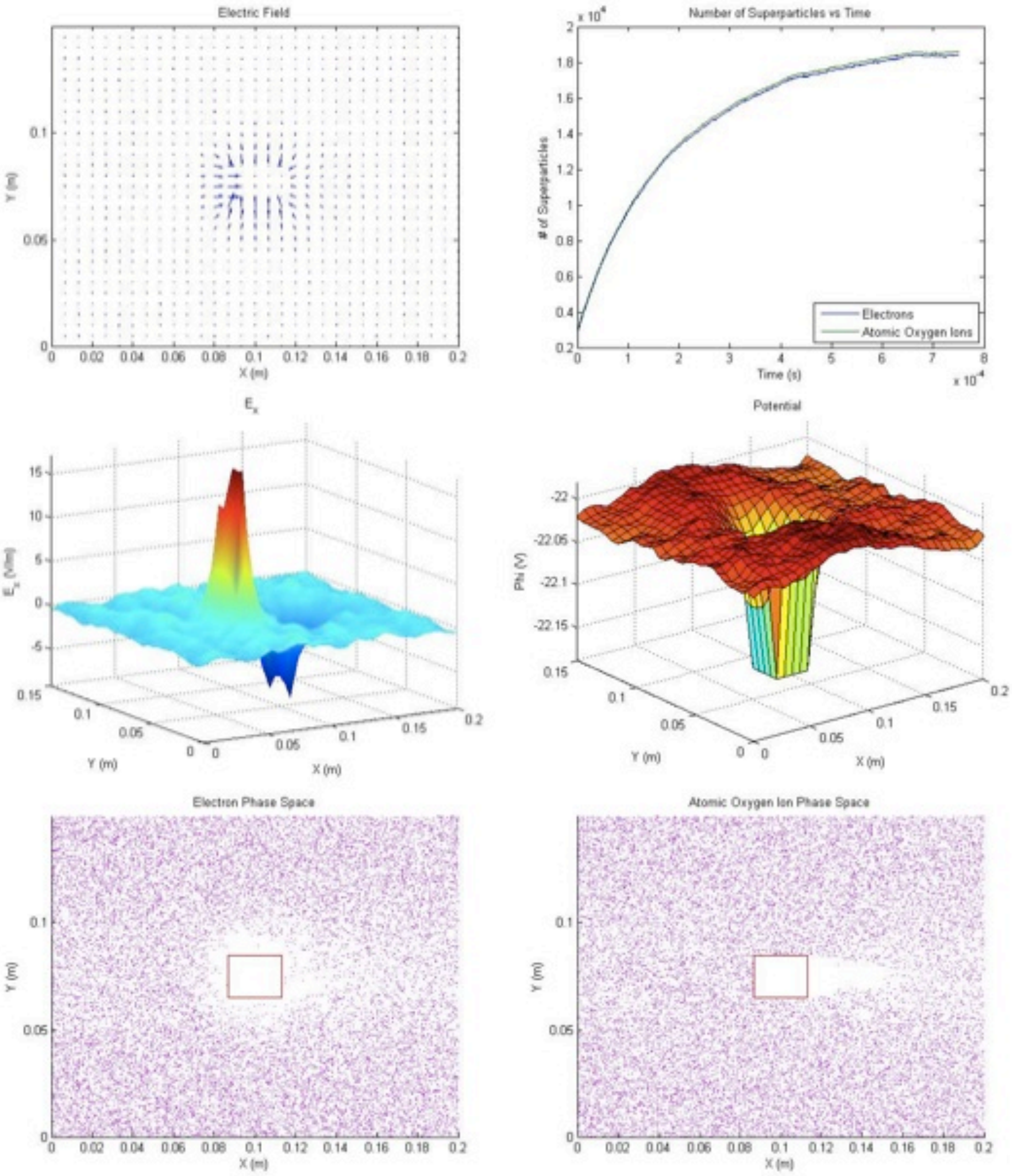

Figure 3.13: Sample Simulation Run of Base Cases at 0.75 ms

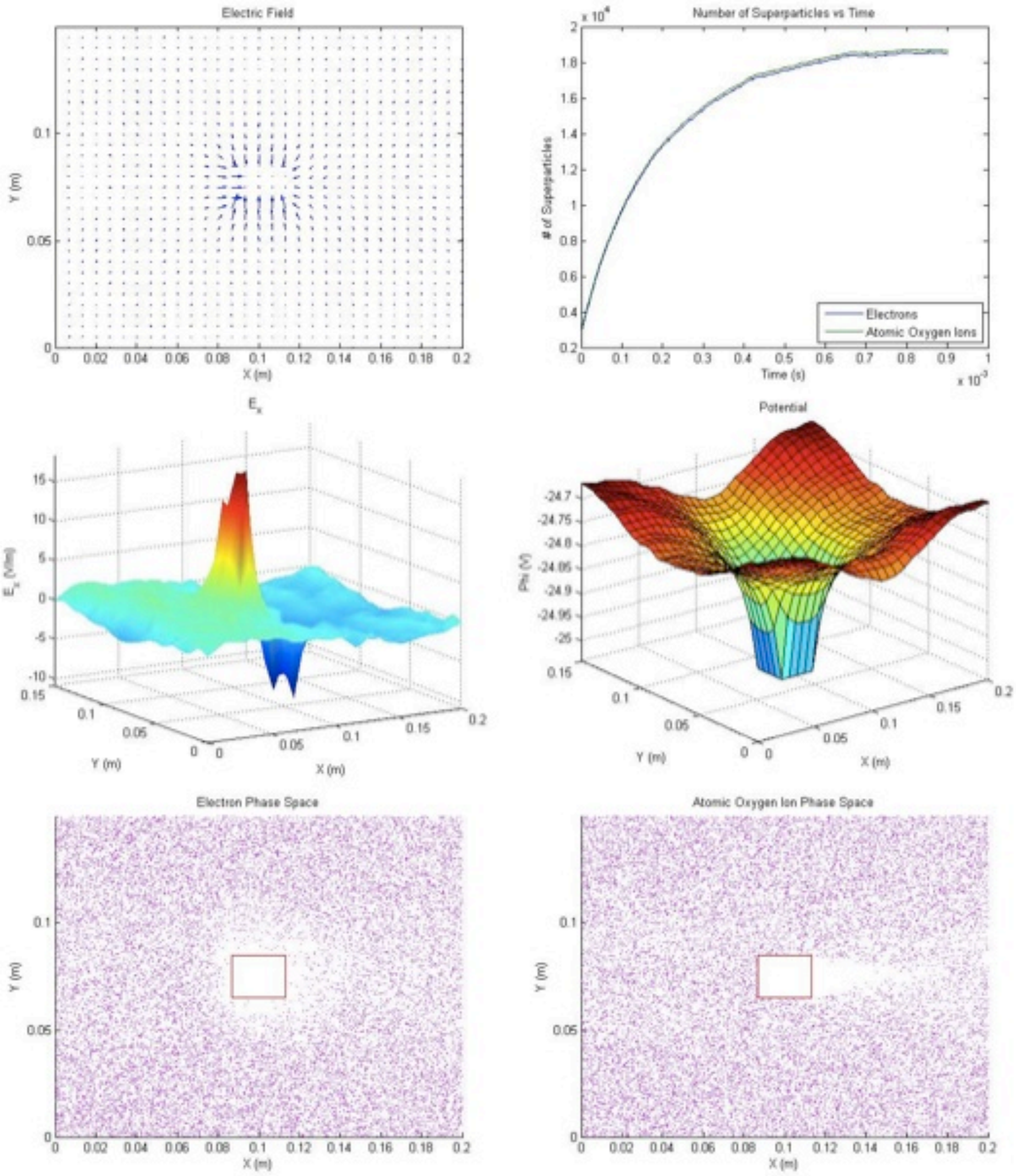

Figure 3.14: Sample Simulation Run of Base Cases at 0.9 ms

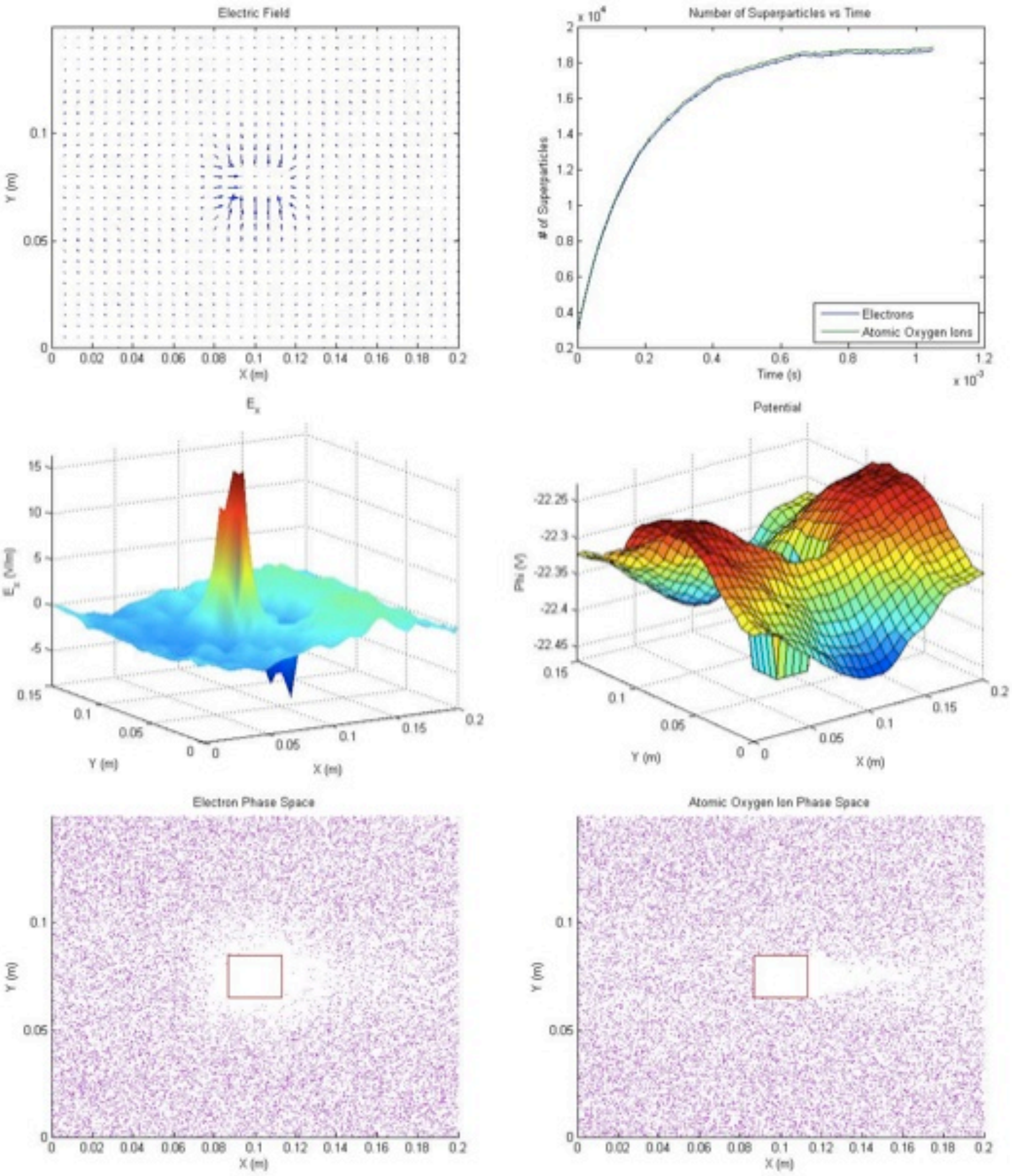

Figure 3.15: Sample Simulation Run of Base Cases at 1.05 ms

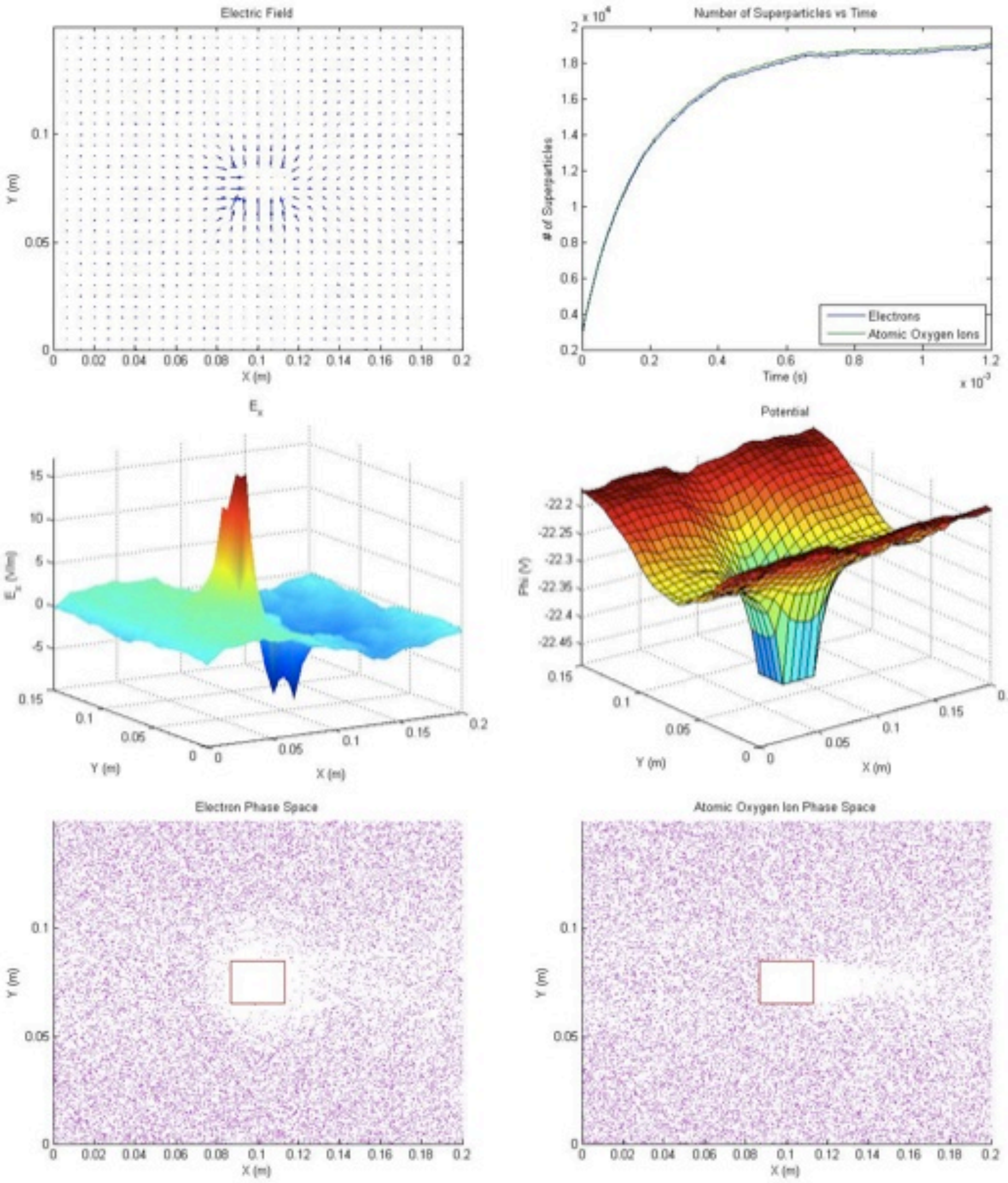

Figure 3.16: Sample Simulation Run of Base Cases at 1.2 ms

These sample simulations show most importantly that there is a large atomic oxygen ion wake effect behind the spacecraft, but that there is no discernible electron wake effect behind the spacecraft, which is as expected as was first quantitatively observed for the first time *in situ* in *Samir et al.* (1973). The lack of a distinguishable electron wake is due to the high electron thermal speed relative to the spacecraft speed and the relatively small size of the spacecraft, thus the electron and ion depletion caused by the spacecraft moving through the plasma is replaced by just the thermally fast moving electrons filling in the wake. The ion wake effect around spacecraft has been studied extensively for a variety of spacecraft varying from spacecraft of a single Debye length, to the space shuttle (*Samir et al.*, 1986; *Samir and Willmore*, 1965; *Samir and Wrenn*, 1969, 1972; *Samir et al.*, 1979; *Samir*, 1981; *Stone and Samir*, 1981; *Enloe et al.*, 1993). The difference between the ion and electron wake has been quantitatively observed by probes placed on the Explorer 31 satellite as discussed in *Samir et al.* (1973).

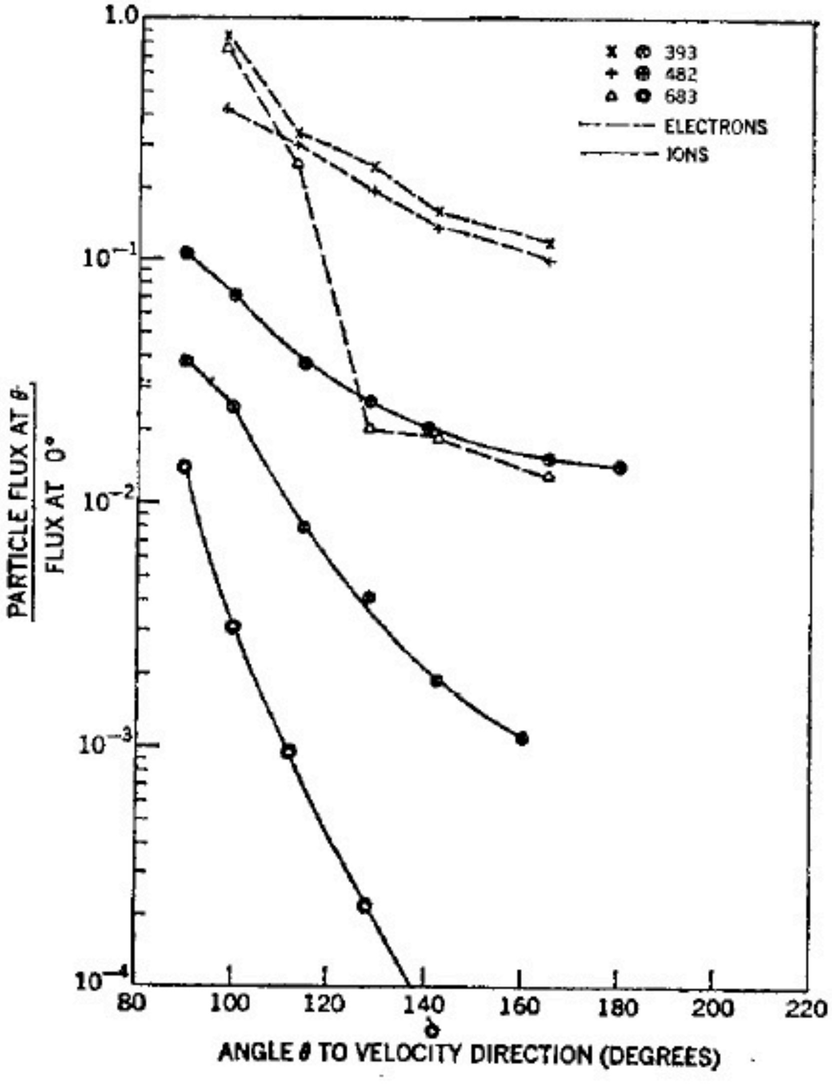

Figure 3.17: Normalized Electron and Ion Flux from Nadir to Wake (*Samir et al.*, 1973)

In Fig. 3.17, all six lines are fluxes normalized to the ram direction flux, with the three dotted lines being normalized electron fluxes, and the three solid lines being the normalized ion fluxes. Each of the different symboled lines represents a different pass. This plot illustrates that the ion wake is depleted by at least an order of magnitude more than the electron wake.

In addition, in *Samir et al.* (1979), it is shown in Fig. 3.18 that as the spacecraft radius increases with respect to the Debye length, the ion wake depletion increases.

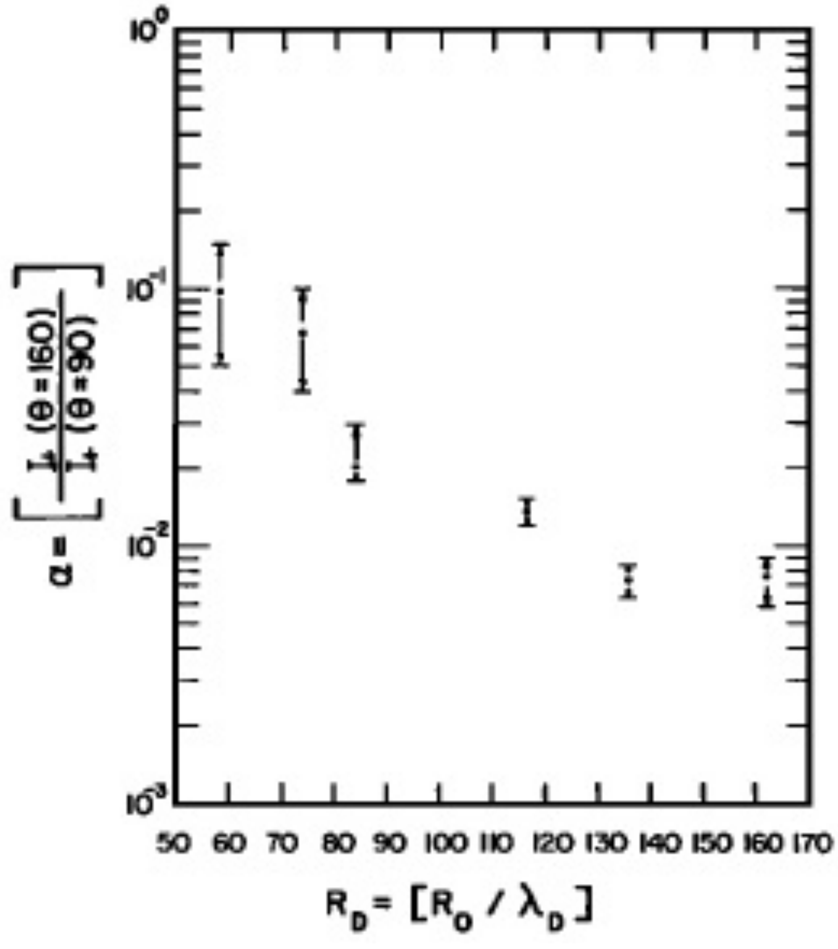

Figure 3.18: Normalized Ion Wake as Spacecraft Size Varies (*Samir et al.*, 1979)

However, there is a sheath that forms around the spacecraft that looks to be a cell size or two wide in all directions in the electron simulation space diagnostic. However, in the atomic oxygen simulation space, there is no distinguishable sheath on the three non-wake sides of the spacecraft as expected as the negatively charged spacecraft attracts the positively charged ions towards it. Additionally, the electric field magnitudes continue to grow as electrons continue to impact the surface and charge up the spacecraft more and more until the plasma reaches steady state which causes the electric field around the spacecraft to reach steady state as well.

3.4.2.2 Floating Potential of Moving Spacecraft in Plasma

An important concept in this chapter is a spacecraft's floating potential when it is placed in any sort of plasma, moving or stationary. When any isolated object is placed into an electropositive plasma, flowing or not and ignoring the possibility of secondary electron emission, it will charge up negatively due to the higher flux rate of electrons (relative to ions) to the object's surface since the electrons are much lighter, and thus much more mobile. However, the spacecraft will not continue to charge up indefinitely, as once the spacecraft reaches a large enough negative potential, electrons will be slowed down and turned away by the negative potential of the spacecraft and ions will be accelerated towards the spacecraft. This negative potential where the Electron Current (I_e) and Ion Current (I_i) to the spacecraft are equal is called the floating potential of the spacecraft as shown in Eq. 3.21, which can be compared to Electron Flux (Γ_e) and Ion Flux (Γ_i) and Electron Impact Area (A_e) and Ion Impact Area (A_i) as shown in Eq. 3.22.

$$I_e = I_i \tag{3.21}$$

$$\Gamma_e A_e = \Gamma_i A_i \tag{3.22}$$

The floating potential phenomena can be seen in Fig. 3.19 during the initial transient phase of the simulation associated with Figures 3.8 - 3.16. Here, the electron and ion current collected by the spacecraft is tracked during the start-up transient phase using a moving average smoothing function over 11 points. Here, a shorter time step (5×10^{-9} seconds, which is ten times shorter than used in Figures 3.8 - 3.16) is used so that as many points as possible can be viewed in the transition to steady-state. As expected the electron current decays over time as the spacecraft charges up negatively deterring additional electrons, whereas ion current stays pretty consistent as it is fully dependent on ions impinging on the ram side of the spacecraft due to the plasma velocity regardless of the floating potential of the spacecraft.

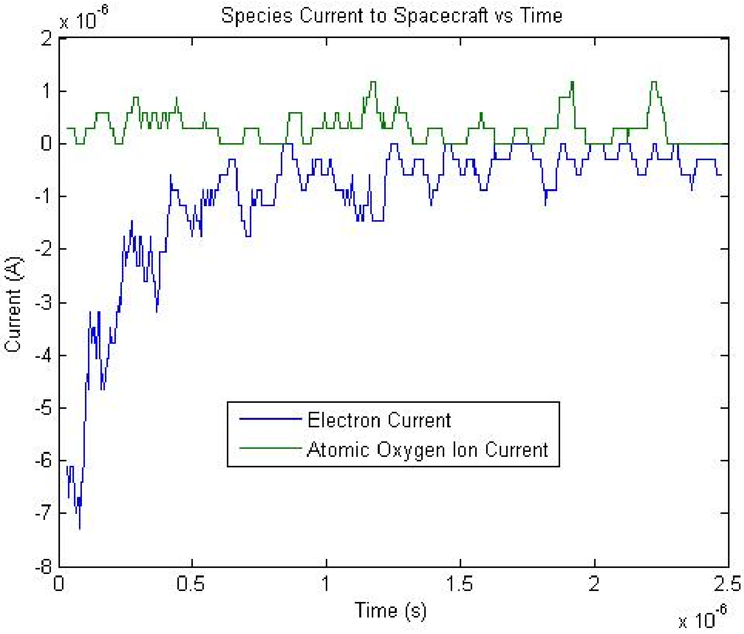

Figure 3.19: Initial Electron and Atomic Oxygen Ion Current to the Spacecraft

This can be compared to the much simpler case of a stationary spacecraft in a nonmoving, non-sourced simulation space (only the load density is present). The plasma only has thermal velocity, and the plasma is only lost to the spacecraft. The electron and ion current to the spacecraft can be seen in Fig. 3.20. Once again there is a large electron current to the initially uncharged spacecraft, which decays as the spacecraft starts to charge up negatively. The only major difference between the moving spacecraft with a plasma source as shown in Fig. 3.19 and the nonmoving spacecraft without a plasma source as shown in Fig. 3.20 is the much smaller ion thermal current to the nonmoving spacecraft which lacks the much larger ion drift current. It is expected that the spacecraft's negative floating potential must be larger since the ion current must be smaller for this case.

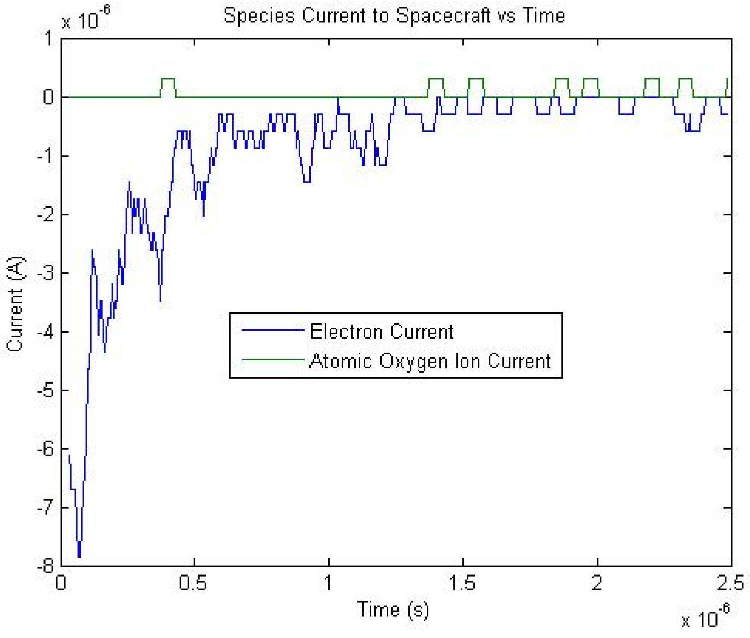

Figure 3.20: Initial Electron and Atomic Oxygen Ion Current to a Spacecraft in an Environment with a Stationary Spacecraft and Non-Flowing Plasma

An analytical estimate of the floating potential of an orbiting spacecraft can be made for low Earth orbit using a few simplifying assumptions. It is assumed that (i) there is no electron photoemission (appropriate for the additional constraint of night-side conditions), (ii) the sheath around the spacecraft (except in the wake) is such that the thin sheath approximation is appropriate (*Gallagher et al.*, 1988), and (iii) the relatively small spacecraft floating potential does not significantly change the ion velocity. All of these assumptions are fairly accurate in the base case where the thermal temperature of the plasma is 0.1 eV and the spacecraft speed is 7500 m/s. In such a case, the ion thermal velocity is 774 m/s and the electron thermal temperature is 133000 m/s meaning that ion thermal velocity $<$ spacecraft velocity $\ll$ electron thermal velocity. As long as this holds, it can be assumed that the ion flux to the spacecraft is entirely due to ions impacting the ram surface of the spacecraft from the Spacecraft Velocity (v_{sp}) as shown in Eq. 3.23 (and also will be shown graphically in

Figures 3.21 - 3.24).

$$\Gamma_i = v_{sp} n_e \tag{3.23}$$

While electron flux can be approximated by using the electron's mean thermal velocity as shown in Eq. 3.24.

$$\Gamma_e = \frac{1}{4} n_e \sqrt{\frac{8eT_e}{\pi m}} e^{\phi/T_e} \tag{3.24}$$

This gives a current equality as shown in Eq. 3.25 which eventually gets simplified to a final floating potential equation as shown in Eq. 3.27.

$$\frac{1}{4} n_e \sqrt{\frac{8eT_e}{\pi m}} e^{\phi/T_e} A_e = v_{sp} n_e A_i \tag{3.25}$$

$$e^{\phi/T_e} = \frac{A_i}{A_e} \sqrt{\frac{2\pi m v_{sp}^2}{eT_e}} \tag{3.26a}$$

$$\phi/T_e = \ln\left[\frac{A_i}{A_e} \sqrt{\frac{2\pi m v_{sp}^2}{eT_e}}\right] \tag{3.26b}$$

$$\phi = -T_e \ln\left[\frac{A_e}{A_i} \sqrt{\frac{eT_e}{2\pi m v_{sp}^2}}\right] \tag{3.27}$$

The initial electron and ion current before the spacecraft starts to charge up can be calculated from the two sides of Eq. 3.25 and compared to the initial electron and ion current measured in the simulation from Fig. 3.19. The electron and ion current calculated from Eq. 3.25 come out to approximately 6.1×10^{-6} A and 2.4×10^{-7} A, which matches up very well with the current levels from Fig. 3.19 at t = 0.

This equation has no dependence on the mass of the ions as one of the assumptions was that ions will only be impacting the spacecraft due to the spacecraft's velocity. This equation is similar to the floating potential equation for a stationary wall or spacecraft as is shown in Eq. 3.28.

$$\phi = -T_e \ln \left[\frac{A_e}{A_i} \sqrt{\frac{M}{2\pi m}} \right] \tag{3.28}$$

And this equation simplifies to the normal sheath potential for a floating wall equation with equal electron and ion collection areas as is shown in Eq. 3.29 (*Lieberman and Lichtenberg*, 2005).

$$\phi = -T_e \ln \left[\sqrt{\frac{M}{2\pi m}} \right] \tag{3.29}$$

The only difference between Eq. 3.27 and Eq. 3.28 being that the spacecraft velocity and electron temperature replaces the mass of an ion with the equivalence shown in Eq. 3.30 and the units analysis working out as shown in Eq. 3.31.

$$M = \frac{eT_e}{v_{sp}^2} \tag{3.30}$$

$$kg = \frac{J}{(m/s)^2} \tag{3.31}$$

And for the base case of atomic oxygen ions, a thermal temperature of 0.1 eV, and a spacecraft velocity of 7500 m/s, the left side of Eq. 3.30 has value of 5.312×10^{-26} kg, while the right side has a value of 2.848×10^{-28} kg, approximately 200 times difference. It is simpler to understand the difference by reorganizing Eq. 3.27 and Eq. 3.28 as shown in Eq. 3.32a and Eq. 3.32b.

$$\phi = -T_e \left[\ln \left(\frac{A_e}{A_i} \sqrt{\frac{1}{2\pi m}} \right) + \ln \left(\sqrt{\frac{eT_e}{v_{sp}^2}} \right) \right] \tag{3.32a}$$

$$\phi = -T_e \left[\ln \left(\frac{A_e}{A_i} \sqrt{\frac{1}{2\pi m}} \right) + \ln \left(\sqrt{M} \right) \right] \tag{3.32b}$$

For the base case simulation, these equations turn into Eq. 3.33a and Eq. 3.33b showing the difference between floating potential of stationary and moving spacecraft. As expected the over two orders of magnitude difference, translates to just over one order of magnitude with the square root, and with the natural log, and multiplication by 0.1, translates to a difference of approximately 0.25, as is shown in the numerical results as well.

$$\phi = -0.1[eV]\left[34.96 + \ln\left(\sqrt{\frac{eT_e}{v_{sp}^2}}\right)\right] = -0.1(34.96 - 31.71) = -0.325\ V \quad (3.33a)$$

$$\phi = -0.1[eV]\left[34.96 + \ln\left(\sqrt{M}\right)\right] = -0.1(34.96 - 29.1) = -0.586\ V \quad (3.33b)$$

Eq. 3.27 shows that the floating potential of the spacecraft varies with thermal electron temperature, spacecraft velocity, and the area of impact for electrons and ions. The impact area for the ion flux is assumed to be the ram side of the spacecraft as described above, but the impact area for electrons is assumed to be all sides of the spacecraft except for the wake side. However, a small portion of electrons were found to strike the wake side wall, as shown below. This is because the spacecraft velocity makes it difficult for electrons to reach the wake side wall, even though the electron thermal (random) velocity is much higher. For the analysis, an upper and lower bound for electron current and therefore floating potential can be defined depending on whether or not the electron impact area includes the wake side wall. Nevertheless, Eq. 3.27 does reveal that floating potential has no dependence on background plasma density.

With the base case conditions of electron thermal temperature of 0.1 eV, spacecraft velocity of 7500 m/s, an upper and lower bound electron impact area of 0.093 m^2 and 0.073 m^2, respectively (the upper bound electron impact area translates to the lower bound floating potential and vice versa), and an ion impact area of 0.02 m, giving an upper bound floating potential of -0.325 V and a lower bound floating potential of

-0.349 V, which is on the order of a few tenths of a negative volt (*Holbert*, 2006).

3.4.3 Validation of Spacecraft in Plasma Simulation

Here, the estimates of spacecraft floating potential in orbit moving through an ionosphere from analytical results in Section 3.4.2.2 are compared with particle-in-cell simulations. Various simulation parameters are able to be varied and then the floating potential of the spacecraft can be calculated through simulation by taking the potential of the spacecraft (which has all surfaces at a common potential) and subtracting from that the average potential of the ambient plasma. The simulated spacecraft floating potential can then be compared to the analytical results.

The one not well-defined parameter in the floating potential equation is the electron collection area of the spacecraft. For a nonmoving plasma and spacecraft, the electron collection area would be all four surfaces of the spacecraft, but in this case where ion thermal velocity $<$ spacecraft velocity $<<$ electron thermal velocity, there will be an ion wake behind the spacecraft where the extent of the wake will depend on the ratio of the spacecraft velocity to ion thermal velocity (*Samir and Willmore*, 1965). The higher electron thermal velocity will enable ambipolar diffusion of the ionospheric electrons into the ion wake. The degree to which electrons reach the wake-side spacecraft surface depends on several factors including spacecraft dimensions, spacecraft velocity, and electron temperature. Thus, in the base case where the above velocity inequalities hold, electrons will still impact the wake side of the spacecraft but at a lower current level than on the other walls as shown in a later figure. Thus the electron collection area can be approximated to be between all four walls and all but the wake side wall. When all four walls are capable of collecting electrons, the spacecraft will charge up more negatively as it needs to repel more electrons making it the upper bound than if all but the wake side wall are capable of collecting electrons making this the lower bound. Thus, an upper and lower bound for floating potential can be established.

By changing the spacecraft in the simulation from one connected current source, which makes the entire boundary and body of the spacecraft float at the same potential, to four disconnected current sources (one for each spacecraft wall) for this specific study, the currents can be observed to each individual spacecraft wall as is shown in Fig. 3.21, Fig. 3.22, Fig. 3.23, and Fig. 3.24.

Fig. 3.21 and Fig. 3.22 shows the current to the top and bottom spacecraft wall, which show a pretty random and equal distribution of electron and ion currents to the two spacecraft walls as all of the current to both of those walls is due to random thermal motion. Fig. 3.23 shows the current to the right spacecraft wall is small and sporadic, single electron currents with no ion current whatsoever. This shows that there is little electron current being collected by the right wall, suggesting that the floating potential should be closer to the lower bound than the upper bound.

Fig. 3.24 shows the current to the left spacecraft wall. The increase in electron and ion current is due to the increase of plasma density initially from the plasma source in addition to the initial load density, but displays the same leveling off behavior as the number of superparticles of electrons and ions in time as was shown in Fig. 3.6.

Also, with the low current level to the right spacecraft wall, and equal electron and ion current to the bottom and top spacecraft walls, the electron and ion current is similar to the electron and ion current to one connected current source spacecraft as shown in Fig. 3.25, which is smoothed out every 10 samples. Also on Fig. 3.25 is the difference in electron and ion current to the single current source spacecraft which hovers around 0 A, as expected as once the spacecraft reaches its floating potential, the net current to the spacecraft will be zero.

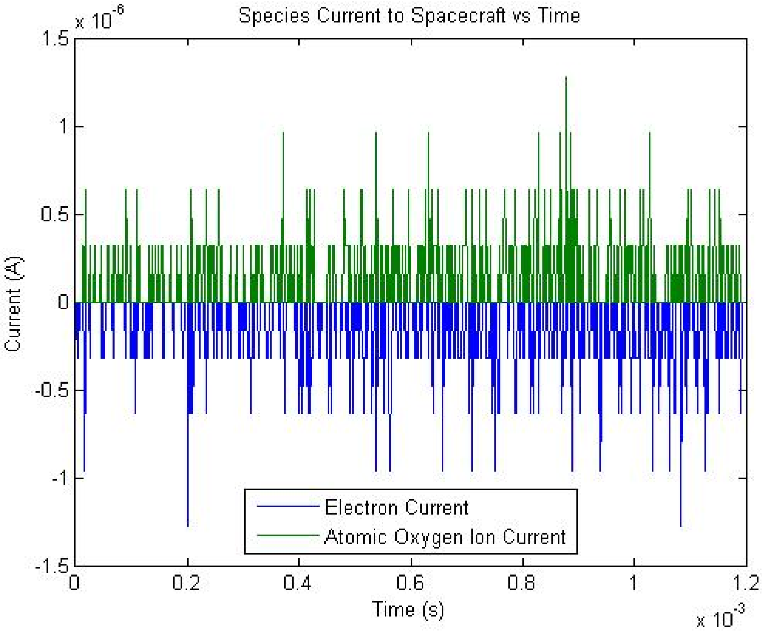

Figure 3.21: Electron and Atomic Oxygen Ion Current to the Bottom Spacecraft Wall

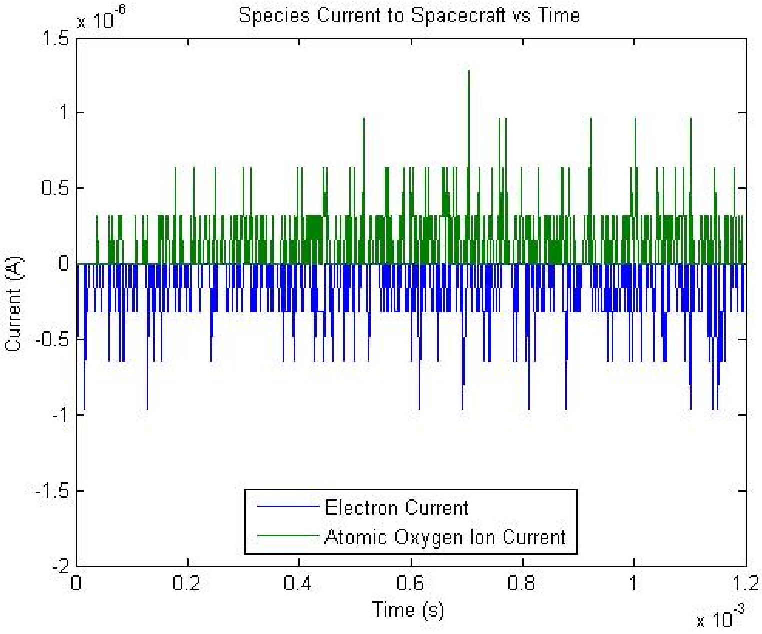

Figure 3.22: Electron and Atomic Oxygen Ion Current to the Top Spacecraft Wall

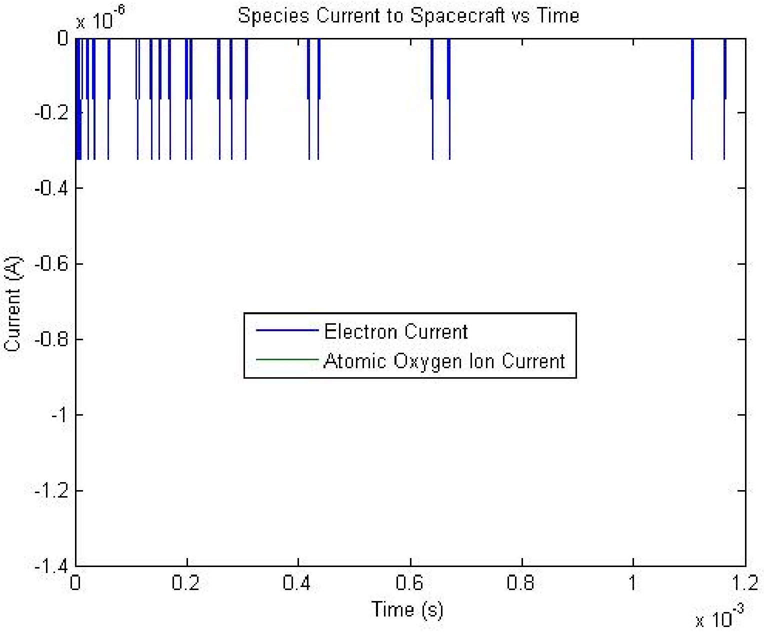

Figure 3.23: Electron and Atomic Oxygen Ion Current to the Right Spacecraft Wall

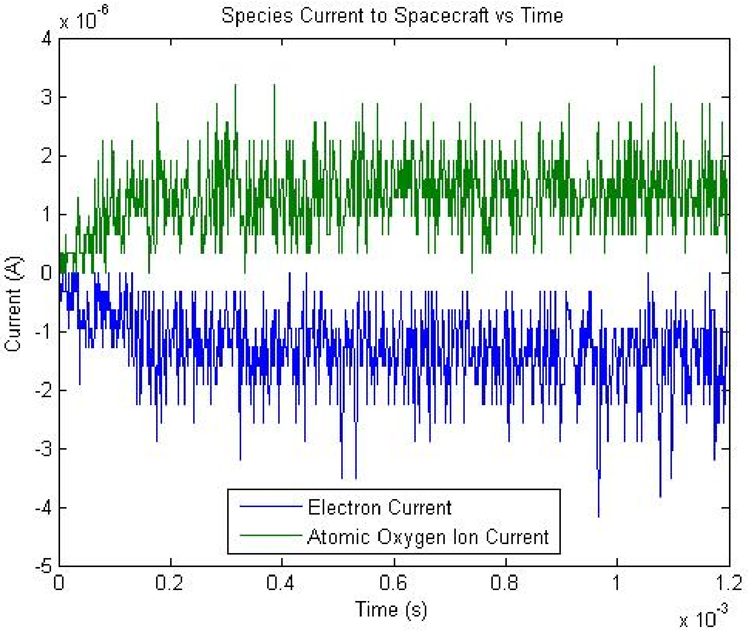

Figure 3.24: Electron and Atomic Oxygen Ion Current to the Left Spacecraft Wall

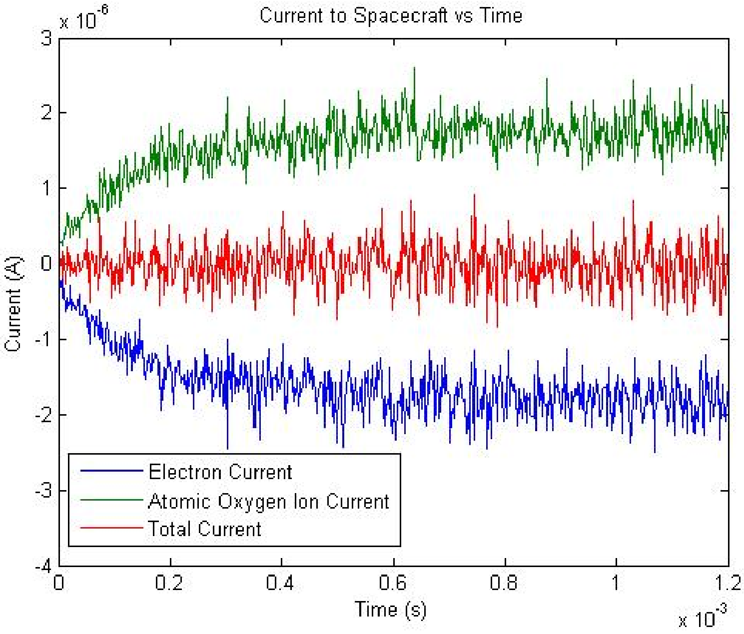

Figure 3.25: Electron and Atomic Oxygen Ion Current to a Single Current Source Spacecraft

3.4.3.1 Validating Spacecraft Floating Potential While Varying Spacecraft Velocity

In order to establish trends, spacecraft velocity, plasma temperature, and plasma density are varied to see how varying parameters match up with the floating potential. In this case, a lower bound and upper bound will be established. The lower bound floating potential is when the electron impact area is assumed to be the three sides of the spacecraft other than the wake side, giving an electron impact area of 0.073 m. The upper bound floating potential is when the electron impact area is all four sides of the spacecraft, giving an electron impact area of 0.093 m.

Spacecraft velocity in the ionosphere will vary from 6800 m/s to 7900 m/s, as was shown in Eq. 3.9a and Eq. 3.9b, with a base case velocity of 7500 m/s. When spacecraft velocity is varied, but all the other parameters are held at the base case conditions specified earlier, the floating potential has a lower bound as is shown in Eq. 3.34a and a higher bound as is shown in Eq. 3.34b.

$$\phi = -1.2176 + 0.1 \ln v_{sp} \tag{3.34a}$$

$$\phi = -1.2417 + 0.1 \ln v_{sp} \tag{3.34b}$$

This implies that as spacecraft velocity increases, the magnitude of the floating potential decreases but at an increasingly slower rate; however, in the narrow spacecraft velocity range of interest here, the bounds look very linear. These bounds only hold when the original assumption that ion thermal velocity < spacecraft velocity $\ll$ electron thermal velocity is true. However, with the spacecraft velocity having such little variation in the ionosphere, this inequality will always hold.

The only simulation parameter other than the velocity of the plasma (of the initially loaded plasma as well as the sourced plasma) that must be changed as spacecraft velocity changes is the source rate of the plasma. Eq. 3.12 establishes the source rate as a function of spacecraft velocity and load density, so as load density is held constant while spacecraft velocity changes, source rate also has to change in order to provide a constant flow. This may cause an unexpected steady state plasma density, but as plasma density does not influence the floating potential, it is only necessary to track the plasma density to ensure that the Debye length is such that it follows all the particle-in-cell simulation rules, especially Eq. 3.5 as well as the simulation space is much larger than a Debye length to ensure that the sheath is fully developed.

In the simulations, the plasma velocity, which simulates the spacecraft velocity, varies from 6800 m/s to 7900 m/s, while the source rate is simultaneously changed in order to account for the different plasma velocities. At the same time, the steady state plasma density is monitored to ensure that no particle-in-cell rules are being violated due to the changing plasma density in different simulations as spacecraft velocity varies. Three simulations are run per spacecraft velocity, and averaged to determine an average floating potential for each spacecraft velocity and plotted against the upper and lower bounds as shown in Fig. 3.26.

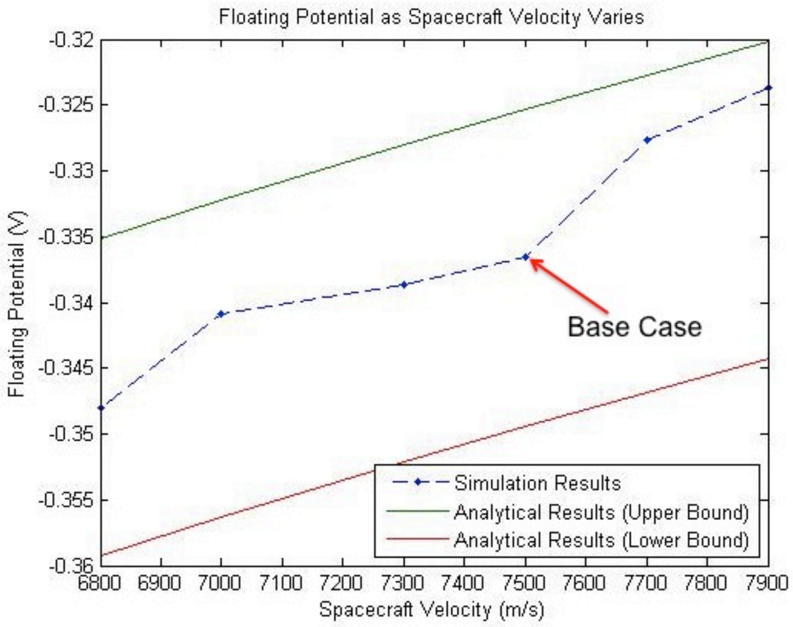

Figure 3.26: Spacecraft Floating Potential as Spacecraft Velocity Varies

Fig. 3.26 shows that the simulation floating potential stays within the analytical bounds, with the expected trend of decreasing floating potential magnitude as spacecraft velocity increases. The simulation results skew towards the upper bound, which is for an electron impact area that is three of the four sides of the spacecraft except for the wake side wall. As is seen in Fig. 3.23, the electron current to the right wall of the spacecraft is much less than the current to any of the other walls, so the electron impact area is closer to three walls than it is to four walls.

As the spacecraft velocity continues to increase, the ion current due to impact on the ram wall increases as well (Eq. 3.3) which is the vast majority of the ion current to the spacecraft. The electron current will also be increased by the increased spacecraft velocity, but due to the higher electron thermal temperature, the increase in electron current will not be as large as the increase in ion current. Thus, the spacecraft will charge up less negatively as the spacecraft velocity increases.

3.4.3.2 Validating Spacecraft Floating Potential While Varying Plasma Temperature

Plasma temperature in the ionospheric range that is of interest varies from 0.043 eV to 0.215 eV, as was shown in Fig. 3.2, with a base case electron temperature of 0.1 eV. When plasma temperature is varied, but all the other parameters are held at the base case conditions specified earlier, the floating potential has a lower bound as is shown in Eq. 3.35a and a higher bound as is shown in Eq. 3.35b.

$$\phi = -4.4T_e - 0.5T_e \ln T_e \tag{3.35a}$$

$$\phi = -4.642T_e - 0.5T_e \ln T_e \tag{3.35b}$$

As thermal temperature in the simulation changes, the Debye length will change even if the steady state plasma density stays constant. Over the range of thermal temperatures of interest (0.043 eV to 0.215 eV) with a plasma density of 6.5×10^{10} m^{-3}, the Debye length will vary from 0.00604 m to 0.0135 m as is calculated by Eq. 3.4. Thus, the cell size needs to be less than 0.0121 m for the lowest thermal temperature to be less than 0.027 m for the highest thermal temperature (Eq. 3.6). The cell sizes in the simulation are 0.005 m and 0.00667 m, and thus they satisfy the particle-in-cell simulation constraints except at the highest plasma temperatures.

In addition, as thermal temperature is directly related to thermal velocity, as was shown in Eq. 3.1 and Eq. 3.2, electron and ion thermal velocities can be calculated for the range of thermal temperatures. For this range of thermal temperatures, the electron and ion thermal velocities will range as shown in Table 3.1.

As can be seen in Table 3.1, for a spacecraft velocity of 7500 m/s, the inequality

	Minimum	Base Case	Maximum
Electron Thermal Velocity (m/s)	87000	133000	194000
Ion Thermal Velocity (m/s)	510	770	1100

Table 3.1: Range of Electron and Ion Thermal Velocities for the Given Range of Ionospheric Thermal Temperatures

ion thermal velocity $<$ spacecraft velocity $\ll$ electron thermal velocity holds true, with the only caveat being at the maximum thermal temperature, the ion thermal velocity starts to be a non-negligible fraction of the 7500 m/s spacecraft velocity.

In the simulations, the thermal temperature varies from 0.043 eV to 0.215 eV, while the steady state plasma density and Debye length is simultaneously monitored to ensure that no particle-in-cell rules are being violated due to the changing plasma density in different simulations as thermal temperature varies. Eq. 3.35a and Eq. 3.35b show that as thermal temperature increases, the floating potential magnitude will also increase in a mostly linear fashion. In addition as thermal temperature increases, the upper bound and lower bound get further apart. Three simulations are run per thermal temperature, and averaged to determine an average floating potential for each thermal temperature and plotted against the upper and lower bounds as shown in Fig. 3.27.

Fig. 3.27 shows that for the most part the floating potential stays within the analytical upper and lower bounds, except for a couple of data points at moderate thermal temperatures of 0.125 and 0.15 eV that are just above the upper analytical bound. At higher thermal temperatures, the Debye length gets to be large enough that the original simulation space of 0.15 m by 0.20 m is not significantly larger than the Debye length and thus the simulation space is not sufficient to accurately simulate the sheath. Therefore, at moderate to high thermal temperatures (0.125-0.215 eV), the simulation space is increased to 0.30 m by 0.40 m, with corresponding increases in cells and source rate. The downside of these simulation changes being a significantly

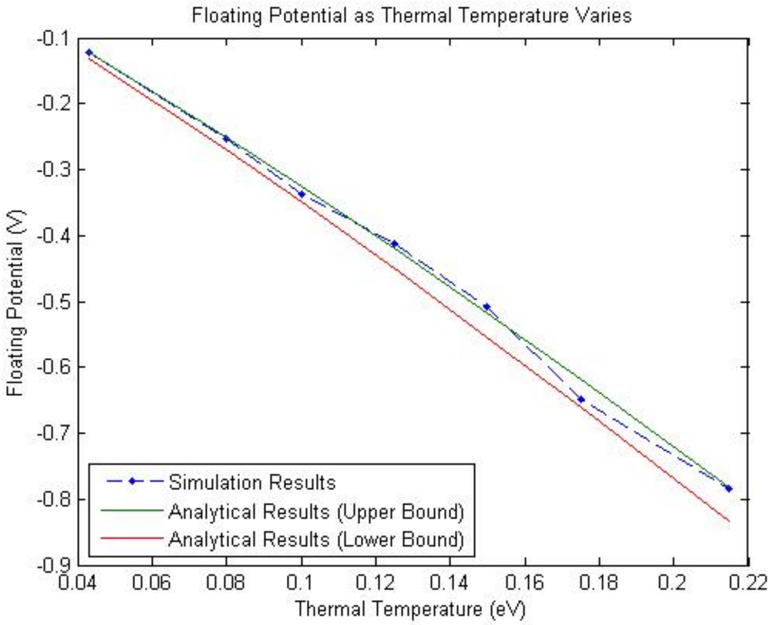

Figure 3.27: Spacecraft Floating Potential as Thermal Temperature Varies

longer simulation run time and a simulation that is more prone to crashes.

3.4.3.3 Validating Spacecraft Floating Potential While Varying Plasma Density

The plasma density in the low Earth orbit portion of the ionosphere ranges mostly from 10^9 m^{-3} to 10^{13} m^{-3}, as was shown in Fig. 3.1. In order to properly simulate different steady state plasma densities, the load density and source rate need to be properly initialized as was developed in Eq. 3.14 and Eq. 3.15. The base case density for these simulations is 6.5×10^{10} m^{-3}. Analytically, plasma density has no effect on a spacecraft's floating potential; however, when varying plasma density, the Debye length will also change, resulting in a multitude of simulation parameter changes in order to accurately simulate the floating potential.

As the plasma density decreases, the Debye length will increase, and thus, the simulation space needs to be increased in order to keep the simulation space much larger than the Debye length in order to see the full shielding effect provided by the plasma. In the simulations, as the plasma density decreases below the base case of 6.5×10^{10} m^{-3}, the simulation space is no longer sufficiently large enough for an accurate simulation. Thus, at moderate plasma densities (1.3×10^{10} m^{-3} and 3×10^{10} m^{-3}), the simulation space is increased to 0.30 m by 0.40 m, with corresponding increases in cells and source rate. And at the lowest plasma densities (1.5×10^{9} m^{-3} and 6.8×10^{9} m^{-3}), the simulation space is increased to 0.75 m by 1.0 m, with corresponding increases in cells and source rate. The downside of these simulation changes being a significantly longer simulation run time and a simulation that is more prone to crashes.

On the other hand, as plasma density increases, the cell size needs to change as the Debye length will decrease and the simulation parameters are constrained by Eq. 3.6; however this is only an issue at the highest portion of the plasma density range. When plasma density gets to the upper limit of 10^{13} m^{-3}, the Debye length is 0.000743 m, and thus the cell size must be less than 0.0015 m in both the X and Y direction.

Analytically, when plasma density is varied, the floating potential of the spacecraft with otherwise base conditions should have a lower bound at -0.325 V and an upper bound at -0.349 V no matter what the plasma density is as shown in Fig. 3.28.

As is seen when varying spacecraft velocity (Section 3.4.3.1), thermal temperature (Section 3.4.3.2), and varying plasma density (Section 3.4.3.3), the base case plasma properties (7500 m/s, 0.1 eV, and 6.5×10^{10} m^{-3}) along with the range of spacecraft velocities, thermal temperatures, and plasma densities provide a situation where the spacecraft floats to a potential that is between the analytical upper and lower bounds.

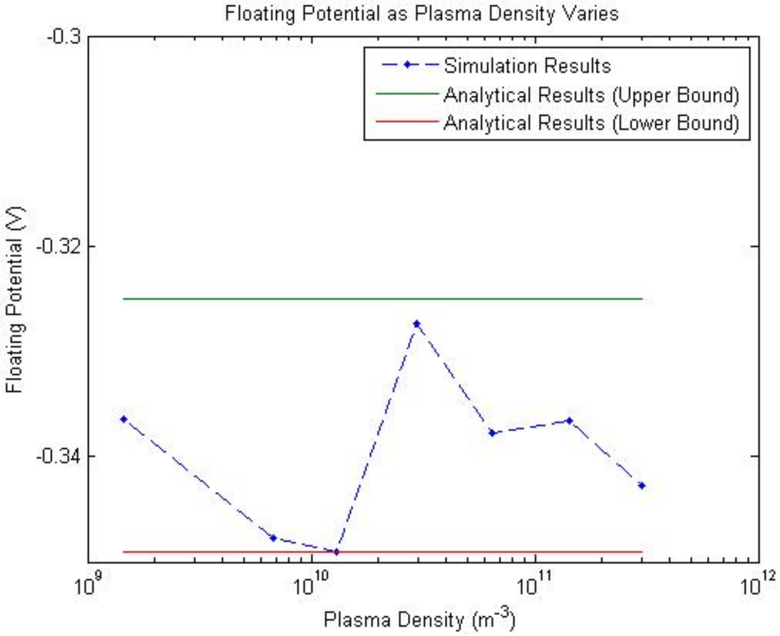

Figure 3.28: Spacecraft Floating Potential as Plasma Density Varies

3.4.4 Presence of a Magnetic Field

The previous simulations have all been conducted assuming no magnetic field; however, there is a small magnetic field in the altitudes of Earth being examined, approximately 0.3 Gauss (*Valleé*, 1998). With this Magnetic Field (B_0) and the equations for the Gyration or Cyclotron Frequency (ω_c) (Eq. 3.36a) and Gyroradius (r_c) (Eq. 3.36b), the cyclotron frequency and gyroradius for electrons and atomic oxygen ions can be determined (*Lieberman and Lichtenberg*, 2005).

$$\omega_c = \frac{qB_0}{m} \tag{3.36a}$$

$$r_c = \frac{v_{\perp 0}}{|\omega_c|} \tag{3.36b}$$

These equations can be simplified for electrons (Eq. 3.37) and ions (Eq. 3.38) where ϵ is the voltage equivalent of energy in volts and B_0 is the magnetic field in Gauss. The light, mobile electrons have a much higher frequency but much smaller gyroradius than the heavy, slow atomic oxygen ions.

$$f_{ce} = 2.8 \cdot 10^6 B_0 \; Hz \tag{3.37a}$$

$$r_{ce} = \frac{3.37\sqrt{\epsilon}}{B_0} \; cm \tag{3.37b}$$

$$f_{ci} = 95 B_0 \; Hz \tag{3.38a}$$

$$r_{ci} = \frac{576\sqrt{\epsilon}}{B_0} \; cm \tag{3.38b}$$

And with the expected small magnetic field of 0.3 Gauss and thermal energy of 0.1 eV, the cyclotron frequencies and gyroradii of the electrons and ions are as listed in Eq. 3.39.

$$f_{ce} = 840\, kHz \tag{3.39a}$$

$$r_{ce} = 3.55\, cm \tag{3.39b}$$

$$f_{ci} = 28.5\, Hz \tag{3.39c}$$

$$r_{ci} = 6.07\, m \tag{3.39d}$$

With an electron gyroradius of 3.55 cm, which is on par with the spacecraft size, and a cyclotron frequency of close to 1 MHz there may be instances where the magnetic field may have an effect on the floating potential of the spacecraft. Thus, this is something that must be examined by implementing a magnetic field into the simulation.

3.5 Emission into Background Plasma

Now that the behavior of the background flowing plasma in the presence of a floating spacecraft has been well established, it is possible to observe the neutralization capabilities of the background plasma as the spacecraft emits negatively charged particles into it as well as the response of the plasma environment. While varying plasma parameters (plasma temperature, plasma density, and plasma velocity), emission parameters can also be varied to determine a relationship between minimum emission parameters and plasma parameters for neutralization of the emitted beam.

3.5.1 Base Case Emission into Background Plasma

Starting with the base case of 0.1 eV thermal temperature, 6.5×10^{10} m^{-3} plasma density, a 7500 m/s drift velocity for plasma parameters and 1000 s specific impulse and 60 nA of current for emission parameters, allows for the observation of relevant diagnostics. The emitted beam will not begin to be emitted until the flowing plasma has reached steady state, which has been determined to be at 1.2 ms previously, thus starting at 1.2 ms, the spacecraft will emit negatively charged particles for 6 μs, which will be sufficiently long to reach steady state. Diagnostics will be observed before emission at 1.2 ms and after emission at 1.206 ms.

Fig. 3.29 shows the emission of the negatively charged particles for 6 μs into the flowing ambient plasma. Fig. 3.30 and Fig. 3.31 show the electrons present in the simulation space immediately before and after negative particle emission, and Fig. 3.32 and Fig. 3.33 show the oxygen ions present in the simulation space immediately before and after negative particle emission. The electrons and oxygen ions in the simulation space show no discernible difference between the simulation space before and after negative particle emission, due to the very low current level of emission.

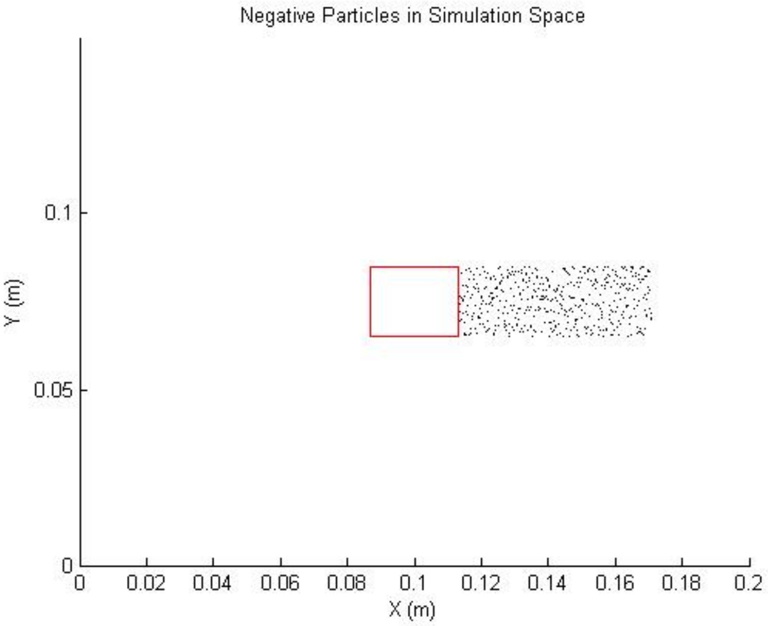

Figure 3.29: 60 nA Emission of Negative Particles into Ambient Plasma

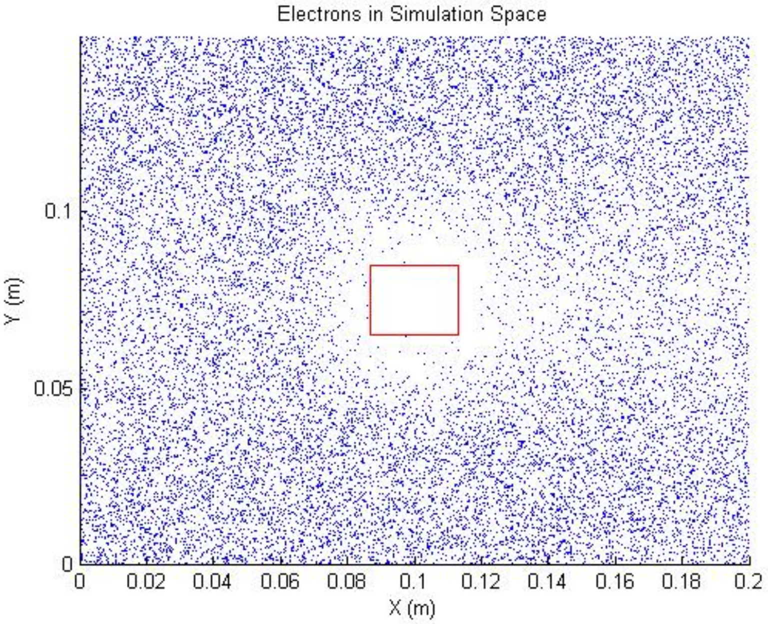

Figure 3.30: Electrons in Simulation Space Prior to 60 nA of Negative Particle Emission

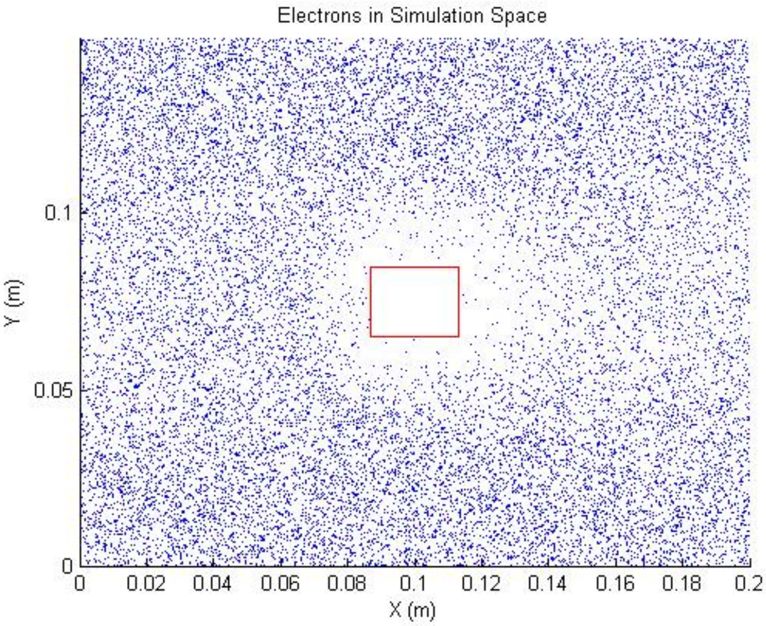

Figure 3.31: Electrons in Simulation Space After 60 nA of Negative Particle Emission

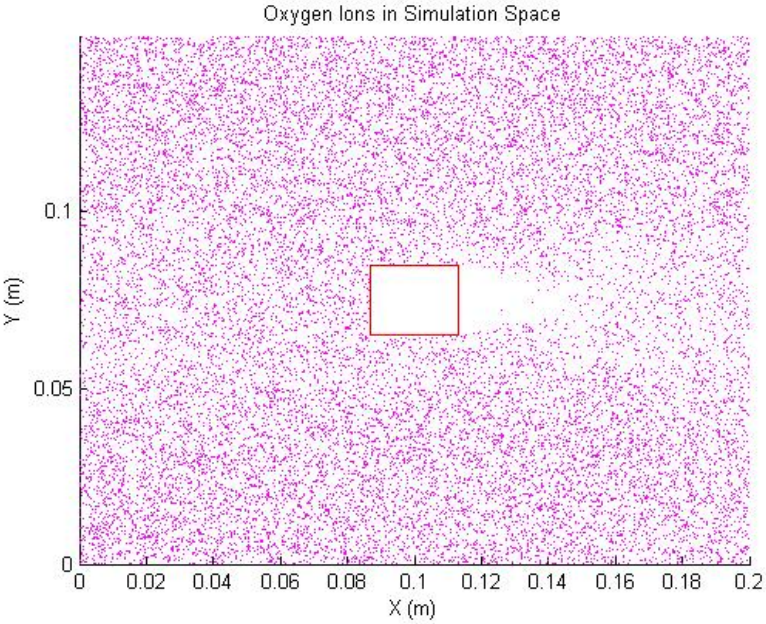

Figure 3.32: Oxygen Ions in Simulation Space Prior to 60 nA of Negative Particle Emission

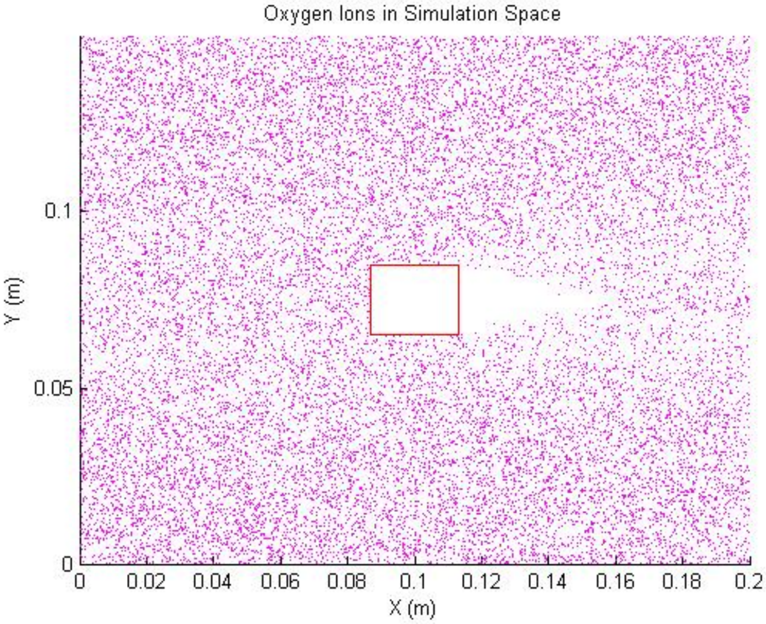

Figure 3.33: Oxygen Ions in Simulation Space After 60 nA of Negative Particle Emission

Fig. 3.34 and Fig. 3.35 show the electric potential across the simulation space immediately before and after negative particle emission. The shape of the electric potential does not change much due to negative particle emission, but there is a slight drop in spacecraft potential due to electrons continuing to impact the spacecraft, but the ambient potential continues to drop as well, causing the spacecraft floating potential to hold steady.

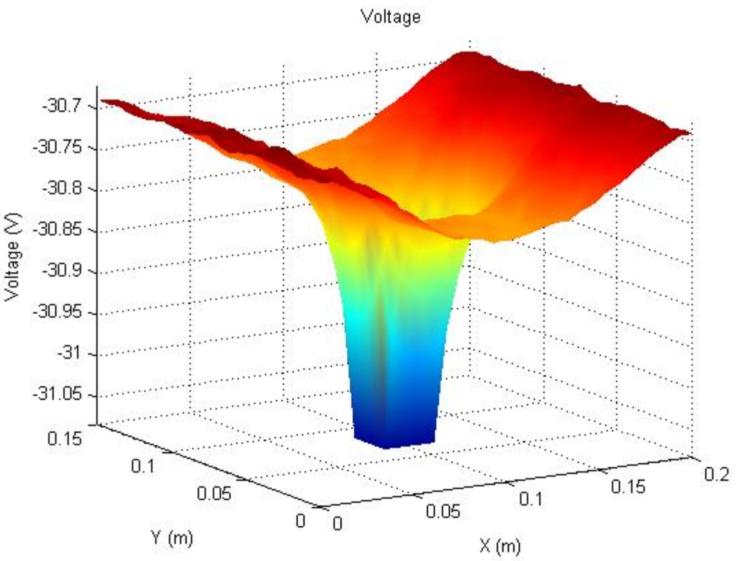

Figure 3.34: Electric Potential Across the Simulation Space Prior to 60 nA of Negative Particle Emission

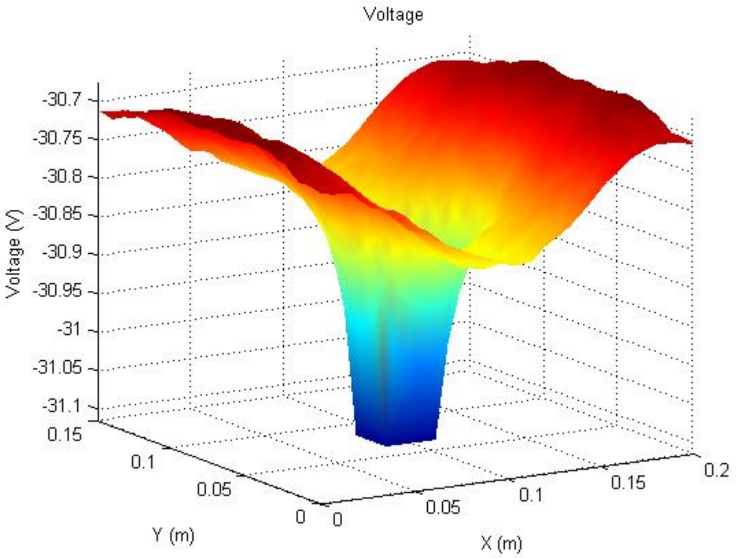

Figure 3.35: Electric Potential Across the Simulation Space After 60 nA of Negative Particle Emission

Fig. 3.36 and Fig. 3.37 show the electric field magnitude in the X direction and

Fig. 3.38 and Fig. 3.39 show the electric field magnitude in the Y direction immediately before and after negative particle emission. These figures show no real change between the electric field magnitudes before and after emission.

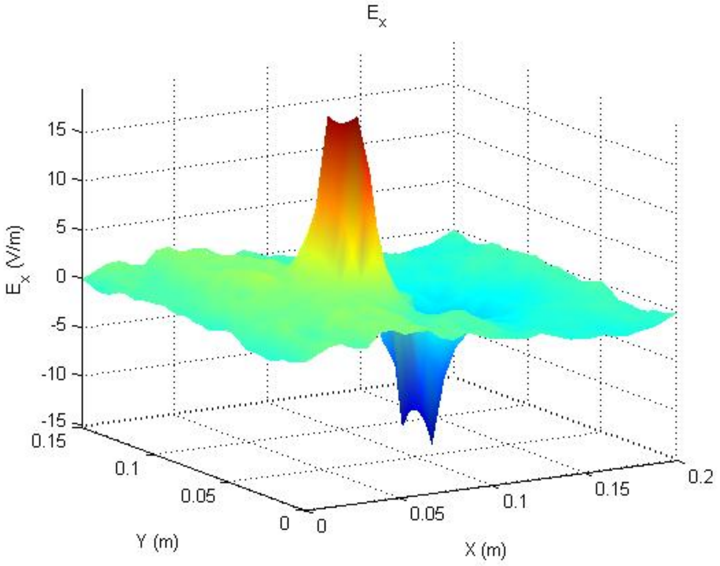

Figure 3.36: Electric Field Magnitude in X Direction Across the Simulation Space Prior to 60 nA of Negative Particle Emission

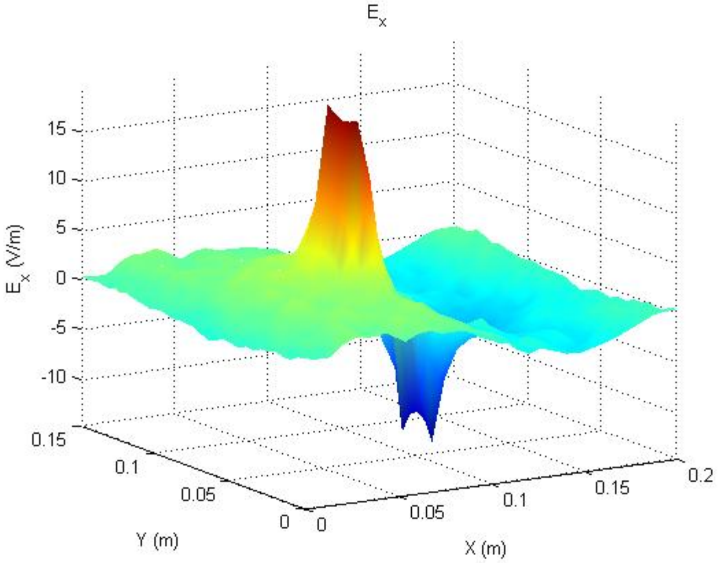

Figure 3.37: Electric Field Magnitude in X Direction Across the Simulation Space After 60 nA of Negative Particle Emission

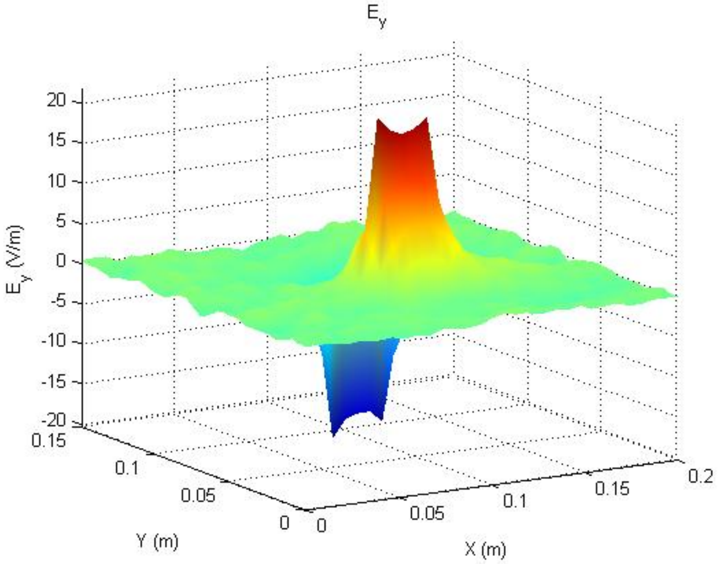

Figure 3.38: Electric Field Magnitude in Y Direction Across the Simulation Space Prior to 60 nA of Negative Particle Emission

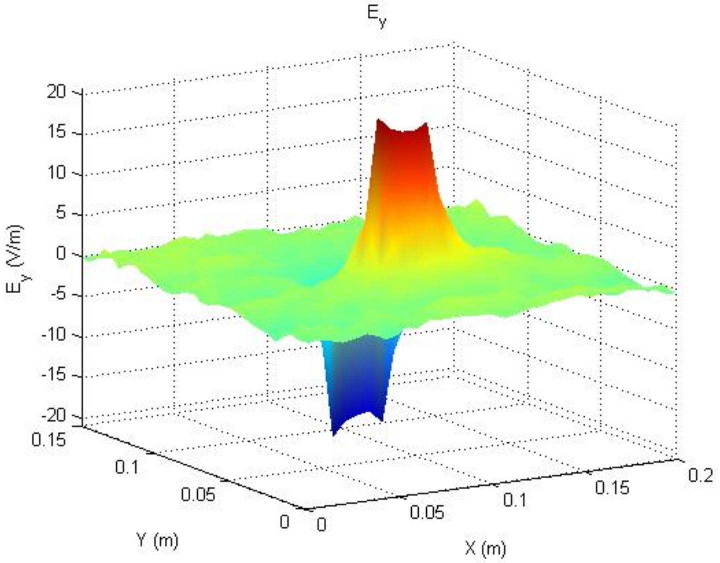

Figure 3.39: Electric Field Magnitude in Y Direction Across the Simulation Space After 60 nA of Negative Particle Emission

Thus, when the emission current is as low as 60 nA, it can easily be neutralized by the surrounding plasma. More generally, when the surrounding plasma is not significantly disturbed by the emitted beam, the plasma is more than capable of neutralizing the emitted beam as well as allowing the spacecraft to reach steady state.

Next, higher current levels are considered. An approximation for the maximum continuous current able to be emitted from a CubeSat is 312.5 μA (50% duty cycle with 25 W of power, and 40 kV of voltage) which is still many orders of magnitude less than space charge limit. This emitted current will be emitted with a specific impulse of 1000 seconds, along with the base case for the plasma parameters.

Fig. 3.40 shows the emission of the 312.5 μA of current after 6 μs, which looks identical to the 60 nA of negative particle emission current in Fig. 3.29 because although the emission current is 5000 times higher, the simulated particle to real particle ratio has also increased by 5000 times. However, the electrons and oxygen ions in the simulation space show drastic changes after this higher current level of negative particle emission.

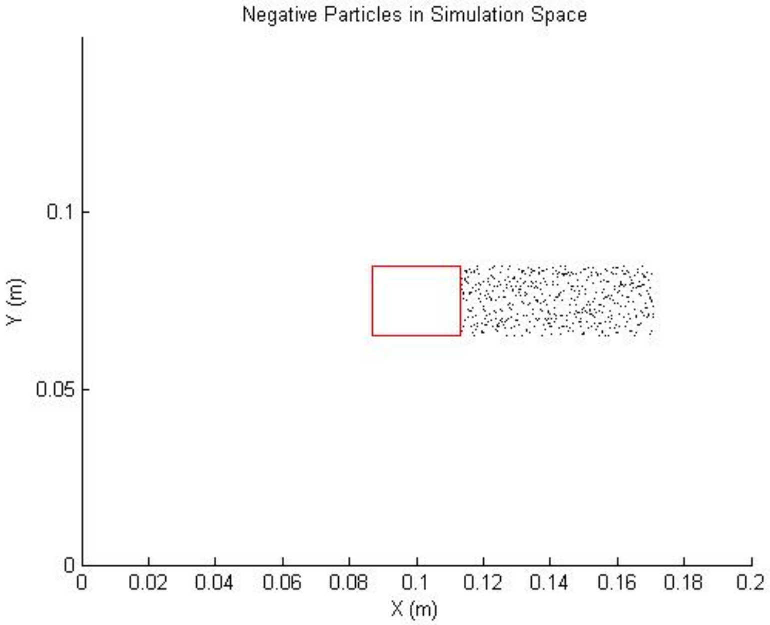

Figure 3.40: 312.5 μA Emission of Negative Particles into Ambient Plasma

Fig. 3.41 and Fig. 3.42 show the electrons in the simulation space immediately before and after the 312.5 μA of negative particle emission. Fig. 3.41 shows the typical electron simulation space around the spacecraft with the sheath in all directions; however, the electron simulation space after the 6 μs of negative particle emission shows a marked difference in Fig. 3.42. The electrons in this case have partially vacated the right side of the simulation space beyond the spacecraft and have migrated over to the left side of the simulation space. The emitted negative particles immediately behind the spacecraft have caused the fast and mobile electrons to vacate the area occupied by the negative particles, not only that but they exhibit such a strong electric field that all electrons to the right of the spacecraft migrate to the left of the spacecraft. This is partially an artifact of the periodic boundaries as any electrons that are expelled off the right side of the simulation space reappear on the left side due to the periodic boundaries and reach steady state in that position and thus a limitation of the simulation.

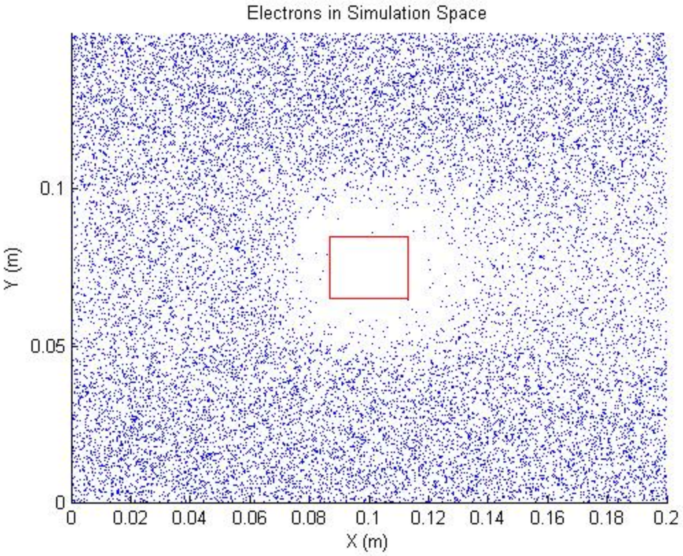

Figure 3.41: Electrons in Simulation Space Prior to 312.5 μA of Negative Particle Emission

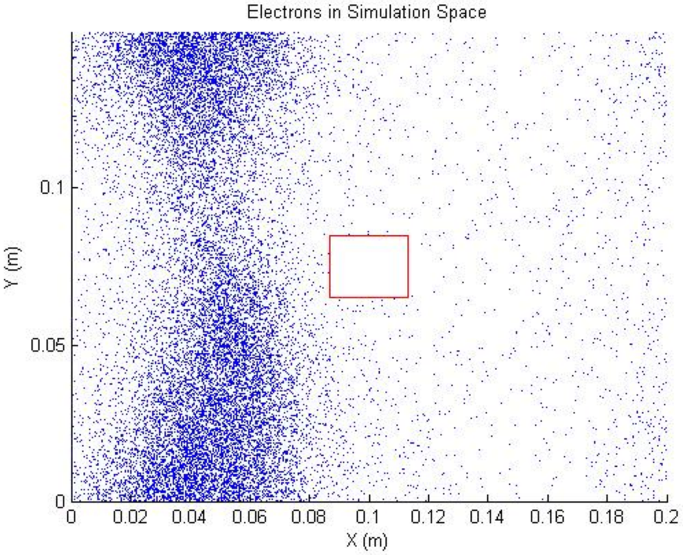

Figure 3.42: Electrons in Simulation Space After 312.5 μA of Negative Particle Emission

Fig. 3.43 and Fig. 3.44 show the oxygen ions in the simulation space immediately before and after the 312.5 μA of negative particle emission. Fig. 3.43 shows the typical oxygen ion simulation space around the spacecraft with the oxygen ions flowing up against the spacecraft in three directions and a large ion wake; however, the oxygen ion simulation space after the 6 μs of negative particle emission shows a marked difference in Fig. 3.44. The oxygen ions have started to be pulled into the area where the negatively emitted particles reside and the cluster of oxygen ions resides at the leading edge of the negative emission beam and move with that leading edge. Even though the oxygen ions are heavy and thus not very mobile, the large electric field generated by the negatively emitted particles are still able to create substantial movement in the oxygen ions, even with the ions flowing by the spacecraft at 7500 m/s in this case. The negative particles at this simulation time go out to approximately 0.17 m in the X direction, and thus the oxygen ions overlap with the negative particles as expected. The oxygen ions accumulate at the leading edge of the negative particle beam as there is a strong electric field (on the order of 1 kV/m) that points from both X directions to the leading edge of the beam. This electric field due to the negative particles is about 50 times higher than the normal electric field due to the flowing plasma without negative particle emission.

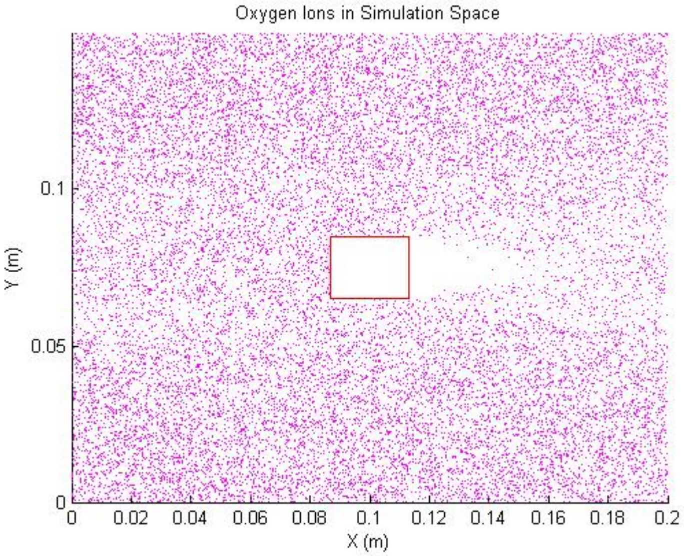

Figure 3.43: Oxygen Ions in Simulation Space Prior to 312.5 μA of Negative Particle Emission

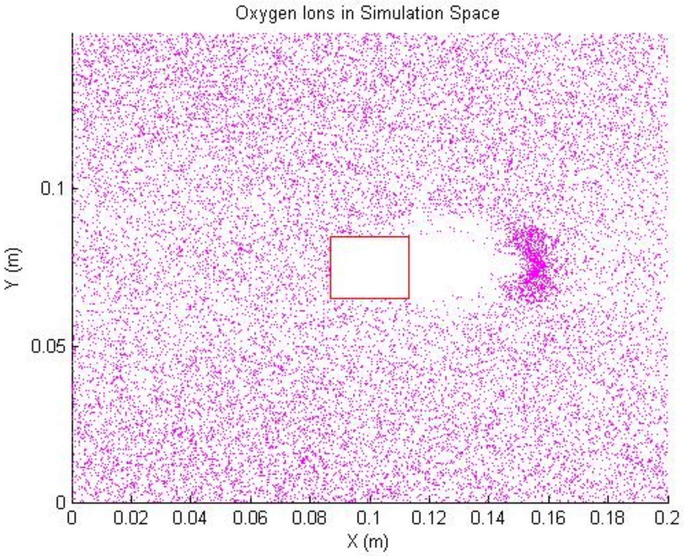

Figure 3.44: Oxygen Ions in Simulation Space After 312.5 μA of Negative Particle Emission

Fig. 3.45 and Fig. 3.46 show the electric field magnitude in the X direction immediately before and after the 312.5 μA of negative particle emission. Fig. 3.45 shows the typical electric field magnitudes in the X direction across the simulation space around the spacecraft with the electric fields pointing towards the spacecraft from the left and right sides as the spacecraft is negatively charged; however, after the 6 μs of negative particle emission, the electric field in the X direction shows a marked difference as seen in Fig. 3.46. The electric fields at this point are still pointing towards the spacecraft but at relatively small magnitudes and thus not very visible. Instead, the large electric field magnitudes are pointing towards the negatively charged beam from both the spacecraft as well as the region to the right of the emitted beam. The electric field magnitudes pointing towards the negatively charged beam are on the order of 1000 V/m which is approximately 50 times higher than the electric fields that were pointing towards the spacecraft prior to negative particle emission.

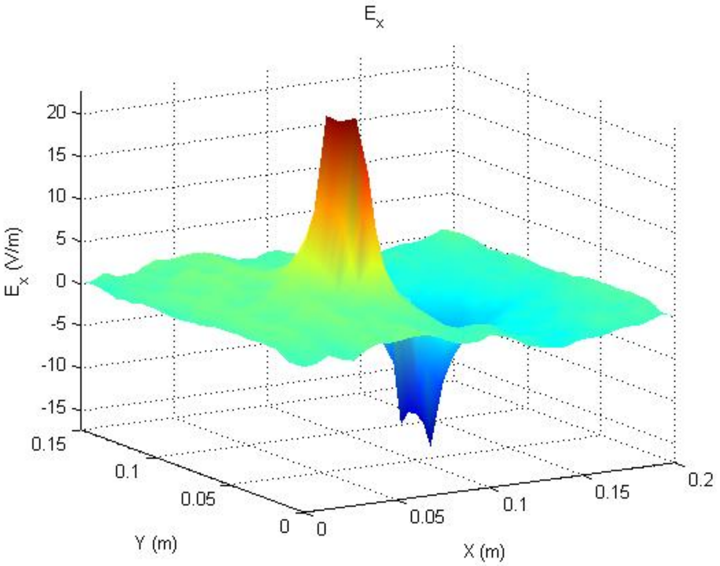

Figure 3.45: Electric Field Magnitude in X Direction Across the Simulation Space Prior to 312.5 μA of Negative Particle Emission

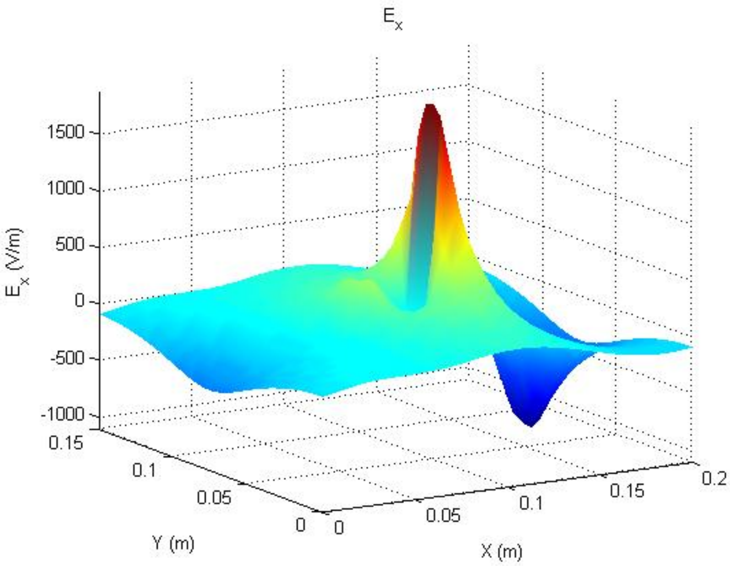

Figure 3.46: Electric Field Magnitude in X Direction Across the Simulation Space After 312.5 μA of Negative Particle Emission

Fig. 3.47 and Fig. 3.48 show the electric field magnitude in the Y direction immediately before and after the 312.5 μA of negative particle emission. Fig. 3.47 shows the typical electric field magnitudes in the Y direction across the simulation space around the spacecraft with the electric fields pointing towards the spacecraft from the top and bottom sides as the spacecraft is negatively charged; however, the electric field magnitude in the Y direction across the simulation space after the 6 μs of negative particle emission shows a marked difference in Fig. 3.48. The electric fields at this point are still pointing towards the spacecraft at relatively small magnitudes, and now the large electric field magnitudes are pointing towards the negatively charged beam from above and below the negatively charged beam. The electric field magnitudes pointing towards the negatively charged beam are on the order of 1000 V/m which is approximately 50 times higher than the electric fields that were pointing towards the spacecraft prior to negative particle emission.

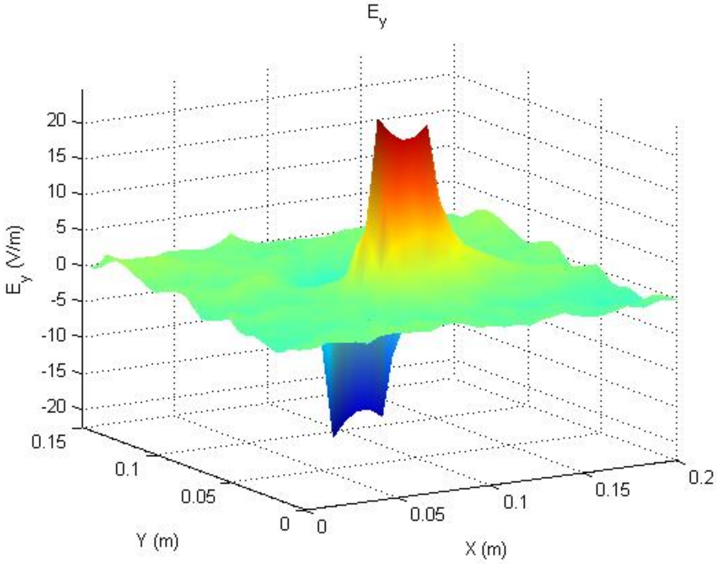

Figure 3.47: Electric Field Magnitude in Y Direction Across the Simulation Space Prior to 312.5 μA of Negative Particle Emission

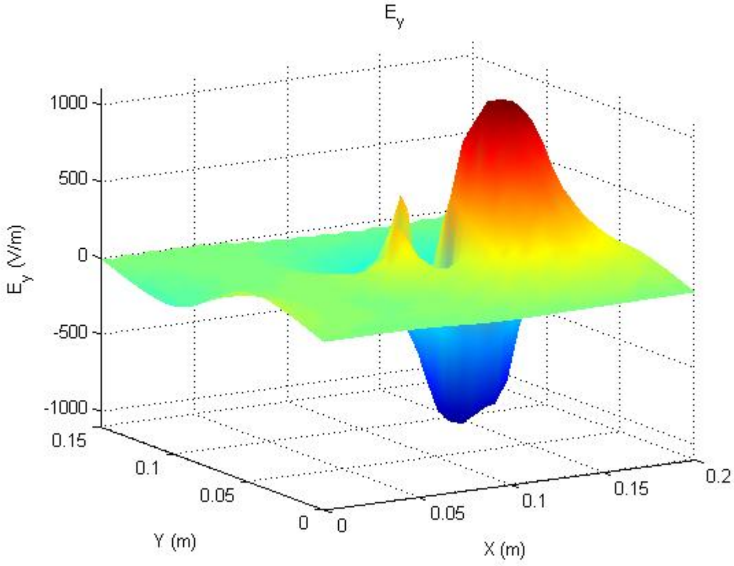

Figure 3.48: Electric Field Magnitude in Y Direction Across the Simulation Space After 312.5 μA of Negative Particle Emission

Fig. 3.49 and Fig. 3.50 provide a good perspective of the electric field vectors around the negative particle beam. There is an obvious shift in electric field vectors from pointing completely towards the spacecraft to pointing towards the negatively charged beam from all directions. Since the spacecraft is becoming as positively charged as there is charge in the negative beam, the largest electric fields will be pointing from the positively charged spacecraft to the negatively charged particle beam. In addition, the electric fields on the non-wake side walls are very small. With the electric field vectors pointing towards the negatively charged beam, the positively charged oxygen ions will move towards the negatively charged beam, and the electrons will vacate the area very quickly.

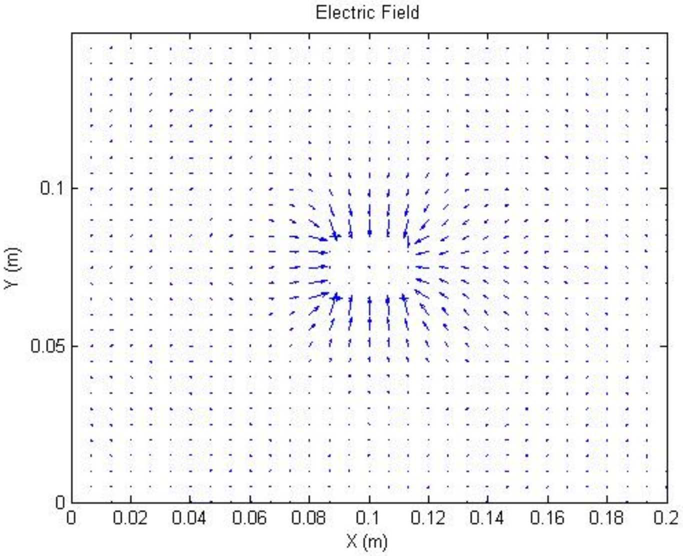

Figure 3.49: Electric Field Vectors Across the Simulation Space Prior to 312.5 μA of Negative Particle Emission

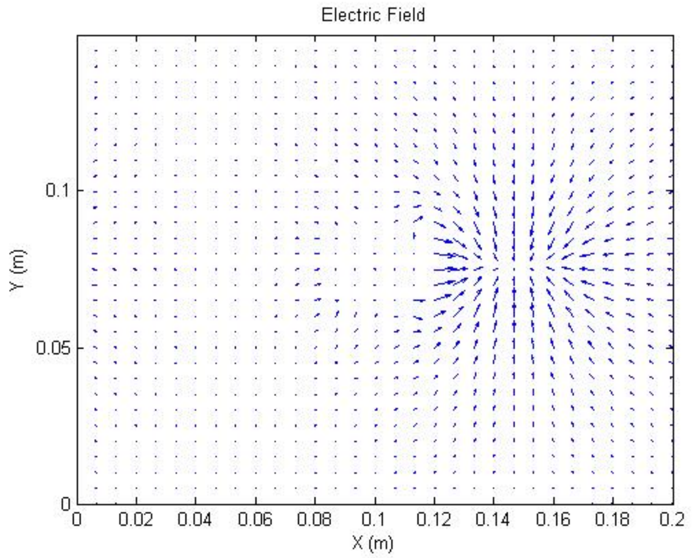

Figure 3.50: Electric Field Vectors Across the Simulation Space After 312.5 μA of Negative Particle Emission

3.5.2 Negative Particle Velocity With and Without Background Plasma

In order to see what role the ambient plasma serves in neutralizing the spacecraft and the negative particle beam, it is imperative to compare the above cases with the case of a beam being emitted into vacuum to determine the ability of the ambient plasma to neutralize the emitted beam by comparing it to emission into vacuum. First explored is whether there is the same drop in particle velocity with and without ambient plasma. As was explained in Section 2.4.1, a drop in particle velocity in the X direction corresponds to a loss in generated thrust. If the presence of the ambient plasma is able to decrease the drop in particle velocity, that means it is able to recover some of the lost thrust. Ideally, the electrons will completely vacate the area that the negatively charged particle beam inhabits, and the positively charged ions will inundate the area, making this region net neutral. This would negate any electric field pointing towards the area occupied by the negatively charged particle beam, and thus there would be no force due to the axial electric field pulling back on the emitted beam, and no reactionary force pulling back on the spacecraft and there will be no thrust lost.

The drop in velocity with and without ambient plasma will be examined as emission parameters (emission current and specific impulse) and plasma parameters (drift velocity, plasma density, and plasma temperature) are varied to determine if the plasma has a strong enough effect to negate the loss in thrust when a singly charged beam is emitted.

As will be seen in the following figures (Fig. 3.51 - Fig. 3.73), at times the velocity will look discretized or quantized which is a result of the analysis rather than a simulation result. When data from the simulations is exported into a text file, only six significant digits can be exported, thus any value under 10000 m/s will have two significant digits following the decimal point, but any value above 10000 m/s will only have a single significant digit following the decimal point.

3.5.2.1 Effect of Ambient Plasma on Thrust Lost While Varying Emission Current

Emission current will vary from 60 nA to 312.5 μA. Fig. 3.51 and Fig. 3.52 show the negative particle velocity in the X direction from 60 nA of negative particle emission with and without ambient plasma, Fig. 3.53 and Fig. 3.54 show the negative particle velocity in the X direction from 60 μA of negative particle emission with and without ambient plasma, and Fig. 3.55 and Fig. 3.56 show the negative particle velocity in the X direction from 312.5 μA of negative particle emission with and without ambient plasma.

As can be seen from the figures, there is no real difference between emission into ambient plasma and into vacuum as the minimum velocity does not change between emission into ambient plasma and into vacuum. For 60 nA emission, there is such little current being emitted that there is no discernible drop in particle velocity after emission. For 60 μA emission, the minimum velocity is 9999.9 m/s, and for 312.5 μA emission, the minimum velocity is 9999.6 m/s. All of the minimum velocities occurred at an X position of 0.1134 m.

These plots showing no difference in minimum velocity between emission into ambient plasma and emission into vacuum imply that there is no emission current at the base level plasma conditions that will cause the plasma to negate the thrust loss due to electric field effects pulling back on the spacecraft. At very low current levels, there is no discernible drop in velocity and thus the ambient plasma cannot be seen having any effect. At higher current levels, the base case ambient plasma

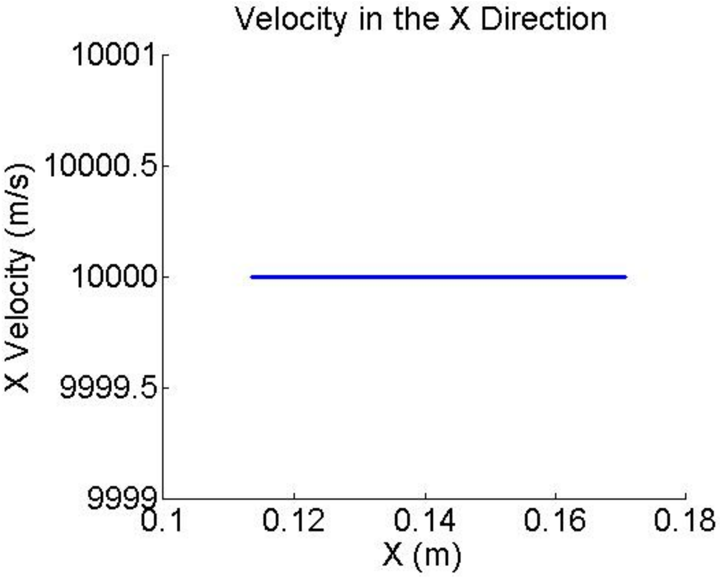

Figure 3.51: Negative Particle Velocity in the X Direction from 60 nA of Negative Particle Emission into Vacuum

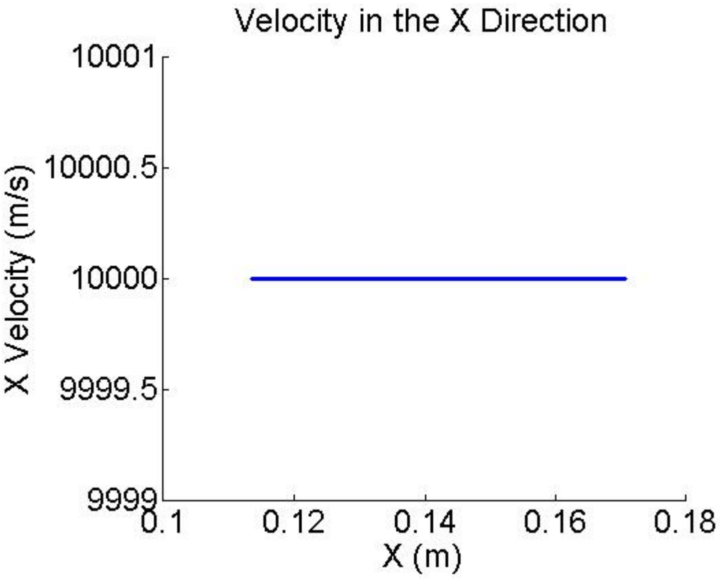

Figure 3.52: Negative Particle Velocity in the X Direction from 60 nA of Negative Particle Emission into Ambient Plasma

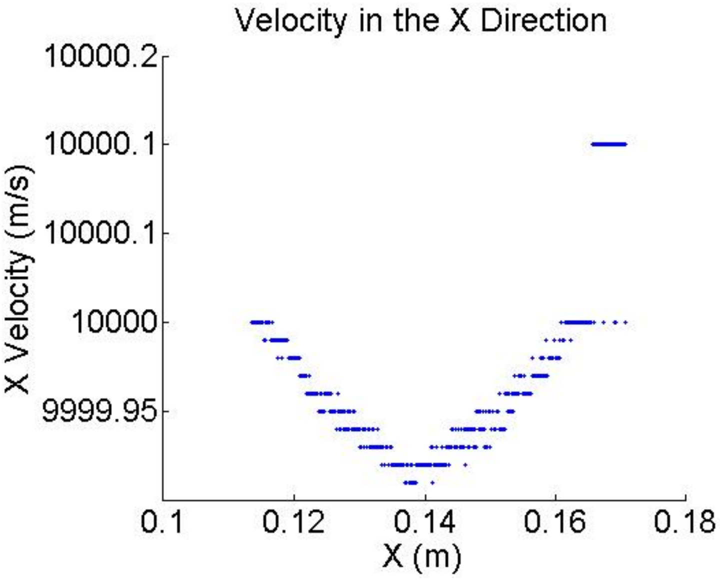

Figure 3.53: Negative Particle Velocity in the X Direction from 60 μA of Negative Particle Emission into Vacuum

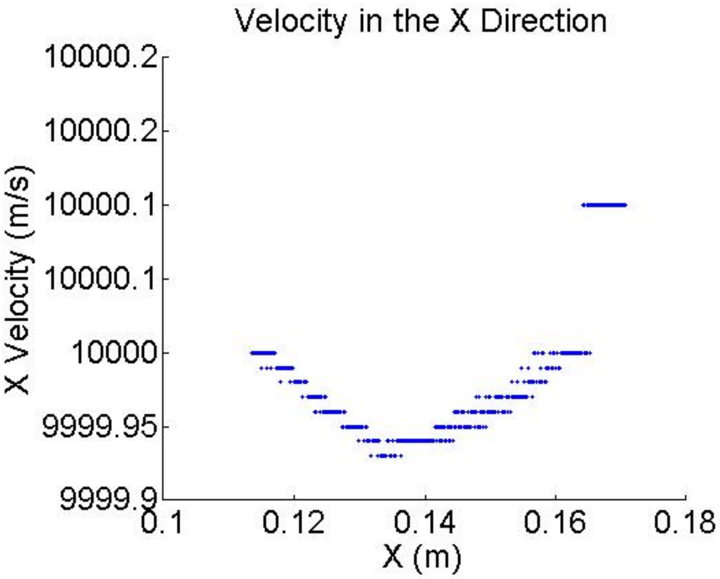

Figure 3.54: Negative Particle Velocity in the X Direction from 60 μA of Negative Particle Emission into Ambient Plasma

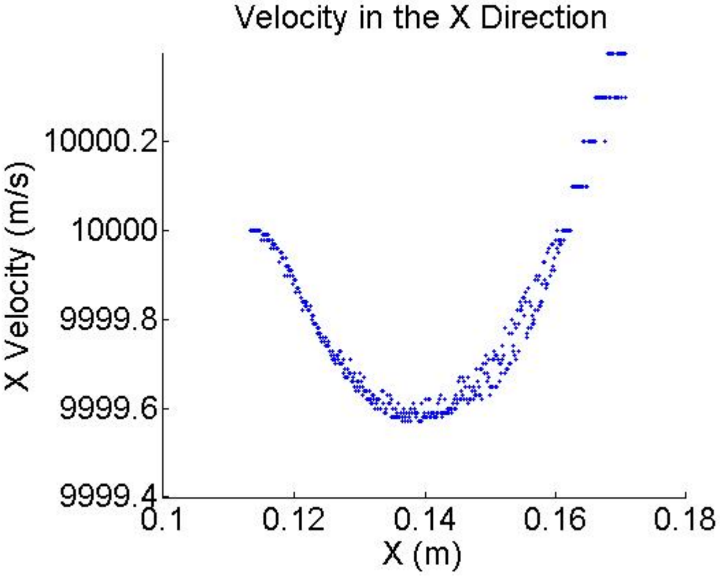

Figure 3.55: Negative Particle Velocity in the X Direction from 312.5 μA of Negative Particle Emission into Vacuum

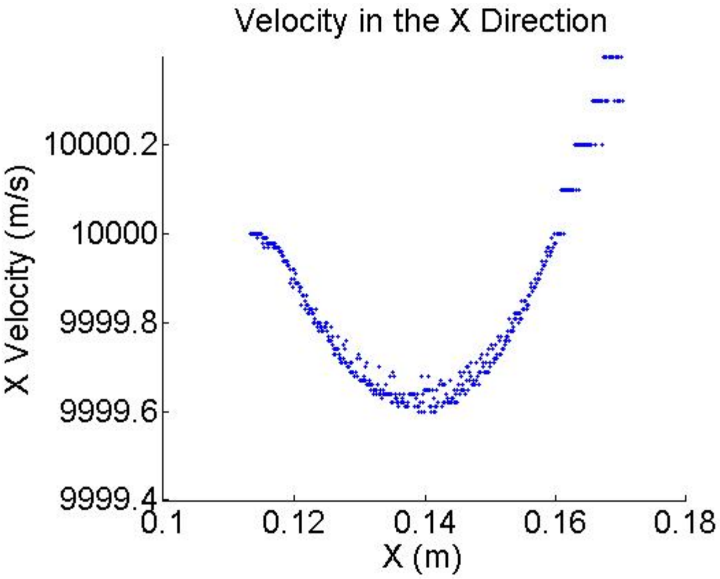

Figure 3.56: Negative Particle Velocity in the X Direction from 312.5 μA of Negative Particle Emission into Ambient Plasma

3.5.2.2 Effect of Ambient Plasma on Thrust Lost While Varying Specific Impulse

Specific impulse will vary from 100 seconds to 2000 seconds for the thrusters being examined (NanoFET and colloidal thrusters). In order to vary specific impulse, the velocity of the negative particles being emitted is varied as shown in Eq. 3.40. This causes the number of particles being emitted to change as well due to Eq. 3.3, and thus the simulated particle to real particle ratio needs to be changed as well. In addition, for the emitted beam to reach the same point in the simulation space, the number of time steps to be run will change as well.

$$v_e = g_0 I_{sp} \tag{3.40}$$

Fig. 3.57 and Fig. 3.58 show the negative particle velocity in the X direction when 312.5 μA of negative particle current at 100 seconds specific impulse is emitted into vacuum and ambient plasma. When emitting into vacuum, the minimum X velocity drops to 954.387 m/s, but when emitting into the ambient plasma, the minimum X velocity drops to 957.713 m/s. The drop in velocity is decreased by 7.3% when emitting into ambient plasma, thus there is a slight negation of lost thrust from the ambient plasma at 100 seconds specific impulse due to the oxygen ions neutralizing a portion of the emitted negative particles.

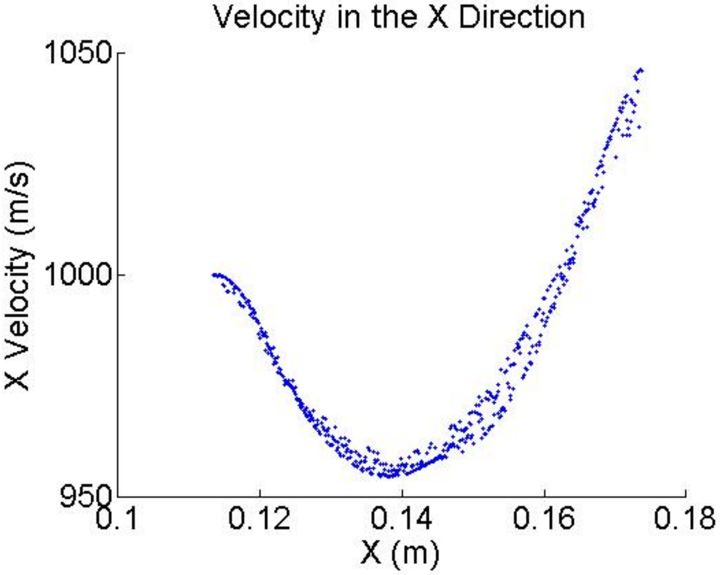

Figure 3.57: Negative Particle Velocity in the X Direction of 312.5 μA of Negative Particle Emission with Specific Impulse of 100 s into Vacuum

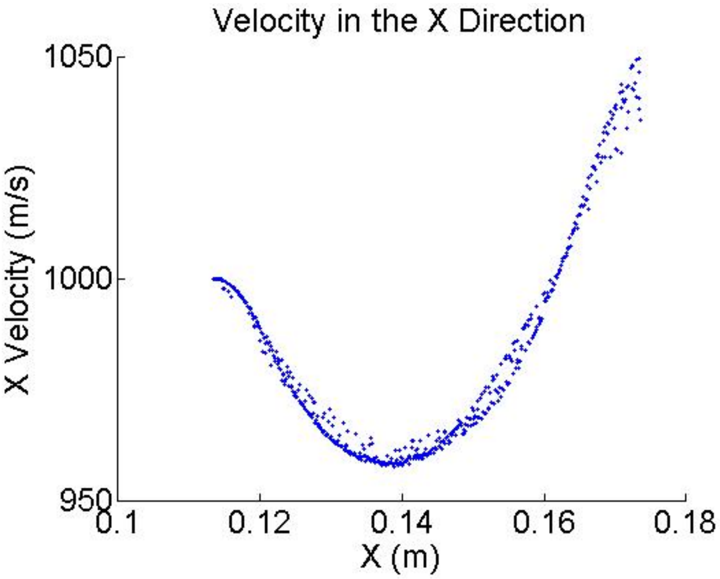

Figure 3.58: Negative Particle Velocity in the X Direction of 312.5 μA of Negative Particle Emission with Specific Impulse of 100 s into Ambient Plasma

Fig. 3.59 and Fig. 3.60 show the negative particle velocity in the X direction when 312.5 μA of negative particle current at 500 seconds specific impulse is emitted into vacuum and ambient plasma. When emitting into vacuum, the minimum X velocity drops to 4998.2 m/s, but when emitting into the ambient plasma, the minimum X velocity drops to 4998.9 m/s. The drop in velocity is decreased by 38.9% when emitting into ambient plasma, thus there is a significant negation of lost thrust from the ambient plasma at 500 seconds specific impulse due to the oxygen ions neutralizing a portion of the emitted negative particles.

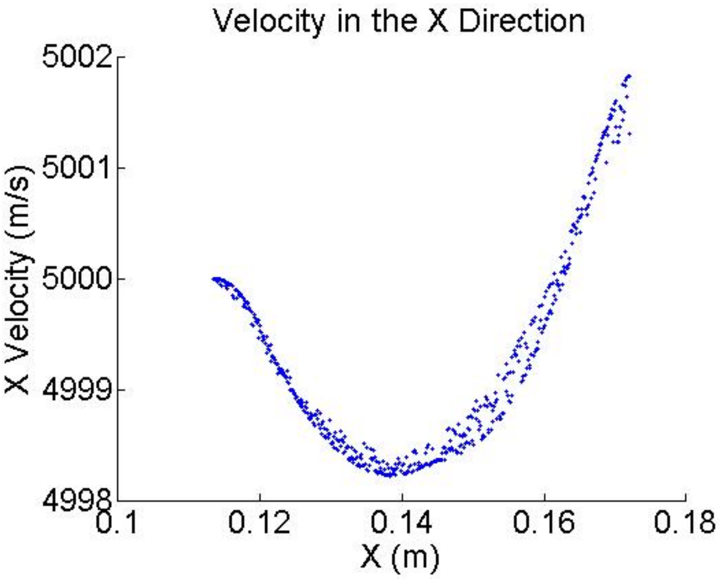

Figure 3.59: Negative Particle Velocity in the X Direction of 312.5 μA of Negative Particle Emission with Specific Impulse of 500 s into Vacuum

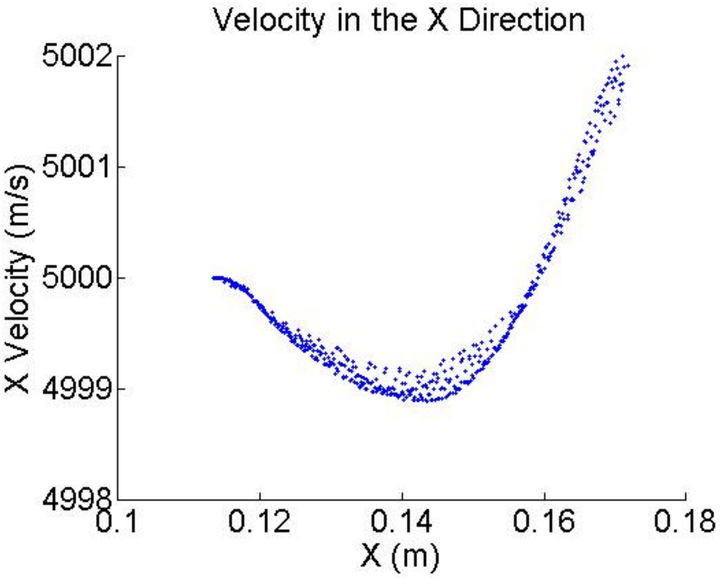

Figure 3.60: Negative Particle Velocity in the X Direction of 312.5 μA of Negative Particle Emission with Specific Impulse of 500 s into Ambient Plasma

Fig. 3.61 and Fig. 3.62 show the negative particle velocity in the X direction when

312.5 μA of negative particle current at 1000 seconds specific impulse, and Fig. 3.63 and Fig. 3.64 are for 2000 seconds specific impulse is emitted into vacuum and ambient plasma. At both of these specific impulses, there is no discernible difference between emitting into vacuum or ambient plasma.

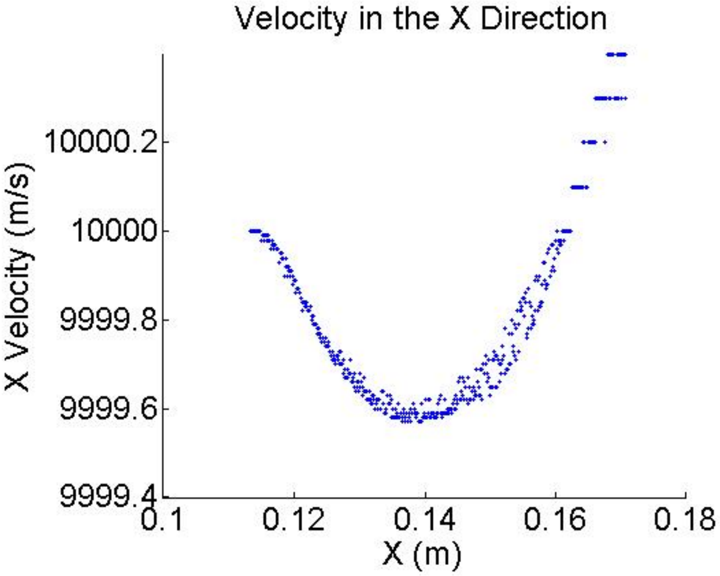

Figure 3.61: Negative Particle Velocity in the X Direction of 312.5 μA of Negative Particle Emission with Specific Impulse of 1000 s into Vacuum

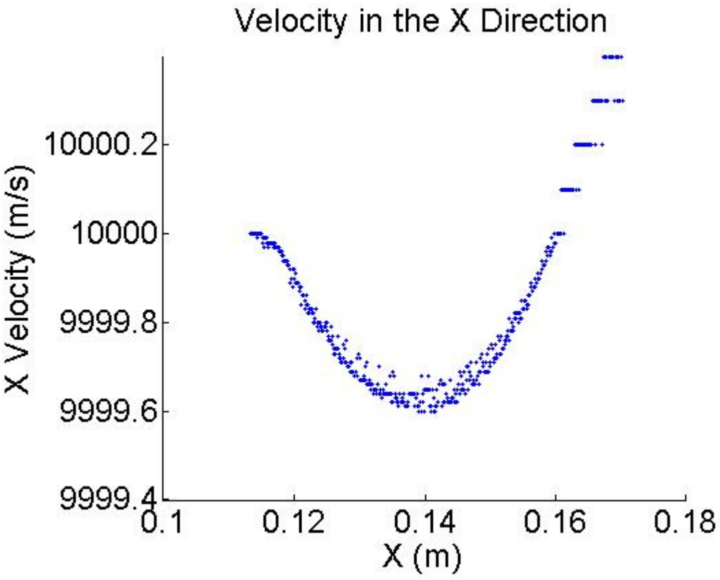

Figure 3.62: Negative Particle Velocity in the X Direction of 312.5 μA of Negative Particle Emission with Specific Impulse of 1000 s into Ambient Plasma

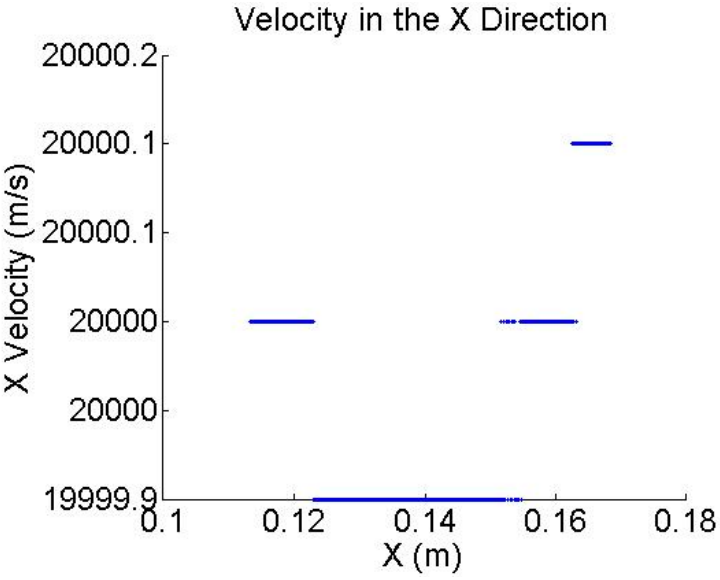

Figure 3.63: Negative Particle Velocity in the X Direction of 312.5 μA of Negative Particle Emission with Specific Impulse of 2000 s into Vacuum

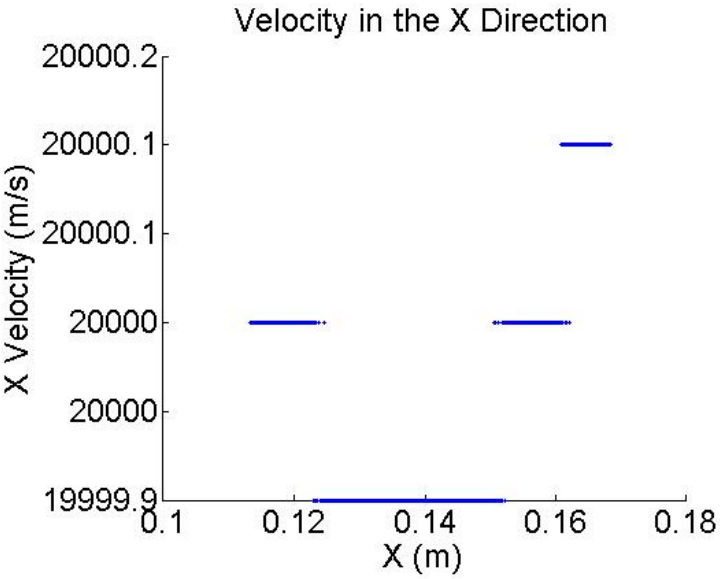

Figure 3.64: Negative Particle Velocity in the X Direction of 312.5 μA of Negative Particle Emission with Specific Impulse of 2000 s into Ambient Plasma

At lower specific impulses (100 and 500 s), the ambient plasma in the base case is able to negate at least a portion of the loss in thrust whereas at higher specific impulses (1000 and 2000 s), the ambient plasma is unable to do that. As specific impulse decreases (with current and current density staying constant), Eq. 3.3 shows that the charge density in the area of the emitted beam will increase, as in there is more charge per unit volume in the area of the emitted beam. Thus, at lower specific impulses, there is more charge which means that there is a larger axial electric field pulling back on the spacecraft. This explains why the drop in velocity increases when the specific impulse is lower.

This also shows why the ambient plasma has a larger effect when the specific impulse is lower. With a larger electric field at lower specific impulses, there is a stronger push on the electrons out of the negative beam and a stronger pull on the electrons towards the spacecraft, thereby decreasing the positive image charge on the spacecraft and allowing for some of the lost thrust to be negated.

3.5.2.3 Effect of Ambient Plasma Velocity on Thrust Lost

As was previously shown in Section 3.4.3.1, accurate simulations have been developed for varying spacecraft velocity. Thus, these validated simulations are the foundation for the simulations used to observe the difference between emitting into vacuum and emitting into ambient plasma. Simulations will be run for emission into vacuum (Fig. 3.65), for emission into plasma with the lower bound drift velocity in the ionosphere of 6800 m/s (Fig. 3.66), and for emission into plasma with the upper bound drift velocity in the ionosphere of 7900 m/s (Fig. 3.67) all with 312.5 μA of emission current.

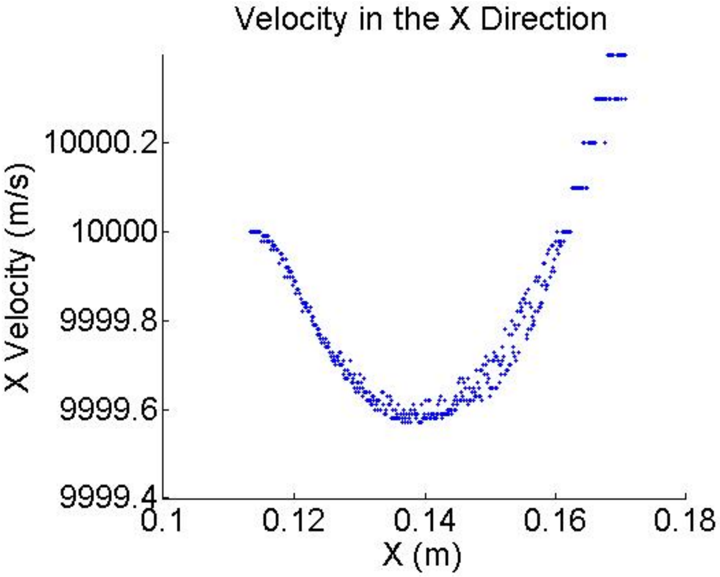

Figure 3.65: Negative Particle Velocity in the X Direction of 312.5 μA of Negative Particle Emission into Vacuum

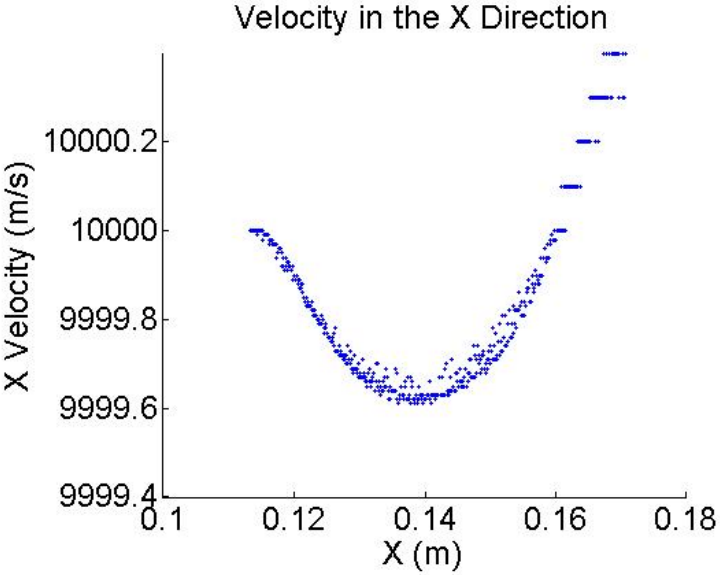

Figure 3.66: Negative Particle Velocity in the X Direction of 312.5 μA of Negative Particle Emission into Ambient Plasma with a Drift Velocity of 6800 m/s

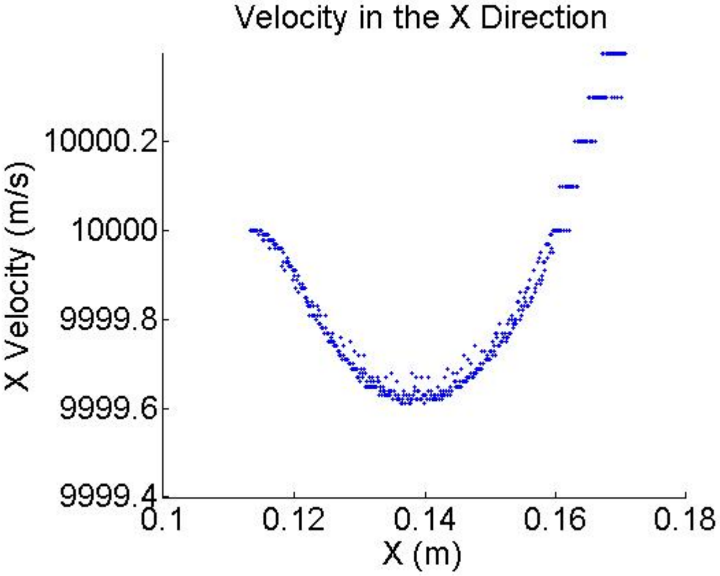

Figure 3.67: Negative Particle Velocity in the X Direction of 312.5 μA of Negative Particle Emission into Ambient Plasma with a Drift Velocity of 7900 m/s

When emitting negative particles into vacuum, there is a drop in velocity from 10000 m/s to 9999.6 m/s, and this same drop in velocity is exhibited even when negative particles are emitted into plasma throughout the ionospheric spacecraft velocity range. Thus, it appears that no matter what the spacecraft velocity is (at least within the spacecraft velocity range applicable in the ionosphere) these plasma parameters will not help neutralize the base case emission parameters.

With the relatively small spacecraft velocity range from 6800 m/s to 7900 m/s, there is not a large difference between the base case velocity and the lower and upper bounds of the range. Even at the lower and upper bounds, the spacecraft velocity is still less than the emitted particle velocity, and thus the changed spacecraft velocity will not have an effect on the ability of the ambient plasma to negate thrust.

3.5.2.4 Effect of Ambient Plasma Temperature on Thrust Lost

As was previously shown in Section 3.4.3.2, accurate simulations have been developed for varying thermal temperature. Thus, these validated simulations are the foundation for the simulations used to observe the difference between emitting into vacuum and emitting into ambient plasma. Simulations will be run for emission into vacuum (Fig. 3.68), for emission into plasma with the lower bound thermal temperature in the ionosphere of 0.08 eV (Fig. 3.69), and for emission into plasma with the upper bound thermal temperature in the ionosphere of 0.215 eV (Fig. 3.70).

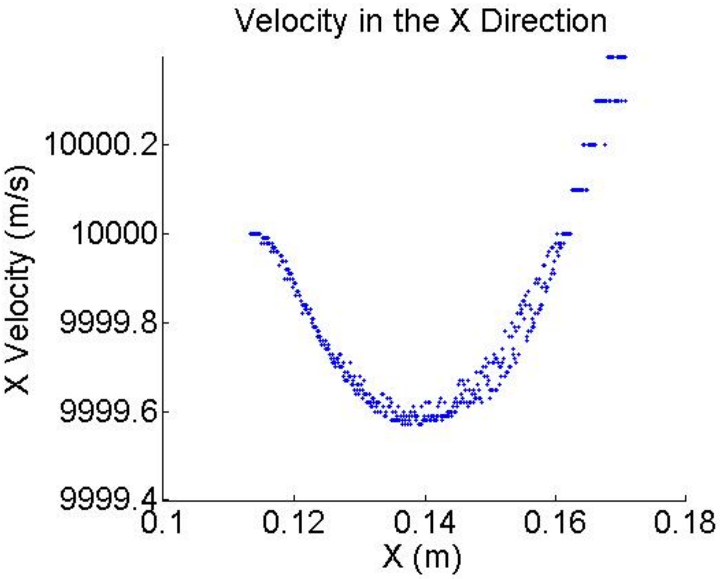

Figure 3.68: Negative Particle Velocity in the X Direction of 312.5 μA of Negative Particle Emission into Vacuum

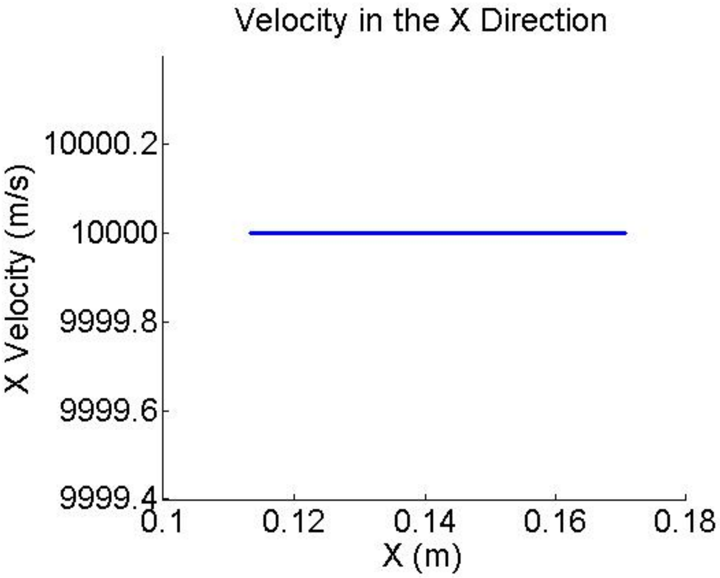

Figure 3.69: Negative Particle Velocity in the X Direction of 312.5 μA of Negative Particle Emission into Ambient Plasma with a Thermal Temperature of 0.08 eV

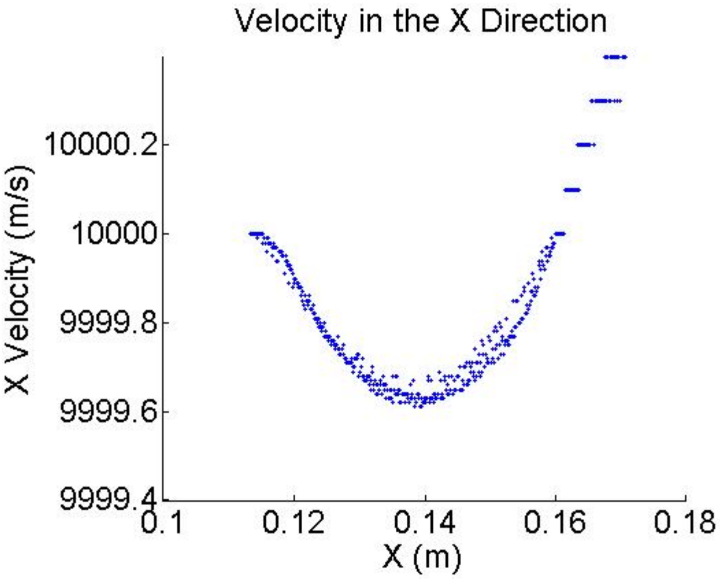

Figure 3.70: Negative Particle Velocity in the X Direction of 312.5 μA of Negative Particle Emission into Ambient Plasma with a Thermal Temperature of 0.215 eV

When emitting negative particles into vacuum, there is a drop in velocity from 10000 m/s to 9999.6 m/s, and this same drop in velocity is exhibited even when negative particles are emitted into plasma with a thermal temperature of 0.215 eV. However, when negative particles are emitted into plasma with a thermal temperature of 0.08 eV, there is no longer a drop in velocity, and it appears that the plasma is able to negate all loss in thrust by neutralizing the emitted beam and spacecraft.

This indicates that as thermal temperature of the plasma decreases past the base case of 0.1 eV, the decreased thermal temperature and decreased random movement of the electrons and ions makes it easier to neutralize the negatively charged particle beam and spacecraft. When the thermal temperature is decreased, the Debye length also decreases as shown in Eq. 3.4. This decreased Debye length means that the negatively charged beam is more easily able to be neutralized and is explained further in Section 3.5.2.5. With the more neutralized beam, the spacecraft will not have the same loss in thrust that would be exhibited if emitted into vacuum.

3.5.2.5 Effect of Ambient Plasma Density on Thrust Lost

As was previously shown in Section 3.4.3.3, accurate simulations have been developed for varying plasma density. Thus, these validated simulations are the foundation for the simulations used to observe the difference between emitting into vacuum and emitting into ambient plasma. Simulations will be run for emission into vacuum (Fig. 3.71), for emission into plasma with the lower bound plasma density in the ionosphere of 10^9 m^{-3} (Fig. 3.72), and for emission into plasma with the upper bound plasma density in the ionosphere of 10^{13} m^{-3} (Fig. 3.73).

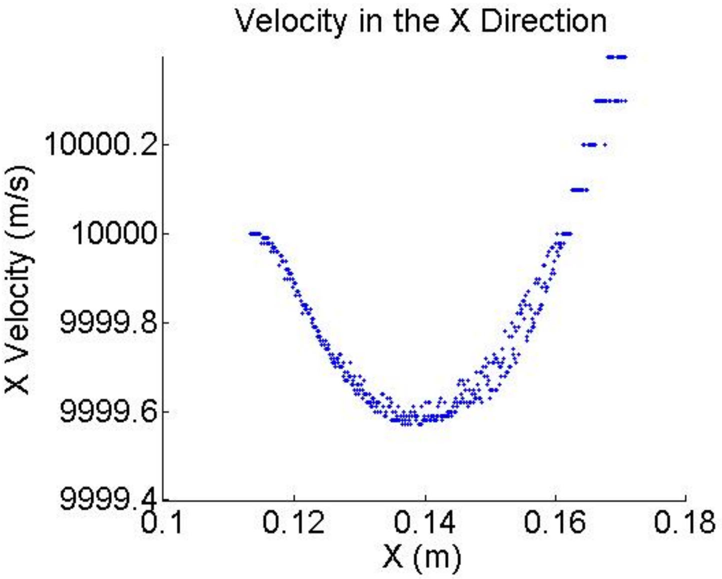

Figure 3.71: Negative Particle Velocity in the X Direction of 312.5 μA of Negative Particle Emission into Vacuum

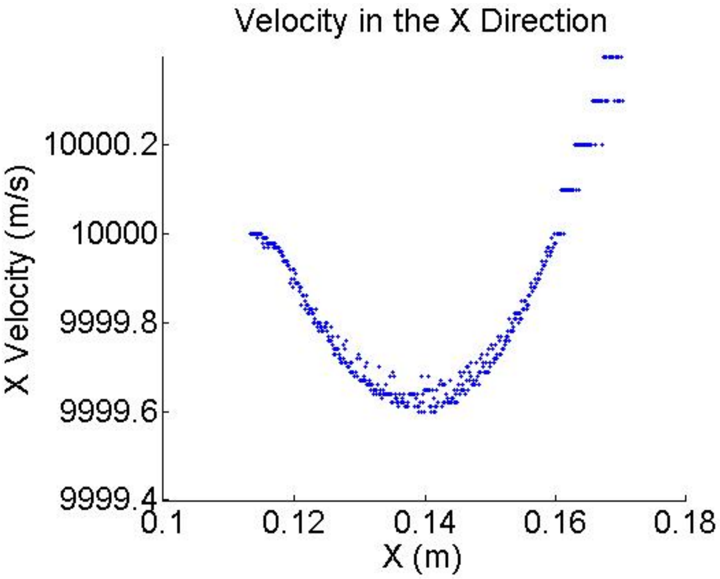

Figure 3.72: Negative Particle Velocity in the X Direction of 312.5 μA of Negative Particle Emission into Ambient Plasma with a Density of 10^9 m^{-3}

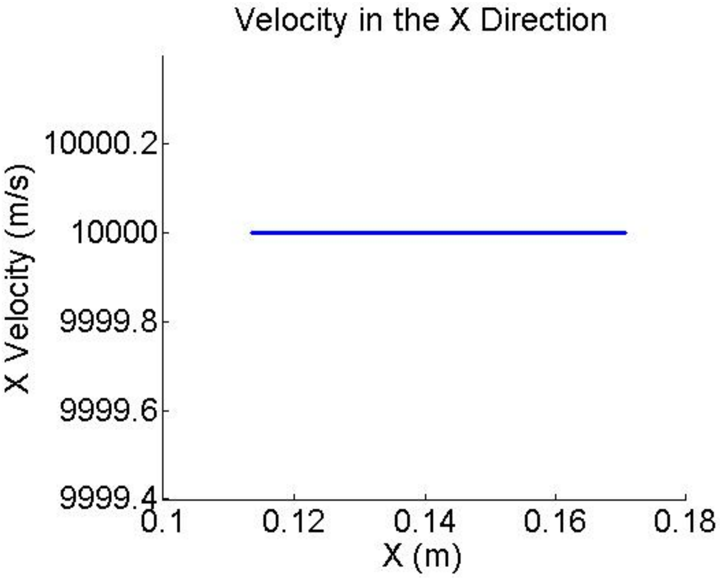

Figure 3.73: Negative Particle Velocity in the X Direction of 312.5 μA of Negative Particle Emission into Ambient Plasma with a Density of $3{\times}10^{11}$ m^{-3}

When emitting negative particles into vacuum, there is a drop in velocity from

10000 m/s to 9999.6 m/s, and this same drop in velocity is exhibited even when negative particles are emitted into plasma with a plasma density of 10^9 m^{-3}. However, when negative particles are emitted into plasma with a plasma density of 3×10^{11} m^{-3}, there is no longer a drop in velocity, and it appears that the plasma is able to negate all loss in thrust by neutralizing the emitted beam and spacecraft; however, when emitted into a plasma with plasma density of the base case of 6.5×10^{10} m^{-3} or 10^9 m^{-3}, this loss in thrust still persists and there is no benefit to emitting into plasma from a thrust standpoint.

It indicates that as the plasma density increases past the base case that the increase in electrons and ions provides an increased ability to "shield" the negative particles and thus able to neutralize the negative particles more effectively. It shows that an increase in plasma density will be more capable of neutralizing the system even if it should not have any effect on the floating potential of the spacecraft as it orbits.

Another way of looking at it is that as the plasma density increases, the Debye length will decrease, thus the length scale on which electric charges will be neutralized decreases, and thus neutralization is easier to accomplish. This corresponds with the results in Section 3.5.2.4 in that when Debye length decreases, the plasma is more capable of neutralizing the emitted beam and able to negate the loss in thrust.

3.6 Limitations of the Simulation

OOPIC PRO^{TM} has many capabilities; however, one frequently occurring problem is the crashing of the software. This often occurs when the NP2C number is too low, which causes the simulation to attempt to track too many particles and perform too many calculations. However, when the NP2C number is too high, there are too few particles in the simulation space, resulting in the simulation not having high fidelity. Through numerous simulations it has been established that when there is a source rate (and accompanying load density, with a relationship as shown in Eq. 3.13) that is 10^{12} times larger than the NP2C number, the simulation no longer is able to handle the high number of superparticles that must be tracked, providing a lower bound for the NP2C number as is shown in Eq. 3.41.

$$\frac{r}{NP2C} < 10^{12} \tag{3.41}$$

On the other end of the spectrum, the NP2C number cannot be so large for a given source rate and load density that the physics are skewed by combining too many real particles into a single superparticle. Thus, there should be a maximum NP2C number for a given load density and source rate. This maximum NP2C value is found by examining steady state plasma densities for a given source rate, with this relationship having been previously defined in Fig. 3.5. For the higher NP2C values, the calculated steady state plasma density will deviate from the expected steady state plasma density, which was able to predict 99.8% of the variance. Thus, for a given source rate, if the calculated steady state plasma density deviates from the expected steady state plasma density by more than 5%, that is deemed an inaccurate simulation. Table 3.2 shows what combinations of NP2C values and source rates will provide running simulations as well as physically accurate results.

NP2C ($\times 10^4$) Source Rate	1	2.5	5	10	20	30	40	50	60	70	80	100
1.125×10^{15}	🟦	🟦	🟦	🟦	🟦	🟦	🟦	🟦	🟦	🟦	🟦	🟦
2.25×10^{15}	🟦	🟦	🟦	🟦	🟦	🟦	🟦	🟦	🟦	🟦	🟦	🟦
2.8125×10^{15}	🟦	🟦	🟦	🟦	🟦	🟦	🟦	🟦	🟦	🟦	🟦	🟦
3.75×10^{15}	🟦	🟦	🟦	🟦	🟦	🟦	🟦	🟦	🟦	🟦	🟦	🟦
5.625×10^{15}	🟦	🟦	🟦	🟦	🟦	🟦	🟦	🟦	🟦	🟦	🟦	🟦
6.75×10^{15}	🟦	🟦	🟦	🟦	🟦	🟦	🟦	🟦	🟦	🟦	🟦	🟥
9×10^{15}	🟦	🟦	🟦	🟦	🟦	🟦	🟦	🟦	🟦	🟦	🟥	🟥
1.125×10^{16}	🟥	🟦	🟦	🟦	🟦	🟦	🟦	🟦	🟦	🟥	🟥	🟥
1.35×10^{16}	🟥	🟦	🟦	🟦	🟦	🟦	🟦	🟥	🟥	🟥	🟥	🟥
1.575×10^{16}	🟥	🟦	🟦	🟦	🟦	🟦	🟦	🟥	🟥	🟥	🟥	🟥
1.8×10^{16}	🟥	🟦	🟦	🟦	🟦	🟦	🟥	🟥	🟥	🟥	🟥	🟥
2.025×10^{16}	🟥	🟦	🟦	🟦	🟦	🟦	🟥	🟥	🟥	🟥	🟥	🟥
2.25×10^{16}	🟥	🟥	🟦	🟦	🟦	🟥	🟥	🟥	🟥	🟥	🟥	🟥
3.375×10^{16}	🟥	🟥	🟦	🟦	🟥	🟥	🟥	🟥	🟥	🟥	🟥	🟥
4.5×10^{16}	🟥	🟥	🟦	🟦	🟥	🟥	🟥	🟥	🟥	🟥	🟥	🟥
5.625×10^{16}	🟥	🟥	🟥	🟥	🟥	🟥	🟥	🟥	🟥	🟥	🟥	🟥
1.125×10^{17}	🟥	🟥	🟥	🟥	🟥	🟥	🟥	🟥	🟥	🟥	🟥	🟥

Table 3.2: Limitations of the Simulation: Relationship Between Source Rate and NP2C Values that Provide Feasible Simulations and Acceptable Results (Blue Squares Indicate Acceptable NP2C and Source Rate, Red Squares Indicate Unacceptable NP2C and Source Rate, Lower Left Red Squares Due to Too Small of NP2C Values Resulting in Non-Running Simulations, Lower Right Red Squares Due to Too Large of NP2C Values Resulting in Inaccurate Results

The blue squares all indicate acceptable combinations of source rates and NP2C values, with the red squares indicating unacceptable combinations. The red squares in the lower left of the chart are unacceptable as the simulations do not run as the NP2C values are too small for the source rates, and thus there are too many superparticles in the simulation space to be simulated. The red squares in the lower right of the chart are unacceptable as the NP2C values are too large and thus the solutions are inaccurate. Thus, it is possible to have source rates that are too large to have any acceptable NP2C value in this case. In order to accurately simulate such high source rates, the computing power needs to be increased to allow the simulation to run properly, or some loss of accuracy must be acceptable.

The relationship between source rate and NP2C value for the simulations that do not run has been established previously in Eq. 3.41. The relationship between source rate and NP2C value for inaccurate simulations is shown in Fig. 3.74.

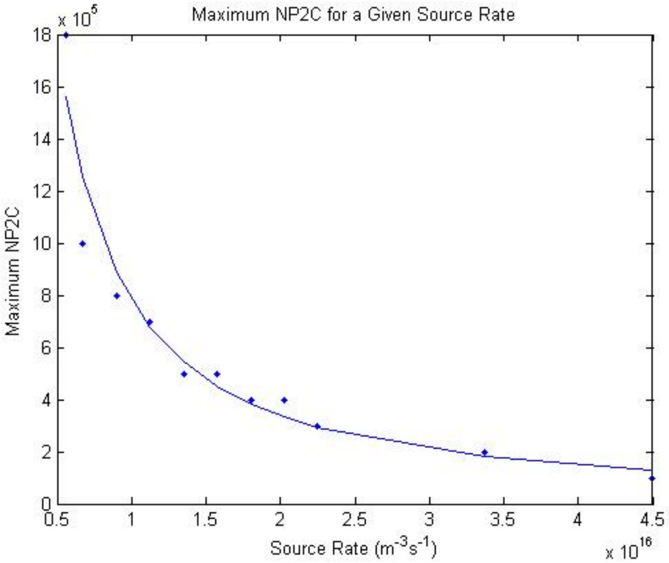

Figure 3.74: Sample Number of Superparticles of Electrons and Atomic Oxygen Ions

Fig. 3.74 shows the simulated maximum NP2C values, as well as a power equation best fit, which accounts for 93.82% of the variance in the best fit Eq. 3.42, which is close to a simpler equation of Eq. 3.43.

$$NP2C < 1.6805 \cdot 10^{25} \cdot r^{-1.2084} \tag{3.42}$$

$$NP2C < \frac{1.6805 \cdot 10^{25}}{r} \tag{3.43}$$

Thus, in the simulations conducted, the NP2C value will be carefully selected to abide by the lower and upper bounds established by the source rate and Eq. 3.41 and Eq. 3.43.

3.7 Summary

Another perceived option for neutralization of a spacecraft orbiting in the ionosphere, other than emission of equal amounts of positive and negative particle emission as was shown in Chapter II, is the utilization of the ambient plasma in the ionosphere to achieve the neutralization of the spacecraft and the emitted beam.

The floating potential of a spacecraft orbiting in the ionosphere was able to be analytically determined for a range of plasma parameters (plasma density, plasma temperature, and spacecraft velocity), and compared to simulations where these plasma parameters are varied. These positive comparisons between the analytic and simulated results show that for the entire range of spacecraft velocities, thermal temperatures, and plasma densities, these simulations accurately represent the plasma and orbiting spacecraft environment.

Now that the simulations have been deemed valid for this range of plasma parameters, these simulations can then be enhanced to determine the feasibility of using the ambient ionospheric plasma to neutralize the beam and the spacecraft. This is done by comparing emission into vacuum to emission into plasma with various parameters. The simulations go to show that for negative particle emission current up to the approximated maximum constant current of 312.5 μA, the base case plasma parameters have no positive effect on helping neutralize the emitted beam and negating the loss in thrust. However, for lower level specific impulse emission down to 100 seconds, the base case ambient plasma is able to capably neutralize the emitted beam and negate the loss in thrust due to electric field interaction. For spacecraft velocities that will be exhibited in the ionosphere, there are no spacecraft velocities that cause the plasma to neutralize the emitted beam. However, when the plasma has a lower Debye length than the base case, as much smaller than 0.0082 m, the ambient plasma is able to suitably neutralize the emitted beam due to the smaller distance needed to shield the emitted negative beam. Thus for some emission and plasma parameters in the ionospheric range that are capable of neutralizing the emitted beam, but there are others that cannot. Therefore, this neutralization method is suitable for missions where the emission and plasma parameters are well defined and within the suitable ranges, but for missions where the parameters are not as well defined this neutralization method cannot be relied upon.

CHAPTER IV

Comparison of 2.5D Simulations to 3D Simulations

4.1 Introduction

All previous simulations have been conducted using OOPIC PRO^{TM}, a 2.5-dimensional particle-in-cell simulator. Thus, this simulation does not fully simulate reality as the simulations do not have the appropriate death. In order to fully simulate the orbiting spacecraft, a 3-dimensional particle-in-cell simulation might be necessary. However, under the right conditions, it may be practical to use the 2.5-dimensional code to derive useful information. The easiest way to determine this is to compare the 2.5-dimensional simulation with the 3-dimensional simulation, and see in which cases the two simulations have the same results, and in which cases the results differ.

The 3-dimensional particle-in-cell simulator used in this chapter is VSim^{TM}, software developed by the same company as OOPIC PRO^{TM}, Tech-X Corporation. Not only does VSim^{TM} have a fully developed third dimension for simulation, but it is also able to simulate in 1 or 2.5 dimensions, which allows for a direct comparison to the 2.5-dimensional OOPIC PRO^{TM}. Additionally, it is able to distribute work over multiple cores in parallel allowing it to run more complicated simulations in an efficient manner, or in some cases possibly be able to run simulations that would fail previously, such as the ones in Section 3.6.

This chapter will focus on comparing a subset of the simulations performed in

2.5 dimensions to their equivalent simulations in 2.5 and pseudo 3 dimensions in VSim^{TM} to determine if a 2.5-dimensional simulation can accurately represent certain 3-dimensional simulations. This will consist of comparing diagnostics between the two simulations to understand how they match and where they may be limitations.

4.2 Simulations to be Conducted

The simulations to be compared will begin with simple emission from one wall of the simulation through an EmitPort. The emission will vary between positive and negative emission and electric fields will be observed. In addition, spatial-varying, common spatial emission schemes as well as time-varying, common spatial emission schemes will be tested where positive and negative particles are emitted in the same simulation, either simultaneously or in succession. First the simulations will be conducted in VSim^{TM} in 2.5 dimensions and then moved on to pseudo 3-dimensional simulations. In all 3-dimensional simulations for comparison purposes, the third dimension will be 1 meter in depth as that is what OOPIC PRO^{TM} simulates, hence the pseudo 3-dimensionality. These simulations will cover the simulations covered in Chapter II.

4.3 Limitations of the Comparison due to VSim^{TM}

VSim^{TM} being a relatively new piece of software still has a few bugs still to be worked out, limiting some aspects of the simulation, making it difficult to make some one-to-one comparisons.

One issue is that the simulations conducted in OOPIC PRO^{TM} have periodic boundaries in both the X and Y direction meaning that any particle leaving the simulation space to the right, immediately reenters on the left, and a particle leaving on the left, immediately reenters on the right, and the same for the top and bottom boundaries.

However, in VSim^{TM}, there is a current bug that allows a simulation with periodic X and Y boundaries to run, but fails after a certain number of time steps. The way around this bug is to turn off one of the periodic boundaries, which is not a problem for some comparison simulations, but does not provide a good one-to-one comparison in other cases.

4.4 VSim^{TM} Simulations and Comparison

For the neutralization using oppositely charged particles as was discussed in Chapter II, the simulations can be broken down into two types, spatial-varying, common time emission scheme and temporal-varying, common spatial emission scheme. Both of these schemes will have OOPIC PRO^{TM} results compared to VSim^{TM} results. In both cases, the OOPIC PRO^{TM} 2.5-dimensional results will be compared to the VSim^{TM} 2.5-dimensional and 3-dimensional results.

4.4.1 VSim^{TM} Simulations and Comparison of Spatial-Varying, Common Time Emission Scheme

For the spatial-varying, common time emission neutralization scheme as is discussed in depth in Section 2.4, this comparison will only examine the single base case where the beams are 0.015 m wide, and are placed directly adjacent to one another. The currents will vary between 14.49 mA, 312.5 μA, and 60 nA. The simulations will be examined at 40, 200, and 360 time steps, where the time steps are 50 ns, and 400 time steps is the time it takes for the simulation to make it all the way across the simulation space. The diagnostics examined most extensively will be the electric field magnitudes in the X and Y direction. A sample of the diagnostics is shown in Figures 4.1 - 4.18 for the case of 312.5 μA current emission at various time steps.

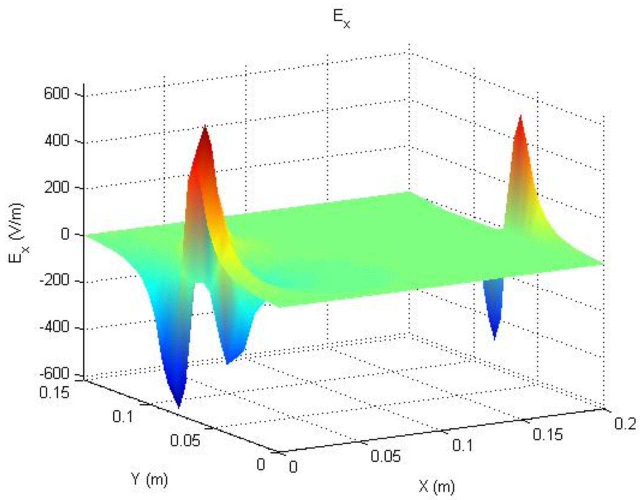

Figure 4.1: E_x Magnitude After 40 Time Steps for a 312.5 μA Beam in OOPIC PRO^{TM}

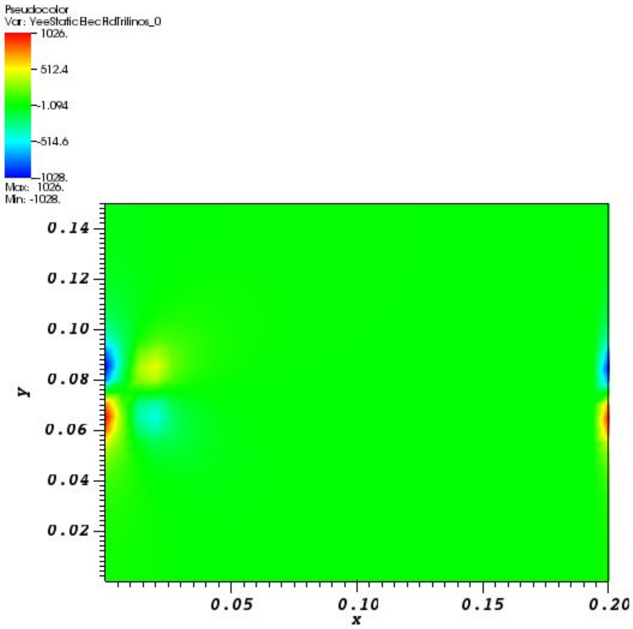

Figure 4.2: E_x Magnitude After 40 Time Steps for a 312.5 μA Beam in VSim^{TM} in 2.5D

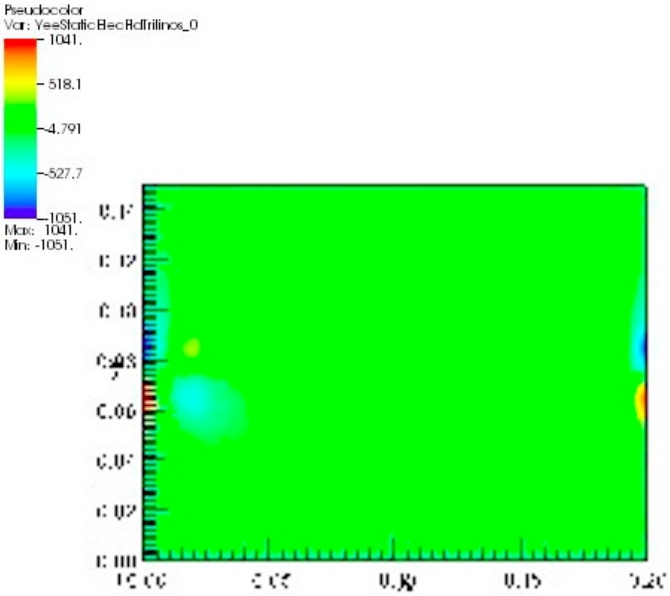

Figure 4.3: E_x Magnitude After 40 Time Steps for a 312.5 μA Beam in VSim^{TM} in 3D

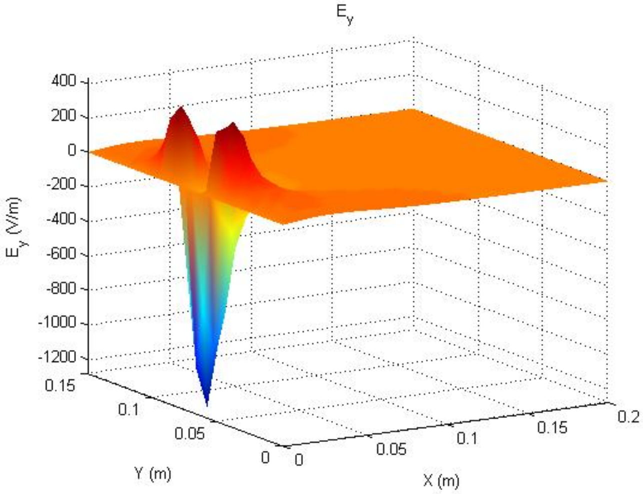

Figure 4.4: E_y Magnitude After 40 Time Steps for a 312.5 μA Beam in OOPIC PRO^{TM}

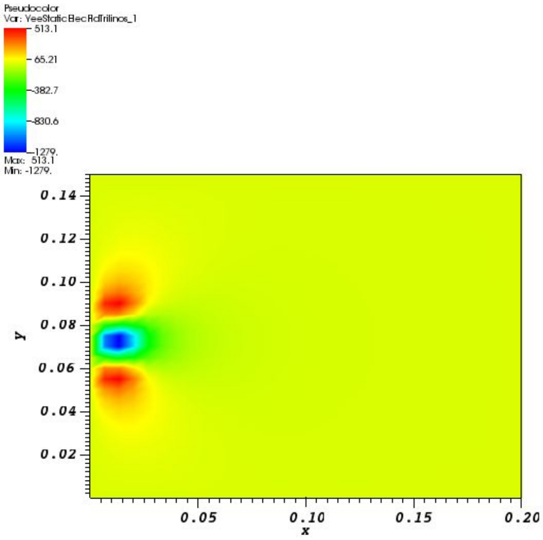

Figure 4.5: E_y Magnitude After 40 Time Steps for a 312.5 μA Beam in VSim^{TM} in 2.5D

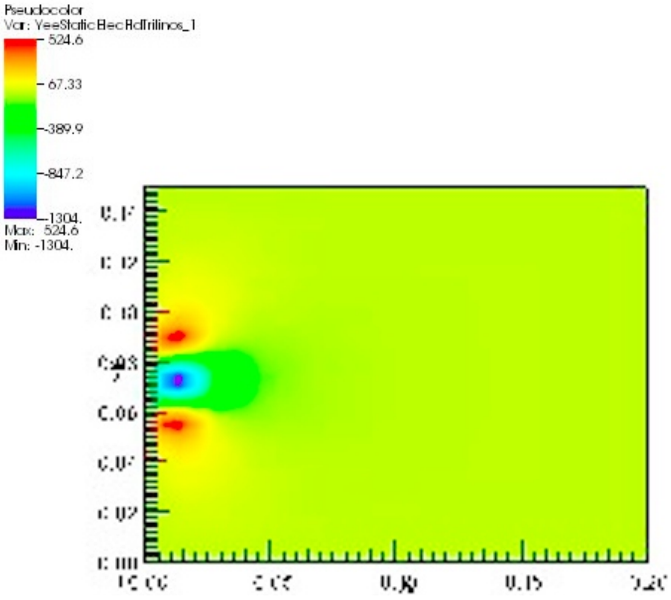

Figure 4.6: E_y Magnitude After 40 Time Steps for a 312.5 μA Beam in VSim^{TM} in 3D

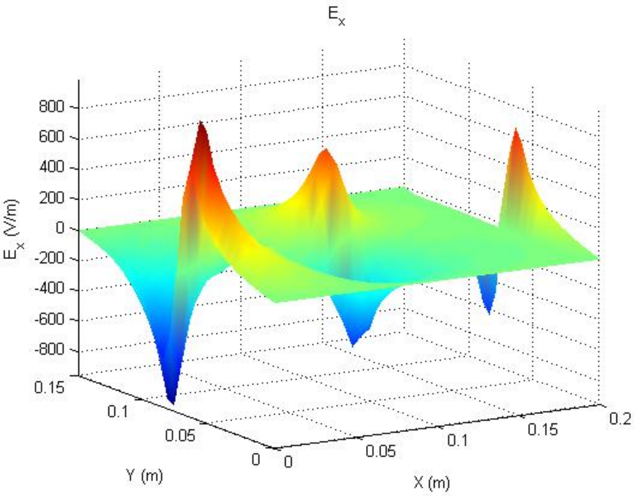

Figure 4.7: E_x Magnitude After 200 Time Steps for a 312.5 μA Beam in OOPIC PRO^{TM}

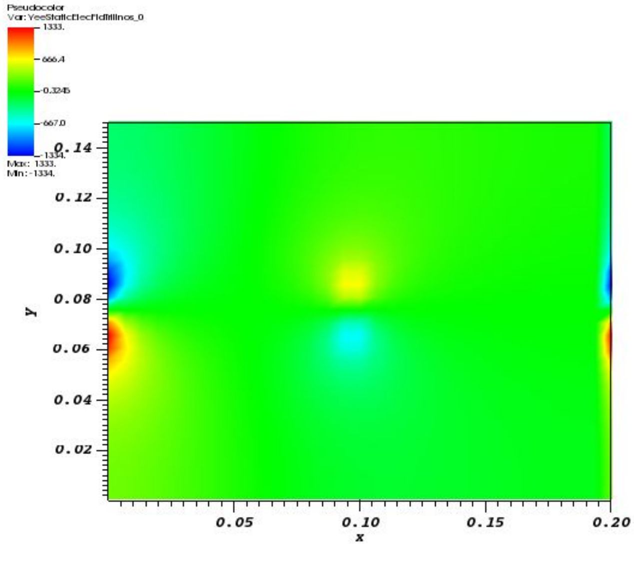

Figure 4.8: E_x Magnitude After 200 Time Steps for a 312.5 μA Beam in VSim^{TM} in 2.5D

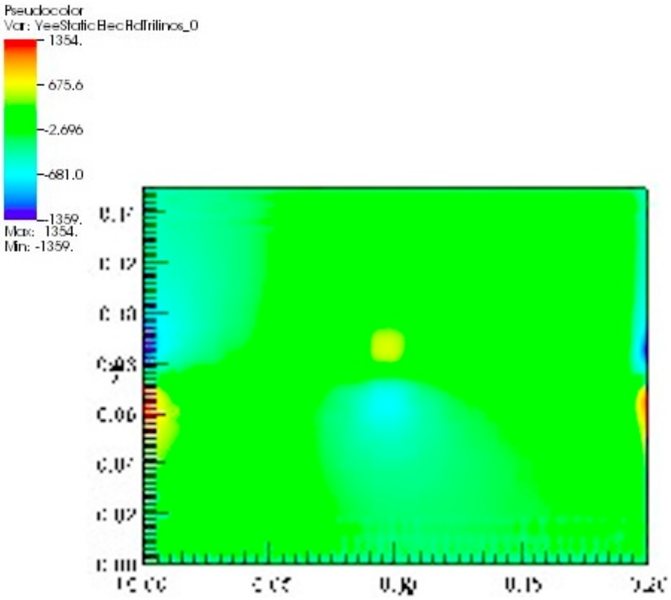

Figure 4.9: E_x Magnitude After 200 Time Steps for a 312.5 μA Beam in VSim^{TM} in 3D

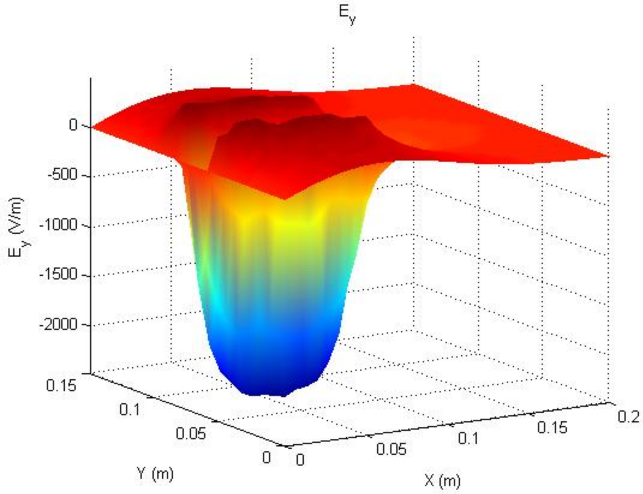

Figure 4.10: E_y Magnitude After 200 Time Steps for a 312.5 μA Beam in OOPIC PRO^{TM}

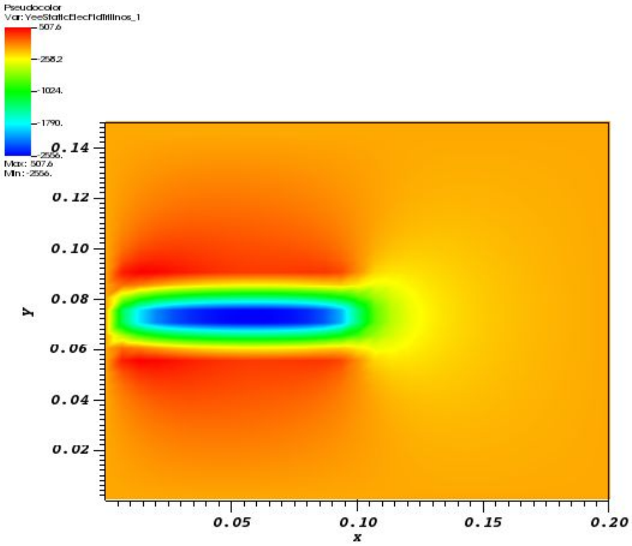

Figure 4.11: E_y Magnitude After 200 Time Steps for a 312.5 μA Beam in VSim^{TM} in 2.5D

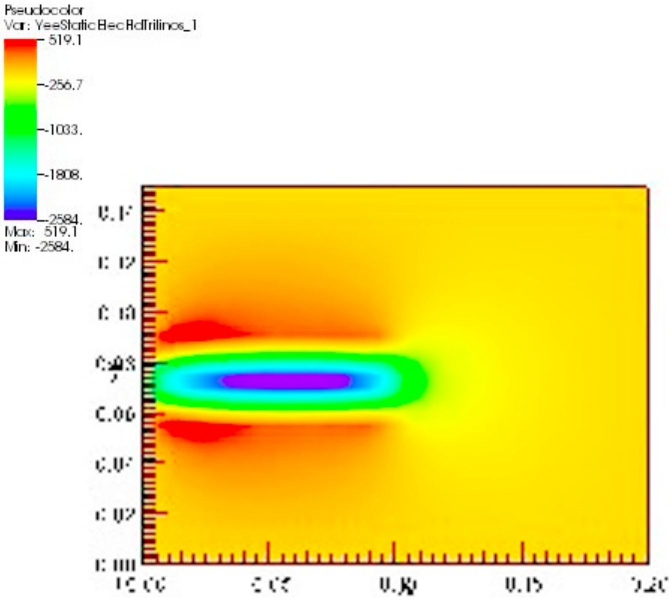

Figure 4.12: E_y Magnitude After 200 Time Steps for a 312.5 μA Beam in VSim^{TM} in 3D

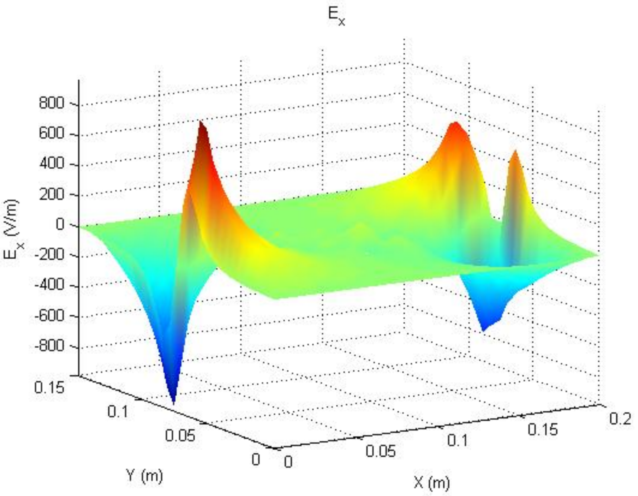

Figure 4.13: E$_x$ Magnitude After 360 Time Steps for a 312.5 μA Beam in OOPIC PRO^{TM}

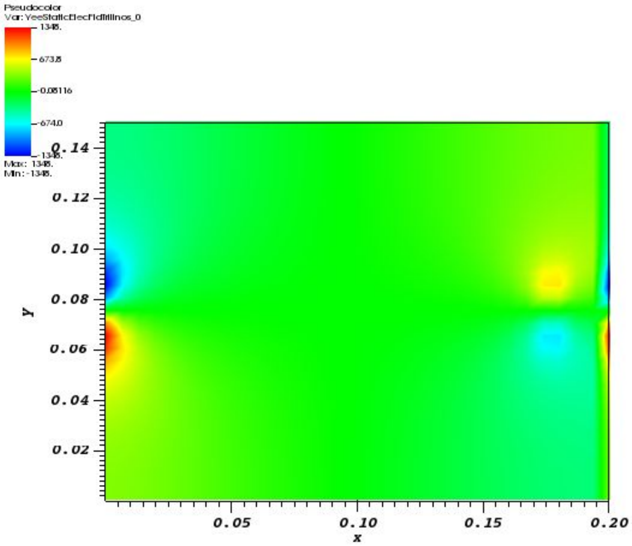

Figure 4.14: E$_x$ Magnitude After 360 Time Steps for a 312.5 μA Beam in VSim^{TM} in 2.5D

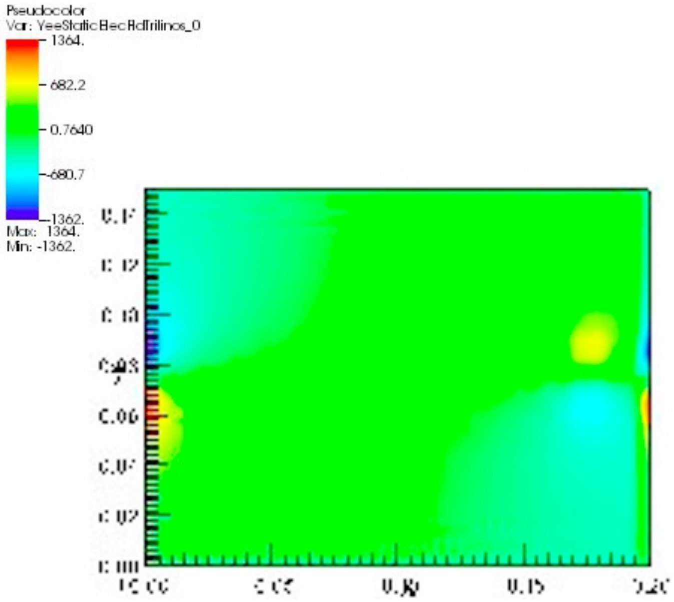

Figure 4.15: E_x Magnitude After 360 Time Steps for a 312.5 μA Beam in VSim^{TM} in 3D

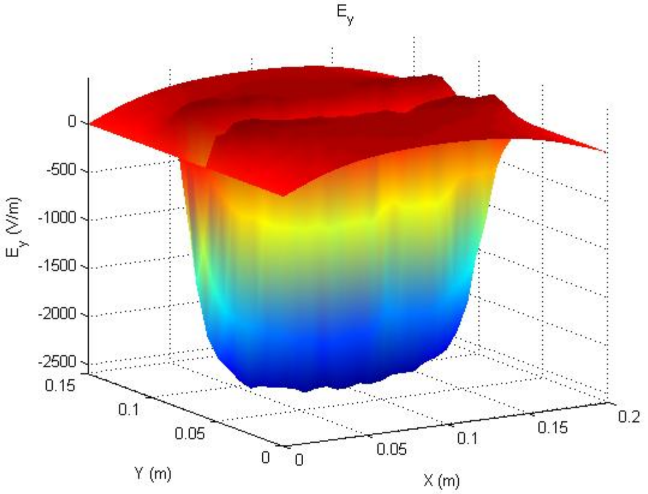

Figure 4.16: E_y Magnitude After 360 Time Steps for a 312.5 μA Beam in OOPIC PRO^{TM}

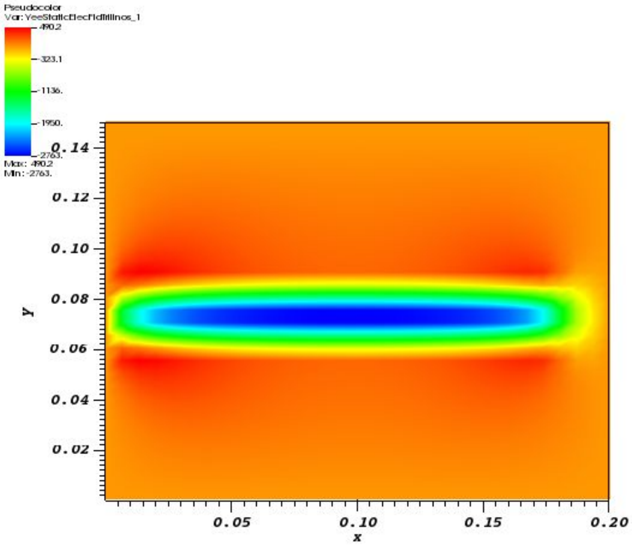

Figure 4.17: E_y Magnitude After 360 Time Steps for a 312.5 μA Beam in VSim^{TM} in 2.5D

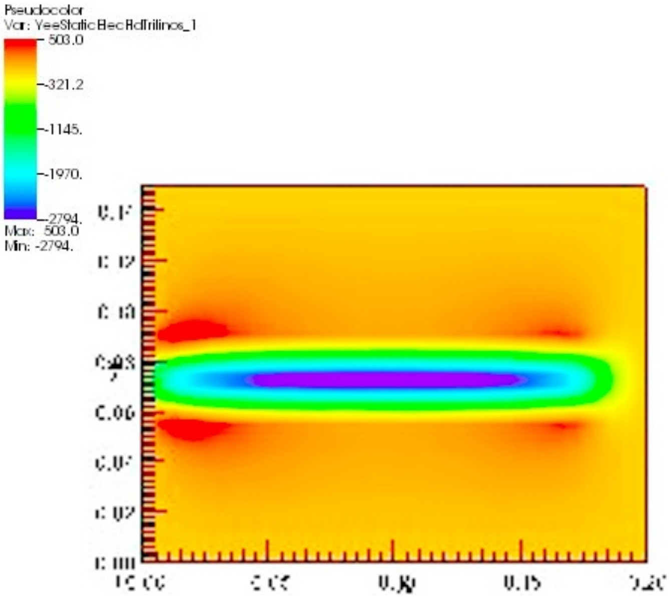

Figure 4.18: E_y Magnitude After 360 Time Steps for a 312.5 μA Beam in VSim^{TM} in 3D

Table 4.1 shows the peak maximum and minimum electric field magnitudes in both directions for all cases examined in the spatial-varying, common time emission scheme. These peaks can be used for comparison as the general shape of the electric fields are the same between the two simulation softwares (OOPIC PRO^{TM}, 2.5D and 3D VSim^{TM}) for all cases, as can be seen in Figures 4.1 - 4.18. In the table, a dark green cell indicates that the magnitudes differ by less than 10%, a light green cell indicates that the magnitudes differ by between 10% and 20%, a light red cell indicates that the magnitudes differ by between 20% and 30%, and a dark red cell indicates that the magnitudes differ by greater than 30%.

The 2.5D and 3D results for VSim^{TM} are very close, and thus from this point forth in this section, they will be treated as the same result in the discussion.

From Table 4.1, the same general trends in electric field magnitude in both directions are seen for both OOPIC PRO^{TM} and VSim^{TM}. The electric field magnitudes in the X direction have approximately equal but opposite maximums and minimums, whereas the electric field magnitudes in the Y direction have a much larger negative peak minimum value than peak maximum value.

In addition, the electric field magnitudes in both the X and Y directions see a significant increase in magnitude from time step 40 to 200, but no increase between time step 200 and 360. This reinforces the notion that there are transient properties early on during the beam propagation, but after a certain point in simulation time, prior to the beam reaching halfway across the simulation space, the electric fields near the spacecraft reach a steady state. As expected, the electric field magnitudes increase as the emission current increases as there is more charge in the simulation space.

In Table 4.1, there are numerous cells that are dark red or light red, indicating at least a 20% difference between VSim^{TM} and OOPIC PRO^{TM} values. Most noticeable is that the differences are in the same range no matter what the emission current is.

The size of the difference between VSim^{TM} and OOPIC PRO^{TM} results only depend on time step and the diagnostic being measured. All of the values that have the larger difference are for the electric field magnitude in the X direction. Every electric field magnitude in the X direction has at least a 20% difference between OOPIC PRO^{TM} and VSim^{TM} results, whereas every electric field magnitude in the Y direction has less than a 20% difference between OOPIC PRO^{TM} and VSim^{TM} results. In addition, only the electric field magnitude in the X direction calculated after 40 time steps show the largest percent difference range of greater than 30%, and only the peak maximum electric field in the Y direction calculated after 40 time steps show a slightly larger percent difference of between 10 and 20% across all emission currents. This indicates that the physics between the oppositely charged beams and the electric fields due to a singly charged beam behave the same in both simulation softwares (Y direction between the two beams, and Y direction pointing towards and away from the singly charged beam from the top and bottom).

However, with the electric field magnitudes in the X direction being so different between the two softwares, there must be something in the software or software model causing this. The peak electric field magnitudes in the X direction occur close to the spacecraft due to the image charge induced axial electric field. Thus, this larger difference in image charge induced axial electric field seems to indicate that VSim^{TM} handles image charge on equipotentials different than OOPIC PRO^{TM} does. Since VSim^{TM} operates by solving Maxwell's curl equations, as opposed to Poisson's equation like OOPIC PRO^{TM} does, there potentially can be very different image charge magnitudes appearing on the spacecraft.

4.4.2 VSim^{TM} Simulations and Comparison of Temporal-Varying, Common Spatial Emission Scheme

For the temporal-varying, common spatial emission neutralization scheme as is discussed in depth in Section 2.5, this comparison will examine the single base case where the beams are 0.015 m wide. The currents will vary between 14.49 mA, 312.5 μA, and 60 nA. The simulations will all be examined at 360 time steps, where the time steps are 50 ns, and 400 time steps is the time it takes for the simulation to make it all the way across the simulation space. The frequency of oscillation between positive and negative emission will vary from 100 kHz to 200 kHz to 1 MHz. The diagnostics examined most extensively will be the electric field magnitudes in the X and Y direction. A sample of the diagnostics is shown in Figures 4.19 - 4.36 for the case of 312.5 μA current emission at various frequencies.

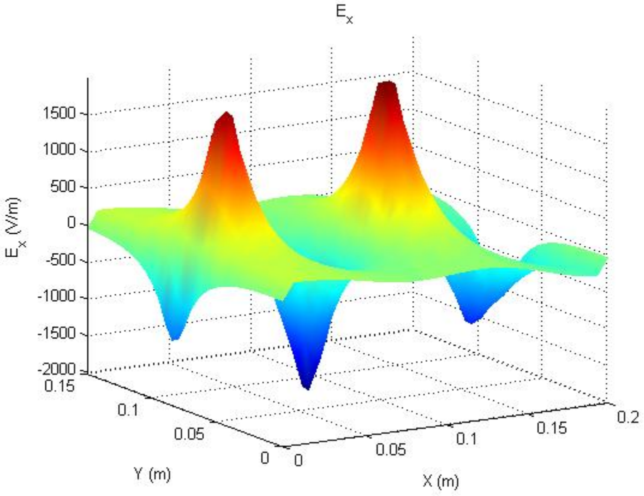

Figure 4.19: E$_x$ Magnitude for a 100 kHz Time-Varying 312.5 μA Beam in OOPIC PRO^{TM}

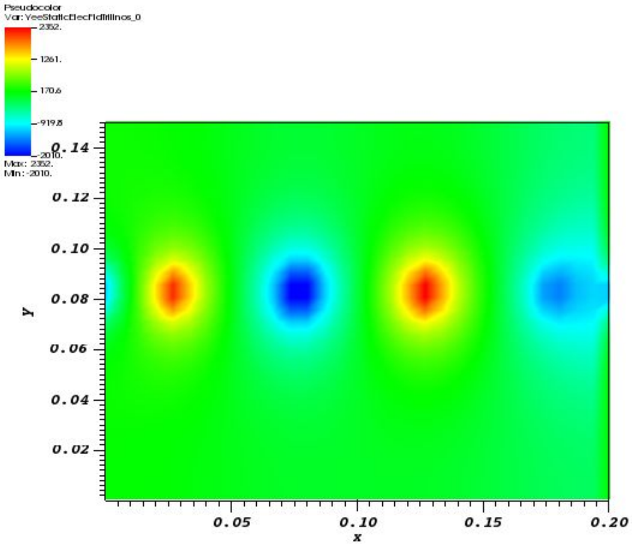

Figure 4.20: E_x Magnitude for a 100 kHz Time-Varying 312.5 μA Beam in VSim^{TM} in 2.5D

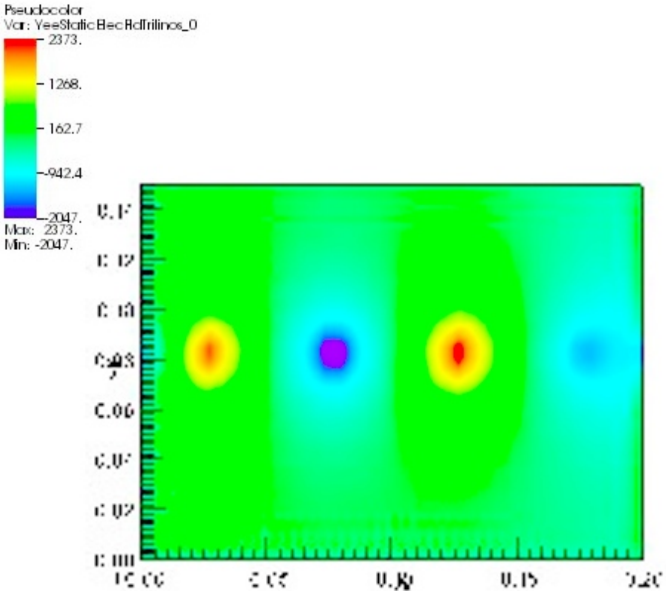

Figure 4.21: E_x Magnitude for a 100 kHz Time-Varying 312.5 μA Beam in VSim^{TM} in 3D

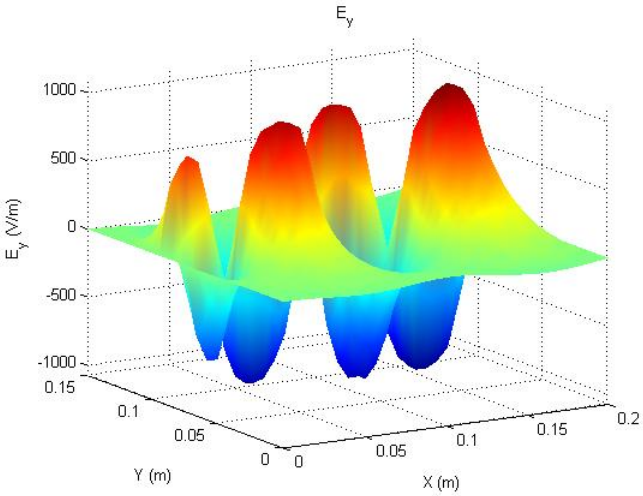

Figure 4.22: E$_y$ Magnitude for a 100 kHz Time-Varying 312.5 μA Beam in OOPIC PRO^{TM}

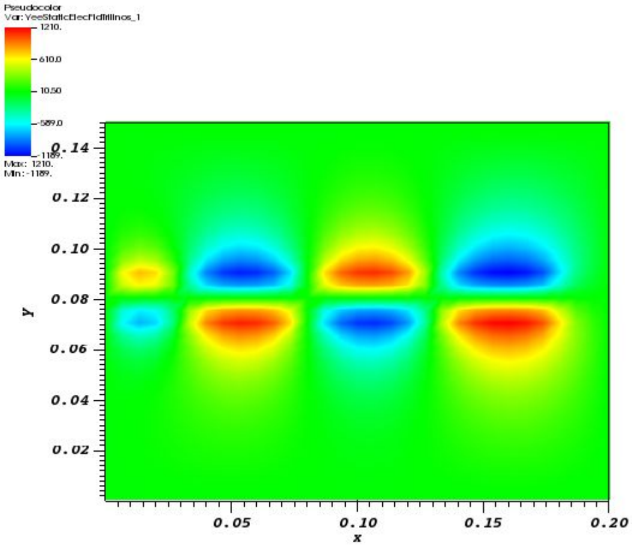

Figure 4.23: E$_y$ Magnitude for a 100 kHz Time-Varying 312.5 μA Beam in VSim^{TM} in 2.5D

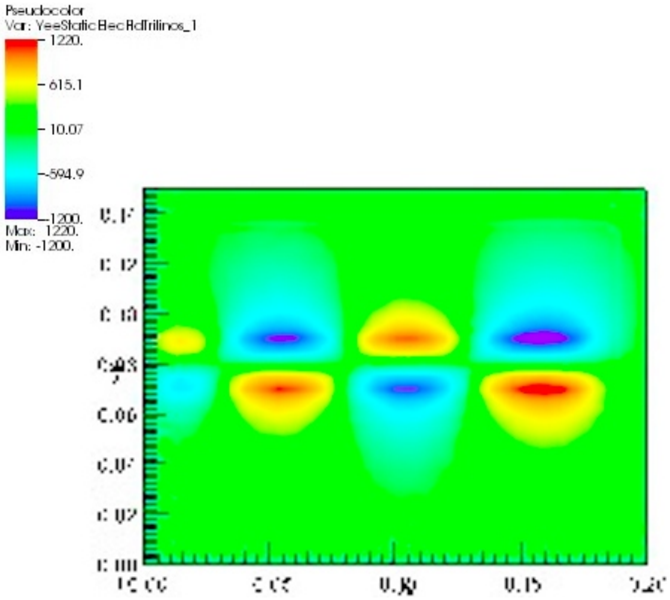

Figure 4.24: E$_y$ Magnitude for a 100 kHz Time-Varying 312.5 μA Beam in VSim^{TM} in 3D

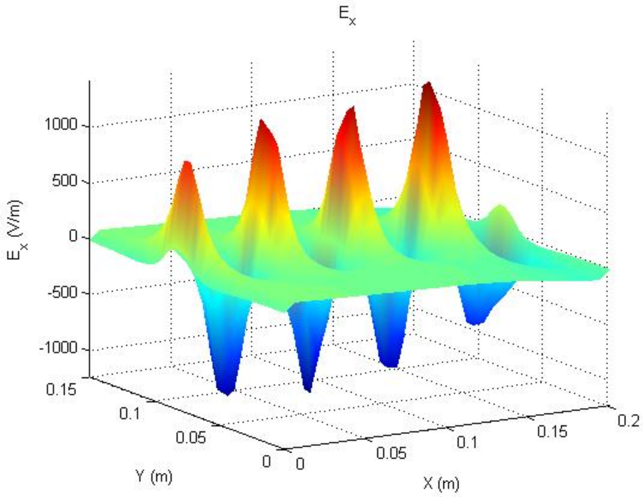

Figure 4.25: E$_x$ Magnitude for a 200 kHz Time-Varying 312.5 μA Beam in OOPIC PRO^{TM}

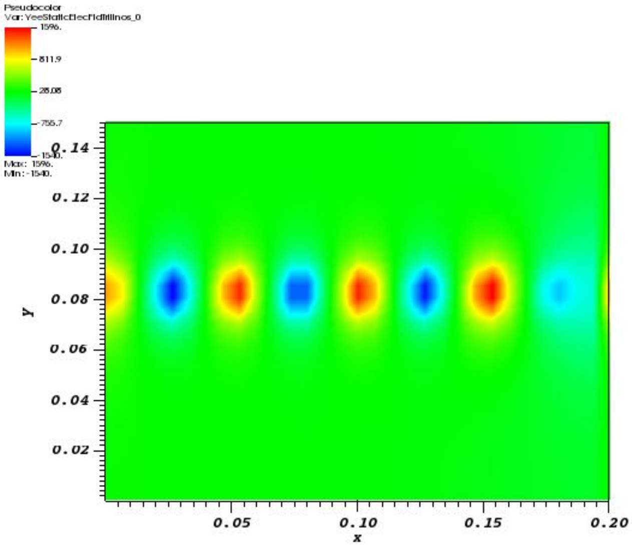

Figure 4.26: E_x Magnitude for a 200 kHz Time-Varying 312.5 μA Beam in VSim^{TM} in 2.5D

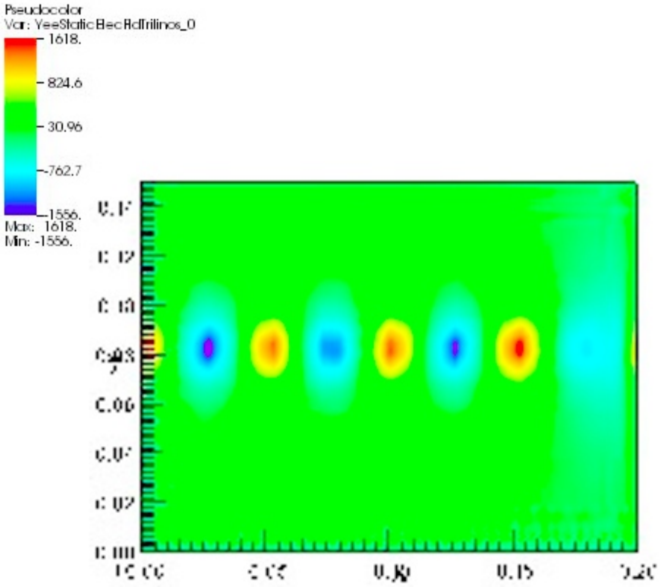

Figure 4.27: E_x Magnitude for a 200 kHz Time-Varying 312.5 μA Beam in VSim^{TM} in 3D

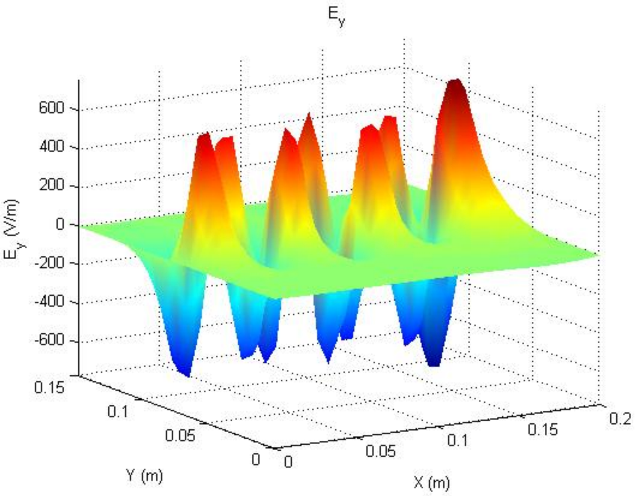

Figure 4.28: E$_y$ Magnitude for a 200 kHz Time-Varying 312.5 μA Beam in OOPIC PRO^{TM}

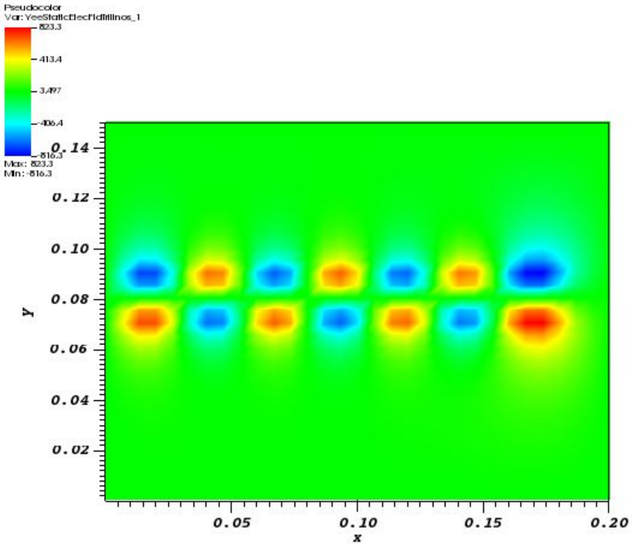

Figure 4.29: E$_y$ Magnitude for a 200 kHz Time-Varying 312.5 μA Beam in VSim^{TM} in 2.5D

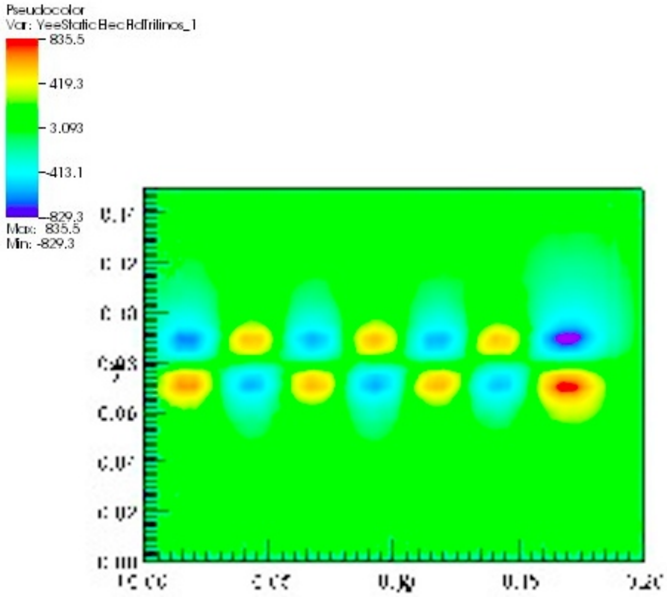

Figure 4.30: E_y Magnitude for a 200 kHz Time-Varying 312.5 μA Beam in VSim^{TM} in 3D

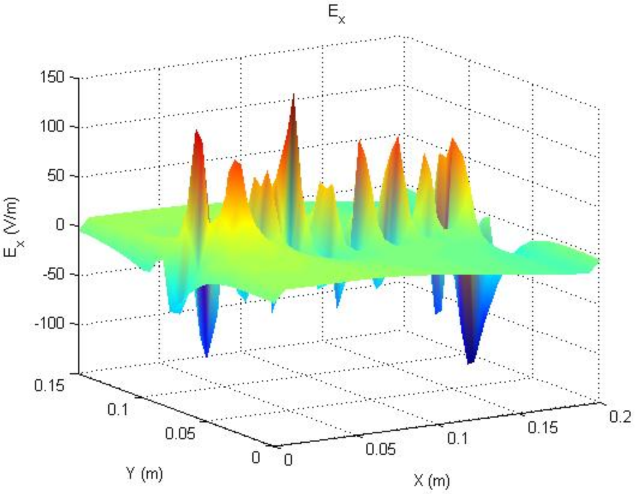

Figure 4.31: E_x Magnitude for a 1 MHz Time-Varying 312.5 μA Beam in OOPIC PRO^{TM}

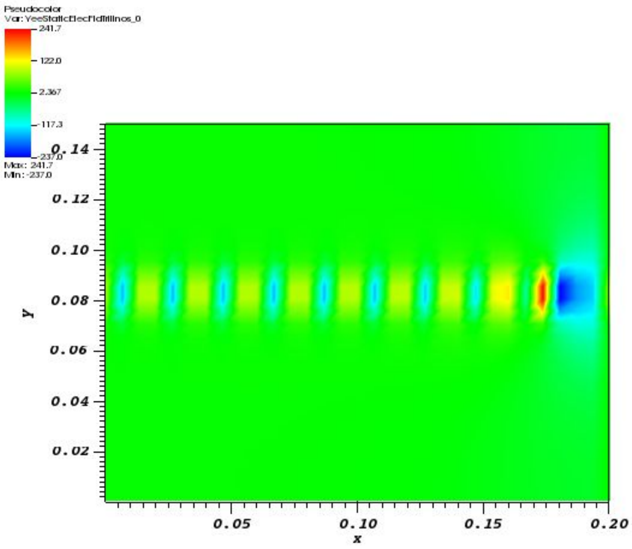

Figure 4.32: E_x Magnitude for a 1 MHz Time-Varying 312.5 μA Beam in VSim^{TM} in 2.5D

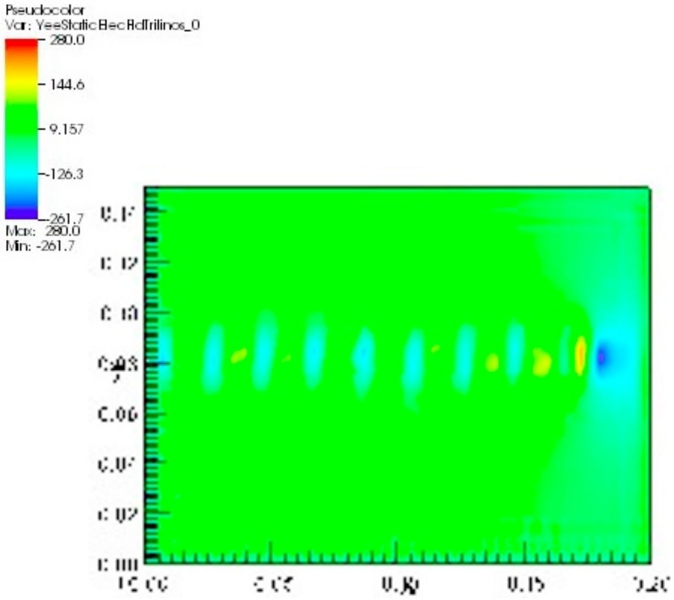

Figure 4.33: E_x Magnitude for a 1 MHz Time-Varying 312.5 μA Beam in VSim^{TM} in 3D

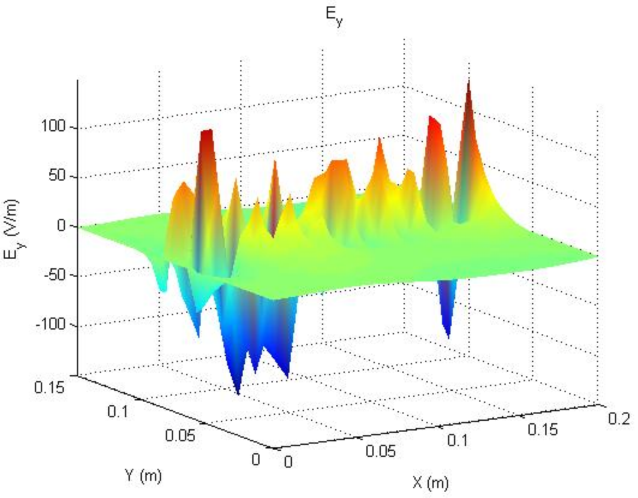

Figure 4.34: E_y Magnitude for a 1 MHz Time-Varying 312.5 μA Beam in OOPIC PRO^{TM}

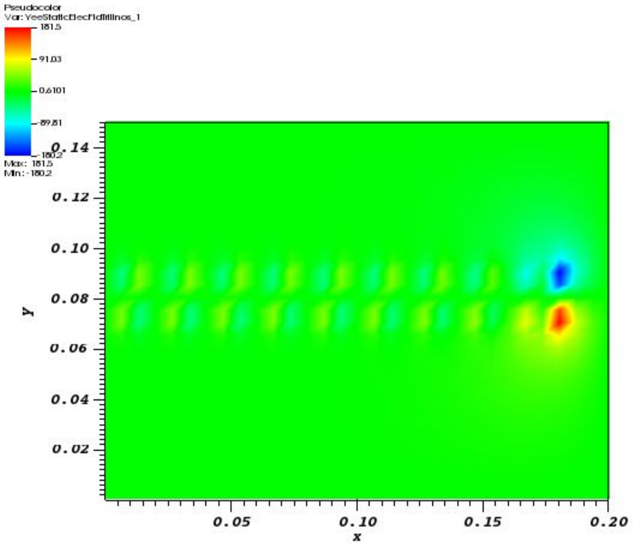

Figure 4.35: E_y Magnitude for a 1 MHz Time-Varying 312.5 μA Beam in VSim^{TM} in 2.5D

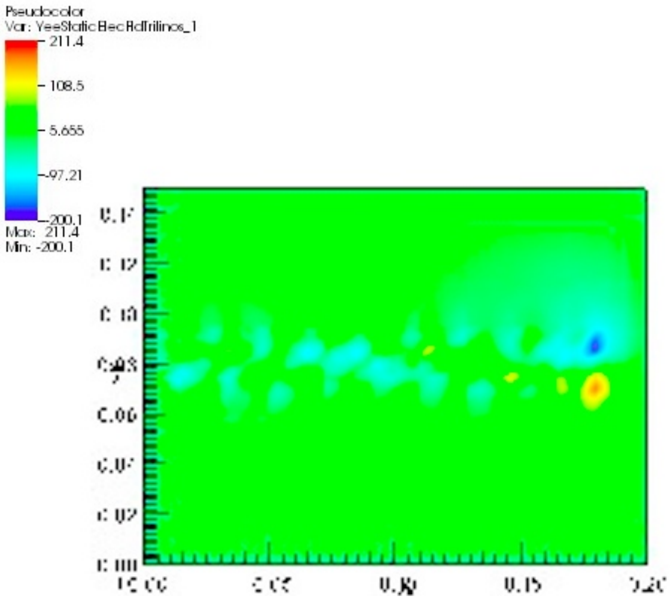

Figure 4.36: E_y Magnitude for a 1 MHz Time-Varying 312.5 μA Beam in VSim^{TM} in 3D

Table 4.2 shows the peak maximum and minimum electric field magnitudes in both directions for all cases examined in the temporal-varying, common spatial emission scheme. These peaks can be used for comparison as the general shape of the electric fields are the same between the two simulation softwares (OOPIC PRO^{TM}, 2.5D and 3D for VSim^{TM}) for all cases, as can be seen in Figures 4.19 - 4.36. In the table, a dark green cell indicates that the magnitudes differ by less than 10%, a light green cell indicates that the magnitudes differ by between 10% and 20%, a light red cell indicates that the magnitudes differ by between 20% and 30%, and a dark red cell indicates that the magnitudes differ by greater than 30%.

It can be easily observed that the 2.5D and 3D results for VSim^{TM} are virtually identical, and thus from this point forth in this section, they will be treated as the same result in the discussion.

From Table 4.2, it can be seen that the same general trends in electric field magnitude in both directions are seen for both OOPIC PRO^{TM} and VSim^{TM}; the electric field magnitudes in both X and Y directions have approximately equal but opposite maximums and minimums.

In addition, the electric field magnitudes in both the X and Y directions see a significant decrease in magnitude as frequency is increased from 100 kHz to 200 kHz to 1 MHz. This reinforces the idea that a higher frequency oscillation between oppositely charged particles is a more neutral beam, with an infinitely high frequency being a completely neutral beam. As expected, the electric field magnitudes increase as the emission current increases as there is more charge in the simulation space.

Table 4.2 shows much more consistency between OOPIC PRO^{TM} and VSim^{TM} than Table 4.1 did. The vast majority of the values that had a large percentage difference between the two softwares occur for 1 MHz (high frequency) oscillations between emission of positive and negative charged particles, with the one exception being a sole case at a low current emission where small changes in electric field will have a large difference on the percent difference. Also the electric field magnitudes in the X direction have a larger variation than their corresponding electric field magnitudes in the Y direction across the board. Lastly, as emission current increases, there seems to be better correlation between the two simulation softwares.

With higher frequency oscillation, the oppositely charged beams will overlap more frequently, and for a larger percentage of the beam, thus there are more chances for the beams to have large random peaks in magnitude in the X direction (Section 2.5.2). Fig. 4.31 and Fig. 4.32 show one example of such a difference. In the OOPIC PRO^{TM} plot, there are large peaks in magnitude wherever there is an overlap between beams;

however, the VSim^{TM} plot shows that the peak maximum and minimum electric field in the X direction occurs on the leading edge of the beam, which is significantly larger than any previous electric field. Disregarding the leading edge electric fields, the two simulation software peaks would match very well. Looking at lower frequency beams, the leading edge electric field is not significantly larger than the electric fields further back in the beam, and thus there is better correlation between the two simulation softwares.

4.5 Summary

This comparison of simulation results between 2.5D simulations in OOPIC PRO^{TM} and 2.5D and pseudo 3D simulations in VSim^{TM} provides a good baseline for understanding which simulations performed in OOPIC PRO^{TM} can be trusted.

In addition, seeing results from simulations performed in 2.5D and 3D in VSim^{TM} show strong similarities, it can be deduced that the 2.5D simulations performed can be translated into pseudo three dimensions. The pseudo 3D simulations can be made more accurate by changing the spacecraft depth from 1 m to something more suitable in future simulations to make the simulations fully three-dimensional.

From the simulation results, it seems as if VSim^{TM} handles image charge on equipotentials somewhat differently than OOPIC PRO^{TM}. This accounts for the differences in the spatial-varying, common time emission neutralization scheme results shown in Table 4.1. This means that it is hard to trust the potential and electric field incident upon an equipotential.

The other large difference is from the high frequency (1 MHz) temporal-varying, common spatial emission neutralization scheme shown in Table 4.2. At the higher frequency, a larger percentage of the positive and negative charged particles overlap, and thus there is more room for variation. Therefore, it is hard to trust the results from 1 MHz and higher simulations.

Current	Time Steps	Diagnostic	Software	Peak Max (V)	Peak Min (V)
60 nA	40	E_x	OOPIC PRO^{TM}	0.1213	-0.123
			2D VSim^{TM}	0.197	-0.1974
			3D VSim^{TM}	0.1999	-0.2017
		E_y	OOPIC PRO^{TM}	0.0798	-0.2624
			2D VSim^{TM}	0.09852	-0.2455
			3D VSim^{TM}	0.1007	-0.2505
	200	E_x	OOPIC PRO^{TM}	0.1937	-0.1915
			2D VSim^{TM}	0.256	-0.2561
			3D VSim^{TM}	0.2599	-0.261
		E_y	OOPIC PRO^{TM}	0.0989	-0.4546
			2D VSim^{TM}	0.09746	-0.4909
			3D VSim^{TM}	0.09966	-0.4963
	360	E_x	OOPIC PRO^{TM}	0.186	-0.1808
			2D VSim^{TM}	0.2588	-0.2588
			3D VSim^{TM}	0.2618	-0.2615
		E_y	OOPIC PRO^{TM}	0.0924	-0.496
			2D VSim^{TM}	0.0941	-0.5312
			3D VSim^{TM}	0.09656	-0.5371
312.5 μA	40	E_x	OOPIC PRO^{TM}	646.2	-616.6
			2D VSim^{TM}	1026	-1028
			3D VSim^{TM}	1041	-1051
		E_y	OOPIC PRO^{TM}	361.5	-672.4
			2D VSim^{TM}	513.1	-1279
			3D VSim^{TM}	524.6	-1304
	200	E_x	OOPIC PRO^{TM}	987.2	-954.2
			2D VSim^{TM}	1333	-1334
			3D VSim^{TM}	1354	-1359
		E_y	OOPIC PRO^{TM}	503.1	-2431
			2D VSim^{TM}	507.6	-2558
			3D VSim^{TM}	519.1	-2584
	360	E_x	OOPIC PRO^{TM}	965.8	-978.9
			2D VSim^{TM}	1345	-1345
			3D VSim^{TM}	1364	-1362
		E_y	OOPIC PRO^{TM}	485.2	-2565
			2D VSim^{TM}	490.2	-2763
			3D VSim^{TM}	503	-2794

Current	Time Steps	Diagnostic	Software	Peak Max (V)	Peak Min (V)
14.49 mA	40	E_x	OOPIC PRO^{TM}	30320	-31240
			2D VSim^{TM}	47570	-47670
			3D VSim^{TM}	48270	-48710
		E_y	OOPIC PRO^{TM}	19727	-61177
			2D VSim^{TM}	23790	-59270
			3D VSim^{TM}	24320	-60470
	200	E_x	OOPIC PRO^{TM}	44710	-44260
			2D VSim^{TM}	61750	-61760
			3D VSim^{TM}	62710	-62970
		E_y	OOPIC PRO^{TM}	23850	-111800
			2D VSim^{TM}	23600	-116700
			3D VSim^{TM}	24130	-117900
	360	E_x	OOPIC PRO^{TM}	44850	-43800
			2D VSim^{TM}	62360	-62370
			3D VSim^{TM}	63100	-63030
		E_y	OOPIC PRO^{TM}	22730	-118000
			2D VSim^{TM}	22870	-122900
			3D VSim^{TM}	23460	-124600

Table 4.1: Spatial-Varying Comparison Between OOPIC PRO^{TM} and 2.5D and 3D Simulations in VSim^{TM} (Dark Green:<10%, Light Green:10%-20%, Light Red:20%-30%, Dark Red:>30%)

Current	Frequency	Diagnostic	Software	Peak Max (V)	Peak Min (V)
60 nA	100 kHz	E_x	OOPIC PRO^{TM}	0.3982	-0.389
			2D VSim^{TM}	0.452	-0.3562
			3D VSim^{TM}	0.456	-0.3933
		E_y	OOPIC PRO^{TM}	0.2072	-0.2126
			2D VSim^{TM}	0.2324	-0.2254
			3D VSim^{TM}	0.2345	-0.2306
	200 kHz	E_x	OOPIC PRO^{TM}	0.2593	-0.2136
			2D VSim^{TM}	0.307	-0.2956
			3D VSim^{TM}	0.3113	-0.2988
		E_y	OOPIC PRO^{TM}	0.1489	-0.1423
			2D VSim^{TM}	0.1582	-0.1569
			3D VSim^{TM}	0.1606	-0.1594
	1 MHz	E_x	OOPIC PRO^{TM}	0.02571	-0.02639
			2D VSim^{TM}	0.04543	-0.04554
			3D VSim^{TM}	0.0538	-0.0503
		E_y	OOPIC PRO^{TM}	0.0302	-0.02116
			2D VSim^{TM}	0.03456	-0.03453
			3D VSim^{TM}	0.04066	-0.03849
312.5 μA	100 kHz	E_x	OOPIC PRO^{TM}	1999	-2015
			2D VSim^{TM}	2352	-2010
			3D VSim^{TM}	2373	-2047
		E_y	OOPIC PRO^{TM}	1091	-1071
			2D VSim^{TM}	1210	-1189
			3D VSim^{TM}	1220	-1200
	200 kHz	E_x	OOPIC PRO^{TM}	1403	-1240
			2D VSim^{TM}	1596	-1540
			3D VSim^{TM}	1618	-1556
		E_y	OOPIC PRO^{TM}	754.1	-769.1
			2D VSim^{TM}	823.3	-816.3
			3D VSim^{TM}	835.5	-829.3
	1 MHz	E_x	OOPIC PRO^{TM}	150.9	-148.5
			2D VSim^{TM}	241.7	-237
			3D VSim^{TM}	280	-261.7
		E_y	OOPIC PRO^{TM}	148.8	-149.4
			2D VSim^{TM}	181.5	-180.2
			3D VSim^{TM}	211.4	-200.1

Current	Frequency	Diagnostic	Software	Peak Max	Peak Min
14.49 mA	100 kHz	E$_x$	OOPIC PRO^{TM}	85290	-93180
			2D VSim^{TM}	101200	-91220
			3D VSim^{TM}	102300	-93020
		E$_y$	OOPIC PRO^{TM}	48720	-48950
			2D VSim^{TM}	53390	-52420
			3D VSim^{TM}	250	-250
	200 kHz	E$_x$	OOPIC PRO^{TM}	56090	-56850
			2D VSim^{TM}	67590	-71020
			3D VSim^{TM}	68660	-71810
		E$_y$	OOPIC PRO^{TM}	32800	-32870
			2D VSim^{TM}	35960	-35650
			3D VSim^{TM}	36530	-36440
	1 MHz	E$_x$	OOPIC PRO^{TM}	7928	-7285
			2D VSim^{TM}	10590	-10460
			3D VSim^{TM}	12630	-11570
		E$_y$	OOPIC PRO^{TM}	8648	-10080
			2D VSim^{TM}	8135	-8075
			3D VSim^{TM}	8968	-8858

Table 4.2: Time-Varying Comparison Between OOPIC PRO^{TM} and 2.5D and 3D Simulations in VSim^{TM} (Dark Green:<10%, Light Green:10%-20%, Light Red:20%-30%, Dark Red:>30%)

CHAPTER V

Alternative Neutralization Techniques for Small Satellites

5.1 Introduction

The one benefit of NanoFET and similar colloidal systems is that they have the ability to charge particles positively or negatively before they are emitted. Other electric propulsion alternatives for satellites do not have such a luxury, and thus other neutralization techniques are needed. A common, well-developed neutralization solution that has endured large levels of testing in space is the hot filament or thermionic cathode. An additional developing neutralization technique is the Field Emitter Array Cathode (FEAC), which is more efficient but much development remains to identify a technologically acceptable approach.

A new class of satellites in development are femtosatellites, which are described as satellites being less than 100 g in mass (*Tristancho*, 2010). The smallest of these femtosatellites are envisioned to be built like a semiconductor wafer chip, termed ChipSats, using microelectromechanical systems (MEMS) and semiconductor fabrication processes.

One major concern of femtosatellites, especially ChipSats, is that they can have a high area to mass ratio due to their mostly flat structure. Thus, atmospheric drag effects can be significant (*Bell*, 2010) in low Earth orbit (LEO). Thus, a low mass and power propulsion system might be needed for some applications of the small spacecraft. Due to the small size and mass of femtosatellites and especially ChipSats, it is difficult to utilize typical propulsion systems.

A propulsion system that had been tested on large satellites (*Bilén et al.*, 1995), including testing on space shuttles (*Gilchrist et al.*, 1998), is the use of electrodynamic tethers. Electrodynamic tethers utilize the Earth's magnetic field in low Earth orbit by combining with current running through the tether to generate a force that can be used to counteract atmospheric drag. Most electrodynamic tethers need to be 100's of meters to kilometers long in order to generate significant levels of thrust. However, on a satellite of the femtosatellite and ChipSat size scale, much less thrust is needed to counteract drag, and thus electrodynamic tethers on the order of a few meters is all that is necessary to generate a drag make-up force (*Bell et al.*, 2012).

In order for current to be sourced through the tether, there needs to be a complete circuit. This requires one end of the tethered satellite system to collect electron current while the other end emits electron current as is depicted in Fig. 5.1. Electron collection schemes can be based on attracting electrons to a moderately biased positive spacecraft at one end. Another challenge altogether, however, is how a small spacecraft with limited onboard power, volume, and surface area can emit enough electrons to complete the electrodynamic tether circuit.

One important consideration in the design of the emission area of femtosatellites is what size and shape to make the emission area, which leads to a trade-off between emission area and possible emitted current as there is a maximum space charge limited current density that can be emitted as well as a limit to the emission capability. As the area on the femtosatellite dedicated to emission increases, then the possible emission current increases as well as there is a maximum current that any emitter technology can emit per area. Since there is a minimum emission current needed to match the

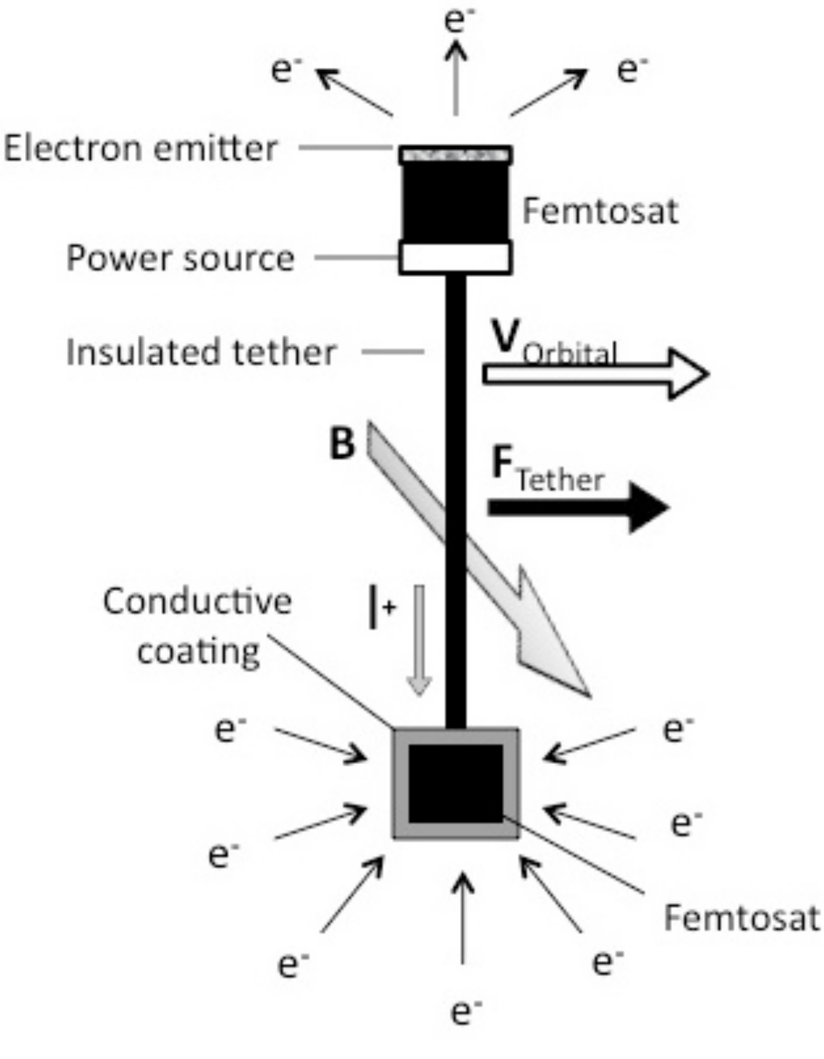

Figure 5.1: Depiction of the Circuit for the Tethered Femtosatellite System (*Bell*, 2010)

collection current, this is a vital constraint.

In addition to a minimum emission current, there is a maximum emission current controlled by the space charge limit. Space charge limited current is the maximum current that can be emitted from a specific emitter, which will vary based on emission parameters as well as the size and geometry of the emission area. Emitted electron current will be space charge limited as previously emitted electrons will occupy the space in front of the emitter and serve to repel newly emitted electrons back towards the emitter thus limiting the current that can come out of an emitter of a given size and shape. The most efficient geometry in terms of emission per area is a circular emission region as geometry of this type allows the emitted beam to expand in two directions, as opposed to a strip emission region where the emitted beam can only expand in the shorter direction (*Luginsland et al.*, 2002) thereby forcing electrons to be confined to a smaller region outside of the emitter.

5.2 Space Charge Limit

The space charge limit can be calculated by multiplying the one-dimensional space charge limited condition containing an initial emission velocity (*Luginsland et al.*, 1998) as in Eq. 5.1 with the three-dimensional space charge limited ratio (*Humphries*, 1990) (*Morris*, 2005) as in Eq. 5.2, giving an overall space charge limit as in Eq. 5.3.

$$J_{SCL}(1) = \frac{4\epsilon_0}{9e}\sqrt{\frac{2}{m_e}}\frac{T_0^{3/2}}{D^2}\left[1+\sqrt{1+\frac{eV}{T_0}}\right]^3 \tag{5.1}$$

$$\frac{J_{SCL}(3)}{J_{SCL}(1)} = 1+\left(\frac{D}{2r_b}\right)^2 \tag{5.2}$$

$$J_{SCL}(3) = \left[\frac{4\epsilon_0}{9e}\sqrt{\frac{2}{m_e}}\frac{T_0^{3/2}}{D^2}\left[1+\sqrt{1+\frac{eV}{T_0}}\right]^3\right]\cdot\left[1+\left(\frac{D}{2r_b}\right)^2\right] \tag{5.3}$$

where T_0 is the initial emission energy, which can be determined by Eq. 5.4

$$T_0 = eV_0 \tag{5.4}$$

and where V_0, is the potential between the cathode and the surrounding atmosphere, which is the cathode potential minus the sheath potential. In a typical ionosphere, the sheath is about 1 V across a 1.5 cm gap (*Morris*, 2005). As Eq. 5.3 shows, with the cathode potential fixed (as will be shown in Section 5.4) for each femtosatellite and altitude, and an approximation for the sheath, the space charge limit will depend solely on the radius of the circular emission area.

5.3 Possible Neutralization Techniques for Electrodynamically Tethered Femtosatellites

For a system of electrodynamically tethered femtosatellites, the propulsion system is a simple short, insulated, semi-rigid, metallic tether combined with the Earth's natural magnetic field. This means that just like NanoFET and colloidal thrusters, the propellant does not need a gas feed system, and thus a typical hollow cathode neutralizer, commonly used for ion and hall thrusters, would require a separate gas feed system which would both significantly increase complexity and decrease efficiency. In addition, the femtosatellite has very little available power as is shown later in Table 5.1, up to a maximum of 1.12 W.

An additional constraint is the previously discussed available emission area, with the requirement that the emission area cannot take up a large amount of the available area on the satellite, as a large portion of the available area has to go to generating power through the use of solar arrays (*Bell et al.*, 2012). Before determining how much room to allocate for the emission area, it is imperative to examine if femtosatellite area is better served as area for solar panels or for electron emission. From experimental data generated from *Whaley and Bellew* (2009), current voltage equations can be derived for two different sized emission regions, with one 75% larger than the other. These two current voltage equations have Fowler-Nordheim Parameters (a_{FN},b_{FN}) as shown in Eq. 5.5

$$a_{FN\_smaller\_area} = 0.017\ A/V^2 \tag{5.5a}$$

$$b_{FN\_smaller\_area} = 488\ V \tag{5.5b}$$

$$a_{FN\_bigger\_area} = 0.030\ A/V^2 \tag{5.5c}$$

$$b_{FN\_bigger\_area} = 487\ V \tag{5.5d}$$

Using these parameters and the Fowler-Nordheim equation, it can be determined that at emission currents of 0.2 mA and 1 mA, the voltage required to emit those current levels drop from 46.4 V to 44.3 V (1 mA) and 41.1 V to 39.4 V (0.2 mA). These are voltage and power drops of 4.5% (1 mA) and 4.1% (0.2 mA). This is compared to an active area increase of 75%. This seems to indicate that there is little incentive to increase the active emission area in order to decrease the power level needed to drive the emission current. It also seems to indicate that any extra available area is better served going to solar arrays rather than emission regions if the only trades are power levels.

5.3.1 Hot Filaments

The most common ways to neutralize charge is to either emit a cloud of plasma (often by utilizing a hollow cathode) or to emit electrons in response to the emission of positive charge for propulsion. While hollow cathodes are the preferred technology for ion thrusters and hall thrusters, for smaller and lighter satellites, such as femtosatellites, heavy gas-based systems are not feasible. Thus, alternative neutralization approaches are needed. One well developed, and well tested technology is a hot filament, or also referred to as a hot cathode, thermionic cathode, or thermionic emitter.

Hot cathodes, at their simplest, are a piece of metal that is heated up to a point so that the most energetic electrons (tail of the Maxwell-Boltzmann distribution) are past the binding potential or work function of the metal, which is termed thermionic emission, and in this situation is considered direct heating. The most common metal originally used in hot filaments was tungsten as it has a high melting point allowing it to be heated up to the point where thermionic emission occurs without it losing its strength. However, over time the method has been refined to make hot cathodes more efficient. The first improvement was tungsten coated with a lower work function material. This lower work function material is called the emissive layer, and due to its lower work function, it has a lower binding potential meaning that a lower temperature is needed before electrons start being emitted. In addition it results in less ions being emitted (ion emission detracts from the emission capability of emitters).

There are various materials that tungsten can be coated or doped with for improved performance. Oxide-coated cathodes, varying from barium oxide to strontium oxide to calcium oxide, are very common as they start emitting electrons at a much lower temperature than normal tungsten due to their low work function; however, their performance will degrade rapidly when exposed to oxygen ions (*Itoh et al.*, 1987), and thus are not great for in-space applications. Another common coating is lanthanum hexaboride (LaB_6) as they have an extremely low work function at about 2.5 eV and they are resistant to oxygen ion poisoning allowing them to hold up well in space. This coating increases the lifetime of the filament by 10-15 times. Another type of boride coating that is even better than LaB_6 is cerium hexaboride (CeB_6), which has a lifetime that is 1.5 times longer than LaB_6. The only downside to these coatings is their high cost. Characteristics of the described technologies are as shown

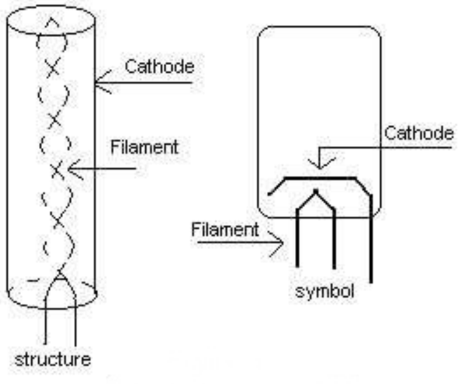

Figure 5.2: Depiction of an Indirectly Heated Hot Filament

below in Table 5.1 (*Turner*, 1976).

Material	Tungsten	Oxide Coated Tungsten	Barium Aluminate
Operating Temperature (K)	2500	1100	1300
Emission Efficiency (mA/W)	5	500	400
Specific Emission (A/cm^2)	0.5	10	4

Table 5.1: Characteristics of Different Hot Filament Materials

A second improvement in addition to changing the metal responsible for the thermionic emission, is the way which it is heated up. Rather than directly heating the filament that emits electrons, a second method is indirect heating. Indirect heating is where the filament is heated, but is not the material responsible for the emission of electrons. Instead, the electrons are emitted by the cathode, which is electrically insulated from the filament, but not thermally insulated as is shown in Fig. 5.2 (*Setiawan*, 2009). Thus, the heat is transferred from the filament to the cathode, which then emits electrons, and in this case the filament is termed the heater. An indirectly heated cathode has the same potential throughout its surface rather than an uneven potential in the case of a directly heated cathode thereby making the electron emission more uniform. The filament, or heater, is still typically made of tungsten due to its high melting point, and the cathode is oftentimes a nickel tube.

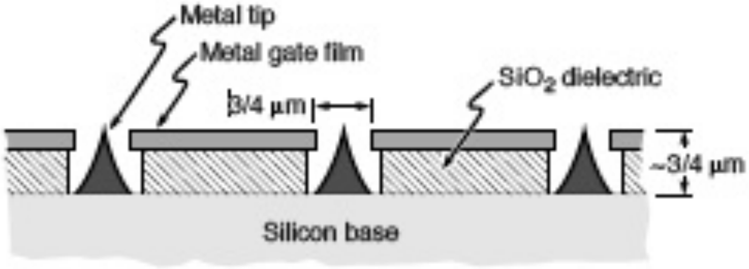

Figure 5.3: Schematic of Spindt Cathode (*Spindt*, 1968)

5.3.2 Field Emitter Array Cathodes

As opposed to the hot filaments, another possible neutralization technology on the other end of the spectrum is the field emitter array cathode which is a type of cold cathode, as opposed to hot cathodes. These devices rely on electron field emission to produce electrons. These cathodes are able to emit electrons at low powers up to well over 1 A of current (*Agüero and Adamo*, 2000), which is well above the threshold needed for the femtosatellite system.

One specific type is the Spindt cathode field emitter array that is manufactured in a specific holed array pattern (*Spindt*, 1968). A Spindt cathode is composed of sharp tips that electrons are actually emitted out of, two conductors that generate the large electric field needed for electron field emission, and an insulating layer to separate the two conductors. The sharp tips rest on the lower conductor, called the base, and there are holes in the top conductor, called the gate, so that electrons emitted from the sharp tips can escape. A schematic of the Spindt cathode is as shown in Fig. 5.3.

Spindt cathodes can have a density of 5×10^7 tips/cm^2 resulting in possible current densities of 5000 A/cm^2 and only voltages of up to 100 V needed to produce such emission, meaning that low power operation is very possible (mA of current requires less than a watt of power). An additional benefit of such a neutralization technology is its flat-panel form, which allows for it to be very easily placed in an unobtrusive manner on the femtosatellite. Major downsides of such a technology are its lack of in-space testing and with the sharp tips being such a critical part of its operation, dulling of the tips by bombardment of oxygen ions is of significant concern as well as surface contamination causing oxidation on the surface of the cathode decreasing its efficiency. Lifetime tests have been run on Spindt cathodes of up to eight years in laboratory though.

5.4 Femtosatellite Space Charge Limit

Now that there is an estimate for the space charge limit, the space charge limit can be compared to the minimum emission current that the femtosatellite needs to reach. Two possible methods of emitting current on a femtosatellite are field emitter array cathodes (FEACs) and hot filaments. By knowing the capabilities of these technologies (*Turner*, 1976), the characteristics of these emitters can also be included in the comparison.

There are four sizes of femtosatellites of interest, which will be described as small, medium, large, and very large. Each of these sizes of femtosatellites have different current levels that need to flow through the electrodynamic tether. The current that flows through the electrodynamic tether generates the thrust needed for the femtosatellite to overcome the natural drag of the system. If this generated thrust is not sufficient to overcome the drag, then the system will slowly fall back down to Earth. In addition, at different altitudes, there are different current levels needed to overcome drag, as drag will be different at each altitude. In order to flow this level of current through the electrodynamic tether, the current must be collected as well as emitted resulting in a minimum required electron emission current. There is also a minimum voltage that the cathode must be at in order to emit. The four femtosatellite characteristics are illustrated below in Table 5.2 (*Bell*, 2010).

In Table 5.2, the available power for each satellite is based on the ability of each satellite to generate power using on-board solar cells. A specific and different cathode and anode voltage are needed to generate a specific tether current, and with the available power, there is a maximum current that can be sourced through the tether, which corresponds with a given cathode and anode voltage providing the anode voltage shown in Table 5.2 as well as the fixed cathode voltage used to determine the space charge limit shown previously (*Bell et al.*, 2012).

	Small	Medium	Large	Very Large
Mass (g)	0.4	2	50	250
Dimensions (cm x cm x cm)	1 x 1 x 0.2	1 x 1 x 1	5 x 5 x 1	5 x 5 x 5
Tether Current @ 350 km (mA)	0.3	0.6	5.4	7.7
Tether Current @ 500 km (mA)	0.2	0.4	3.4	4.7
Cathode Voltage (V)	39	42	51	53
Anode Bias (V)	12	25	42	88
Available Power (mW)	15	45	524	1120

Table 5.2: Constraints for Various Sized Femtosatellites

Fig. 5.4 and Fig. 5.5 compare the space charge limited current with the minimum emission current and the maximum emission capabilities of FEACs and hot filaments for the small femtosatellites, whereas Fig. 5.6 and Fig. 5.7, Fig. 5.8 and Fig. 5.9, and Fig. 5.10 and Fig. 5.11 do the same for medium, large, and very large femtosatellites respectively.

With these plots, the two dotted lines are the minimum emission current needed for that particular femtosatellite, with the green dotted line being the current needed at 350 km and the magenta dotted line being the current needed at 500 km. For the FEACs, the various emission current lines are determined by the capabilities of different FEACs. For the hot filaments, the various emission current lines are determined by the different hot cathodes. Thus, in order for the femtosatellite to operate properly, the current emitted must be above the dotted line of relevance depending on height, and must also stay below the dark blue space charge limit line as that is the maximum current that can be emitted by that specific geometry. In addition, the current cannot exceed the FEAC or hot cathode performance line as

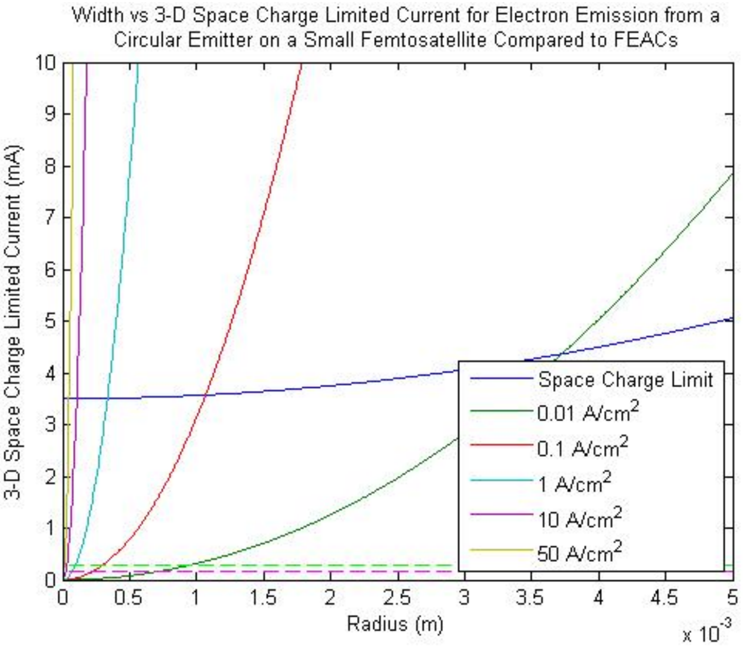

Figure 5.4: Comparison of Space Charge Limit with Minimum Emission Current and Maximum Emission Capabilities of FEACs for a Small Femtosatellite

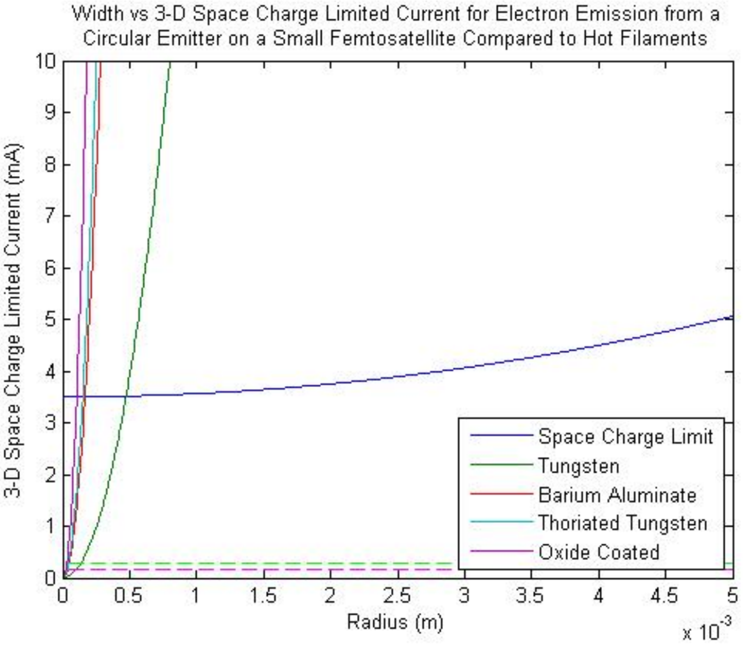

Figure 5.5: Comparison of Space Charge Limit with Minimum Emission Current and Maximum Emission Capabilities of Hot Filaments for a Small Femtosatellite

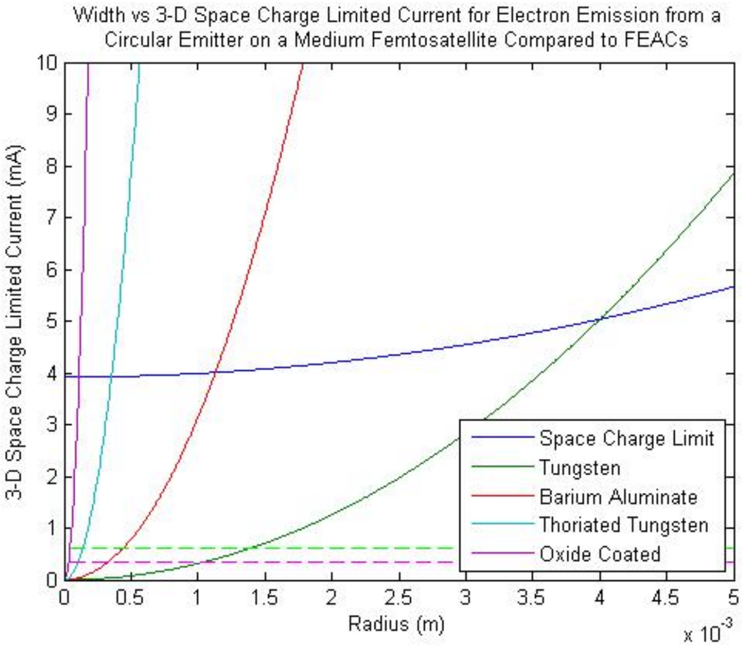

Figure 5.6: Comparison of Space Charge Limit with Minimum Emission Current and Maximum Emission Capabilities of FEACs for a Medium Femtosatellite

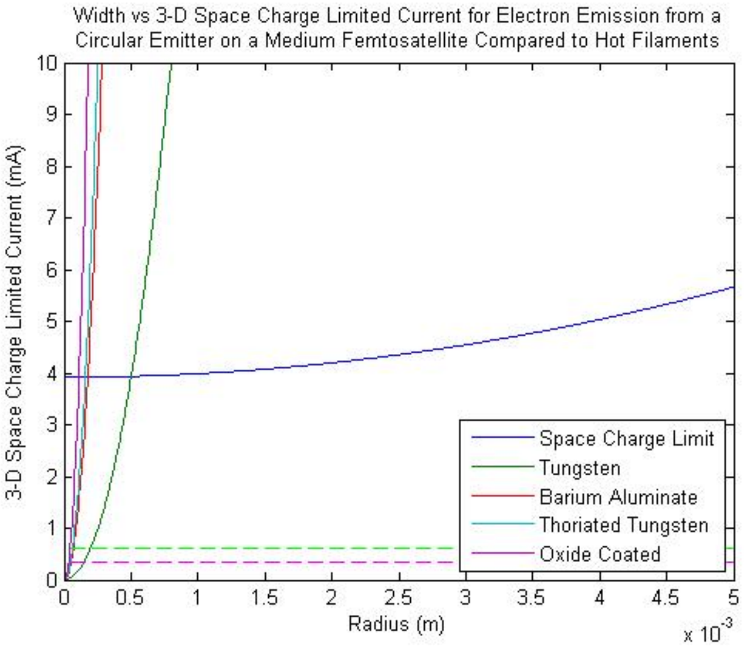

Figure 5.7: Comparison of Space Charge Limit with Minimum Emission Current and Maximum Emission Capabilities of Hot Filaments for a Medium Femtosatellite

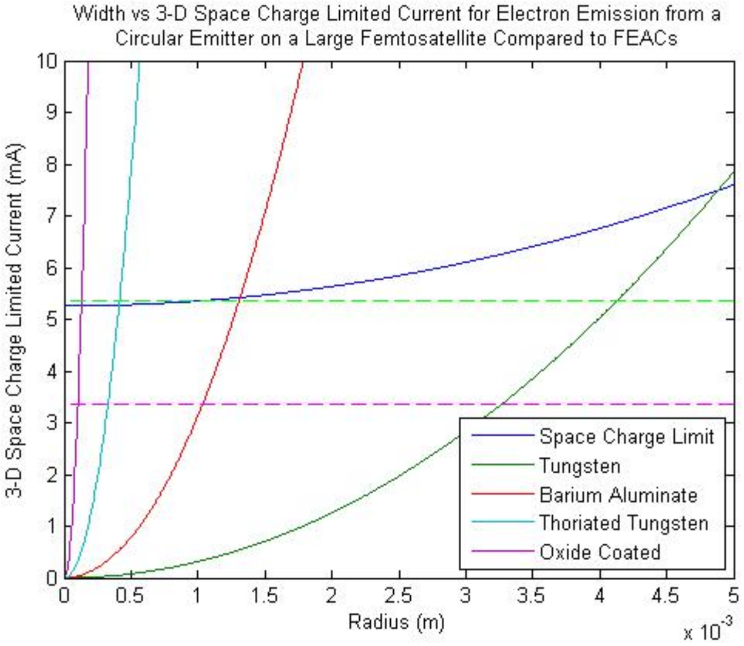

Figure 5.8: Comparison of Space Charge Limit with Minimum Emission Current and Maximum Emission Capabilities of FEACs for a Large Femtosatellite

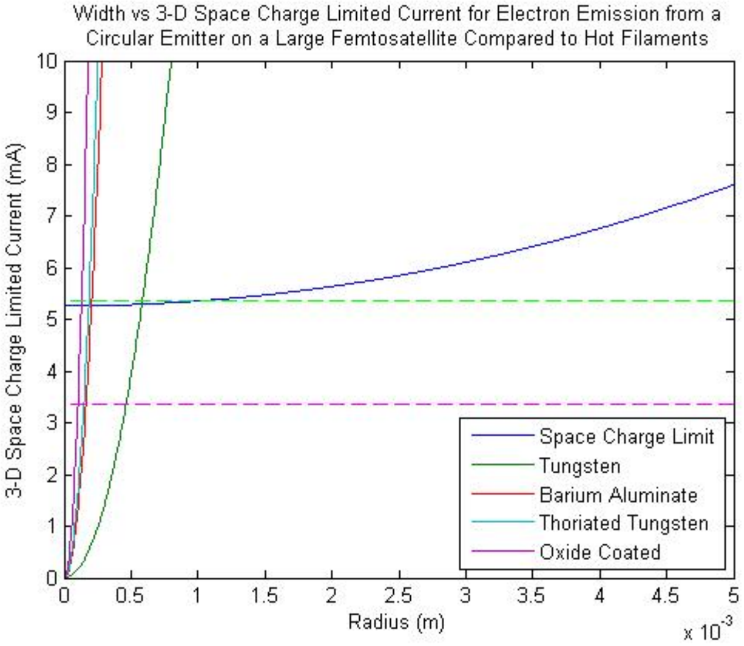

Figure 5.9: Comparison of Space Charge Limit with Minimum Emission Current and Maximum Emission Capabilities of Hot Filaments for a Large Femtosatellite

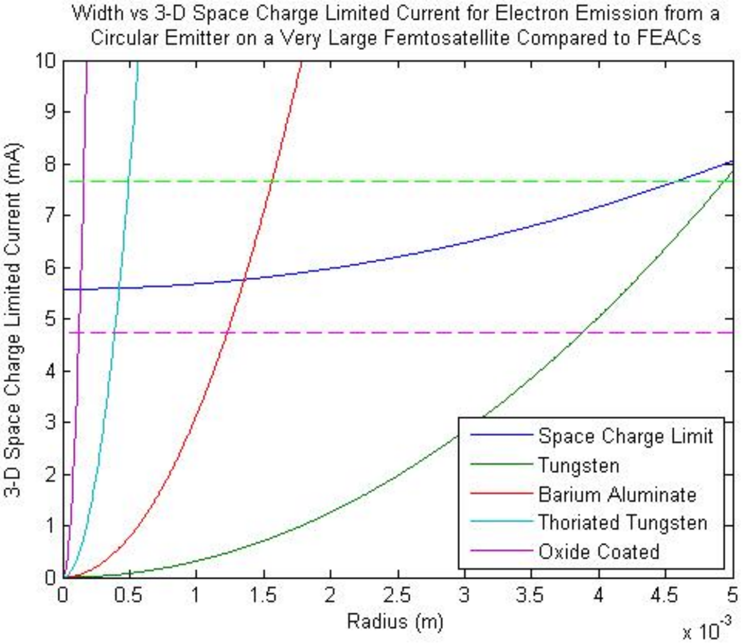

Figure 5.10: Comparison of Space Charge Limit with Minimum Emission Current and Maximum Emission Capabilities of FEACs for a Very Large Femtosatellite

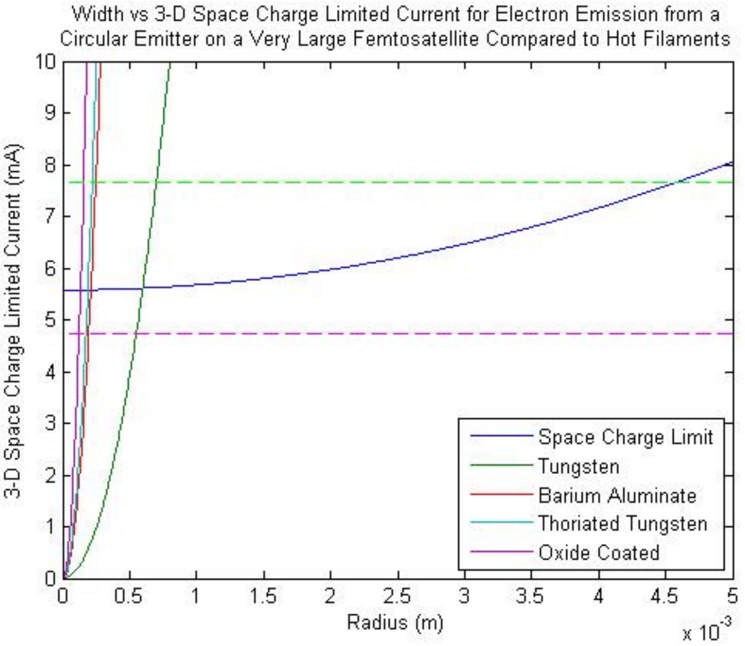

Figure 5.11: Comparison of Space Charge Limit with Minimum Emission Current and Maximum Emission Capabilities of Hot Filaments for a Very Large Femtosatellite

that is the maximum capability of that technology. Thus, for a small femtosatellite, a 1 mm radius emitter with the least effective technology, is enough to meet the constraints. A medium femtosatellite needs a slightly larger emitter of approximately 1.35 mm radius is enough to meet the constraints. In both these cases, the space charge limit is well above the necessary emission current meaning that there should be no issues of exceeding it. In addition, the emission area accounts for under 6% of the surface area for a single face of the femtosatellite. A large femtosatellite needs to have an emission area that is at least 1 mm in radius at 350 km regardless of emission capability due to space charge limited current density. However, a large femtosatellite could need an emitter up to 4 mm in radius in the worst case scenario of 350 km in altitude, and the worst capability FEAC. This still accounts for just 2% of the surface area for a single face of the femtosatellite. A very large femtosatellite needs to have an emission area that is at least 4 mm in radius at 350 km regardless of emission capability. However, it could need an emitter that is close to 5 mm in radius in the worst case scenario, which accounts for just over 3% of the surface area.

5.5 Summary

As the sizes and requirements of the femtosatellites change, the emitter constraints change as well. Typically, as the femtosatellite increases in size, the cathode potential increases as well, which increases the space charge limited current density. In addition, the minimum emitter current continues to increase with size as well. Thus based on these constraints, and the capabilities of the various available emitters, the emission region can be well determined, and in all current scenarios the emission region is under 6% of one side of a femtosatellite.

CHAPTER VI

Conclusions and Recommendations for Future Research

This dissertation focuses on neutralization techniques for various charged particle thrusters such as NanoFET and colloidal thrusters, as well as electrodynamically tethered femtosatellites. The feasibility, practicality, and effectiveness of these various neutralization techniques are thoroughly studied with the available particle-in-cell software and analytics. In some cases the results showed a difficult neutralization technique to implement properly, but in other cases the neutralization technique seemed feasible. These techniques all require continued study either with a more developed software with additional tools to simulate the real world situation as closely as possible, or experimentation to corroborate capabilities that are assumed to be possible.

6.1 Summary and Conclusions of Research

This thesis examines the possibility of a self-neutralizing charged particle thruster which was previously assumed to be feasible without careful examination. The research in this thesis examined the feasibility of various neutralization techniques of electric propulsion thrusters principally for nanospacecraft.

6.1.1 Spatial-Varying, Common Time Emission (SVCTE) Neutralization Scheme

A spatial-varying, common time emission beam will be net neutral and be emitted from a net neutral spacecraft. However, the emitted neutral beam creates equal amounts of image charge back on the spacecraft that do not neutralize one another. Thus, an axial electric field will be generated pulling the spacecraft and the emitted beam towards one another causing a degradation in thrust.

This degradation in thrust is minimized when the oppositely charged emitted beams are moved closer to one another (the best case, although unrealistic, is when they overlap) and the beam width is minimized. In addition, the loss in thrust is reduced when the specific charge is increased as this will cause the emitted beams will overlap more thereby reducing the electric field near the spacecraft.

Most importantly, degradation in thrust will increase linearly with increase in emitted current density. This means that although there is a 0.01% loss in thrust when emitting a physical maximum 0.967 A/m^2 (14.49 mA) of current, there will be significantly less thrust lost when emitting the steady state maximum current of 312.5 μA. This implies that a spatial-varying, common time emission scheme is capable of self-neutralizing if moving the beams close together is practical.

6.1.2 Time-Varying, Common Spatial Emission (TVCSE) Neutralization Scheme

A time-varying, common spatial emission beam will also be net neutral and be emitted from a net neutral spacecraft. The one additional benefit is that both the positive and negative image charge are confined within the same emitter region on the spacecraft and thus the net image charge will be neutralized at certain times.

With a time-varying, common spatial emission scheme, the image charge on the spacecraft, electric field near the spacecraft, and thus the thrust degradation will exhibit local maximums and minimums throughout the beam emission period. The timing and magnitude of these local maximums and minimums will vary depending on the frequency of oscillation between positive and negative emission along with parameters such as current density and specific charge.

The higher the frequency of oscillation, the lower the average thrust degradation will be. At a very high frequency of 5 MHz, there is just a 0.00001% loss in thrust as the emitted beam at such a high frequency is essentially a neutral beam. However, such a beam is impractical to emit. A beam that is practical, a 20 kHz 0.967 A/m^2 beam generates just a 0.1% loss in thrust. It requires a 200 kHz 0.967 A/m^2 beam to generate just a 0.01% loss in thrust equivalent to the spatial-varying, common time emission neutralization scheme.

6.1.3 Neutralization by Background Plasma

A neutralization scheme utilizing the background plasma has the benefit of a single emitter that only needs to emit at one polarity thereby reducing complexity. However, the simulations are much more complex due to the background plasma that must be introduced.

The floating potential of a surface immersed in a stationary plasma is a well-established analytical quantity, and can be extrapolated to analytically determine the floating potential of a flowing spacecraft immersed in a co-rotating plasma. Such a floating potential will vary based on spacecraft size and shape, spacecraft velocity, and ambient plasma temperature, but will not depend on plasma density.

Analytical and simulation results for the floating potential of such a spacecraft can be calculated and compared while varying spacecraft velocity, plasma temperature, and plasma density across the typical range experienced in lower Earth orbit. When spacecraft velocity, plasma temperature, and plasma density are varied, the simulated floating potential stays between the upper and lower analytical bounds.

At the base case plasma parameters it appears that for all emission current levels, the presence of the ambient plasma does not provide the spacecraft with negating the degradation of thrust. However, when the particles are emitted with a specific impulse of less than 1000 seconds, the ambient plasma is able to negate a portion of the degradation in thrust, but not when the specific impulse is at 1000 seconds or above.

However, spacecraft velocity within the lower Earth atmosphere range will not affect the ability of the ambient plasma to negate degradation in thrust. However, at low plasma temperatures and high plasma densities, the ambient plasma is able to negate the degradation in thrust.

6.1.4 Transition from 2D to 3D Particle-in-Cell Code

From the simulations conducted in both 2.5 dimensions (OOPIC PRO^{TM} and VSim^{TM}) and 3 dimensions (VSim^{TM}), it can be seen that the 2.5-dimensional simulations can for the most part be considered accurate in the three-dimensional world as well, with the only difference being an assumed depth of 1 meter for purposes of calculations. This provides a simple beginning transition to three-dimensional particle-in-cell simulations, with the only caveat being a different handling of image charge on the spacecraft wall between the two simulation softwares providing slightly different electric fields near the spacecraft.

6.1.5 Feasibility of Hot Filaments and FEACs for Neutralization of Femtosatellites

Femtosatellites provide a unique challenge as they have unique requirements for emission. As they are limited in both size and power, an emitter must be cognizant of these constraints. Thus, two very different emitters are considered, a hot filament (well-tested technology with significant flight heritage) and a field emitter array cathode (relatively new technology with no testing in a space environment).

Significant concerns are if these emitters have the capability to emit at the minimum required current levels, the percentage of surface area that the emitters will occupy, and if the emitters will be able to operate below the space charge limit.

In all cases, the emitter will occupy less than 6% of just a single face of the femtosatellite, making emission area less of a concern. In addition, the only time that space charge limit is of significant concern is when operating the very large spacecraft at the lower altitude (thereby requiring more current to overcome drag), but it is still able to be accomplished with just over 3% of a single face of the very large femtosatellite needing to be allocated for the emitter.

6.2 Recommendations for Future Work

This thesis provides simulation results for various neutralization techniques for charged particle thrusters in 2.5 dimensions combined with a transition to 3 dimensions along with possible neutralization techniques for electrodynamically tethered femtosatellites. However, various aspects of the simulation and analytical results can be expanded upon with an even more developed software and through experimentation.

6.2.1 Expansion of Neutralization Parameters

The simulations shown here focus on a relatively narrow range of parameters based on the needs and capabilities of charged particle thrusters such as NanoFET and colloidal thrusters. For example the simulations are conducted for a narrow range of specific impulse, specific charge, and emitter region sizes. The simulations are also conducted well below space charge limit. If the results shown are to be used for other thrusters, the simulation parameters will need to be expanded so that the thruster under study is more accurately simulated.

6.2.2 Presence of Magnetic Field

The impact that the Earth's magnetic field has on the simulation is touched on briefly in Section 3.4.4 but only in an analytical fashion. The Earth's magnetic field can also be introduced into the simulation by changing the electrostatic simulation into an electromagnetic simulation, preferably in three dimensions. Changing a simulation into an electromagnetic simulation has some unexpected consequences other than a velocity in a third direction, such as a shorter time step required for the simulation to run properly.

6.2.3 Three-Dimensional Simulations

With the new three-dimensional particle-in-cell simulation software VSim^{TM}, the possibility of increasingly realistic simulations is feasible. VSim^{TM} provides the ability to conduct three-dimensional simulations as was shown in Chapter IV. However Chapter IV just scratches the surface of the three-dimensional capabilities of VSim^{TM} by restricting the three-dimensional simulations to a depth of 1 meter. WIth this new three-dimensional particle-in-cell software, it is possible to fully simulate a CubeSat sized spacecraft flying through the ionosphere while emitting nanoparticles or colloids and determine the potential of the spacecraft before and after emission. This should allow for determination of feasibility of different neutralization techniques in a realistic three-dimensional world.

6.2.4 Other VSim^{TM} Capabilities

Three-dimensionality is not the only additional capability that VSim^{TM} possesses that would provide even more accurate simulations. One is a spatially varying grid or mesh, which would help resolve the issue of Debye length to spacecraft size. At higher densities, the Debye length is short and thus, the cell size needs to be relatively small, making it difficult to fit a CubeSat sized spacecraft onto the simulation space in a relatively small number of cells. However, with a variable mesh, the spacecraft can be constructed out of a larger cell size, while the remainder of the simulation consists of the smaller cell size.

Certain VSim^{TM} packages also have the capability for particle interactions, including elastic scattering, impact ionization, recombination, charge exchange, impact excitation, and field ionization. The inclusion of such particle-particle collisions or interactions increases the accuracy of the conducted simulations. This new capability also creates the ability to compare simulated results with the analytical conclusions drawn in Section 2.6 regarding the infrequency of collisions in the simulation space focusing on elastic scattering.

6.2.5 Femtosatellite Emitter Capabilities

With space charge limitations for femtosatellites being established, and with the determination that the emitter size is a relatively insignificant portion of the femtosatellite surface area, it is important to test the actual capabilities of the two emitter types described in Chapter V. FEACs are a relatively novel and untested technology that requires testing for characterization of emission capabilities, and while hot filaments are a well developed technology, it also requires testing for characterization of emission capabilities at the very low power levels allocated for the emitter. These results will show whether or not the provided emitter capabilities used for determination of emitter area is accurate or will require adjustment.

APPENDICES

APPENDIX A

OOPIC PRO^{TM} Code for Spatial-Varying, Common Time Neutralization Emission Scheme

The base input (.inp) file for Section 2.4 is as follows:

```
default

{

Free expansion of the beam, with no applied magnetic field

}

Variables

{

currentDensity = 0.967

lengthX = 0.2

cellsX = 30

lengthPerCellX = lengthX/cellsX

lengthY = 0.15

cellsY = 30

lengthPerCellY = lengthyY/cellsY

beamWidth = 0.015
```

```
beamWidthCells = beamWidth/lengthPerCellY

beamSeparation = 0.015

beamSeparationCells = beamSeparation/lengthPerCellY

current = currentDensity*beamWidth

currentNP2C = current*16666666

driftVelocity = 1e4

}

Region

{

Grid

{

Geometry = 1

J = cellsX

x1s = 0.0

x1f = lengthX

n1 = 1.0

K = cellsY

x2s = 0.0

x2f = lengthY

n2 = 1.0

Rule

{

 Limit

 n1 < 0.25

 Fatal -- n1 < 0.25 grid spacing too nonuniform to ensure accuracy

}

Rule
```

```
{
 Algebra
 J * K > 10000
 Warning -- J*K >= 10000 may mean memory problems!
}
PeriodicFlagX1=1
PeriodicFlagX2=1
}
Control
{
dt = 5e-8
Rule
{
 Limit
 dt <= 0.0
 Fatal -- time step must be positive
}
}
Species
{
name = posparts
m = 4.4E-18
q = 7.32e-16
}
Species
{
name = negparts
```

```
m = 4.4E-18

q = -7.32e-16

}

EmitPort

{

speciesName = posparts

j1 = 0

k1 = 15

j2 = 0

k2 = 15+beamWidth

normal = 1

np2c = currentNP2C

I = current

thetadot = 0.0

v1drift = driftVelocity

v2drift = 0

v3drift = 0

v1thermal = 0

v2thermal = 0

v3thermal = 0

}

EmitPort

{

speciesName = negparts

j1 = 0

k1 = 15-beamSeparation

j2 = 0
```

```
k2 = 15-beamSeparation+beamWidth
normal = 1
np2c = currentNP2C
I = current
thetadot = 0.0
v1drift = driftVelocity
v2drift = 0
v3drift = 0
v1thermal = 0
v2thermal = 0
v3thermal = 0
}
Equipotential
{
Segment
{
j1 = 0
k1 = 0
j2 = 0
k2 = cellsY
normal = 1
}
C = 0
}
Dielectric
{
QuseFlag = 0
```

```
Segment

{

j1 = 0

k1 = cellsY

j2 = cellsX

k2 = cellsY

normal = -1

}

}

Dielectric

{

QuseFlag = 0


Segment

{

j1 = cellsX

k1 = 0

j2 = cellsX

k2 = cellsY

normal = -1

}

}

Dielectric

{

QuseFlag = 0
```

```
Segment

{

j1 = 0

k1 = 0

j2 = cellsX

k2 = 0

normal = 1

}

}

}
```

APPENDIX B

OOPIC PRO^{TM} Code for Temporal-Varying, Common Spatial Neutralization Emission Scheme

The base input (.inp) file for Section 2.5 is as follows:

```
default

{

Free expansion of the beam, with no applied magnetic field

}

Variables

{

pi = 3.14159265358979323846

currentDensity = 0.967

lengthX = 0.2

cellsX = 30

lengthPerCellX = lengthX/cellsX

lengthY = 0.15

cellsY = 30

lengthPerCellY = lengthyY/cellsY
```

```
frequency = 10^6

omega = 2*pi*frequency

current = currentDensity*beamWidth

currentNP2C = current*16666666

driftVelocity = 1e4

}

Region

{

Grid

{

Geometry = 1

J = cellsX

x1s = 0.0

x1f = lengthX

n1 = 1.0

K = cellsY

x2s = 0.0

x2f = lengthY

n2 = 1.0

Rule

{

 Limit

  n1 < 0.25

 Fatal -- n1 < 0.25 grid spacing too nonuniform to ensure accuracy

}

Rule

{
```

```
 Algebra
 J * K > 10000
 Warning -- J*K >= 10000 may mean memory problems!
}
PeriodicFlagX1=1
PeriodicFlagX2=1
}
Control
{
ElectrostaticFlag = 4
dt = 5E-8
Rule
{
 Limit
  dt <= 0.0
 Fatal -- time step must be positive
}
}
Species
{
          name = posparts
        m = 4.4E-18
         q = 7.32e-16
}
Species
{
name = negparts
```

```
m = 4.4E-18

q = -7.32e-16

}

EmitPort

{

speciesName = negparts

j1 = 0

k1 = 15

j2 = 0

k2 = 18

normal = 1

np2c = currentNP2C

I = current

thetadot = 0.0

v1drift = driftVelocity

v2drift = 0

v3drift = 0

v1thermal = 0

v2thermal = 0

v3thermal = 0

xtFlag = 1

F = step(sin(omega*t))

}

EmitPort

{

speciesName = posparts

j1 = 0
```

```
k1 = 15

j2 = 0

k2 = 18

normal = 1

np2c = currentNP2C

I = current

thetadot = 0.0

v1drift = driftVelocity

v2drift = 0

v3drift = 0

v1thermal = 0

v2thermal = 0

v3thermal = 0

xtFlag = 1

F = step(-sin(omega*t))

}

Equipotential

{

C = 0


Segment

{

j1 = 0

k1 = 0

j2 = 0

k2 = cellsY

normal = 1
```

```
}

}

Dielectric

{

QuseFlag = 0


  Segment

{

j1 = 0

k1 = cellsY

j2 = cellsX

k2 = cellsY

normal = -1

}

}

Dielectric

{

QuseFlag = 0


  Segment

{

j1 = cellsX

k1 = 0

j2 = cellsX

k2 = cellsY

normal = -1

}
```

```
}

Dielectric

{

QuseFlag = 0


Segment

{

j1 = 0

k1 = 0

j2 = cellsX

k2 = 0

normal = 1

}

}

}
```

APPENDIX C

OOPIC PRO^{TM} Code for Background Plasma Neutralization Scheme

The base input (.inp) file for Chapter III is as follows, with the simulation run for 24000 time steps to establish the background plasma before a 120 time step run of negative particle emission:

```
default
{
Free expansion of the beam, with no applied magnetic field
}
Variables
{
pi = 3.14159265358979323846
currentDensity = 0.967
lengthX = 0.2
cellsX = 30
lengthPerCellX = lengthX/cellsX
lengthY = 0.15
```

```
cellsY = 30

lengthPerCellY = lengthyY/cellsY

current = currentDensity*beamWidth

currentNP2C = current*16666666

driftVelocity = 1e4

speedOfLight = 2.99792458e+08

electronMass = 9.1093897e-31

unitCharge = electronMass * 1.75881962e11

electronCharge = -1. * unitCharge

ionCharge = unitCharge

unitMassMKS = electronMass / 5.48579903e-04

oxygenMassNum = 15.9994

oxygenMass = unitMassMKS * lithiumMassNum

}

Region

{

Grid

{

Geometry = 1

J = cellsX

x1s = 0.0

x1f = lengthX

n1 = 1.0

K = cellsY

x2s = 0.0

x2f = lengthY

n2 = 1.0
```

```
Rule

{

Limit

n1 < 0.25

Fatal -- n1 < 0.25 grid spacing too nonuniform to ensure accuracy

}

Rule

{

Algebra

J * K > 10000

Warning -- J*K >= 10000 may mean memory problems!

}

PeriodicFlagX1=1

PeriodicFlagX2=1

}

Control

{

ElectrostaticFlag = 4

dt = 5E-8

Rule

{

 Limit

dt <= 0.0

Fatal -- time step must be positive

}

}

Species
```

```
{
name = bgelectrons
m = electronMass
q = electronCharge
}
Species
{
name = oxygen
m = oxygenMass
q = ionCharge
}
Species
{
        name = posparts
        m = 4.4E-18
        q = 7.32e-16
}
Species
{
name = negparts
m = 4.4E-18
q = -7.32e-16
}
PlasmaSource
{
speciesName1 = bgelectrons
units1 = MKS
```

```
v1drift1 = 7500

temperature1 = 132608.7

speciesName2 = oxygen

units2 = MKS

v1drift2 = 7500

temperature2 = 774.6

j1 = 0

j2 = 1

k1 = 0

k2 = 30

sourceRate = 1.125*10^16

np2c=100000

}

EmitPort //This block will be commented out when emission is not desired

{

speciesName = negparts

j1 = 17

k1 = 13

j2 = 17

k2 = 17

normal = 1

np2c = 1

I = 6*10^-8

thetadot = 0.0

v1drift = 1e4

v2drift = 0

v3drift = 0
```

```
v1thermal = 0

v2thermal = 0

v3thermal = 0

xtFlag = 1

F = step(t-1.2*10^-3)

}

Load //ions

{

speciesName = oxygen

units = MKS

v1drift = 7500

temperature = 774.6

//density = DENSITY

density = 1E+10

x1MinMKS = 0

//x1MaxMKS = ZDIM/100

x1MaxMKS = 0.2*13/30

x2MinMKS = 0

//x2MaxMKS = RDIM/100

x2MaxMKS = 0.15

//np2c = (2E14)*CURRENT*ZDIM/(SLOWNESS*EMISSIONVELOCITY)

//np2c=(1e-7)*DENSITY/5 //0=unmoving background charge

np2c = 5e-5*10000000000/5

}

Load //electrons

{

speciesName = bgelectrons
```

```
units = MKS

v1drift=  7500

temperature = 132608.7

//density = DENSITY

density = 1E+10

x1MinMKS = 0

//x1MaxMKS = ZDIM/100

x1MaxMKS = 0.2*13/30

x2MinMKS = 0

//x2MaxMKS = RDIM/100

x2MaxMKS = 0.15

//np2c = (1e-7)*DENSITY/5

np2c = 5e-5*10000000000/5

}

Load //ions

{

speciesName = oxygen

units = MKS

v1drift = 7500

temperature = 774.6

//density = DENSITY

density = 1E+10

x1MinMKS = 0.2*13/30

//x1MaxMKS = ZDIM/100

x1MaxMKS = 0.2*17/30

x2MinMKS = 0

//x2MaxMKS = RDIM/100
```

```
x2MaxMKS = 0.15*13/30
//np2c = (2E14)*CURRENT*ZDIM/(SLOWNESS*EMISSIONVELOCITY)
//np2c=(1e-7)*DENSITY/5 //0=unmoving background charge
np2c = 5e-5*10000000000/5
}
Load //electrons
{
speciesName = bgelectrons
units = MKS
v1drift = 7500
temperature = 132608.7
//density = DENSITY
density = 1E+10
x1MinMKS = 0.2*13/30
//x1MaxMKS = ZDIM/100
x1MaxMKS = 0.2*17/30
x2MinMKS = 0
//x2MaxMKS = RDIM/100
x2MaxMKS = 0.15*13/30
//np2c = (1e-7)*DENSITY/5
np2c = 5e-5*10000000000/5
}
Load //ions
{
speciesName = oxygen
units = MKS
v1drift = 7500
```

```
temperature = 774.6
//density = DENSITY
density = 1E+10
x1MinMKS = 0.2*13/30
//x1MaxMKS = ZDIM/100
x1MaxMKS = 0.2*17/30
x2MinMKS = 0.15*17/30
//x2MaxMKS = RDIM/100
x2MaxMKS = 0.15
//np2c = (2E14)*CURRENT*ZDIM/(SLOWNESS*EMISSIONVELOCITY)
//np2c=(1e-7)*DENSITY/5 //0=unmoving background charge
np2c = 5e-5*10000000000/5
}
Load //electrons
{
speciesName = bgelectrons
units = MKS
v1drift = 7500
temperature = 132608.7
//density = DENSITY
density = 1E+10
x1MinMKS = 0.2*13/30
//x1MaxMKS = ZDIM/100
x1MaxMKS = 0.2*17/30
x2MinMKS = 0.15*17/30
//x2MaxMKS = RDIM/100
x2MaxMKS = 0.15
```

```
//np2c = (1e-7)*DENSITY/5

np2c = 5e-5*10000000000/5

}

Load //ions

{

speciesName = oxygen

units = MKS

v1drift = 7500

temperature = 774.6

//density = DENSITY

density = 1E+10

x1MinMKS = 0.2*17/30

//x1MaxMKS = ZDIM/100

x1MaxMKS = 0.2

x2MinMKS = 0

//x2MaxMKS = RDIM/100

x2MaxMKS = 0.15

//np2c = (2E14)*CURRENT*ZDIM/(SLOWNESS*EMISSIONVELOCITY)

//np2c=(1e-7)*DENSITY/5 //0=unmoving background charge

np2c = 5e-5*10000000000/5

}

Load //electrons

{

speciesName = bgelectrons

units = MKS

v1drift = 7500

temperature = 132608.7
```

```
//density = DENSITY

density = 1E+10

x1MinMKS = 0.2*17/30

//x1MaxMKS = ZDIM/100

x1MaxMKS = 0.2

x2MinMKS = 0

//x2MaxMKS = RDIM/100

x2MaxMKS = 0.15

//np2c = (1e-7)*DENSITY/5

np2c = 5e-5*10000000000/5

}

Dielectric

{

QuseFlag = 0


Segment

{

j1 = 0

k1 = 0

j2 = 0

k2 = 30

normal = 1

}

name = boundary

IdiagFlag = 1

}

Dielectric
```

```
{
QuseFlag = 0

  Segment
{
j1 = 0
k1 = 30
j2 = 30
k2 = 30
normal = -1
}
}
Dielectric
{
QuseFlag = 0

  Segment
{
j1 = 30
k1 = 0
j2 = 30
k2 = 30
normal = -1
}
name = right
IdiagFlag = 1
}
```

```
Dielectric
{
QuseFlag = 0

Segment
{
j1 = 0
k1 = 0
j2 = 30
k2 = 0
normal = 1
}
}
CurrentSource
{
C=0

Segment
{
j1 = 13
k1 = 13
j2 = 13
k2 = 17
normal = 1
}

Segment
```

```
{
j1 = 13
k1 = 17
j2 = 17
k2 = 17
normal = -1
}

Segment
{
j1 = 17
k1 = 13
j2 = 17
k2 = 17
normal = -1
}

Segment
{
j1 = 13
k1 = 13
j2 = 17
k2 = 13
normal = 1
}
}
}
```

BIBLIOGRAPHY

BIBLIOGRAPHY

Agüero, V., and R. Adamo (2000), Space Applications of Spindt Cathode Field Emission Arrays, in *Spacecraft Charging Technology Conference.*

Bell, I. (2010), Electrodynamic Tethers for ChipSat and Nanospacecrafts, in *Spacecraft Charging Technology Conference.*

Bell, I., D. Liaw, B. Gilchrist, S. Bilén, J. McTernan, R. Hoyt, and N. Voronka (2012), The Potential of Miniature Electrodynamic Tethers to Enhance Capabilities of Femtosatellites, in *Spacecraft Charging Technology Conference.*

Beynon, J., E. Cohen, D. Goldin, M. Huberman, P. Kidd, and S. Zafran (1968), Present Status of Colloid Microthruster Technology, *Journal of Spacecraft and Rockets*, *5*, 1319–1324.

Bilén, S. (1998), Pulse Propagation Along Conductors in Low-Density Cold Plasmas as Applied to Electrodynamic Tethers in the Ionosphere, Ph.D. thesis, University of Michigan.

Bilén, S., B. Gilchrist, C. Bonifazi, and E. Melchioni (1995), Transient response of an electrodynamic tether system in the ionosphere: TSS-1 first results, *Radio Science*, *30*, 1519–1535.

Birdsall, C. (1991), Particle-in-Cell Charged-Particle Simulations, Plus Monte Carlo Collisions with Neutral Atoms, PIC-MCC, *IEEE Transactions on Plasma Science*, *19*, 65–85.

Busek (2010), Space propulsion and systems, `http://www.busek.com/`, accessed: 2010-03-01.

Byers, D. (2009), Personal Communication at MACEEP Kick-Off Meeting in September 2009.

Cairns, I. (1999), Earth's atmosphere, `http://www.physics.usyd.edu.au/~cairns/teaching/lecture16/node2.html`, accessed: 2011-09-01.

Casalino, L., and G. Colasurdo (2004), Optimization of Variable-Specific-Impulse Interplanetary Trajectories, *Journal of Guidance, Control, and Dynamics*, *27*, 678–684.

di Geofisica e Vulcanologia, I. N. (2011), Ionosphere, `http://roma2.rm.ingv.it/en/research_areas/4/ionosphere`, accessed: 2011-09-01.

Domonkos, M., A. Gallimore, and M. Patterson (1997), An Evaluation of Hollow Cathode Scaling to Very Low Power and Flow Rate, in *International Electric Propulsion Conference*.

Enloe, C., D. Cooke, S. Meassick, C. Chan, and M. Tautz (1993), Ion collection in a spacecraft wake: Laboratory simulations, *Journal of Geophysical Research*, *98*, 13,635–13,644.

Félici, N. (1966), Forces et Charge de Petits Objets en Contact avec une Électrode Affectée d'un Champ Électrique, *Revue Générale de l'Électricité*, *75*, 1145–1160.

Gallagher, D., P. Craven, and R. Comfort (1988), An Empirical Model of the Earth's Plasmaphere, *Advances in Space Research*, *8*, 15–24.

Gilchrist, B., C. Bonifazi, S. Bilén, W. Raitt, W. Burke, N. Stone, and J. Lebreton (1998), Enhanced electrodynamic tether currents due to electron emission from a neutral gas discharge: Results from the TSS-1R mission, *Geophysical Research Letters*, *25*, 437–440.

Gilchrist, B., K. Jensen, A. Gallimore, and J. Severns (2000), Space Based Applications For FEA Cathodes (FEACs), in *Materials Issues in Vacuum Microelectronics: Symposium Proceedings*.

Hays, P., and A. Nagy (1973), Thermal Electron Energy Distribution Measurements in the Ionosphere, *Planetary Space Sciences*, *21*, 1301–1306.

Hibbeler, R. (2007), *Engineering Mechanics Dynamics*, 11 ed., Pearson Prentice Hall, Upper Saddle River, New Jersey.

Holbert, K. (2006), Spacecraft charging, `http://holbert.faculty.asu.edu/eee560/spc-chrg.html`, dr. Holbert's EEE 598 Course at ASU.

Humphries, S. (1990), *Charged Particle Beams*, John Wiley and Sons, Inc., Hoboken, New Jersey.

Itoh, S., M. Yokoyama, and K. Morimoto (1987), Poisonous Gas Effects on the Emission of Oxide-Coated Cathodes, *Journal of Vacuum Science and Technology A: Vacuum, Surfaces, and Films*, *5*, 3430–3435.

Kidd, P. (1968), Parametric Studies with a Single-Needle Colloid Thruster, *Journal of Spacecraft and Rockets*, *5*, 1034–1039.

Langmuir, D., E. Stuhlinger, and J. Sellen, Jr. (1961), *Electrostatic Propulsion: A Selection of Technical Papers Based Mainly on a Symposium of the American Rocket Society*, Academic Press, New York, NY.

Lau, Y. (2001), A Simple Theory on the Two-Dimensional Child-Langmuir Law, *Physical Review Letters*, *87*.

Liaw, D., T. Liu, and B. Gilchrist (2011a), Simulation of Self-Neutralization Techniques for Charged Particle Thrusters, in *International Electric Propulsion Conference*.

Liaw, D., T. Liu, and B. Gilchrist (2011b), Simulation of Self-Neutralization Techniques for Charged Particle Thrusters, in *AIAA/ASME/SAE/ASEE Joint Propulsion Conference*.

Liaw, D., T. Liu, and B. Gilchrist (2012), Simulation of Using Background Plasma to Neutralize Charged Particle Thrusters on Nanospacecraft, in *Spacecraft Charging Technology Conference*.

Lieberman, M., and A. Lichtenberg (2005), *Principles of Plasma Discharges and Materials Processing*, John Wiley and Sons, Inc., Hoboken, NJ.

Liu, T. (2010), The Design Space of a Micro/Nano-Particle Electrostatic Propulsion System, Ph.D. thesis, University of Michigan.

Lozano, P. (2003), Studies on the Ion-Droplet Mixed Regime in Colloid Thrusters, Ph.D. thesis, Massachusetts Institute of Technology.

Luginsland, J., Y. Lau, and R. Gilgenbach (1996), Two-Dimensional Child-Langmuir Law, *Physical Review Letters*, *77*, 4668–4670.

Luginsland, J., S. McGee, and Y. Lau (1998), Virtual Cathode Formation due to Electromagnetic Transients, *IEEE Trans. Plasma Sci.*, *26*, 901–904.

Luginsland, J., Y. Lau, R. Umstattd, and J. Watrous (2002), Beyond the Child-Langmuir law: A Review of Recent Results on Multidimensional Space-Charge-Limited Flow, *Physics of Plasmas*, *9*, 2371–2376.

Marrese, C., and A. Gallimore (1998), Field Emission Array Cathode Performance in Electric Propulsion System Environments, in *IEEE International Conference on Plasma Science*.

Martinez-Sanchez, M. (2004), Colloidal engines, `http://ocw.mit.edu/courses/aeronautics-and-astronautics/16-522-space-propulsion-spring-2004/lecture-notes/lecture23_25.pdf`, lecture 23-25 of Course 16.522.

Morris, D. (2005), Optimizing Space-Charge Limits of Electron Emission Into Plasmas With Application to In-Space Electric Propulsion, Ph.D. thesis, University of Michigan.

Musinski, L. (2009), Investigation of a Micro- and Nano-Particle In-Space Electrostatic Propulsion Concept, Ph.D. thesis, University of Michigan.

NASA (2004), Ion propulsion: Farther, faster, cheaper, `http://www.nasa.gov/centers/glenn/technology/Ion_Propulsion1.html`, accessed: 2013-03-01.

Otsuka, Y., S. Kawamura, N. Balan, S. Fukao, and G. Bailey (1998), Plasma Temperature Variations in the Ionosphere over the Middle and Upper Atmosphere Radar, *Journal of Geophysical Research: Space Physics*, *103*, 20,705–20,713.

Patel, P., D. Scheeres, and A. Gallimore (2006), Maximizing Payload Mass Fractions of Spacecraft for Interplanetary Electric Propulsion Missions, *Journal of Spacecraft and Rockets*, *43*, 822–827.

Patterson, M. (1997), Low-Power Ion Propulsion for Small Spacecraft, in *AIAA/ASME/SAE/ASEE Joint Propulsion Conference*.

Samir, U. (1981), Bodies in flowing plasmas: Spacecraft measurements, *Advances in Space Research*, *1*, 373–384.

Samir, U., and A. Willmore (1965), The distribution of charged particles near a moving spacecraft, *Planetary Space Sciences*, *13*, 285–296.

Samir, U., and G. Wrenn (1969), The dependence of charge and potential distribution around a spacecraft on ionic composition, *Planetary Space Sciences*, *17*, 693–706.

Samir, U., and G. Wrenn (1972), Experimental evidence of an electron temperature enhancement in the wake of an ionospheric satellite, *Planetary Space Sciences*, *20*, 899–904.

Samir, U., E. Maier, and B. Troy, Jr. (1973), The angular distribution of ion flux around an ionospheric satellite, *Journal of Atmospheric and Terrestrial Physics*, *35*, 513–519.

Samir, U., R. Gordon, L. Brace, and R. Theis (1979), The near-wake structure of the atmosphere explorer C (AE-C) satellite: A parametric investigation, *Journal of Geophysical Research*, *84*, 513–525.

Samir, U., N. Stone, and K. Wright, Jr. (1986), On plasma disturbances caused by the motion of the space shuttle and small satellites: A comparison of in situ observations, *Journal of Geophysical Research*, *91*, 277–285.

Sasaki, S., et al. (1987), Neutralization of Beam-Emitting Spacecraft by Plasma Injection, *Journal of Spacecraft and Rockets*, *24*, 227–231.

Setiawan (2009), Setiawan audio pages, `http://www.oocities.org/tube_theory/ElectronEmission.htm`, accessed: 2013-03-01.

Spindt, C. (1968), A Thin-Film Field-Emission Cathode, *Journal of Applied Physics*, *39*, 3504–3505.

Stone, N., and U. Samir (1981), Bodies in flowing plasmas: Laboratory studies, *Advances in Space Research*, *1*, 361–272.

Temple, D. (1999), Recent Progress in Field Emitter Array Development for High Performance Applications, *Materials Science and Engineering*, *24*, 185–239.

Tristancho, J. (2010), Implementation of a Femto-Satellite and a Mini-Launcher, Master's thesis, Universitat Politècnica de Catalunya.

Tskhakaya, D., K. Matyash, R. Schneider, and F. Taccogna (2007), The Particle-in-Cell Method, *Contributions to Plasma Physics*, *47*, 563–594.

Turner, L. (1976), *Electronics Engineer's Reference Book*, 4 ed., Newnes-Butterworths, Boston, Massachusetts.

VACCO (2010), Engineering fluid controls and etched products, `http://www.vacco.com/vacco/pdfs/mips2112.pdf`, accessed: 2010-03-01.

Valleé, J. (1998), Observations of the magnetic fields inside and outside the solar system: From meteorites (∼10 attoparsecs), asteroids, planets, stars, pulsars, masers, to protostellar cloudlets (<1 parsec), *Fundamentals of Cosmic Physics*, *19*, 319–422.

Verboncoeur, J. (2005), Particle Simulations of Plasmas: Review and Advances, *Plasma Physics and Controlled Fusion*, *47*, 1–29.

Verboncoeur, J., M. Alzes, V. Vahedi, and C. Birdsall (2001), Simultaneous Potential and Circuit Solution for 1-D Bounded Plasma Particle Simulator Codes, *Journal of Computational Physics*, *104*, 321–328.

Whaley, D., and C. Bellew (2009), 100 W Operation of a Cold Cathode TWT, *IEEE Transactions on Electron Devices*, *56*, 896–905.